©Copyright 2016
Todd Karin

Optical and Spin Properties of Defect-Bound Excitons in Semiconductors

Todd Karin

A dissertation
submitted in partial fulfillment of the
requirements for the degree of

Doctor of Philosophy

University of Washington

2016

Reading Committee:

Kai-Mei C. Fu, Chair

Xiaodong Xu

Boris Spivak

Program Authorized to Offer Degree:
Physics

University of Washington

Abstract

Optical and Spin Properties of Defect-Bound Excitons in Semiconductors

Todd Karin

Chair of the Supervisory Committee:
Professor of Physics Kai-Mei C. Fu
Physics Department

The physical properties of semiconductor defects are highly relevant for future quantum technologies and current semiconductor device performance. Optical spectroscopy is a powerful tool for investigating a wide variety of defect properties, motivating us to develop a generalized theory of spontaneous emission from multi-carrier bound excitons. We apply this theory to the neutral-acceptor bound exciton, finding three distinct radiative lifetimes. Next, we utilize our knowledge of bound-exciton transitions to measure the spin lifetime of donor-bound electrons. These measurements motivate the use of shallow-dopant-bound spins as qubits for quantum information, and we explore possible pathways for isolating a single shallow donor or acceptor. Lastly, we investigate excitons bound to stacking faults, a common extended semiconductor defect, finding ultra-homogeneous linewidths and a giant exciton dipole moment. These feature imply that stacking faults could potentially be useful for studying many-body physics in strongly-interacting exciton gases.

TABLE OF CONTENTS

Page

List of Figures v

List of Tables viii

Chapter 1: Introduction to semiconductor defects 1
- 1.1 Fundamental properties of point and extended semiconductor defects 1
- 1.2 Crystal defects for investigating condensed matter physics 3
- 1.3 Quantum information processing with defect spins 4
- 1.4 Effects of defects on classical devices 6

Chapter 2: Radiative properties of multi-carrier bound excitons in GaAs . . 8
- 2.1 Abstract 8
- 2.2 Introduction 8
- 2.3 Radiative decay of multi-carrier bound excitons: theory 9
- 2.4 Acceptor-bound exciton system 12
- 2.5 Validity of the $k = 0$ approximation for acceptor-bound exciton . . . 16
- 2.6 Time- and polarization-resolved photoluminescence of A^0X 17
- 2.7 Density matrix model of A^0X photoluminescence 17
- 2.8 Conclusion 19

Chapter 3: Radiative properties of Stacking Faults in GaAs 20
- 3.1 Abstract 20
- 3.2 Introduction 20
- 3.3 Stacking fault photoluminescence. 21
- 3.4 Nature of hole in SF exciton 22
- 3.5 Non-reciprocal photoluminescence 24
- 3.6 Magneto-Stark effect 25
- 3.7 Polarization dependence of SF-bound-exciton PL 28

3.8 Transport of 2D excitons 29
3.9 Conclusion 30

Chapter 4: Dislocations 32
4.1 Introduction 32
4.2 Experiment 34
4.3 Conclusion 37

Chapter 5: Longitudinal spin-flip time of donor-bound electron 39
5.1 Abstract 39
5.2 Introduction 39
5.3 Samples and experimental technique 41
5.4 Experimental Results 44
5.5 Theory 46
5.6 Conclusion 58

Chapter 6: Progress towards isolating a single point defect 60
6.1 Introduction 60
6.2 Stimulated emission of acceptor-bound exciton 61
6.3 Donor isolation with ground state depletion microscopy 68
6.4 Isolating a single shallow dopant with a semiconductor heterostructure 71

Chapter 7: Outlook 80

Appendix A: Dipole operator for band-to-band transitions 82

Appendix B: Basis states and dipole matrix elements for A^0X 85
B.1 Basis states for A^0X 85
B.2 Dipole Matrix Elements of A^0X 87

Appendix C: Generalized Weisskopf-Wigner theory for spontaneous emission from multiple excited levels 89

Appendix D: Supplemental information for donor-bound electron spin relaxation 94
D.1 Magneto-photoluminescence spectra for GaAs, InP, and CdTe 94
D.2 GaAs and CdTe T_1 measurements 94

D.3 Surface depletion effects 96
D.4 Numerical solution of donor-bound electron in magnetic field 98
D.5 Theory of spin-relaxation via the admixture mechanism 99
D.6 Spin relaxation via the direct spin-phonon mechanism 110

Appendix E: Numerical modeling of time and polarization-resolved A^0X photoluminescence 114
E.1 Density matrix model for time-resolved photoluminescence 114
E.2 Fit of time resolved data to model 115
E.3 Polarization of PL to determine dominant coupling in A^0X 118
E.4 Photoluminescence Excitation Spectroscopy of A^0X 121

Appendix F: Details of stacking fault experiments and theory 123
F.1 Stacking Fault formation 123
F.2 Stacking fault photoluminescence linewidth 123
F.3 Homogeneity of PL from the SF pyramid structure 125
F.4 Temperature and power dependence 127
F.5 Magneto-Stark Hamiltonian 128
F.6 Heavy hole – light hole splitting 130
F.7 Hamiltonian by symmetry 133
F.8 Supplemental Angle Resolved Data 135
F.9 Quantitative interpretation of Angle Resolved Data 138
F.10 Spectrally resolved confocal imaging of stacking fault structures . . . 139
F.11 Temperature and power dependence 140
F.12 Polarization dependence of Stacking Fault PL 143
F.13 Experimental polarization dependence 152
F.14 Methods 153
F.15 Photoluminescence spectroscopy system 153
F.16 2D Exciton Transport 156
F.17 Stacking Fault Generation 158
F.18 SEM of surface 159

Appendix G: Selected Character Tables 161

Bibliography 163

LIST OF FIGURES

Figure Number Page

2.1 Dipole matrix elements for exciton recombination 10
2.2 Acceptor bound exciton PL spectrum in GaAs 12
2.3 Energy level diagram of A^0X and A^0 13
2.4 Polarization- and time-resolved photoluminescence from acceptor-bound exciton 14
3.1 Radiative recombination at stacking fault structures in GaAs 21
3.2 Stacking fault photoluminescence as a function of magnetic field and orientation 23
3.3 Angle-resoved photoluminescence of stacking fault bound exciton . . . 26
3.4 Polarization dependence of stacking fault exciton and comparison to theory 29
3.5 Transport of excitons in stacking fault plane 31
4.1 Confocal scan of dislocations bordering stacking fault structures . . . 33
4.2 Geometry of stacking fault structures 34
4.3 Radiative and non-radiative recombination at dislocations 36
4.4 Correlation of dislocation and stacking fault PL energy for trapezoid defects 37
5.1 Optical pumping and spin-lifetime measurement of donor-bound electrons in InP 43
5.2 Experimental donor-bound electron spin lifetimes vs Zeeman splitting 44
5.3 Temperature dependence of donor-bound electron spin lifetimes . . . 45
5.4 T_1 as a function of Zeeman splitting for CdTe 46
5.5 Schematic of spin-relaxation mechanisms 50
5.6 Theoretical spin-relaxation time for donor-bound electrons via the admixture mechanism 52
5.7 Theoretical spin-relaxation time for donor-bound electrons via the direct spin-phonon mechanism 57

6.1 Schematic of super-resolution enhancement needed to isolate single point defect . . . 61
6.2 Stimulated emission of acceptor bound exciton. . . . 63
6.3 Power dependence of stimulated emission of acceptor bound exciton. . 64
6.4 Spectral hole burning of A^0X . . . 65
6.5 Stimulated emission depletion of A^0X theory predictions . . . 67
6.6 STED laser power broadening . . . 68
6.7 Principle of ground state depletion microscopy . . . 69
6.8 Ground state depletion proof of principle . . . 70
6.9 Schematic for isolating a single impurity with a heterostructure . . . 72
6.10 Surface Fermi level pinning . . . 73
6.11 Tunneling ionization rate of an exciton in GaAs . . . 75
6.12 Band structure of final heterostructure device for isolating a single impurity. . . . 78
6.13 Confocal scan showing spatial inhomogeneity of acceptor PL . . . 79

B.1 Dominant interactions and splittings for acceptor-bound exciton . . . 86

C.1 Radiative decay for near-degenerate optical transitions . . . 92

D.1 Magneto-photoluminescence spectra for GaAs, InP and CdTe . . . 95
D.2 Optical pumping and spin-lifetime measurement of donor-bound electrons in CdTe . . . 96
D.3 Brightening effect of above-band-gap laser . . . 98
D.4 Energies of excited state orbitals vs. magnetic field of hydrogen atom 99
D.5 Gaussian approximation of Hydrogen wavefunction size vs. magnetic field . . . 104

E.1 Raw data and error analysis for acceptor-bound exciton lifetime measurement . . . 116
E.2 Acceptor-bound exciton polarization dependence under spin-spin coupling scheme and crystal field scheme . . . 120
E.3 Photoluminescence excitation spectroscopy of acceptor-bound exciton in GaAs . . . 122

F.1 Geometry of stacking fault defects . . . 124
F.2 High resolution photoluminescence spectrum of stacking fault . . . 124

F.3 Spectrometer instrument resolution and stacking fault linewidth . . . 125
F.4 Photoluminescence spectra homogeneity amongst stacking fault structures . . . 126
F.5 Stacking fault structures in two different orientations . . . 127
F.6 Temperature and power dependence of the stacking fault photoluminescence . . . 129
F.7 GaAs crystalline lattice showing stacking fault plane . . . 130
F.8 Symmetry operations of C_{3v} . . . 133
F.9 Photoluminescence spectra at magnetic field for different stacking fault structures . . . 136
F.10 Asymmetry of stacking fault photoluminescence line center vs. magnetic field . . . 137
F.11 Homogeneity of SF emission line center over a single SF . . . 141
F.12 Temperature and power dependence of the SF PL line at zero applied field . . . 142
F.13 Coordinate system for stacking fault polarization dependence . . . 144
F.14 Polarization dependence of stacking fault exciton PL, comparison to theory . . . 152
F.15 Polarization dependence of stacking fault emission . . . 153
F.16 Schematic of the scanning confocal microscopy system . . . 154
F.17 Stacking fault pyramid size schematic . . . 156
F.18 Resonant excitation of stacking fault bound exciton . . . 157
F.19 Transport of stacking fault excitons created with resonant excitation . 158
F.20 Resonant excitation of stacking fault exciton and observation of transport without background subtraction . . . 159
F.21 Scanning electron micrograph of oval defects . . . 160

LIST OF TABLES

Table Number Page

5.1 Sample parameters for donor-bound electron spin-lifetime study . . . 42
5.2 Material parameters relevant to donor-bound electron spin-relaxation in GaAs, InP, and CdTe 51

B.1 Normalized dipole matrix elements for acceptor-bound exciton 88

E.1 Error analysis for acceptor-bound exciton lifetime measurement . . . 118
E.2 Normalized dipole matrix elements for acceptor-bound exciton in the (incorrect) spin-spin coupling scheme 119

G.1 Character table for double group of T_d 161
G.2 Character table for the double group of C_{3v} 161
G.3 Character table for double group of O_h 162

ACKNOWLEDGMENTS

This dissertation is the product of many years of collaboration with countless smart and dedicated scientists.

First, I would like to express my sincere appreciation to my advisor Kai-Mei Fu. The optical spintronics lab has been an excellent place to study both experimental and theoretical condensed matter physics. I cannot imagine a better advisor: Kai-Mei both challenged me and gave me the freedom to develop my own ideas and methods.

I'd also like to thank the members of my reading committee: Boris Spivak and Xiaodong Xu, whose expertise in condensed matter is invaluable.

Next, I'd like to thank all of the researchers I've had the pleasure of working with over the years. Russell Barbour taught me much of what I know about optical systems. Xiayu Linpeng worked tirelessly on most of the experiments and theories presented in this thesis. M. M. Glazov is responsible for much of the theory on spin-relaxation and the magneto-Stark effect. In addition, I acknowledge my collaborators John Schaibley, Pasqual Rivera, M. V. Durnev, Ivchenko, Cameron Johnson, Kelsey Bates, Patrick Wihelm, Benjamin Ebinger, Sarah Harvey, E. Ya. Sherman, Kyle Seyler, Ding Zhong, Maria Viitaniemi and Lauren Gagnon.

I'd also like to acknowledge past and present Fu lab members for providing an excellent research community: graduate students Michael Gould, Ed Kleinsasser, Nicole Thomas, Yaxuan Zhou and Srivatsa Chakravarthi; postdoc Emma Schmidgall; undergraduates Kelsey Bates, Maya Dunn, Seth Hyra, Brianna Birkel, Matthew Stanfield, Ian Christen, Jannel Banks, Feng Xiong, John Shin, Kevin Jamison, John Raihala, Chris Chen, Chuting Wang, Edward Roberts, Zhiting Zhu, Emma Lorenzen and Alyssa Trinh.

I would like to thank the physics department at the University of Washington for providing a strong foundation and an excellent research space. In addition our graduate student coordinator; Catherine Provost was an exceptionally helpful resource.

I'm also grateful for to our growth collaborators, especially Arne Ludwig, Andreas

Wieck and Ashish Rai for producing the stacking fault and heterostructure samples. We also relied on a number of high-quality samples from Satoru Seto, Colin Stanley, M. C. Holland, Simon Watkins, H. Hiroyama and M. L. W. Thewalt.

Lastly, I'd like to thank my friends, family and partner Adrianne for providing continual love and support over the years.

Chapter 1

INTRODUCTION TO SEMICONDUCTOR DEFECTS

The importance of defects to the creation of useful semiconductor devices cannot be overstated—introducing charged impurities creates an electronic potential that controls the motion of charge carriers. Point and extended defects are numerous in kind and varied in behavior, making some defects attractive for next-generation quantum technologies, others intriguing for their fundamental physics, and still others a challenging hurdle for real-world devices.

We can divide the motivation for this work into three main areas. First, crystal defects have emerged as an attractive system for quantum information processing. We will explore one promising qubit system, spins bound to point defects, in order to determine their overall viability for quantum information. Second, many crystal defects have a well-understood structure, making them useful testbeds for condensed matter theory. We will investigate the extent to which spin-relaxation rates can be computed from well-understood theories. Lastly, extended defects can strongly affect the performance of semiconductor devices. Through optical studies, we probe the nature of extended defects, yielding information which can be used to improve devices.

A fundamental understanding of semiconductor defect physics is crucial to all of these larger goals. In this work, we will repeatedly return to how the symmetry of a crystalline defect can predict its optical and electronic properties. The concrete predictions arising from defect symmetry can often be rigorously tested using photoluminescence spectroscopy.

1.1 Fundamental properties of point and extended semiconductor defects

The fundamental properties of semiconductor defects have far-reaching importance to a wide variety of fields. These fundamental properties refer to a number of questions, including

(i) **Defect structure.** What is the atomic structure of the defect? Do defects have multiple possible configurations? Does the structure depend on the electronic state? What is the energy barrier to reconfiguration? Is the defect surrounded by an extended strain field?

(ii) **Defect symmetry.** What is the symmetry group of the crystal defect, i.e. which proper and improper rotations leave the defect unchanged?

(iii) **Energy levels.** What are the eigenenergies and eigenstates of the defect? Can the defect's electronic potential be described with effective mass theory (shallow defects) or is a tight-binding model more appropriate (deep defects)? Which charge states are stable? How do the energy levels depend on strain?

(iv) **Radiative properties.** What are the dipole moments, selection rules, polarization dependencies, and radiative lifetimes of optical transitions between energy levels?

(v) **Non-radiative relaxation.** Is the defect an efficient center for non-radiative recombination? How do these rates depend on the Fermi level?

(vi) **Spin properties.** What are the spin states and spin-relaxation rates of carriers bound to the defect? Does the defect have a nuclear spin? How do the spins interact with each other and with phonons?

(vii) **Defect Interactions.** Can carriers tunnel from one defect to another? Can defects lower their energy by merging with another defect?

Photoluminescence (PL) spectroscopy is a powerful tool for studying a variety of defect properties because radiative transitions are sensitive to the underlying energy levels, state occupation and symmetry of the defect. Moreover, optical excitation changes state occupation levels, allowing PL to probe time-dependent processes. Lastly, in contrast to electron microscopy, PL micrscopy can be performed with sub-band-gap light, allowing optical imaging of the interior of a semiconductor.

Many semiconductor defects can bind multi-carrier excitons, and there is a need for a unified theory of the optical properties of these complexes. In Chapter 2, we develop a general theory for using the basic defect symmetry to derive radiative properties such as polarization selection rules and radiative lifetimes for multi-carrier excitons. We confirm this theory with time- and polarization-resolved spectroscopy

of the neutral-acceptor bound exciton, finding three distinct lifetimes.

Next, in Chapter 3, we observe that for stacking-fault bound excitons, the photoluminescence energy surprisingly depends on the sign of the magnetic field. Using a symmetry analysis of the stacking fault, we explain this feature by the magneto-Stark effect. We also find that the general theory developed in Ch. 2 is useful for determining the nature of the hole in the stacking fault exciton.

In Chapter 4, we study dislocations that exist at the edges of stacking faults, finding that some dislocations are efficient centers for radiative recombination, contrary to the typical expectation that dislocations are strong non-radiative recombination centers.

Next, in Chapter 5, we turn to a detailed experimental and theoretical treatment of spin-relaxation rates for donor-bound electrons. Because the donor-bound electron is a well-understood defect, it is possible to perform analytic and numerical calculations of the spin-relaxation rates due to various phonon interactions. For some materials, we find excellent agreement with experiment with no fit parameters.

The long spin-relaxation times for donor-bound electrons motivates using these spins as a qubit for quantum information. However, even in the most pure samples, donors densities are too high to probe a single donor with a diffraction limited microscope. However, for most quantum information schemes, single quantum systems must be isolated. In Chapter 6, we explore methods for isolating a single shallow donor or acceptor in a bulk semiconductor. We find encouraging results towards using super-resolution microscopy and using a semiconductor heterostructure for isolating a single donor or acceptor.

1.2 Crystal defects for investigating condensed matter physics

Semiconductor defects are powerful probes of condensed matter physics. In many cases, defects can be described by a straightforward, albeit complex, physical theory, e.g. effective mass theory or *ab initio* methods. The modern advent of density functional theory has proven a major boon to the understanding of crystal physics. Now, more than ever, the fundamental properties of individual defects can be precisely predicted, allowing for detailed experimental tests of the basic theories used to describe defects.

Many defects have shallow binding potentials for electrons and holes, leading to

wavefunctions that extend over many lattice sites. Carriers bound to these defects are well described in the effective-mass approximation. This feature makes complex calculations on defects reducible to a simpler few-particle Schrodinger equation, where the carriers can have a mass that depends on direction. In Chapter 5, we calculate, from basic principles, the spin-relaxation rate of electrons bound to donors. These measurements are a basic test of the theory of spin-phonon interactions in the effective mass approximation.

Lastly, we note that high-quality 2D systems have resulted in a wide variety of experimental discoveries, including the quantum hall and fractional quantum hall effects [51, 205]. Moreover, there has been recent interest in the physics of indirect excitons in coupled quantum wells, which can show effects such as Bose-Einststein condensation [94, 155] and exciton-exciton interactions [35]. In Chapter 3, we find that large-area stacking faults in GaAs form an ultra-homogeneous 2D excitonic system, similar to the indirect-exciton system in coupled quantum wells. The large dipole moments of these stacking fault excitons make this system promising for studying the physics of a strongly interacting exciton gas.

1.3 Quantum information processing with defect spins

The field of quantum information processing (QIP) is currently one of the most vibrant and exciting areas of physics research. QIP has great interest both for the fundamental physics it explores and the technologies it promises to enable.

The basic unit of quantum information is the qubit, which in it's simplest implementation is a controllable two-level quantum system. The states of the system are denoted $|0\rangle$ and $|1\rangle$ and a fundamental postulate of quantum mechanics is that a superposition of those two states, $\alpha |0\rangle + \beta |1\rangle$, is an equally valid state. The enormous power of quantum computers over classical ones comes from two physical phenomena: interference and superposition. An example is the unstructured search problem: for example, finding a name that corresponds to a given phone number in a phone book [17]. Classical algorithms can do no better than check each phone number until the correct one is found. In quantum algorithms, the initial state can be put into a superposition of all phone numbers and every number can be partially tested at the same time. After building up statistics, the correct name can be found with a quadratic speed up over classical computing.

Quantum simulation strives to study a complex quantum system by performing experiments on an engineered quantum system. Modeling large quantum systems is difficult with classical computers because the computation cost scales exponentially with system size [10]. Because of this exponential cost, quantum computers with only 30-100 qubits can surpass the abilities of even the best classical supercomputers [10].

There are multiple physical implementations for QIP, each with advantages and disadvantages. The most advanced technologies for quantum information are currently [126]: trapped ions [143, 23], superconducting circuits [53], photonic networks [147] and defect spins in solids. The different technologies have different strengths and could each find a niche application.

Because of the highly-advanced semiconductor industry, solid-state-based quantum information technologies are expected to be scalable. Of the solid-state quantum systems, the most popular are quantum dots [213], the nitrogen-vacancy center in diamond [19], rare-earth doped crystals [120] and donor-bound electrons [188]. Quantum dots have many attractive properties, but entangling multiple qubits is difficult due to optical inhomogeneity. The nitrogen-vacancy center is also a promising qubit candidate, but suffers from a low rate of zero-phonon emission, meaning that emission of a photon is often accompanied by a coherence-destroying phonon. Rare-earth ions can have extremely long ~ 1 s coherences times, but suffer from low fluorescence yield [120]. By contrast, donor-bound electrons have long milisecond to second spin-relaxation times [74, 164, 188], high optical homogeneity, and strong zero-phonon emission, making them a promising qubit candidate. The current main roadblock for using defect spins is the difficulty of isolating a single one. Single center isolation is necessary because realistic QIP requires error correction, which typically must be performed on isolated single qubits.

A donor is a substitutional impurity in the crystal lattice that has one more valence electron than the host atom it replaces. In addition, the nucleus of the impurity has one more proton than the atom it replaces. This effectively creates a fixed positive charge in the lattice and an extra mobile electron. At low enough temperatures, the electron binds to the donor as an effective hydrogen atom. Surprisingly, even though the effective Bohr radius of the donor bound electron includes thousands of lattice sites, the average spin-flip time for the electron can exceed 1 ms [74]. In Chapter 5, we explore how the spin-relaxation time depends on magnetic field and donor density

in GaAs, InP and CdTe. This work clarifies the fundamental limits for using donor-bound electrons as qubits for QIP. Finally, in Chapter 6, we investigate novel methods for isolating single impurity-bound spins, making strides towards solving the single-qubit-isolation problem for shallow donor or acceptor.

1.4 Effects of defects on classical devices

Defects can affect semiconductor devices in a wide variety of ways, some of the most important are:

(i) **Band engineering.** Dopants introduce fixed and mobile charges, modifying the Fermi level and creating a spatially-varying electronic potential.

(ii) **Mobility.** Defects act as scattering centers for electrons and holes, lowering the mobility and lowering device performance.

(iii) **Degradation.** Defects can form during device operation, leading to finite device lifetimes.

(iv) **Non-radiative recombination.** Point and extended defects can have energy levels in the band gap leading to non-radiative recombination pathways.

(v) **Mechanical properties.** Extended defects are responsible for many of the mechanical properties of materials, e.g. plasticity.

(vi) **Optical properties.** Defects have optical transitions, and even a small number of defects can dominate the optical properties of a material.

Defects are complicated, and understanding their properties is essential to designing better semiconductor devices. In the following, we will expand on the typical issues created by a few specific defects.

Point defects are 0D defects comprised of a few substitutional and/or vacant atoms in the host crystal and are key players in determining semiconductor device performance. For example, solar cells made from p-type silicon suffer from a variety of defects. Fe impurities are positively charged in p-type silicon, leading to a large reduction of minority-carrier lifetime. The second main issue with p-type silicon is the boron used for doping can bind with available oxygen to form a permanent impurity complex, providing non-radiative recombination centers [29]. The detailed electronic structure and configuration-dependent energy is important for understanding how

defects affect device performance and why these defects form. Understanding defect physics is often the first step to solving problems caused by point defects.

Dislocations are a 1D extended defect that have a serious impact on the quality of solar cells and light emitting diodes (LEDs). The dislocation core can contain dangling bonds, which often result in mid-band-gap energy levels. These deep energy levels provide non-radiative recombination centers and limit the performance of LEDs and solar cells.

Stacking faults are a 2D extended defect composed of a few mis-ordered lattice planes. Generally stacking faults are electrically neutral; stacking faults by themselves do not introduce mid-gap energy levels because they do not contain any dangling bonds. However, when stacking faults terminate or change direction, a dislocation exists at the border. In Chapter 4 we use optical imaging to demonstrate that certain dislocations are strong non-radiative recombination centers, while others are not.

Lastly, we note that these defects can interact in many ways. Stacking faults and dislocations can attract point defects because point defects often have lower energy if they migrate to a location where the crystal is already perturbed. For example, sodium can migrate along stacking faults in silicon solar cells, leading to a conductive channel between the p and n regions and shorting out the solar cell [144]. Defect interactions are widespread and complex; a study of one type of defect often needs to consider its interaction with others.

Point and extended defects are crucial players influencing nearly all aspects of semiconductor devices. Moreover, with the advent of new experimental and theoretical tools, crystal defects can be studied with ever-greater precision. It is a testament to the richness of the field that despite decades of concentrated research and a trillion-dollar semiconductor industry, crystal defects are still a vibrant field of study.

Chapter 2

RADIATIVE PROPERTIES OF MULTI-CARRIER BOUND EXCITONS IN GAAS

2.1 Abstract

Excitons in semiconductors can have multiple lifetimes due to spin dependent oscillator strengths and interference between different recombination pathways [111]. In addition, strain and symmetry effects can further modify lifetimes via the removal of degeneracies. In this chapter, we present a convenient formalism for predicting the optical properties of $k = 0$ excitons with an arbitrary number of charge carriers in different symmetry environments. Using this formalism, we predict three distinct lifetimes for the neutral acceptor bound exciton in GaAs, and confirm this prediction through polarization dependent and time-resolved photoluminescence experiments. We find the acceptor bound-exciton lifetimes to be $T_o \times (1, 3, \frac{3}{4})$ where $T_o = (0.61 \pm 0.12)$ ns. Furthermore, we provide an estimate of the intra-level and inter-level exciton spin-relaxation rates by fitting a 12-level density matrix model to the time and polarization resolved data. We find that these rates make good predictions for the polarization dependence of A^0X under continuous-wave excitation. Lastly, we expand upon Ref. [111] by confirming the applicability of the $k = 0$ approximation for A^0X in Sec. 2.5.

2.2 Introduction

The radiative properties of excitons in semiconductors are of fundamental interest in current semiconductor physics as well as of technological interest due to their impact on optoelectronic device performance. While the optical selection rules for the recombination of a conduction band electron and valence band hole are well understood [60, 45], the selection rules for excitonic complexes with more than two carriers are complicated due to the multiple spin and angular degrees of freedom. In high symmetry environments, exciton lifetimes can be modified by interference between different recombination pathways [62, 217, 209]. Reducing the symmetry can

modify exciton lifetimes by energetically separating excitonic states, thus removing the possibility for interference. Alternately, in quantum dots, spin selection rules forbid the so-called dark exciton from recombining, creating a radiative bottleneck in applications requiring bright sources [50] or alternatively a possible long-lived storage state for quantum information applications [153].

In this chapter, we provide a convenient and general framework for describing the optical properties of arbitrary $k = 0$ excitonic complexes. We use the second quantization formalism [117] for calculating dipole matrix elements of an excitonic complex with an arbitrary number of electrons and holes in a III-V direct band gap semiconductor. Using a generalized Weisskopf-Wigner theory, we show how special spontaneous emission eigenstates and multiple radiative lifetimes may emerge. We predict three radiative lifetimes of the neutral acceptor bound-exciton ($\mathrm{A^0X}$) in bulk GaAs. We confirm the theory by performing polarization dependent and time-resolved photoluminescence experiments on the $\mathrm{A^0X}$ system.

2.3 Radiative decay of multi-carrier bound excitons: theory

Exciton lifetimes in III-V direct band gap semiconductors can be derived from the dipole operator $\boldsymbol{\mu} = e\mathbf{r}$ for band-to-band recombination between a $j = \frac{1}{2}$ conduction-band electron and a $j = \frac{3}{2}$ valence-band hole [45, 60], shown schematically in Fig. 2.1(a). In the second quantization formalism, the dipole operator is

$$\begin{aligned}\boldsymbol{\mu} = \mu_o \Bigg[& \frac{\hat{\mathbf{x}} + i\hat{\mathbf{y}}}{\sqrt{2}} \left(h_{\frac{3}{2}} e_{-\frac{1}{2}} + \frac{1}{\sqrt{3}} h_{\frac{1}{2}} e_{\frac{1}{2}} \right) \\ & - \frac{\hat{\mathbf{x}} - i\hat{\mathbf{y}}}{\sqrt{2}} \left(h_{-\frac{3}{2}} e_{\frac{1}{2}} + \frac{1}{\sqrt{3}} h_{-\frac{1}{2}} e_{-\frac{1}{2}} \right) \\ & + \sqrt{\frac{2}{3}} \hat{\mathbf{z}} \left(h_{-\frac{1}{2}} e_{\frac{1}{2}} + h_{\frac{1}{2}} e_{-\frac{1}{2}} \right) + \mathrm{H.C} \Bigg],\end{aligned} \tag{2.1}$$

where e_m (h_m) is the annihilation operator for an electron (hole) in the angular momentum state m, H.C. is the Hermitian conjugate, and μ_o is a spin-independent constant, shown schematically in Fig. 2.1(b), see Appendix A for derivation. We define the coordinate system $\hat{\mathbf{x}}$, $\hat{\mathbf{y}}$ and $\hat{\mathbf{z}}$ to be oriented along the [100], [010] and [001] crystallographic directions. The hole angular momentum state is labeled with the opposite sign of the corresponding unoccupied electron angular momentum state.

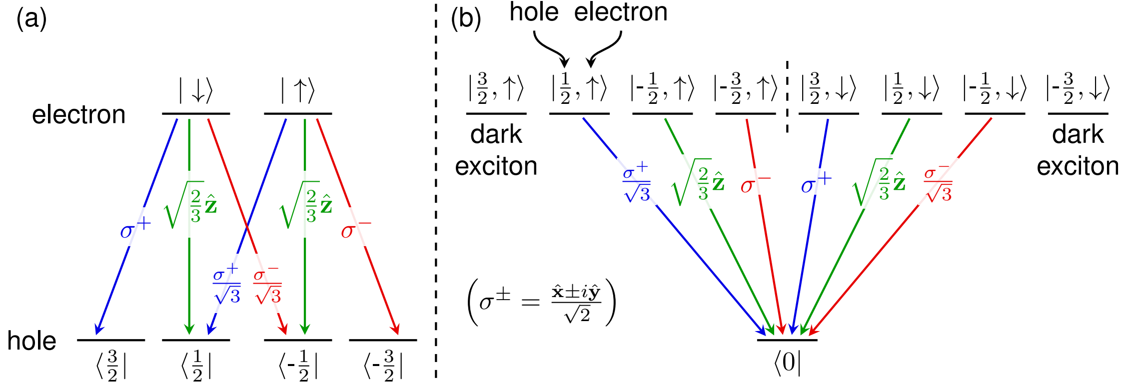

Figure 2.1: (a) Dipole matrix elements for exciton recombination in the electron picture. In this picture, an electron at the $k = 0$ point point makes a transition from the conduction band to the valence band, resulting in a photon of the specified polarization. Dipole matrix elements are for conduction to valence transitions, those for valence to conduction transitions are the complex conjugate. (b) Dipole matrix elements for annihilation of an electron-hole pair in the second quantization picture. The labeled arrows show the polarization of light emitted upon recombination of the corresponding electron-hole pair.

The dipole operator is shown schematically in Fig. 2.1.

Eq. 2.1 can be conveniently used to calculate the dipole matrix element between exciton states with an arbitrary number of charge carriers. For example, the dipole matrix element $\mathbf{p}_{ij}$ corresponding to the recombination of a two-carrier exciton with electron spin $-\frac{1}{2}$ and hole spin $+\frac{3}{2}$ is

$$\mathbf{p}_{0,e^\dagger_{-\frac{1}{2}}h^\dagger_{\frac{3}{2}}} = \langle 0| \boldsymbol{\mu} e^\dagger_{-\frac{1}{2}} h^\dagger_{\frac{3}{2}} |0\rangle = \mu_o \frac{\hat{\mathbf{x}} + i\hat{\mathbf{y}}}{\sqrt{2}}, \tag{2.2}$$

where $|0\rangle$ is the semiconductor vacuum state.

We describe the radiative lifetimes of excitons using a generalized Weisskopf-Wigner theory. The spontaneous emission rates from a set of degenerate excited states to a set of degenerate ground states are the eigenvalues of αS, where $S = \mathbf{p}^\dagger \cdot \mathbf{p}$ (Appendix C). Here $\mathbf{p}$ is a matrix of the vector dipole matrix elements $\mathbf{p}_{ij} = \langle g, i| \boldsymbol{\mu} |e, j\rangle$ between ground state i and excited state j, $\alpha = (1/4\pi\epsilon)(4\omega^3 n^3/3\hbar c^3)$, ω the frequency of the transition, ϵ the permittivity of the material, n the index of refraction, and c the speed of light. The time dependence of the excited state probability amplitudes

b satisfy

$$\frac{d}{dt}\mathbf{b} = -\frac{\alpha}{2} S\, \mathbf{b}, \tag{2.3}$$

corresponding to exponential decay. Physically, Eq. 2.3 implies that radiative lifetimes are modified by constructive or destructive interference between different recombination pathways. In addition, it highlights how exciton states organize into spontaneous emission eigenstates (eigenvectors of S) with decay rates given by the eigenvalues of αS.

Before applying this formalism to the three-carrier acceptor bound-exciton system, as an example we treat the simpler two-carrier light-hole exciton. Light-hole excitons, consisting of an $m_j = \pm\frac{1}{2}$ valence hole and a conduction electron, split from heavy-hole excitons ($m_j = \pm\frac{3}{2}$) in reduced symmetry environments such as quantum dots, quantum wells and strained GaAs. The formalism yields the expected four spontaneous emission (SE) recombination rates [62]:

SE Rate (normalized)	SE eigenstate
1/3	$e^\dagger_{\frac{1}{2}} h^\dagger_{\frac{1}{2}} \vert 0\rangle$
1/3	$e^\dagger_{-\frac{1}{2}} h^\dagger_{-\frac{1}{2}} \vert 0\rangle$
4/3	$\frac{1}{\sqrt{2}}\left(e^\dagger_{\frac{1}{2}} h^\dagger_{-\frac{1}{2}} + e^\dagger_{-\frac{1}{2}} h^\dagger_{\frac{1}{2}}\right) \vert 0\rangle$
0	$\frac{1}{\sqrt{2}}\left(e^\dagger_{\frac{1}{2}} h^\dagger_{-\frac{1}{2}} - e^\dagger_{-\frac{1}{2}} h^\dagger_{\frac{1}{2}}\right) \vert 0\rangle$.

(2.4)

The aligned spin $e^\dagger_{\frac{1}{2}} h^\dagger_{\frac{1}{2}}|0\rangle$ and $e^\dagger_{-\frac{1}{2}} h^\dagger_{-\frac{1}{2}}|0\rangle$ excitons decay independently because of the orthogonal polarizations (σ^+ and σ^-) of the transitions. On the other hand, constructive and destructive interference of the $\hat{\mathbf{z}}$ recombination pathway leads to a bright and dark exciton. While it is experimentally challenging to observe the brightest light-hole exciton due its $\hat{\mathbf{z}}$ polarization, this exciton has recently been observed using magnetic-field measurements in strain-engineered quantum dots [98]. We note that identification could alternatively be made through lifetime measurements at zero magnetic field.

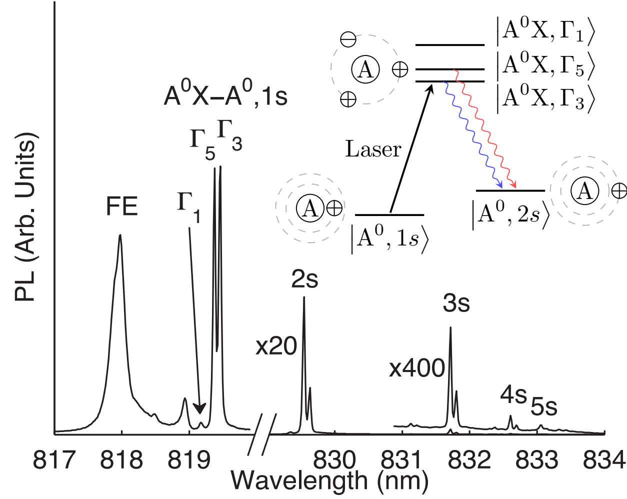

Figure 2.2: PL spectrum of $|A^0X\rangle \rightarrow |A^0, ns\rangle$ and free exciton (FE) transitions using above band and resonant excitation. The A^0X Γ_3-Γ_5 splitting is clearly resolved. The spectrum left of the cut was taken using above band excitation at 815 nm. The spectrum right of the cut used resonant excitation of $|A^0, 1s\rangle \rightarrow |A^0X, \Gamma_5\rangle$. Because of spin relaxation between A^0X states, the different excitation conditions result in different Γ_3 to Γ_5 intensity ratios left and right of the cut. The inset shows an energy level diagram and cartoon of the A^0-A^0X system. $T = 2.3\,\mathrm{K}$.

2.4 Acceptor-bound exciton system

We now turn to the neutral acceptor-bound exciton (A^0X), consisting of two $j = \frac{3}{2}$ holes and one $j = \frac{1}{2}$ electron bound to a substitutional acceptor impurity [26, 86]. By recombination of the electron with one of the holes, A^0X decays radiatively to a neutral acceptor (A^0, a hole bound to an acceptor). Effective mass theory can be used to show that A^0 has hydrogenic levels 1s, 2s, etc. In high-purity p-type GaAs, A^0X to A^0 1s, 2s, etc. photoluminescence (PL) is readily observed and provides a useful probe for resonant excitation, as shown in Fig. 2.2. Remarkably, the ensemble transition linewidths of this solid-state ensemble system are less than 40 μeV (Appedix E.4, spectral linewidths in Fig. 2.2 are limited by the instrument resolution).

Though the origin of the A^0X fine structure was once a controversy, strain experiments support hole-hole and crystal field coupling as the dominant mechanisms for splitting the 12 fold degenerate A^0X [139, 108]. In this scheme, the two holes lie in

antisymmetric spin states with total spin 0 and 2 [139]. Hole-hole coupling splits the $j = 0$ states from $j = 2$ states. In zinc-blende semiconductors which possess crystal fields with T_d symmetry, the $j = 2$ states further split into two manifolds: Γ_5 with multiplicity 3 and Γ_3 with multiplicity 2 (character table for T_d in Appendix. G). The full specification of A^0X also includes the spin of the electron, denoted as $\uparrow$ or $\downarrow$ (Fig. 2.3).

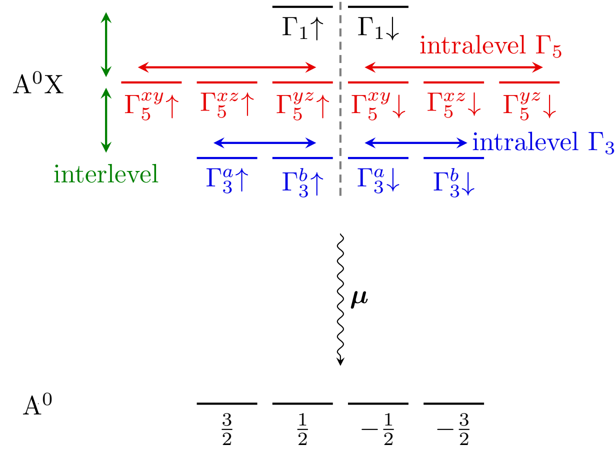

Figure 2.3: Full energy level diagram for A^0X and A^0 system. The spin of the electron is denoted by $\uparrow$,$\downarrow$. Intra-level and inter-level relaxation cause a decay of the polarization visibility (Fig. 2.4b). Electron spin flips are not allowed, as depicted schematically by the dashed line. The crystal fields that split Γ_3 and Γ_5 lead to $\hat{\mathbf{x}}$, $\hat{\mathbf{y}}$, $\hat{\mathbf{z}}$ oriented along the crystallographic axes.

Our theory and experiments show that A^0X has multiple radiative lifetimes. To find the A^0X radiative lifetimes, we first compute the dipole matrix elements $\mathbf{p}_{ij} = \left\langle A^0, i \right| \boldsymbol{\mu} \left| A^0X, j \right\rangle$ for the different A^0 and A^0X states (Appendix C). The eigenvalues of $\mathbf{p}^{\dagger}{\cdot}\mathbf{p}$ are the radiative recombination rates of A^0X, and the inverse of these eigenvalues are the radiative lifetimes. An energy splitting between excited states causes a fast oscillation in the Weisskopf-Wigner theory which destroys the coupling between non-degenerate states (Appendix B.2). As such, only degenerate excited states are included in the dipole matrix when calculating the eigenvalues of $\mathbf{p}^{\dagger}{\cdot}\mathbf{p}$.

The A^0X spontaneous emission rates in spherical symmetry and no hole-hole spin

Figure 2.4: **a.** Dependence of light emitted from Γ_3 and Γ_5 on incident and collected polarization for $\mathrm{A}^0\mathrm{X} \to \mathrm{A}^0$ relaxation in resonant CW excitation. The dark green line shows the angle of excitation polarization, with horizontal $\hat{\mathbf{x}}$ corresponding to [100]. The polar plots show the PL emitted at the corresponding collection polarization angle. The ideal theory curves depict the polarization dependence in the absence of excited state relaxation. The theory curves give the angular PL dependence expected from the density matrix model fit to the time-resolved data (Fig. 2.4b). The data is PL collected from the $|\mathrm{A}^0\mathrm{X}, \Gamma_n\rangle \to |\mathrm{A}^0, 2\mathrm{s}\rangle$ transition while exciting the Γ_3 or Γ_5 line at $\hat{\mathbf{x}}$ or $(\hat{\mathbf{x}} - \hat{\mathbf{y}})/\sqrt{2} = -45^\circ$ polarizations (Fig. 2.2). All the data is normalized using the same constant. The normalization between the ideal curves and the theory curves is arbitrary. $T = 2.3$ K. **b.** The Γ_3 and Γ_5 PL as a function of time for polarizations x $\propto$ [100], y $\propto$ [010], 45° $\propto$ [110] and -45° $\propto$ $[1\bar{1}0]$ after an excitation pulse at $t = 0$. The lines are a simultaneous fit of the density matrix model to the 16 observed time dependent PL curves. Best fit parameters are given in the text.

coupling are proportional to

$$\overbrace{\left(1, 1, 2, 2, 2, 2, \tfrac{1}{3}, \tfrac{1}{3}, \tfrac{1}{3}, \tfrac{1}{3}, \tfrac{1}{3}, \tfrac{1}{3}\right)}^{\frac{3}{2}\otimes\frac{3}{2}\otimes\frac{1}{2}}. \tag{2.5}$$

When hole-hole spin coupling is introduced, $j = 0$ states split from $j = 2$ states, but the spontaneous emission rates remain unchanged:

$$\overbrace{(1, 1)}^{j=0}, \overbrace{\left(2, 2, 2, 2, \tfrac{1}{3}, \tfrac{1}{3}, \tfrac{1}{3}, \tfrac{1}{3}, \tfrac{1}{3}, \tfrac{1}{3}\right)}^{j=2}. \tag{2.6}$$

With the inclusion of the zinc-blende crystal fields (which cause a Γ_5-Γ_3 splitting), we find that the spontaneous emission rates become proportional to

$$\overbrace{(1,1)}^{\Gamma_1},\overbrace{(1,1,1,1)}^{\Gamma_3},\overbrace{\left(\tfrac{4}{3},\tfrac{4}{3},\tfrac{4}{3},\tfrac{4}{3},\tfrac{1}{3},\tfrac{1}{3}\right)}^{\Gamma_5}. \tag{2.7}$$

Whereas previous studies of A^0X report only one lifetime [99, 67] ($T_o = (1.6\pm0.6)$ ns), a full study including spin and symmetry shows that A^0X has multiple lifetimes differing by up to a factor of 4. We can experimentally test this theory by studying the polarization dependence of photoluminescence (PL). If the system starts in an incoherent mixture of the four ground A^0 states, excitation light of polarization $\hat{\epsilon}_\mathrm{i}$ resonant with Γ_n will create an excited state density matrix in the Γ_n subspace proportional to

$$\rho_e^{(\Gamma_n)} = M_{\epsilon_\mathrm{i}}^{(\Gamma_n)\dagger} M_{\epsilon_\mathrm{i}}^{(\Gamma_n)}, \tag{2.8}$$

where $M_{\epsilon_\mathrm{i}}^{(\Gamma_n)} = \mathbf{p}^{(\Gamma_n)} \cdot \hat{\epsilon}_\mathrm{i}$, $\hat{\epsilon}_\mathrm{i}$ is the incident polarization and $\mathbf{p}^{(\Gamma_n)}$ are the dipole matrix elements corresponding to Γ_n (Appendix F.12). Eq. E.6 is valid in the limit of low excited state population. We note that this prescription includes the possibility of of hole-spin coherence, which is ignored in other treatments [101]. The PL emission from the states in Γ_n with polarization ϵ_f is proportional to

$$\mathrm{PL}^{(\Gamma_n)} = \mathrm{tr}\left(M_{\epsilon_\mathrm{f}}^{(\Gamma_n)} \rho_e^{(\Gamma_n)} M_{\epsilon_\mathrm{f}}^{(\Gamma_n)\dagger}\right). \tag{2.9}$$

Eq. 2.9 can be used to compute the arbitrary polarization dependence of A^0X-A^0 transitions. In the case of exciting Γ_n with linear polarization at an angle ϕ_i in the x-y plane and collecting linearly polarized light at ϕ_f ($\phi_n = 0$ corresponds to polarization along [100]), the angle dependent PL intensity is given by

$$\begin{aligned}
\mathrm{PL}^{(\Gamma_5)} &= \frac{I_o}{18}[5 + 4\cos(2\phi_\mathrm{i})\cos(2\phi_\mathrm{f}) + \sin(2\phi_\mathrm{i})\sin(2\phi_\mathrm{f})] \\
\mathrm{PL}^{(\Gamma_3)} &= \frac{I_o}{36}[4 + 3\sin(2\phi_\mathrm{i})\sin(2\phi_\mathrm{f})] \\
\mathrm{PL}^{(\Gamma_1)} &= \frac{I_o}{18},
\end{aligned} \tag{2.10}$$

where I_o is a constant. These functions are plotted in Fig. 2.4a for Γ_3 and Γ_5. Here we note that this simple angular dependence of excitonic PL can be used to verify

the relative inter-carrier and crystal field coupling for A^0X, once a subject of debate, without the need for applied strain or magnetic fields (Appendix F.12) [139, 108] . In the case where crystal fields have an observable effect, the excitonic PL can also be used to determine crystal orientation: e.g. Γ_5 emission will be strongest when exciting along [100] and collecting [100].

2.5 Validity of the $k = 0$ approximation for acceptor-bound exciton

In the previous sections, we developed the theory for radiative recombination of $k = 0$ excitons. In this section, we will discuss the reason for this constraint and when the results can be applied in more general circumstances.

The valence-band hole can be described by the Luttinger-Kohn Hamiltonian,

$$H_{LK} = \frac{\hbar^2}{2m_0}\left[-\left(\gamma_1 + \frac{5}{2}\gamma_2\right)\mathbf{k}^2 + 2\gamma_3(\mathbf{k}\cdot\mathbf{J})^2 - 2(\gamma_3-\gamma_2)(k_x^2J_x^2 + k_y^2J_y^2 + k_z^2J_z^2)\right], \tag{2.11}$$

where m_0 is the electron mass, γ_j are the Luttinger parameters, $\mathbf{k} = -i\nabla$ and $\mathbf{J}$ are the angular momentum matrices for $j = 3/2$ [215, 45, 134]. When $k = 0$, $H_{LK} = 0$, and the Luttinger-Kohn Hamiltonian does not affect the hole-spin states entering into the eigenstates of the problem. In the following, we will refer to the "$k = 0$ theory" when we calculate radiative properties without regard to how the Luttinger-Kohn Hamiltonian affects the quantization axis.

When $k \neq 0$, the Luttinger-Kohn Hamiltonian in the spherical approximation (i.e. $\gamma_3 = \gamma_2$) results in a hole quantization axis along $\mathbf{k}$. In this case, the hole spin eigenstate will be a function of $\mathbf{k}$ and it follows that holes with different $\mathbf{k}$ will have different luminescence properties using the prescription in Sec. 2.3 and 2.4. These complications can often be ignored. For the Luttinger Hamiltonian to have a significant affect on the hole eigenstates, it must have a magnitude comparable to other interactions which define a quantization axis and a state modification must be allowed by symmetry.

In the case of the A^0, symmetry of the ground state precludes any affect of the Luttinger-Kohn Hamiltonian on the eigenstates. The ground state acceptor-bound hole has a spherically symmetric envelope state and a $j = 3/2$ angular momentum state [215]. Thus the ground state lies in the irreducible representation $\Gamma_1^+ \otimes \Gamma_8^+ = \Gamma_8^+$ of the double group of O_h (Table G.3). This in turn implies that the cubic symmetry

of the Luttinger-Kohn Hamiltonian cannot cause a splitting of the A^0 1s ground state. We also note that because of the crystal field splitting of symmetry T_d (which splits the A^0X states split into Γ_1, Γ_3 and Γ_5 irreducible representations of T_d), the further introduction of the Luttinger-Kohn Hamiltonian with O_h symmetry does not cause additional splitting because T_d is a subgroup of O_h. A full solution of A^0 including the Luttinger-Kohn Hamiltonian has been performed in the literature [211, 215].

2.6 Time- and polarization-resolved photoluminescence of A^0X

We measure the polarization dependence of the $A^0 - A^0X$ transition using resonant continuous-wave (CW) excitation. Experiments were performed on a p-type GaAs crystal (6 μm GaAs grown by molecular beam epitaxy on a GaAs substrate, $N_a = 1.2 \cdot 10^{14}$ cm^{-3}). The sample was mounted without strain in pumped liquid He (1.9 K) and excited with a Ti:Sapphire laser. Fig. 2.4a shows the polarization dependence of $|A^0X\rangle \rightarrow |A^0, 2s\rangle$ emission under resonant excitation of $|A^0, 1s\rangle \rightarrow |A^0X\rangle$ with $\hat{\mathbf{y}}$ and 45° polarized excitation. The polarization visibility $C = I_{\max}/I_{\min}$ observed is somewhat less than would be expected from the ideal theory. The difference can be explained by relaxation between A^0X spin states.

We investigate the effect of inter-level relaxation on the diminished polarization visibility with time- and polarization-resolved measurements. Either the Γ_5 or Γ_3 transitions were excited resonantly with 2 ps Ti:Sapphire pulses, spectrally filtered to obtain 16 ps pulses with 0.03 nm bandwidth. Photoluminescence to $|A^0, 2s\rangle$ was collected and imaged using a combined spectrometer/streak camera setup with a timing resolution of 27 ps. Four excitation conditions were studied, resonant excitation of Γ_5 or Γ_3 with $\hat{\mathbf{y}}$ or 45° linearly polarized light. PL polarized parallel and perpendicular to the excitation polarization was collected. The complete time-resolved data set is shown in Fig. 2.4b.

2.7 Density matrix model of A^0X photoluminescence

We observe a strong initial polarization visibility at $t = 0$ that later decays because of inter-level relaxation. The initial polarization visibility of $C = 7.2 \pm 1$ for $\Gamma_5 - y$ excitation is close to the ideal value 9 for no excited state relaxation. (The uncertainty here is due to the uncertainty in the $t = 0$ time.) The decay of polarization visibility

indicates the existence of spin flip processes on the same timescale as the radiative lifetime.

We use the time-resolved data to obtain estimates of the inter- and intra-level relaxation rates in the exciton system (Fig. 2.4b). The time resolved data were fit to a 12 state density matrix model including inter-state relaxation (Appendix E). In the model, an optical pulse of a given polarization coherently creates an excited state density matrix given by Eq. E.6. The subsequent time evolution of the excited state density matrix ρ satisfies

$$\frac{d\rho}{dt} = \frac{1}{i\hbar}[H_o, \rho] - \frac{1}{2}\left\{\rho, \alpha \mathbf{p}^{\dagger}\cdot\mathbf{p}\right\} + L(\rho),$$

where H_o is a diagonal matrix of the excited state energies, the second term describes radiative recombination and $L(\rho)$ is the Linbladian operator describing phenomenological relaxation between excited states (Appendix E). From the solution $\rho(t)$ we calculate the relative PL intensity emitted into different polarizations using Eq. 2.9.

This model gives a good fit to the observed time dependence of A^0X emission (Fig. 2.4b, Appendix E.2). The 16 curves in Fig. 2.4b are fit simultaneously using 6 fit parameters: overall spontaneous emission rate (1.48 ns^{-1}), inter-level relaxation (0.89 ns^{-1}), intralevel Γ_3 relaxation (3.6 ns^{-1}), intralevel Γ_5 relaxation (1.8 ns^{-1}), temperature (4.7 K) and overall intensity normalization (5100 counts). These relaxation rates are shown schematically in Fig 2.3. The resulting A^0X radiative lifetimes are $T_o(1, 3, \frac{3}{4})$ where T_o lies in the range 0.49 to 0.74 ns. A detailed error analysis found the main source of uncertainty in the spontaneous emission rate to be due to an ambiguity in the choice of the background level (Appendix E.2). Since hole spin flips are predicted to be much faster than electron spin flips [74, 124], we do not include electron spin flip processes in the model (shown schematically in Fig. 2.3). Temperature was included as a fit parameter because the effective temperatures for bound excitons can be larger than the bath temperature [163].

Using the best fit model parameters from the time resolved experiment, we are now able to predict the polarization dependence of PL in resonant CW excitation in the presence of spin relaxation. These curves are shown in Fig. 2.4a as "theory," and agree well with the experimental data.

2.8 Conclusion

In conclusion, we presented a convenient and general formalism for calculating the optical properties of $k = 0$ excitons in III-V semiconductors with an arbitrary number of carriers. We used this formalism to derive a model of the optical properties of A^0X in strain-free bulk GaAs which predicts 3 distinct radiative lifetimes. The model was confirmed using polarization and time-resolved experiments. The results are in contrast to previous reports for this system and highlight the importance of a unified treatment of all recombination pathways when deriving the radiative properties of multi-carrier excitons.

Chapter 3

RADIATIVE PROPERTIES OF STACKING FAULTS IN GAAS

3.1 Abstract

In this chapter we investigate the magneto-optical properties of excitons bound to single stacking faults in high-purity GaAs. We find that the two-dimensional stacking fault potential binds an exciton composed of an electron and a heavy-hole, and confirm a vanishing in-plane hole g-factor, consistent with the atomic-scale symmetry of the system. The unprecedented homogeneity of the stacking-fault potential leads to ultra-narrow photoluminescence emission lines (with full-width at half maximum $\lesssim 80$ μeV) and reveals a large magnetic non-reciprocity effect that originates from the magneto-Stark effect for mobile excitons. These measurements unambiguously determine the direction and magnitude of the giant electric dipole moment ($\gtrsim e \cdot 10$ nm) of the stacking-fault exciton, making stacking faults a promising new platform to study interacting excitonic gases. We expand upon Ref. [113] in Sec. 3.7 using the formalism of Chapter 2 to analyze the the polarization dependence of the stacking fault photoluminescence.

3.2 Introduction

The stacking fault (SF), a planar, atomically thin defect, is one of the most common extended defects in zinc-blende, wurtzite, and diamond semiconductors. A fundamental understanding of the SF potential is important for determining how the defect affects semiconductor device performance [84, 46], engineering heterostructures based on crystal phase [39, 5, 11], and providing a new two-dimensional (2D) platform for fundamental physics [33, 95]. Here we report on excitons bound to large-area, single SFs in high-purity GaAs, a unique system where SFs are easily isolated with far-field optical techniques. The atomic smoothness of the potential and extreme perfection of the surrounding semiconductor result in ultra-high optical homogene-

ity ($\lesssim 80$ μeV). This enables optical resolution of the SF exciton fine-structure and thus direct measurement of the giant built-in dipole moment ($\gtrsim e \cdot 10$ nm) via the magneto-Stark effect. These results indicate that the extremely-homogeneous SF potential may be promising for studies of many-body excitonic physics, including coherent phenomena [182, 34, 175], spin currents [93], superfluidity [68], long-range order [80, 183, 145, 14, 94], and large optical nonlinearities [8, 146, 107].

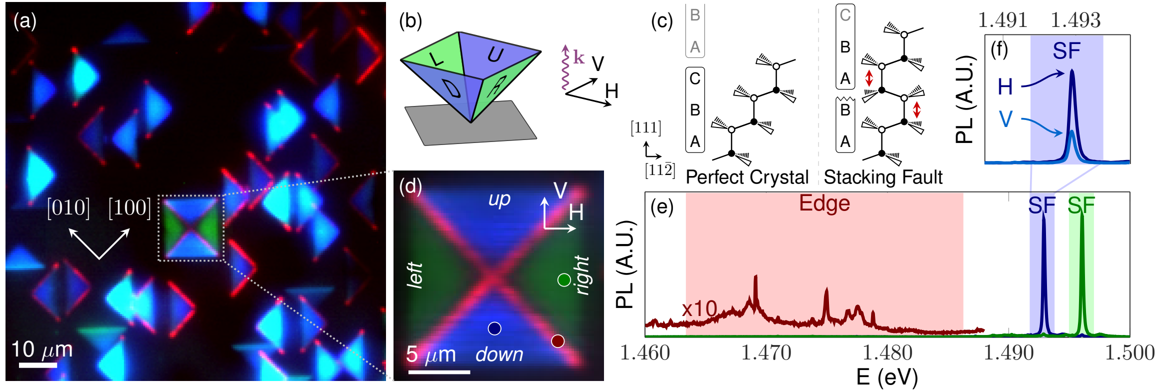

Figure 3.1: (a) Confocal scan of SF structures. The image is formed by coloring emission in different wavelength bands as red, blue or green, as depicted in e. Excitation at 1.53 eV, 100 μW, 1.9 K, excite and collect H polarization (see b). (b) Diagram of SF pyramid. The *up, down, left* and *right* SFs are labeled, along with the H and V polarizations. (c) Comparison of perfect zinc-blende and stacking fault crystal structure. (d) Detail of SF pyramid structure. Excitation at 1.53 eV, 100 μW, 1.7 K. (e) Low power PL spectra at colored dots in d. Polarizations: blue - excite/collect H; green, red - excite/collect V. Broad-band luminescence is observed from the SF edges (red). 1.53 eV, 2 μW, 1.7 K. (f) PL from *down* SF (blue dot in d). Polarizations: dark blue - excite/collect H; light blue - excite/collect V.

3.3 Stacking fault photoluminescence.

Figure 3.1(a) shows a spectrally resolved confocal scan of SF structures in a GaAs epilayer, excited with an above band-gap laser (1.65 eV, 1.5 K) (see Appendix F.1 for growth information, Appendix F.1. The image is colored red, green or blue according to three characteristic emission bands shown in Fig. 3.1e. The narrow-band PL at 1.493 and 1.496 eV originates from excitons, electron-hole pairs, bound to the 2D SF

potential [114, 128]. The sample consists of a 10 μm GaAs layer on 100 nm AlAs on a 5 nm/5 nm AlAs/GaAs (10×) superlattice grown directly on a semi-insulating (100) GaAs substrate. Stacking fault structures nucleate near the substrate-epilayer interface during epitaxial growth (Appendix. F.1).

The physical origin of the potential can be understood from the atomic structure of the SF defect: the lattice-plane ordering in the [111] direction of zinc-blende is modified by subtracting a layer (intrinsic SF, see Fig. 3.1c) or adding a layer (extrinsic SF). The intrinsic SF can be viewed as a monolayer of wurtzite (AB AB stacking) surrounded by zinc-blende (ABC ABC stacking) [6, 39]. Due to the band offset [16, 185, 90] and spontaneous polarization at the stacking fault [127], electrons and/or holes are attracted to the SF plane. While useful for physical motivation, this bulk phase change model must be taken with caution when applied to atomically thin SFs, which can deviate from simple theory [199]. Here, however, we find that single SFs in bulk GaAs bind excitons, confirming that the potential is attractive for at least one carrier.

In the confocal scan in Fig. 3.1(a), most of the SF defects appear as single triangles, which we identify as a pair of nearby SFs [75, 201]. Because the binding energy of excitons to a pair of SFs depends on the distance between the SFs [48], the PL emission energy from excitons bound to these structures has a high variability of 10 meV between structures. Strikingly, this inhomogeneity disappears when four SFs grow in an inverted pyramid structure consisting of four well-isolated {111} SF planes [Fig. 3.1(b)], which we refer to as *up*, *down*, *left* and *right* [106]. The full width at half-maximum (FWHM) of the SF PL line in our sample is (77 ± 19) μeV at zero magnetic field, see Appendix F.2, somewhat narrower than excitonic lines associated with stacking faults in previous work [114, 121]. In comparison, the narrowest reported linewidth for a GaAs/AlGaAs quantum well is 130 μeV [154], while PL linewidths from analogous zinc-blende/wurtzite quantum discs in nanowires range from $0.6-10$ meV [90, 81, 148, 178]. This unprecedented homogeneity allows us to resolve the SF-bound exciton fine structure

3.4 *Nature of hole in SF exciton*

In this novel system, it is important to know which exciton spin states are responsible for the observed luminescence. The bulk exciton in GaAs is composed of a spin

$\frac{1}{2}$ electron and a spin $\frac{3}{2}$ hole. Symmetry considerations narrow the possibilities for excitonic spin states contributing to the 2D SF exciton to only two options. A stacking fault lowers the symmetry of a zinc-blende crystal from T_d to C_{3v}. The lower symmetry splits the four-fold degenerate valence band maximum at the Γ point, leaving only two possibilities for the nature of SF excitons: either they are heavy-hole excitons or light-hole excitons (Appendix. F.6).

Experimentally, we determine that the SF exciton is composed of an electron and a heavy-hole using polarization resolved PL, consistent with the atomic-scale symmetry of the system (Appendix. F.6). For linearly polarized light incident from above (along the [001] axis), the largest overlap between the light polarization and the in-SF-plane heavy-hole dipole occurs when exciting and collecting along the H direction for the *down* SF [Fig. 3.1(d)], in agreement with our experimental data [Fig. 3.1(f)]. On the other hand, the main dipole moment for the light-hole exciton is along the SF normal, which would give rise to a maximum signal at V polarization, contrary to what is observed. Further, we also note that no hole Zeeman splitting is observed for in-plane magnetic fields B up to 7 T (Fig. 3.2). This observation is fully consistent with our symmetry analysis, which finds that B-linear splitting for in-plane fields is forbidden for heavy-holes but allowed for light-holes, see Appendix F.7. The substantial separation of the heavy- and light-hole states prevents their magnetic-field induced mixing, in line with experiments on GaAs nanowires [186].

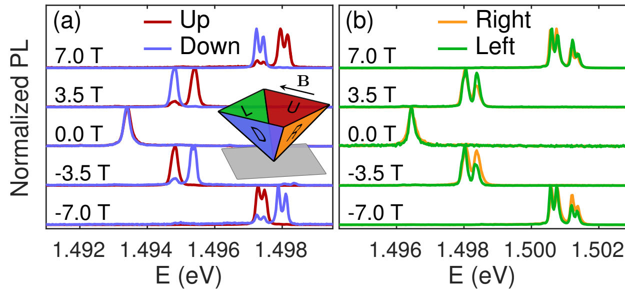

Figure 3.2: (a) Spectra from *up* and *down* SFs as a function of in-plane magnetic field. The spectra show a non-reciprocity with applied magnetic field. Excite at 1.65 eV, 0.5 μW, 1.6 K, excite and collect H. Inset shows the geometry of the stacking fault pyramid and applied magnetic field. (b) Spectra from *left* and *right* SFs as a function of partially out-of-plane magnetic field. The spectra are similar at positive and negative fields. Excitation at 1.65 eV, 0.5 μW, 1.6 K, excite and collect V.

3.5 Non-reciprocal photoluminescence

PL from SFs shows a remarkable non-reciprocity with in-plane applied magnetic field: Figure 3.2(a) shows that the PL detected in linear polarization from the *up* SF occurs at a different energy depending on whether the magnetic field is parallel (positive) or antiparallel (negative) to the $[\bar{1}10]$ axis. Interestingly, the *down* SF demonstrates the opposite behavior. Such an asymmetric behavior of the PL is surprising because in general, time reversal symmetry makes $\mathbf{B}$ and $-\mathbf{B}$ equivalent. (Our sample is non-magnetic and we use linearly polarized light to avoid dynamic polarization of nuclear spins.) The observed non-reciprocal behavior of the PL spectrum with respect to inversion $\mathbf{B} \to -\mathbf{B}$ is only possible if the PL arises from moving excitons. In this case, time reversal changes the direction of both the magnetic field and the exciton wavevector $\mathbf{K}$.

Based on the C_{3v} point symmetry of the SF and time reversal invariance, the effective Hamiltonian for an exciton moving in the presence of an in-SF-plane magnetic field $\mathbf{B}$ is

$$\mathcal{H}_{KB} = \frac{g_e}{2}\mu_B(\sigma_x B_x + \sigma_y B_y) + \beta B^2 + \beta'[\mathbf{K} \times \mathbf{B}]_z, \tag{3.1}$$

where g_e is the electron g-factor, μ_B is the Bohr magneton, $\sigma_{x,y}$ are the electron spin Pauli matrices, β is a parameter describing the excitonic diamagnetic shift, and β' is a constant responsible for the non-reciprocal effect (Appendix F.7). In Eq. (3.1) we only retain 1st- and 2nd-order terms in $\mathbf{B}$ and use a frame of axes related to the SF plane: $z \parallel [111]$ is the SF normal, $x||[11\bar{2}]$ and $y||[\bar{1}10]$. Each symmetry-derived term in Eq. (3.1) manifests itself in the energetic shift of the SF PL lines with magnetic field (Fig. F.4). The first term is the electron Zeeman effect and gives rise to the doublets visible at ± 7 T, since an electron with a particular spin projection can recombine with the corresponding hole. The second term is the exciton diamagnetic shift, arising from the magnetic-field-induced shrinking of the exciton wavefunction [118]. The last term is the magneto-Stark effect, which, as we show below, quantitatively explains the non-reciprocal PL spectra.

The experimental geometry, Fig. 3.1(b), is such that only light emitted normal to the sample surface is collected. For a high quality 2D potential, in-plane exciton momentum is transferred to the photon during recombination, as depicted in Fig. 3.3(a).

This conservation of momentum implies

$$K_x = \frac{\omega n}{c} \sin\theta'', \tag{3.2}$$

where θ'' is the angle between the SF normal and the emitted photon momentum inside the semiconductor, Fig. 3.3(a), ω is the photon frequency, n is the refractive index and c the speed of light. Thus, the collected SF PL arises only from excitons with a specific center of mass momentum. (Experimentally, the NA = 0.7 objective lens collects luminescence from a range of angles. In our system, light is collected from excitons momenta within 7% of $\hbar K_x$ in Eq. (3.2).) The last term in Eq. (3.1) provides, for a fixed K_x (Eq. 3.2), an odd in B_y contribution to the overall PL energy shift, giving rise to a magnetic non-reciprocity effect. It is worth noting that the *up* and *down* SFs are related by a mirror reflection in the (110) plane and such a reflection is accompanied by $B_y \to -B_y$, resulting in the opposite behavior of *up* and *down* PL spectra observed in Fig. 3.2(a).

3.6 Magneto-Stark effect

The physical origin of the non-reciprocal PL is the magneto-Stark effect, the interaction of a moving exciton's electric dipole moment with a magnetic field [82, 192]. The effect can be understood with a relativistic argument: motion with velocity $\mathbf{v} = (\hbar K_x/M)\hat{\mathbf{x}}$ through a magnetic field $\mathbf{B} = B_y\hat{\mathbf{y}}$ gives rise to an electric field $\mathbf{E}_{\text{eff}} = \hbar K_x B_y/(Mc)\hat{\mathbf{z}}$ in the moving frame of reference, where M is the exciton mass in translational motion and c the speed of light. Since for the SF, $\hat{\mathbf{z}} \propto [111]$ and $-\hat{\mathbf{z}}$ directions are not equivalent, the SF-bound exciton has a non-zero dipole moment $\mathbf{p} = ed_{he}\hat{\mathbf{z}}$, where $e = |e|$ is the elementary charge, and d_{he} is the average separation between the hole and electron along the z-axis. The Stark effect $H_s = -\mathbf{p} \cdot \mathbf{E}_{\text{eff}}$ in the exciton's reference frame thus becomes the magneto-Stark effect:

$$\mathcal{H}_{\text{S}} = -\frac{e\hbar}{Mc} d_{he} K_x B_y, \tag{3.3}$$

in agreement with Eq. (3.1) with $\beta' = -e\hbar d_{he}/(Mc)$, see Ref. [118] and Appendix F.9 for formal derivation.

Physically, the dipole moment of a SF bound exciton is a consequence of symmetry breaking and spontaneous polarization similar to that in zinc-blende/wurtzite

heterostructures [128, 103]. The hole in the exciton is presumably localized in the SF plane while the electron is weakly bound via the Coulomb interaction. The spontaneous polarization shifts the electron cloud to one side of the SF, resulting in a giant excitonic dipole moment.

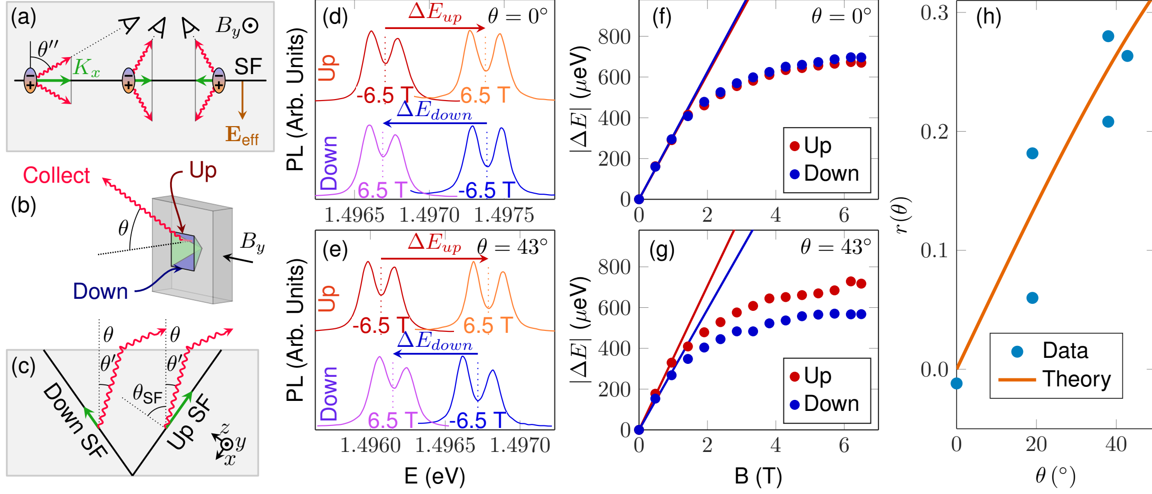

Figure 3.3: (a) Because of conservation of in plane momentum during exciton recombination, the angle of light emission depends on the exciton wavevector. Collecting different angles probes different exciton momenta. The SF has a built in potential that creates a zero-field dipole moment for the SF exciton. In the exciton frame of reference, the in-plane magnetic field becomes an out-of-plane electric field, leading to the magneto-Stark effect. (b) Spectra of *up* and *down* SFs as a function of θ and in-plane magnetic field B_y. (c) Light from the *up* SF originates from excitons with larger K_x than light from the *down* SF (for $\theta > 0$). (d-e) Spectra of *up* and *down* SF at positive and negative B_y for $\theta = 0°$ and $43°$. At $\theta = 0°$, ΔE_{up} and ΔE_{down} have the same magnitude, while for $\theta = 43°$, the magnitude of ΔE_{up} is larger than ΔE_{down}. (f-g) Splitting $\Delta E_{up/down}$ as a function of magnetic field. Data are obtained from Voigt fits to spectra similar to those shown in d-e. Solid lines are a fit to $\Delta E = aB$ for the first three data points. (h) The ratio of $B = 0$ slopes, Eq. (3.6), depends only on geometrical constraints. The theory (solid line) has no adjustable parameters. Data for other angles in Appendix F.9.

Equations (3.1)-(3.3) predict that the asymmetric energy shift of exciton PL is linearly related to the in-plane wavevector $\mathbf{K}$. Since the angle of light collection determines the exciton momentum [Eq. (3.2)], we test the applicability of the model by recording spectra of the *up* and *down* SFs as a function of the collection angle θ

and magnetic field B_y [Fig. 3.3(b)]. The collection angle is related to the emission angle from the up/down SF by $\sin\theta = n\sin\theta' = \pm n\sin(\theta'' - \theta_{\text{SF}})$, where θ_{SF} is the angle the SF normal $\hat{\mathbf{z}}||[111]$ makes with [001] [Fig. 3.3(c)].

In this experiment, we modified the collection angle by mounting the sample at different angles. Since the sample was removed from the cryostat to change the angle, different SF pyramids were used at different angles. This does not introduce artifacts because of the extreme similarity of different SFs, which have a standard deviation of line-center energies of only 57 μeV, less than the linewidth. Spectra were acquired with B_y ranging from -6.5 T to 6.5 T on the *up* and *down* SFs. We fit the spectra to one or a sum of two Voigt function(s) depending on whether the electron Zeeman splitting is resolved. The singlet or doublet line center is denoted $E_{up/down}(B_y)$. The part of the exciton energy odd with magnetic field is found by computing

$$\Delta E_{up/down}(B_y) = E_{up/down}(B_y) - E_{up/down}(-B_y) \tag{3.4}$$

It follows from Eq. (3.3) that the asymmetric shift is

$$\Delta E_{up/down}(B_y) = \mp 2n\hbar\omega\frac{ed_{he}}{Mc}\sin(\theta_{SF} \pm \theta')B_y. \tag{3.5}$$

Thus the proportionality constant of $\Delta E_{up/down}$ vs. B_y provides a measurement of the SF exciton's built-in dipole moment. The experimental values and first-order theory for ΔE are shown in Fig. 3.3(f)-(g). Further, the ratio

$$r(\theta) = \frac{|\Delta E_{up}| - |\Delta E_{down}|}{\frac{1}{2}\left(|\Delta E_{up}| + |\Delta E_{down}|\right)} \tag{3.6}$$

depends (to first order in B_y) only on the experimental geometry and the index of refraction: $r(\theta)$ vanishes for collection angle $\theta = 0$ and increases as a function of θ [Fig. 3.3(h)]. We obtain good agreement between $r(\theta)$ calculated experimentally from the $B = 0$ slope of ΔE without any fit parameters [Fig. 3.3(h)].

Further, by fitting $\Delta E_{up/down}(B_y)$ with a B_y-linear function, we can estimate the dipole moment of the exciton $p = ed_{he} = e \cdot (10^{+20}_{-1})$ nm. The main uncertainties result from the accuracy of the B_y-linear fit and the value of the in-(111)-plane heavy-hole mass, which depends on the details of the SF potential, see Appendix F.6. The exciton mass can be roughly estimated as $0.17\,m_o$, the sum of the bulk-GaAs in-

(111)-plane heavy-hole mass and the isotropic electron mass, where m_o is the free electron mass. In addition, we note the magneto-Stark induced splitting saturates at high fields [Fig. 3.3(f,g)], possibly due to a decreased exciton dipole moment from the magnetic-field-induced shrinking of the exciton wavefunction. Future work will investigate exciton confinement potentials consistent with the observed dipole moment, diamagnetic shift and saturation of the magneto-Stark effect. A microscopic understanding of the confinement potential may enable predictions for the binding potential and excitonic dipole moment for SFs in other semiconductors.

3.7 Polarization dependence of SF-bound-exciton PL

We next perform a detailed test of the polarization dependence of SF-bound-exciton PL. We measured the dependence of the SF-bound exciton PL line on above-band-gap excitation polarization and collected polarization, shown in Fig. 3.4(a). Experimentally, this is accomplished using automated rotation of two half-wave plates.

In order to analyze the polarization dependence we first determine whether the $k = 0$ theory (Ch. 2) applies. If the size of the Luttinger-Kohn Hamiltonian, Eq. 2.11, is small compared with the ~16 meV HH-LH splitting caused by the SF [186], then the Luttinger-Kohn Hamiltonian may be ignored. The in-plane wavevector of the SF exciton can be estimated using Eq. 3.2 to be 27 μm^{-1}. The term of the Luttinger-Kohn Hamiltonian that competes with the quantization axis defined by the stacking fault is $\hbar^2\gamma_3(\mathbf{k}\cdot\mathbf{J})^2/2m_0$, which has a magnitude of 75 μeV for the stacking fault exciton, much smaller than the HH-LH splitting. Thus the quantization axis is completely defined by the symmetry of the stacking fault and the polarization dependence of the SF exciton is well described using the $k = 0$ theory.

We develop the polarization dependence of the stacking fault exciton in detail in Appendix. F.12. This detailed theory includes hole-spin relaxation (Γ_h) and dephasing, occurring between the creation of free carriers and recombination of the stacking fault (time t). Electron spin-relaxation is ignored ($\Gamma_e = 0$). The theory for heavy-hole excitons makes an excellent match with experiment, as shown in Fig. 3.4(b). However, we note that the experimental polarization dependence has a somewhat rectangular shape, where the theory curve does not. At this point, it is unclear what is responsible for this discrepancy. For comparison, we also plot the expected PL dependence for light-hole SF excitons, which does not agree with the data.

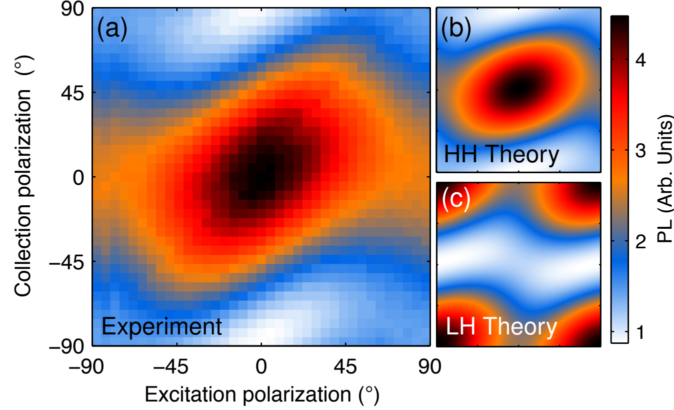

Figure 3.4: (a) Experimental polarization dependence of PL emitted from left SF in Fig. 3.1d ($\theta = 0$ corresponds to vertical.). Excitation laser above band-gap at 1.53 eV. 1.8 K, 40 μW, pinhole in. (b) Fit of polarization dependence to theory of heavy hole excitons described in Appendix F.12. Fit parameters are $\Gamma_h t = (0.572 \pm 0.009)$, $\Gamma_e t = 0$ (fixed at bound), norm $= (13\,400 \pm 200)$, bg $= (600 \pm 20)$, $\Delta\theta_{\text{in}} = (-0.3 \pm 0.5)°$, $\Delta\theta_{\text{out}} = (-2.7 \pm 0.3)°$. The polarization dependence of the up SF also confirms the heavy-hole nature of the SF exciton (Appendix. F.13). The fit parameters $\Delta\theta_{\text{in}}$ and $\Delta\theta_{\text{out}}$ correspond to correcting a small error in the zero-alignment of the half-wave plates. (c) Plot of light hole theory for same parameters as b.

3.8 Transport of 2D excitons

Lastly, we perform an experiment to confirm that the SF photoluminescence is due to mobile 2D excitons. We expect the 2D excitons to travel freely within the plane, potentially with high mobilities due to the atomic-level spatial homogeneity of the potential. Up to this point, measurements use above band-gap excitation to create excitons in the bulk, which subsequently diffuse to the SF and recombine. To investigate diffusion within the 2D SF layer, we resonantly excite the SF exciton. Resonant excitation creates SF excitons less efficiently than does above band-gap excitation because of the delta-function-like SF potential compared to the 10 μm-thick bulk epilayer. Resonant excitation is considerably less efficient than above band-gap excitation at creating SF excitons, understandable given the delta-function-like SF potential compared to the 10 μm-thick bulk epilayer. We also note that absorption efficiency is further reduced by the small overlap of the electron and hole envelope

functions expected for an exciton with such a large electron-hole separation. Because of this low absorption efficiency, we use a high laser power to resonantly excite the stacking fault exciton. The reflected laser light dwarfs the small PL intensity, thus precluding the direct observation of exciton diffusion within a single stacking fault.

To circumvent this challenge, we investigate 2D exciton transport by resonantly exciting the SF exciton and observing luminescence at other locations in the pyramid structure. In this experiment, the excitation laser stays spatially fixed on the sample while the collection point scans over the sample (Appendix. F.15). Resonantly exciting the up SF results in PL from the 1D edges neighboring the up SF, but not from 1D edges further away (Fig. 3.5a). This implies that the edge PL is due to resonantly created 2D SF excitons that migrate to the edges and recombine. By scanning the laser energy over the narrow SF exciton line, this transport was confirmed to be due to the 2D SF exciton and not bulk carrier diffusion (Appendix. F.16). Surprisingly, we observe excitonic emission from neighboring SF planes, which indicates that excitons can travel from one SF to another through the 1D potential. This diffusion is observed both to the lower energy SF (Fig. 3.5c-d) and to the higher energy SF (Fig. 3.5a-b), suggesting that carrier-exciton or exciton-exciton interactions can assist the tunneling of an exciton through the 1D edge, even to higher energy. These experiments show that resonant excitation can create mobile 2D excitons bound to a single stacking fault.

3.9 Conclusion

We have shown that SFs in GaAs are an almost perfect 2D potential which binds heavy-hole excitons. These excitons freely propagate in the SF plane, a conclusion confirmed via the magneto-Stark effect. Further, an asymmetry of the SF potential induces a giant dipole moment of the SF-bound exciton. Such excitons could be useful for studying the many-body physics of interacting dipoles. In conventional excitonic systems, typical electron-hole separations are on the order of several nm [33, 204], whereas the SF-bound exciton has a gigantic electron-hole separation of 10 nm and the possibility to modify this value with an applied field. In addition, the ultra-narrow linewidths in the SF system will allow the small energy shifts present in many-body interactions to be observed. As a rough estimate, the interaction energy of two such dipoles will exceed the SF FWHM of 77 μeV when the exciton density is greater than

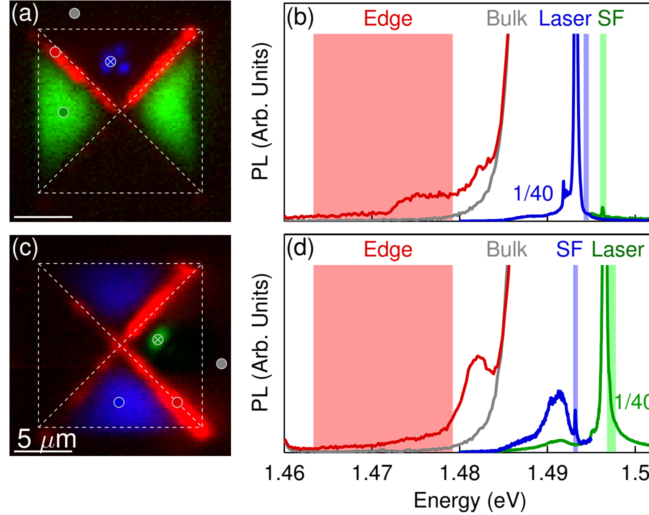

Figure 3.5: Transport of 2D excitons. **a**. Laser spatial position fixed at blue dot throughout scan and resonantly exciting SF exciton at 1.4929 eV. Luminescence is observed at 1D edge state and on neighboring SFs (green). PL integration bands are shown as colored rectangles in b. The red and green images are obtained by subtracting out the bulk PL and laser tail. 400 μW for edge scan (red), 20 μW for SF scan (green). The laser spot appears distorted due to cross polarization. **b**. Spectra at locations specified by colored dots in a. The laser (blue) leaks through due to non-perfect extinction. The integration band for the laser is offset from the center to avoid the image saturation. Bulk donor-acceptor pair emission is observed (gray). The edge PL is the difference between the edge (red) and bulk (gray) spectrum. PL from left and right SFs is visible (green). **c-d.** Similar to a-b, except laser resonantly excites right SF at 1.4961 eV. The process used for subtraction of bulk PL is described in Appendix. F.16. 400 μW for edge scan (red), 20 μW for SF scan (blue). 6 K.

230 μm^{-2}. Using a wavefunction size of approximately 10 nm, the critical density for exciton overlap in the 2D potential is 10 000 μm^{-2}. Therefore, the SF-bound exciton system could show sizable dipole-dipole interactions and may demonstrate coherent phenomena at reasonable exciton densities.

Chapter 4

DISLOCATIONS

Individual dislocations in an ultra-pure GaAs epilayer are investigated with spatially and spectrally resolved photoluminescence imaging at 5 K. We find that some dislocations act as strong non-radiative recombination centers, while others are efficient radiative recombination centers. We characterize luminescence bands in GaAs due to dislocations, stacking faults, and pairs of stacking faults. These results indicate that low-temperature, spatially-resolved photoluminescence imaging can be a powerful tool for identifying luminescence bands of extended defects. This mapping could then be used to identify extended defects in other GaAs samples solely based on low-temperature photoluminescence spectra.

4.1 Introduction

Multijunction photovoltaics have been the leader in solar cell efficiency for over 20 years [2]. For high-efficiency multi-junction photovoltaics, the constituent semiconductor bandgaps must be precisely tuned to the solar spectrum and the resulting heterostructure must be grown with low dislocation densities. These requirements cannot be simultaneously satisfied using lattice-matched materials [193], leading to a trade-off between more-optimal band gaps and higher dislocation densities due to lattice mismatch. Currently the highest efficiency cells avoid this issue either by wafer bonding [193], or by using compositionally-graded buffer layers to minimize the presence of dislocations in specific regions [78]. Since energy devices often contain dislocations that degrade device quality, it is advantageous to develop new tools for characterizing material quality.

In this work, we use a model system to investigate the radiative and non-radiative properties of individual dislocations and stacking faults. We use photoluminescence mapping to image 10 μm-scale extended defects in an ultra-pure GaAs epilayer, finding that different types of dislocations show markedly different luminescence behaviors. This non-destructive technique can be used to characterize individual dislo-

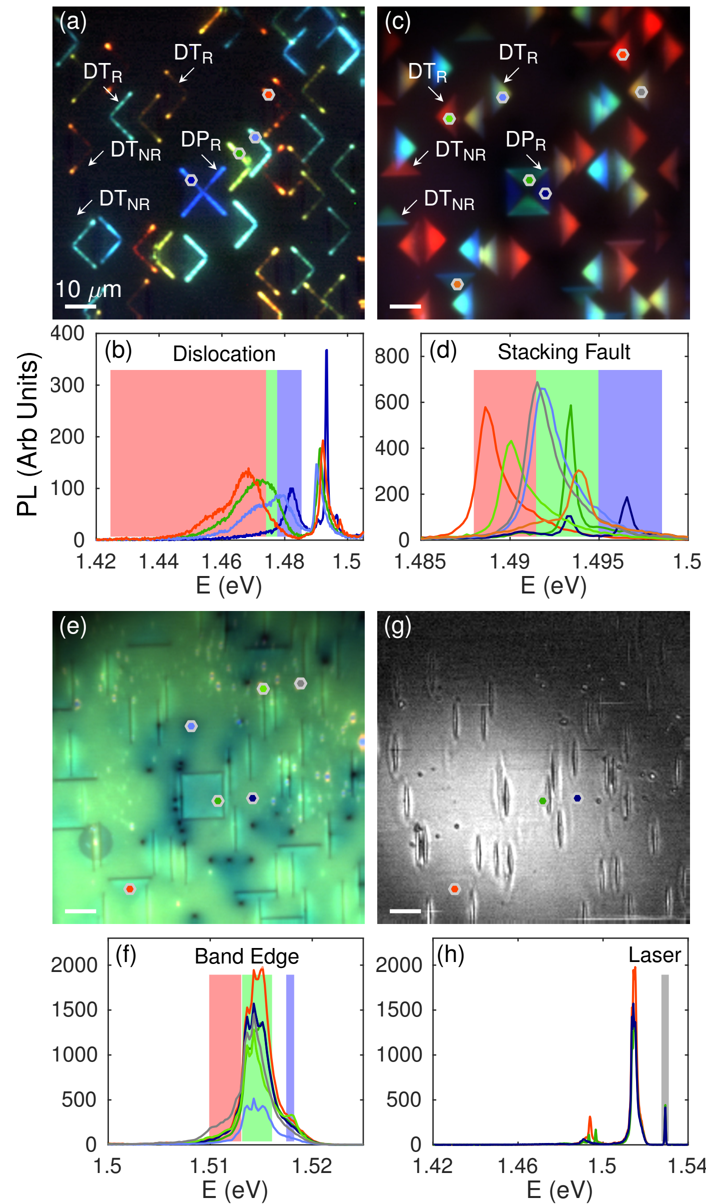

Figure 4.1: (a) Confocal scan of dislocations bordering stacking faults. The image is formed by coloring emission in different wavelength bands as red, blue or green, as depicted in b. Both radiative and non-radiative dislocations are observed. (b) Spectra of the sample at colored dots in a. PL is observed at the dislocations bordering the stacking faults. (c-d) Same as a-b, except with integration bands centered on the stacking fault bound exciton PL. (e-f) Same as a-b except with integration bands centered on the band edge PL. Dark lines are observed where the stacking faults intersect the sample surface. (f-h) Laser reflection image of sample. The vertical lines are oval defects. Scale bar 10 μm. Excitation at 1.53 eV, 100 μW, 1.9 K, excite and collect horizontal polarization.

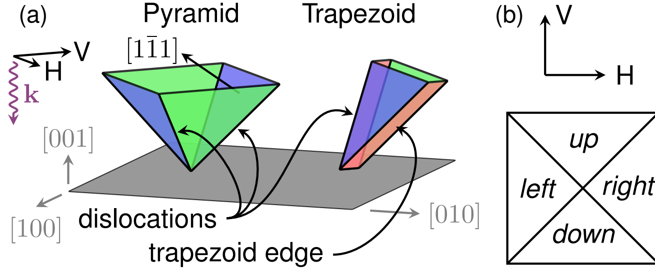

Figure 4.2: (a) Two types of stacking fault structures are observed. Stacking fault pyramids consists of four stacking faults (colored planes) bounded by dislocations. Stacking fault trapezoids consist of a closely spaced ($\sim$ 10 nm) pair of intrinsic and extrinsic stacking faults, bounded by dislocations. H and V define the light polarizations and **k** the wavevector of excitation light. (b) Experimental geometry with labeling scheme for stacking faults.

cations in samples where the dislocation density is low compared with the optical resolution ($\lesssim 10^7$ cm^{-2}). This work is in stark contrast to other studies of dislocations, which typically explore average material properties as a function of defect densities. Further, the knowledge gained from unambiguous studies of defects in ultra-pure samples can be used to characterize materials where single defects cannot be optically isolated.

4.2 Experiment

4.2.1 Sample preparation

Stacking fault (SF) structures and associated dislocations are embedded in a 10-μm-thick [001] GaAs epilayer grown by molecular beam epitaxy, see Ref. [113] for details. The stacking fault defects nucleate at the substrate-epilayer interface during epitaxial growth [106, 41]. Two kinds of defects are observed, see Fig. 3.1, and are depicted schematically in Fig. 4.2: stacking fault pyramids and stacking fault trapezoids, which are each bordered by dislocations. We will refer to the dislocations surrounding the pyramid as DP_R and DP_{NR} and those surrounding the trapezoid as DT_R and DT_{NR}, where the subscript denotes whether radiative (R) or non-radiative (NR) transitions are observed. Since we did not perform structural microscopy, we cannot confirm the identity of the dislocations observed. However, previous studies typically find stacking

fault structures to be bordered by stair-rod partial dislocations [203, 4, 202, 66].

4.2.2 Photoluminescence imaging

Figure 4.1(a) shows a low-temperature confocal scan of the sample in which photoluminescence (PL) is excited with an above-bandgap laser. The PL arises from excitons generated in the bulk that bind to extended defects and recombine radiatively. There are four main spectral bands of interest: PL from dislocations, PL from stacking faults, band edge PL, and laser reflection from the sample surface.

Strong photoluminescence is observed at 1.480 eV from the DP_R defect in Fig. 4.1(a), arising from excitons bound to the dislocation at the intersection of two SFs in a pyramid defect. We also observe luminescence due to excitons bound to the trapezoid edges, which is comprised of a dislocation-SF-dislocation structure as seen in Fig. 4.2(a). PL at the trapezoid edges shows a large spread of ~ 20 meV in the center of the PL emission energy. We attribute this to the variable distance between the two edge dislocations in a trapezoid defect [75], leading to a variable binding energy of excitons to the edge. Considering that the typical distance between stacking faults in a trapezoid defect is ~ 14 nm [75, 12] and the typical SF-bound exciton size is > 10 nm [113], the dislocations must play a role in the exciton binding potential at the trapezoid edge. In particular, strong non-radiative recombination at a dislocation would quench the PL. Therefore, we will also refer to the luminescence originating from the trapezoid edges as due to excitons bound to dislocations.

Moreover, at the low experimental temperature (~ 2 K) even a small excitonic potential of ~ 1 meV is sufficient to bind excitons. Due to the non-isotropic strain fields surrounding a dislocation, we expect nearly all dislocations to create an attractive potential either to the electron or the hole, thus leading to a bound exciton [65]. Therefore, if no radiative recombination is observed at a dislocation, we conclude that the dislocation is a strong non-radiative recombination center.

Luminescence from stacking faults is shown in Fig. 4.1(c)-(d). In comparing Figs. 3.1(a) and 3.1(c) we note that the *up* and *down* stacking faults show no PL from the dislocations at their edges, while the majority of the *left* and *right* stacking faults have strong PL from the adjacent dislocations [directions explained in Fig. 4.2(b)]. This demonstrates that there are two types of partial dislocations, DT_R and DT_{NR}, with markedly different effects on charge carriers. These results are in contrast with

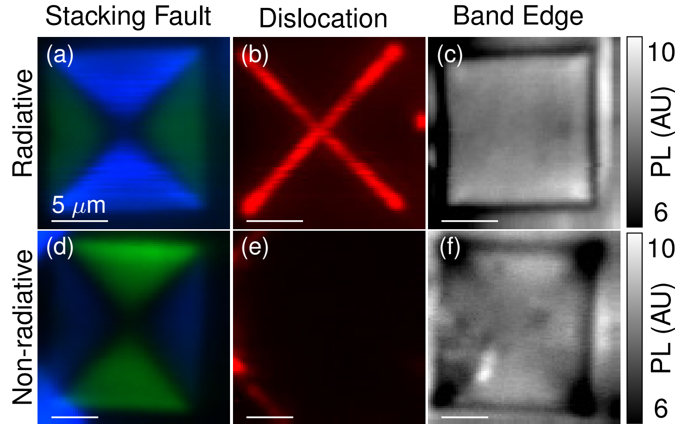

Figure 4.3: (a-c) Confocal scan of the stacking fault pyramid visible in Fig. 4.1 using integration bands green: 1.495–1.497 eV, blue: 1.492–1.494, red: 1.463–1.486 eV, grey: 1.511–1.520 eV. The stacking fault luminescence decreases where the stacking faults intersect the sample surface, but not where the stacking faults intersect one another. Excite at 1.52 eV, 1 mW, 1.47 K, excite H, collect H. (d-f) Confocal scan of a SF pyramid that does not show dislocation luminescence in (e). Compared with (a), the stacking fault luminescence in (d) decreases more at the dislocations. The band edge luminescence is slightly quenched at the dislocations. Excite at 1.52 eV, 0.15 mW, 6.1 K, excite H, collect H.

the typical expectation that dislocations introduce strong non-radiative recombination centers [212, 131], but in line with related experiments where the type of dislocation changes the strength of non-radiative recombination observed [149, 88, 174, 27]. Further, we observe pyramid defects where the dislocations are all DP_{NR} or all DP_{R}, see Fig. 4.3. In Figs. 4.3(d) and 4.3(f), the stacking fault and band-edge PL appear quenched near the DP_{NR} defects.

The band-edge PL, Figs. 4.1(e),(f) quenches wherever the stacking faults intersect the surface. Surprisingly, this quenching seems unrelated to the surface oval defects, visible in Fig. 4.1(g)-(h), which only occur on the *left* and *right* stacking faults [114]. Thus surface oval defects do not significantly affect the strength of non-radiative recombination occurring at the intersection of a stacking fault and the sample surface.

Lastly, we found the center-of-mass of the dislocation and stacking-fault PL for each trapezoid defect visible in Fig. 4.1, and performed a cross-correlation of these two emission energies (Fig. 4.4). The PL center energy from the dislocation and

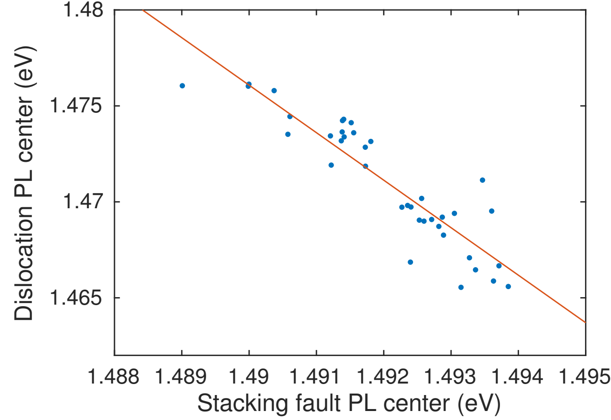

Figure 4.4: Correlation of the dislocation and stacking fault PL center energies for the trapezoid defects in Fig. 4.1. The stacking fault PL center energy is inversely related to the corresponding dislocation PL center energy.

the nearby stacking fault have a strong inverse correlation. This emission energy is related to the exciton binding energy, which is a function of the inter-stacking-fault distance in the trapezoid defect. Future work incorporating the full solution of the exciton effective-mass wavefunction could elucidate the physical mechanism behind this inverse correlation.

4.3 Conclusion

We use spatially and spectrally resolved exciton luminescence to investigate the properties of individual dislocations and stacking faults in GaAs. We find that some dislocations are efficient centers for radiative recombination while others have strong non-radiative recombination. Future work combining structural microscopy and photoluminescence mapping can determine which dislocation varieties lead to radiative or non-radiative recombination.

This study was enabled by our unique sample, which contains a low density of 10-μm-scale extended defects embedded in a high-purity GaAs crystal. This enables us to determine the spectral characteristics of dislocations and stacking faults in an optical microscope. The unambiguous identification of these defects may be useful for identifying stacking faults and dislocations in materials with high defect densities where individual defects cannot be optically isolated. For example, stacking fault

densities could be estimated by comparing PL intensity to a reference sample. Lastly, we note that stacking faults and dislocations are present in a wide variety of zinc-blende and wurtzite materials, and that the same PL imaging techniques can be used to study other materials.

Chapter 5

LONGITUDINAL SPIN-FLIP TIME OF DONOR-BOUND ELECTRON

5.1 Abstract

We measure the donor-bound electron longitudinal spin-relaxation time (T_1) as a function of magnetic field (B) in three high-purity direct-bandgap semiconductors: GaAs, InP, and CdTe, observing a maximum T_1 of 1.4 ms, 0.4 ms and 1.2 ms, respectively [112]. In GaAs and InP at low magnetic field, up to ∼2 T, the spin-relaxation mechanism is strongly density and temperature dependent and is attributed to the random precession of the electron spin in hyperfine fields caused by the lattice nuclear spins. In all three semiconductors at high magnetic field, we observe a power-law dependence $T_1 \propto B^{-\nu}$ with $3 \lesssim \nu \lesssim 4$. Our theory predicts that the direct spin-phonon interaction is important in all three materials in this regime in contrast to quantum dot structures. In addition, the "admixture" mechanism caused by Dresselhaus spin-orbit coupling combined with single-phonon processes has a comparable contribution in GaAs. We find excellent agreement between high-field theory and experiment for GaAs and CdTe with no free parameters, however a significant discrepancy exists for InP. This work is published in Ref. [112] and is reproduced here without significant changes.

5.2 Introduction

In the last decade, the prospects for spin-based quantum information have spurred renewed interest in the fundamental mechanisms for spin relaxation in semiconductors [105, 197, 194, 116]. Shallow impurities in direct-bandgap materials are promising candidates for quantum applications relying on spin-photon interfaces [15, 44, 179], as these systems boast high optical homogeneity [73], strong spin-photon coupling, and the potential in II-VI materials [49] to enhance spin coherence times with isotope purification [13, 198]. While electron spin relaxation is now relatively well un-

derstood in III-V semiconductor quantum dots both theoretically and experimentally [116, 142, 124, 64, 89, 7, 133], it is still an open question whether the same processes dominate in the similar direct band-gap donor system. In contrast to quantum dots, in which the size, shape, composition, and strain field for each dot are to a large extent unknown, the physical properties relevant to spin relaxation for the homogeneous donor system have been measured. This enables quantitative comparison of spin-relaxation rates between theory and experiment which should help predict which donor systems are most promising for future applications.

Here we measure the longitudinal spin-flip time T_1, the fundamental limit for the storage time for quantum information, in three semiconductors: GaAs, InP, and CdTe. All three are direct bandgap materials with similar band structure allowing for the optical pumping of the donor-bound electron spins under resonant exciton excitation. We show that at low magnetic fields, T_1 is proportional to B^2 with a proportionality constant highly dependent on temperature and donor density. At high magnetic fields, we find that T_1 is proportional to $B^{-\nu}$, with the power ν in the range $3 \lesssim \nu \lesssim 4$. The competition of these two dependencies leads to a maximum of T_1 in GaAs and InP at relatively high magnetic field: (1.4 ± 0.1) ms at 4 T for GaAs and (0.40 ± 0.01) ms at 1.9 T for InP. Due to technical issues, we are unable to observe this maximum for CdTe; however, the highest T_1 measured is (1.23 ± 0.07) ms at 1.1 T with T_1 expected to rapidly increase at lower fields.

The low magnetic-field T_1 behavior for GaAs and InP is consistent with a spin relaxation mechanism controlled by the hyperfine coupling of the electron spin with static fluctuations of the host-lattice nuclear spins. In this situation, spin precession is randomized due to the finite electron correlation time at each donor site [141, 61]. Although the mechanism for the extremely-short correlation time τ_c ($\tau_{c,\mathrm{GaAs}} \simeq 25$ ns, $\tau_{c,\mathrm{InP}} \simeq 40$ ns) is not completely clear, our measurement is consistent with prior works [61, 20]. Our results show that the nuclear-spin environment, known to be the dominant factor in spin dephasing [142, 197], plays an important role in longitudinal relaxation even at low doping densities ($\sim 10^{14}$ cm^{-3}) and moderate magnetic fields (up to several tesla).

On the high-field side, the similar magnetic-field dependence observed in all three semiconductors is suggestive of a universal mechanism. We theoretically investigate the dominant spin-relaxation mechanisms and find that two mechanisms, (i) the direct

spin-phonon interaction and, (ii) the admixture mechanism caused by Dresselhaus spin-orbit coupling combined with the piezoelectric electron-phonon interaction, can account for the magnitude of the observed relaxation in GaAs and CdTe. The strength of the direct spin-phonon interaction is surprising because it was found to be negligible in the similar quantum dot system [116]. We find, however, that both interactions are too weak to account for the observed relaxation in InP.

The paper is organized as follows: Section 5.3 presents the studied samples and experimental technique to measure T_1, the experimental results are summarized in Sec. 5.4. Section 5.5 presents the theory and comparison with experiment. The paper is summarized by a short conclusion 5.6. Appendices include additional experimental and theoretical details.

5.3 Samples and experimental technique

We study two GaAs, three InP, and two CdTe n-doped samples with the parameters given in Table 5.1. Spin-relaxation is measured optically in the Voigt geometry (photon wave vector $\mathbf{k} \perp \mathbf{B}$) with the magnetic field aligned parallel to the sample surface. Magneto-photoluminescene spectra exhibiting optically resolved Zeeman transitions for all three semiconductors are shown in Appendix D.1. Λ-transitions suitable for optically pumping the electron spin are found by resonantly exciting one of the Zeeman sublevels of the neutral donor (D^0) to the lowest neutral donor-bound exciton (D^0X) transition and observing the corresponding Raman transition. The optically excited and collected transitions for InP (GaAs, CdTe) are labelled in the energy diagram and photoluminescence spectra in Figs. 5.1(a),(b) [Appendix D.2, Figs. D.2(a),(b),(e),(f)].

To measure the spin relaxation time in the magnetic field, we optically deplete one of the Zeeman spin sublevels and monitor the recovery of its thermal population in the course of spin relaxation. At high magnetic fields, the optically-resolved spin Raman transitions enable frequency-selective optical pumping of the donor electron state. At low fields, while the transitions cannot be spectrally resolved, optical pumping is still obtained by utilizing the optical polarization selection rules. Optical pumping is confirmed by monitoring the time-dependence of the collected transition intensity during optical excitation after the system has reached thermal equilibrium. A typical high-field optical pumping pulse sequence and photoluminescence trace are depicted in Figs. 5.1(c),(d). The decrease in photoluminescence intensity is only observed with

Table 5.1: Sample parameters. $N_e = N_D - N_A$ is the electron density, ℓ is the sample thickness. Metal organic vapour phase epitaxy and molecular beam epitaxy are abbreviated by MOCVD and MBE respectively. The InP epilayer is grown directly on an InP substrate. InP samples were grown by metalorganic vapour phase epitaxy at between 540 and 580$^{\cdot}$ C using trimethylindium and either phosphine or tertiary-butylphosphine. The GaAs epilayer is grown on 4 microns of $Al_{0.3}Ga_{0.7}As$ on a GaAs substrate. For the CdTe samples, carrier concentration was not measured but is believed to be greater than 10^{14} cm^{-3} and less than 10^{15} cm^{-3} based on measurements on samples grown from the same starting material. The lineshapes of the one LO-phonon replica of the free exciton support this; the inverse Maxwell-Boltzmann distribution of CdTe-1 is sharper than that of CdTe-2. Further details on sample growth are given in the references.

Sample	N_e (cm^{-3})	ℓ (μm)	Growth Method
InP-1	5.6×10^{13}	5.1	MOCVD
InP-2	2.3×10^{14}	7.4	MOCVD
InP-3	1.8×10^{15}	4.2	MOCVD
GaAs-1 [187]	3×10^{13}	15	MBE
GaAs-2	5×10^{13}	10	MBE
CdTe-1 [172]	1×10^{14}	>1000	Bridgman
CdTe-2	$> 10^{14}$	>1000	Bridgman

resonant spin excitation. Two-laser experiments in GaAs have also confirmed that this decrease is due to spin-pumping and not, for example, due to photo-induced ionization [74]. A clear optical pumping signal cannot be observed in the highest purity InP sample, InP-1. The cause is attributed to surface depletion effects discussed further in Appendix D.3. For the remainder of the paper we will restrict ourselves to the remaining six samples, where reliable signals are detected.

Spin-relaxation measurements are performed by varying the recovery time between optical pumping pulses which are produced by an acousto-optic modulator (AOM) from the output of a narrow-band continuous-wave Ti:Sapphire laser. The AOM extinction ratio, r_e was measured to be $>10^4$ giving an upper-bound of the maximum measurable T_1 of $r_e \tau_{op}$, in which τ_{op} is the characteristic timescale of optical pumping. Given the several microsecond τ_{op} [Fig. 5.1(d)], we have the ability to measure T_1 exceeding 10 ms. The "Raman" photoluminescence is collected during the first part of the optical pumping pulse, see Fig. 5.1(e). As the recovery time increases, we ob-

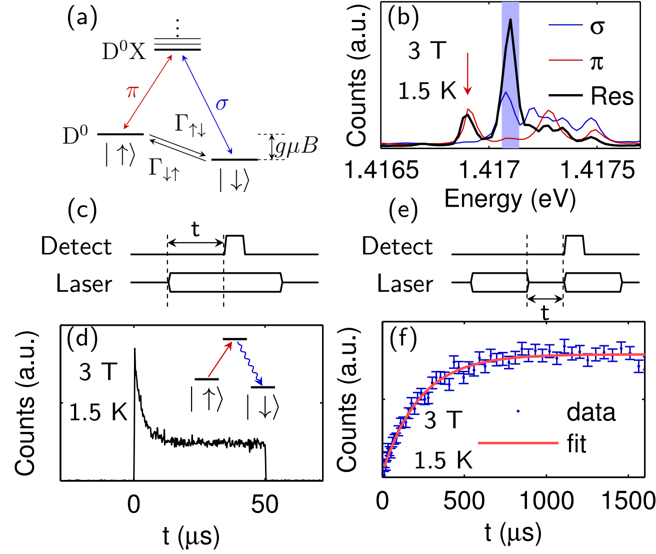

Figure 5.1: (a) Energy level diagram for the InP donor system. (b) Photoluminescence spectrum of InP. Excitation at 1.549 eV with 50 μW power, for the two above-bandgap excitation spectra (red and blue). σ (π) denote linear collection polarization perpendicular (parallel) to the magnetic field. Resonant excitation spectrum (black) uses excitation at 1.417 eV with 100 μW π-polarized light, with σ-polarized light collected. (c) Pulse sequence for optical pumping. The Ti:Sapphire laser is pulsed on and off repetitively on the π transition, while PL from the σ transition is detected. The time between pulses significantly exceeds T_1. (d) Optical pumping trace for InP with laser power 10 μW. The inset sketches the population transfer process during optical pumping. The amplitude of the exponential curve is proportional to the population in $\uparrow$. (e) Pulse sequence for T_1 measurement. The detector gate-on time is 2 μs and the laser pulse length is 50 μs. (f) T_1 measurement for InP with laser power 10 μW. The data is fit with an exponential plus a background yielding the time constant $T_1 = (0.23 \pm 0.1)$ ms. Error bars denote the standard deviation of the recovery signal in each time bin over the many repetitions of the pulse sequence. The corresponding representative data for GaAs and CdTe are given in Appendix D.2. All experiments used $\sim$30 μm laser spot size.

serve an increase in the collected signal as the system returns to thermal equilibrium. At each magnetic field, the recovery is fitted to a weighted exponential with time constant T_1 [195], as shown in Fig. 5.1(e). Measurements are performed for fields up to 7.0 T. Reduced visibility of the optical pumping signal places a technical limit on the minimum magnetic field measurement for each sample.

5.4 Experimental Results

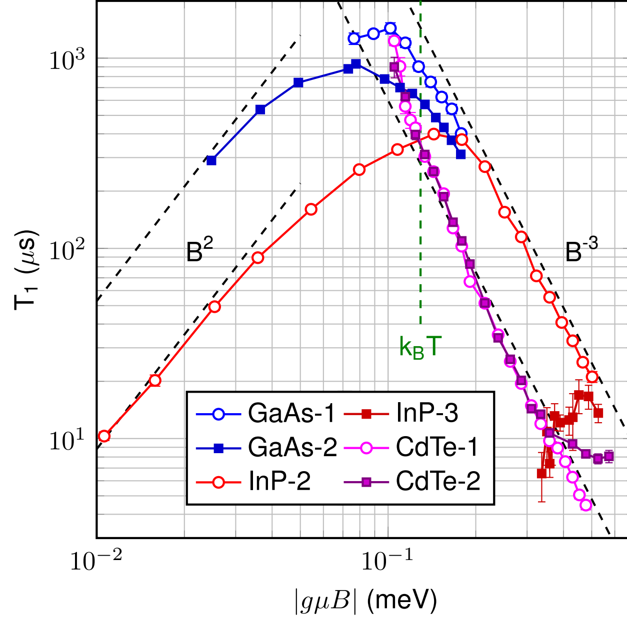

Figure 5.2: T_1 as a function of Zeeman splitting for the six different samples at 1.5 K. The absolute values of the electron g-factors used to convert from B to the Zeeman splitting for GaAs, InP and CdTe are 0.44, 1.3, and 1.65, respectively. Sample descriptions are given in Table 5.1. The black dashed lines in the high energy (low energy) side denote a B^{-3} (B^2) dependence for reference. They are offset from the experimental data for clarity. The green dashed line denotes the thermal energy k_BT for reference.

The longitudinal spin relaxation times T_1 as a function of the electron Zeeman splitting $\Delta E = |g\mu B|$ for InP, GaAs and CdTe are shown in Fig 5.2. Here, g is the effective electron g-factor and μ is the Bohr magneton. The data show several notable features. First, all samples approach a $T_1 \sim B^{-\nu}$ dependence, with $3 \lesssim \nu \lesssim 4$, at high magnetic fields. The proportionality constant depends on the semiconductor sample. A B^{-3} dependence, included in Fig. 5.2, fits all curves well, however we note that higher-field data would be desirable for GaAs because the small electron g-factor prevents us from accessing the high-Zeeman-splitting limit, where $|g\mu B| \gg k_BT$. Also, a B^{-4} power-law is reasonable for CdTe, as the magnetic field dependence becomes steeper in CdTe with decreasing field, see also Fig. 5.4. The high-field T_1 process

appears to be independent of donor concentration. Even the T_1 curve for the high-density InP-2 sample approaches the InP-1 curve at the highest fields. At low fields, T_1 in InP and GaAs approaches a B^2 dependence with a donor-concentration-dependent pre-factor. This is extremely pronounced for the InP samples in which the donor-bound electron density N_e, the difference between the donor and acceptor densities in the sample, $N_D - N_A$, differs by a factor of 4. The effect is also present in GaAs in which N_e differs by a factor of 1.7. Finally, the maximum T_1 observed in all three materials is similar: $T_1 = 1.4$, 0.4, and 1.2 ms for GaAs, InP, and CdTe respectively.

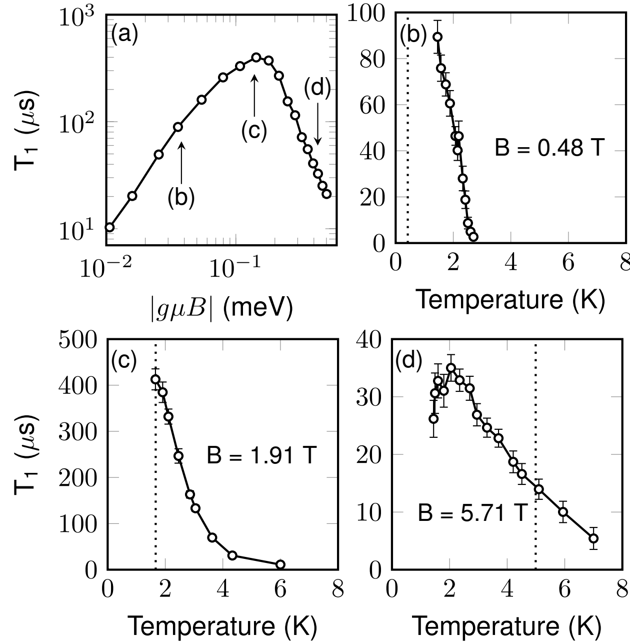

Figure 5.3: (a) T_1 as a function of the Zeeman splitting for InP-2 at 1.5 K. The arrows show the magnetic field values at which the temperature dependence study was performed. (b-d) Temperature dependence of T_1 at (b) $B = 0.48$ T, (c) 1.9 T, and (d) 5.7 T. The dotted line denotes $|g\mu B|/k_B$.

Measurements of the temperature T effect on T_1 are also performed. In InP-2, the sample in which T_1 can be obtained for the largest range of Zeeman energies, $T_1(T)$ was measured at 0.5 T (low field regime), 1.9 T (peak T_1), and 5.7 T (high-field regime) with the results depicted in Fig. 5.3. In the low-field regime, an extremely-steep inverse dependence of T_1 on temperature is observed indicative of

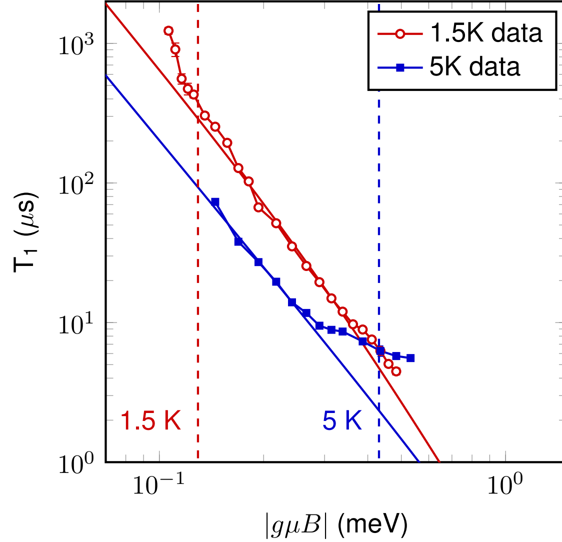

Figure 5.4: T_1 as a function of Zeeman splitting for CdTe-1 at $T = 1.5$ K and $T = 5$ K. The red and blue lines are mutually fitted by an empirical formula $T_1 = bB^4/F_{ph}$, where $b = 2000\ \mu s/\mathrm{T}^4$. The red and blue dashed lines denote the energy at 1.5 K and 5 K.

a strong phonon-assisted process. In the high-field regime, the relaxation time is almost independent of temperature at the lowest temperatures in our experiments, and drops with an increase in T. This high-field behavior is consistent with a model in which T_1 is inversely dependent on the phonon factor $F_{ph} = 2N_{ph} + 1$, in which $N_{ph} = [\exp(|g\mu B|/k_B T) - 1]^{-1}$ is the phonon occupation number. A comparison of magnetic-field-dependent measurements at 1.5 K and 5 K for CdTe-1 also support a high-field single-phonon mechanism. The ratio of the two curves in Fig. 5.4 is given by $F_{ph}(5\text{ K})/F_{ph}(1.5\text{ K})$.

5.5 Theory

Here we consider the mechanisms resulting in spin relaxation of donor-bound electrons. We start with the limit of relatively-low magnetic fields, where spin relaxation is controlled by the hyperfine coupling of the electron and nuclear spins. Next, we turn to the regime of high enough magnetic fields where the nuclei-induced spin relaxation is unimportant and the spin-flip processes caused by the joint effects of the

electron-phonon and the spin-orbit interactions play the major role.

5.5.1 *Low-field spin-relaxation*

At low temperatures and low donor densities, the electrons in bulk semiconductors are localized. At low and moderate magnetic fields, the electron spin relaxation is controlled by the hyperfine interaction with the host lattice nuclei [141, 57]. The spin dynamics of the electron in the ensemble of donors obey the set of kinetic equations [79, 177]

$$\frac{d\boldsymbol{S}_i}{dt} + \boldsymbol{S}_i \times \boldsymbol{\Omega}_i = \boldsymbol{\mathcal{Q}}_i, \tag{5.1}$$

where $\boldsymbol{S}_i$ is the electron spin at the site i, $\boldsymbol{\Omega}_i = \boldsymbol{\Omega}_{i,\mathrm{nucl}} + \boldsymbol{\Omega}_B$ is the electron spin precession frequency caused by the hyperfine interaction with nuclear spins, $\boldsymbol{\Omega}_{i,\mathrm{nucl}}$, and by the Larmor precession in the external field, $\boldsymbol{\Omega}_B$. The collision integral $\boldsymbol{\mathcal{Q}}_i$ describes the variations of the spins due to the electron hopping between sites, processes of ionization and recombination, exchange diffusion, etc. [141, 115]. The schematic illustration of the spin dynamics of localized electrons is presented in Fig. 5.5(a). Here we employ the simplest model of the collision integral by introducing a single correlation time τ_c, disregarding the spread of the transition probabilities [141, 79]. We assume that the nuclear fluctuations are frozen on the timescale of τ_c and that the Zeeman splitting in the external field is negligible as compared with the thermal energy. Hence, we obtain a simple analytical formula for the relaxation time of the spin component parallel to the magnetic field $\mathbf{B} \parallel z$ [79]:

$$T_{1,hf} = \frac{\tau_c \mathcal{A}}{1 - \mathcal{A}}, \tag{5.2}$$

where

$$\mathcal{A} = \left\langle \frac{1 + \Omega_{i,z}^2 \tau_c^2}{1 + \Omega_i^2 \tau_c^2} \right\rangle, \tag{5.3}$$

and the angular brackets denote the averaging over the distribution of random nuclear fields.

Equation (5.2) is valid for an arbitrary relationship between the spin precession frequency and τ_c. In the experimentally relevant range of magnetic field, $\Omega_B = |g\mu B|/\hbar$ exceeds by far the spin precession frequency in the field of nuclear fluctuations and

the inverse correlation time. It follows then from Eqs. (5.2), (5.3) that

$$T_{1,hf} = \frac{3\tau_c \Omega_B^2}{2\langle\Omega_{\rm nucl}^2\rangle} \propto \tau_c B^2, \tag{5.4}$$

where $\langle\Omega_{\rm nucl}^2\rangle$ is the mean square fluctuation of the nuclear field averaged over the ensemble of donors. This expression shows the B^2 power law which is observed in experiment, Fig. 5.2.

This increase in spin-relaxation time with increasing field is related to the suppression of the relaxation by the magnetic field: At $\Omega_B \gg \tau_c^{-1}, \langle\Omega_{\rm nucl}^2\rangle^{1/2}$, the electron spin precesses around the total field $\mathbf{\Omega}_B + \mathbf{\Omega}_{i,\rm nucl}$ during the correlation time. Its precession axis is almost parallel to $\mathbf{\Omega}_B$ and its orientation changes by a small random angle $\sim \Omega_{i,\rm nucl}/\Omega_B$ when the electron hops between the localization sites. Such a random process results in the spin relaxation rate $\sim \tau_c^{-1}(\Omega_{i,\rm nucl}/\Omega_B)^2 \propto 1/(\tau_c B^2)$ in agreement with Eq. (5.4). For known mechanisms of electron correlation time at a donor, such as electron hopping and the exchange diffusion, see Ref. [115] for review, an exponential sensitivity to the donor density (and, in the former case, to the temperature) is expected [115, 176]. Correspondingly, for these mechanisms T_1 should be strongly affected by these parameters. Such trends are clearly seen in the experiment, Fig. 5.2 and Fig. 5.3(b).

The developed model enables quantitative comparison with the experiment. To that end, we evaluate the mean square of the donor-bound electron spin precession frequency in the nuclear field as [59]

$$\langle\Omega_{\rm nucl}^2\rangle = \frac{V_0}{8\pi(a_B^*)^3\hbar^2}\sum_\alpha \left(A_\alpha^{hf}\right)^2 I_\alpha(I_\alpha+1), \tag{5.5}$$

where $a_B^* = \varepsilon\hbar^2/(m^* e^2)$ is the donor Bohr radius, $V_0 = a_0^3$ is the unit lattice volume, I_α is the spin of $\alpha^{\rm th}$ nucleus in a unit cell, A_α is the hyperfine interaction constant. Taking for GaAs $A_{^{69}\rm Ga} = 38.2$ μeV, $A_{^{71}\rm Ga} = 48.5$ μeV and $A_{^{75}\rm As} = 46$ μeV [189] we obtain $\sqrt{\langle\Omega_{\rm nucl}^2\rangle} = 0.47 \times 10^8$ s^{-1}. Fitting the experimental data with Eq. (5.4), we determine a correlation time $\tau_c \approx 25$ ns for the GaAs-2 sample. Such a value of the correlation time is consistent with previous studies of GaAs samples with similar donor densities [61, 20]. A somewhat longer τ_c of ~ 40 ns is determined for the InP-2 sample, where the hyperfine interaction is dominated by ^{115}In isotopes

with $I_{\rm In} = 9/2$. The estimate for $A_{\rm In}$ comes from Ref. [83] where the Overhauser effect for InSb was measured. The literature reports a spread of $A_{\rm In}$: 47 μeV [42], 56 μeV [191] and 84 μeV [189]. Here we use the middle value of $A_{\rm In} = 56$ μeV, which yields $\sqrt{\langle \Omega^2_{\rm nucl} \rangle} = 1.6 \times 10^9$ s^{-1}.

Although the experimental sensitivity of T_1 to temperature and carrier density are consistent with the known mechanisms contributing to the donor electron correlation time, the magnitude of τ_c is orders of magnitude shorter than these mechanisms predict for the low donor densities used in this study. Our result is consistent with prior works [61, 20] and suggests additional, unknown mechanisms may be at play, such as an inhomogeneous donor distribution resulting in the formation of clusters with a relatively high donor density, and short τ_c.

According to Eq. (5.4), the electron spin relaxation time associated with the hyperfine interaction strongly increases with an increase in field. Hence, at sufficiently strong magnetic fields this mechanism becomes inefficient as compared with mechanisms caused by the combination of the electron-phonon and spin-orbit interactions described below. By contrast, T_1 due to these processes decreases with an increase in B.

5.5.2 High-field spin-relaxation

While the spin-orbit interaction alone is not sufficient to cause a spin-flip of a localized charge carrier, a combination of the electron-phonon interaction and spin-orbit coupling serves as a main source of localized electron spin relaxation at high magnetic fields [152, 3, 71]. Phonons can also modulate the hyperfine coupling of the electron and the lattice-nuclei spins giving rise to $T_1 \propto B^{-3}$ dependence [152]. Similar to the quantum dot case, this effect is negligible for donor-bound electrons. Two-phonon processes [3] are also very weak for the range of temperatures and fields studied here.

An exhaustive theoretical investigation of the spin-flip mechanisms has been performed for the related GaAs quantum dot system [116, 208, 138]. In GaAs quantum dots, all reported spin-orbit related mechanisms exhibit a $T_1 \propto B^{-\nu}$ dependence with $\nu \geq 5$. For bulk GaAs-like semiconductors, such a study has not been performed before to the best of our knowledge. The orbitals for the donor-bound electron differ from those for quantum dots, leading to the use of a different approximation for the Dresselhaus spin-orbit Hamiltonian and different selection rules.

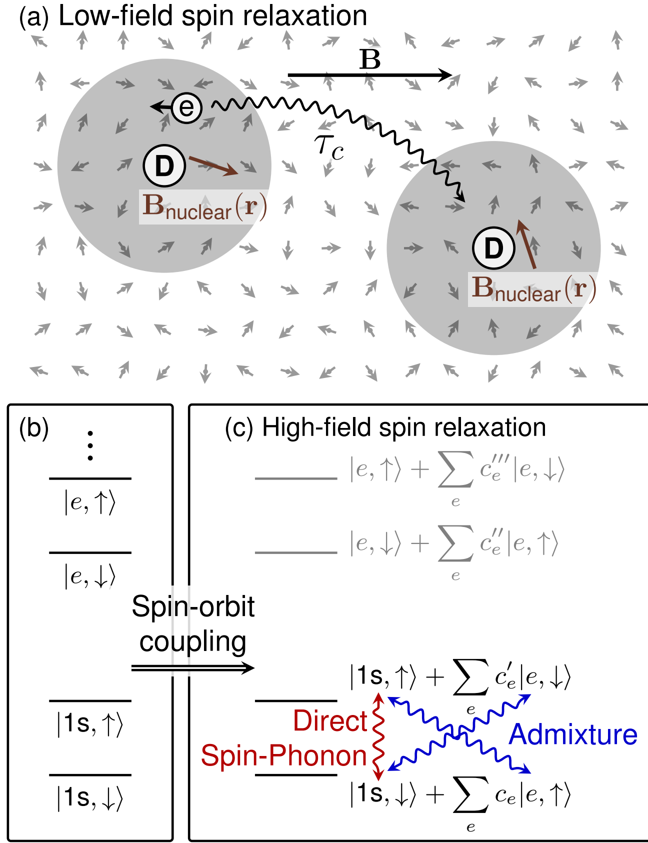

Figure 5.5: Schematic of spin-relaxation mechanisms. (a) At low magnetic fields, spin-relaxation is dominated by the interaction of the electron spin with lattice nuclear spins. Panels (b,c) are relevant for the high-field spin relaxation mechanism. (b) Energy level structure for unperturbed donor-bound electron in magnetic field, described by zero-field quantum numbers. (c) Dresselhaus spin-orbit coupling mixes states with opposite spin and different angular momentum components. In the admixture mechanism, phonons cause relaxation between the two eigenstates via the components with like spin. The direct spin-phonon interaction causes spin-relaxation via the components with opposite spin.

Experimentally we observe that the high-field spin relaxation is consistent with a single phonon process. This limits us to mechanisms that combine Dresselhaus spin-orbit coupling and spin-conserving phonon-induced relaxation, and direct spin-phonon mechanisms. In this section, we present the detailed calculation for the high-field T_1 due to both mechanisms and compare our theoretical results to the experimental data.

Table 5.2: Material parameters relevant to the donor-bound electron spin-relaxation in GaAs, InP, and CdTe. g is the effective electron g-factor, m^* is the electron effective mass (m_0 is the free electron mass), h_{14} is the piezoelectric constant, γ is the Dresselhaus spin-orbit coupling constant, ρ is the mass-density, s_l is the longitudinal sound velocity, s_t is the transverse sound velocity, ε is the relative permittivity of the material, v_0 characterizes the strength of the direct spin-phonon coupling interaction, and D is the deformation potential interaction constant.

	GaAs	InP	CdTe
g	-0.44	1.3	-1.67
m^*	$0.067m_0$	$0.08\,m_0$	$0.106m_0$ [150]
h_{14} (V/m)	14.5×10^8 [135]	7.4×10^8 [161]	3.94×10^8 [150]
γ (eV·Å^3)	23.7 [104]	10.1 [104]	11.74 [150]
ρ (kg/m^3)	5.32×10^3 [1]	4.81×10^3 [1]	4.85×10^3 [150]
s_l (m/s)	4.73×10^3 [1]	4.58×10^3 [1]	3.08×10^3 [150]
s_t (m/s)	3.35×10^3 [1]	3.08×10^3 [1]	1.85×10^3 [150]
ε	12.56	12.5 [1]	~ 10.3 [136]
v_0 (m/s)	8×10^5 [58]	4×10^5 [58]	unknown
D (eV)	-5.55 [77]	-4.4 [77]	-5.45 [77]

5.5.3 *Admixture mechanism caused by Dresselhaus spin-orbit coupling*

We are first interested in the spin relaxation between the Zeeman sublevels of the donor-bound electron ground state mediated by spin-orbit and electron-phonon coupling (admixture mechanism). This is the dominant relaxation mechanism for III-V quantum dots [116, 208] and naively may also be expected to play the dominant role in the similar donor system. For this mechanism, the spin-orbit interaction modifies the ground-state Zeeman sublevels by the admixture of the excited sublevels with the opposite spin component. Hence, the spin-independent electron-phonon coupling causes spin-relaxation through the components of the states with the same spin, as depicted in Fig. 5.5(b)-(c).

The interaction Hamiltonian for the admixture mechanism is

$$H_{adm} = U_{ph} + H_{so}, \tag{5.6}$$

where U_{ph} is the spin-conserving electron-phonon interaction Hamiltonian and H_{so}

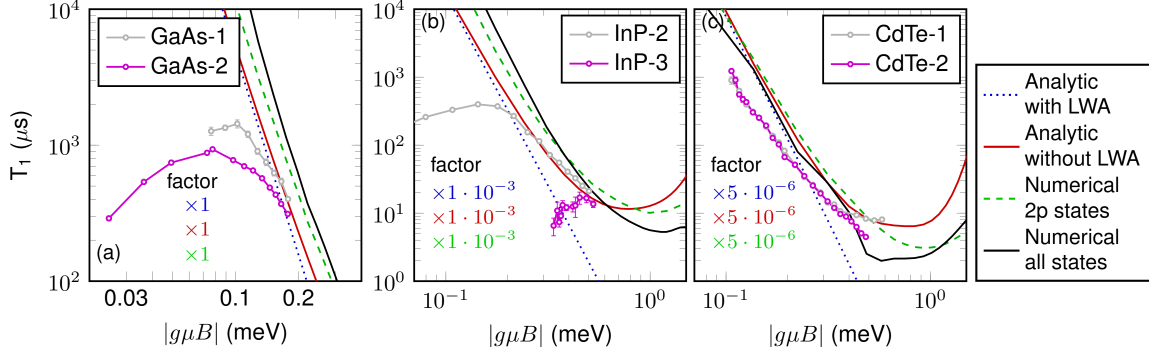

Figure 5.6: Theoretical results for spin-relaxation time T_1 via the admixture mechanism, using both analytic and numerical wave functions. Pink and grey dots show the experimental data. For GaAs [panel (a)], the theory matches the data reasonably well with no fit parameters. For InP (b) and CdTe (c), the calculated values are multiplied by the factor specified in the figure for ease of comparison. $T = 1.5$ K. We note that the numerically calculated T_1 which includes only the 2p states is slightly shorter than the full numerical solution. This is due to destructive interference between the orbital states in Eq. (5.8).

is the spin-orbit Hamiltonian. In the high-field limit, the Zeeman splitting can be comparable or even exceed the thermal energy. In such a case, the transition rates from the Zeeman sublevel $\downarrow$ to $\uparrow$, $\Gamma_{\uparrow\downarrow}$, and back, $\Gamma_{\downarrow\uparrow}$, differ. The observed longitudinal spin relaxation time satisfies

$$T_1 = (\Gamma_{\uparrow\downarrow} + \Gamma_{\downarrow\uparrow})^{-1}.$$

The individual rates are found using Fermi's golden rule, e.g.,

$$\Gamma_{\downarrow\uparrow} = \frac{2\pi}{\hbar} \sum_{\mathbf{q},\alpha} |M_{\downarrow\uparrow}|^2 \delta(\hbar q s_\alpha - |g\mu B|), \tag{5.7}$$

where $\mathbf{q}$ is the phonon wavevector, s_α is the speed of sound in phonon branch α and $\alpha = t, l$ for the transverse and longitudinal modes, respectively. Hereafter we assume for convenience that the spin-up state has higher energy than the spin-down one, hence, $g\mu B > 0$, as illustrated in Fig. 5.5, so that the rate in Eq. (5.7) corresponds to the phonon emission process. Electron spin-relaxation occurs via a second order process due to the quantum interference of U_{ph} and H_{so} in the Hamiltonian (5.6), see

Ref. [116] for details,

$$M_{\downarrow\uparrow,adm} = -\sum_e \left[\frac{\langle 1\mathrm{s}, \downarrow | U_{ph} | e, \downarrow \rangle \langle e, \downarrow | H_{so} | 1\mathrm{s}, \uparrow \rangle}{E_e - E_{1\mathrm{s}} + g\mu B} + \frac{\langle 1\mathrm{s}, \downarrow | H_{so} | e, \uparrow \rangle \langle e, \uparrow | U_{ph} | 1\mathrm{s}, \uparrow \rangle}{E_e - E_{1\mathrm{s}} - g\mu B} \right], \tag{5.8}$$

where $|1\mathrm{s}\rangle$ is the ground orbital state of the donor-bound electron, $|e\rangle$ denotes the excited orbital states, and E_e, $E_{1\mathrm{s}}$ are the energies of the corresponding orbitals.

Due to the small localization energy of the donor-bound electron ($\lesssim 10$ meV), the electron wave function in a magnetic field is well described with effective mass theory using the hydrogenic Hamiltonian

$$H_0 = \frac{\hbar^2}{2m^*} \left(\mathbf{k} - \frac{e}{\hbar} \mathbf{A} \right)^2 - \frac{1}{4\pi\varepsilon_0} \frac{e^2}{\varepsilon r} + \frac{1}{2} g\mu \boldsymbol{\sigma} \cdot \mathbf{B}, \tag{5.9}$$

where m^* is the electron effective mass, e is the electron charge, $\mathbf{A}$ is the vector potential of the magnetic field $\mathbf{B}$, $\mathbf{r}$ is the position vector, $r = |\mathbf{r}|$, $\mathbf{k} = -i\partial/\partial\mathbf{r}$ is the wavevector, ε is the relative dielectric constant of the material, and $\boldsymbol{\sigma}$ is the vector composed of the Pauli matrices. In the presence of the magnetic field, the Hamiltonian, Eq. (5.9), possesses an axial symmetry and its eigenstates are characterized by four quantum numbers: principal quantum number ν, angular momentum z-projection m, z-parity π_z and spin z-projection m_s. To establish a link with the hydrogen-like series of donor-bound electron states at $B = 0$, we will label the orbitals by their zero-field quantum numbers nlm, where n is the principal quantum number and l is the angular momentum quantum number, when appropriate.

The energy of a phonon involved in the spin-flip transition is the Zeeman splitting between the spin sublevels. Therefore, the phonon wavevector $q_\alpha = g\mu B/(\hbar s_\alpha) \to 0$ as $B \to 0$. Thus, at moderate magnetic fields in piezoelectric crystals such as GaAs, InP and CdTe studied here, we found that the piezoelectric electron-phonon interaction with $U_{ph}^{(pz)} \propto q^{-1/2}$ dominates over the deformation potential interaction, where $U_{ph}^{(dp)} \propto q^{1/2}$ [76], see Appendix D.5. The piezoelectric electron-phonon interaction reads

$$U_{ph}^{(pz)} = \sqrt{\frac{\hbar}{2\rho\omega_{\mathbf{q},\alpha}}} e^{i(\mathbf{qr} - \omega_{\mathbf{q},\alpha} t)} (eA_{\mathbf{q},\alpha}) b_{\mathbf{q},\alpha}^\dagger + \text{c.c.}, \tag{5.10}$$

where

$$A_{\mathbf{q},\alpha} = h_{14} \sum_{ijk} \beta_{ijk} \xi_i \xi_j \hat{e}_k^{(\mathbf{q},\alpha)}, \tag{5.11}$$

ρ is the mass density of the material, $\omega_{\mathbf{q},\alpha}$ is the phonon frequency, $b^{\dagger}_{\mathbf{q},\alpha}$ is the creation operator for a phonon, $\boldsymbol{\xi} = \mathbf{q}/q$ is the unit vector along the phonon wavevector, $\hat{\boldsymbol{e}}$ is the phonon polarization vector, the only nonzero components of β_{ijk} are those with different subscripts, $\beta_{xyz} = \ldots = \beta_{zyx} = 1$, and h_{14} is the piezoelectric constant [76].

Since all the samples studied here are bulk semiconductors characterized by the T_d point symmetry group, the only relevant spin-orbit coupling comes from the cubic-in-the-electron-wavevector Dresselhaus spin-orbit term, H_{so}. It arises from the lack of inversion symmetry in zinc-blende crystals and has the form

$$H_{so} = \gamma \sum_i \sigma_i k_i (k_{i+1}^2 - k_{i+2}^2), \tag{5.12}$$

where γ is the Dresselhaus spin-orbit coupling constant and the subscript i cycles through x, y, z.

Depending on the relation between the magnetic length, $l_b = \sqrt{\hbar/|eB|}$, and the effective Bohr radius, a_B^*, various regimes of the spin-flip can be realized. At sufficiently weak magnetic fields, where $l_b \gg a_B^*$, the magnetic field does not affect the hydrogen-like states of the donor-bound electron. In this case, the Dresselhaus spin-orbit interaction admixes nf-shell states with principal quantum numbers $n = 4, 5, \ldots$ and orbital momentum $l = 3$ to the 1s-shell state. With the long wavelength approximation (LWA) for the phonons, where $|g\mu B| a_B^*/(\hbar s_\alpha) \ll 1$, we obtain the longitudinal spin relaxation time

$$T_{1,adm}^{(low)} \propto B^{-9} F_{ph}^{-1}, \tag{5.13}$$

see Appendix D.5 for details. Hence, at low temperatures, T_1 is inversely proportional to B^9, while for $k_B T \gtrsim g\mu B$, $T_1 \propto B^{-8}$. We do not observe this regime in experiments due to the dominating low-field nuclear-electron hyperfine mechanism.

In the opposite limit, where $l_b \ll a_B^*$ and, moreover, $\hbar\omega_c \gg \mathcal{E}_{Ry}^*$, where $\omega_c = |eB/m^*|$ is the cyclotron frequency and $\mathcal{E}_{Ry}^* = m^* e^4/[2(4\pi\varepsilon\varepsilon_0)^2\hbar^2]$ is the donor-bound-electron binding energy, the magnetic field shrinks the wave functions of the ground and excited states of the donor-bound electron. This situation is similar to the case of an electron localized in the (xy) plane by a parabolic potential, like in the quantum dot

system studied in Ref. [116]. Here the excited states with $|m| = 1$ (in addition to those with $|m| = 3$) are admixed and, in the LWA, we obtain for the spin flip time

$$T_{1,adm}^{(high)} \propto B^{-3} F_{ph}^{-1}, \tag{5.14}$$

see Appendix D.5. This high-field limit is not realized for the studied samples and magnetic fields accessible in our experiments. Moreover, in this limit, the LWA in our system is no longer valid.

Therefore, we have performed the full numerical evaluation of the spin relaxation time according to Eqs. (5.7) and (5.8) using the numerical solutions to Eq. (5.9) [167] and the material parameters from Table 5.2. Additional details on the numerical calculation can be found in Appendix D.4. These results, which include 18 excited state orbitals, are given by the black curves in Fig. 5.6. We numerically find that the first excited state which evolves from $2p_-$ makes the dominant contribution to the spin relaxation rate, as shown by the dashed green curves in Fig. 5.6.

This numerical result, together with the analysis of the wavefunctions in Appendix D.5, motivates using Gaussian shapes of the ground and excited state wave functions, Eqs. (D.9), to obtain an analytic solution for further insight into the intermediate field behavior. The magnetic field induced shrinking is taken into account by assuming different characteristic lengths $l_{z,1s} = a_B^*$ and $l_{\rho,1s} = [1/(a_B^*)^2 + 1/(2l_b^2)]^{-1/2}$ for the motion along and perpendicular to the field. After some transformations, we obtain (see Appendix D.5 for details):

$$\frac{1}{T_{1,adm}} = \frac{256\chi^{10}}{35(1+\chi^2)^{12}} \frac{\gamma^2 e^4 h_{14}^2 |g\mu|^3 B^5}{\pi\rho\hbar^6} \left(\frac{1}{\Delta E} - \frac{1}{\Delta E + \hbar\omega_c}\right)^2 \left(\frac{f_l}{s_l^5} + \frac{4f_t}{3s_t^5}\right) F_{ph} . \tag{5.15}$$

Here, $\Delta E = E_{2p_-} - E_{1s}$ is the energy difference between the hydrogen-like ground 1s and excited $2p_-$ state. The factors $f_\alpha = \exp\{-(\chi g\mu B l_\rho)^2/[(1+\chi^2)\hbar^2 s_\alpha^2]\}$ take into account that the phonon wavelength can be comparable with the donor-bound electron state size. These factors are particularly sensitive to the wavefunction shape. Finally, the parameter χ is a parameter of the wave functions which characterizes the ratio of the effective radii for the excited and the ground states, see Eqs. (D.9). By comparing the trial wavefunction to the numerical 2p wavefunction, we find reasonable

choices for χ of 1.5, 1.7 and 2.2 for GaAs, InP and CdTe over the experimental range of magnetic field, as shown in Fig. D.5. The magnitude of $T_{1,adm}$ calculated according to Eq. (5.15) is quite sensitive to the choice of χ.

A comparison between the experimental, numerical, and analytic results for T_1 is shown in Fig. 5.6. We stress that these calculations contain no fitting parameters. Qualitatively we observe similar behavior between the analytic and numerical calculations. At sufficiently strong magnetic fields, we find the LWA fails for InP and CdTe due to their relatively large electron g-factors as compared with GaAs. This effect is taken into account by factors f_l and f_t in Eq. (5.15). It softens the exponent in B-dependence giving approximately $3 \lesssim \nu \lesssim 4$ in the accessible field range. Further increase in B results in a minimum in $T_1(B)$. It is noteworthy that at such magnetic fields, the deformation potential interaction may become important, see [173] and Appendix D.5 for details; moreover, in such fields the result could be quite sensitive to the shape of the wave functions. Hence, for sufficiently high fields, Eq. (5.15) provides only an indication of the trend.

We find that the numerically calculated values of T_1 for InP and CdTe are orders of magnitude longer than the experimentally observed spin relaxation times in these samples, which indicates the importance of other spin-flip mechanisms in the materials, see below. By contrast, in GaAs the calculated magnitude of T_1 is quite close to the experimental values, demonstrating that the admixture mechanism is significant in this material.

5.5.4 Direct spin-phonon interaction

Although the direct spin-phonon interaction was not found to be a dominant relaxation mechanism for electrons in semiconductor quantum dots [116], we demonstrate here that it contributes significantly to donor-bound electron spin relaxation. To some extent, this is because the role of the admixture mechanism is diminished due to the cubic-in-the-wavevector spin-orbit splitting in the bulk material, as compared with **k**-linear terms used for quantum dot systems [116]. The direct spin-phonon interaction Hamiltonian is [58]

$$U_{dir} = \frac{\hbar v_0}{2}[\sigma_x(u_{xy}k_y - u_{xz}k_z) + \sigma_y(u_{yz}k_z - u_{yx}k_x) + \sigma_z(u_{zx}k_x - u_{zy}k_y)], \qquad (5.16)$$

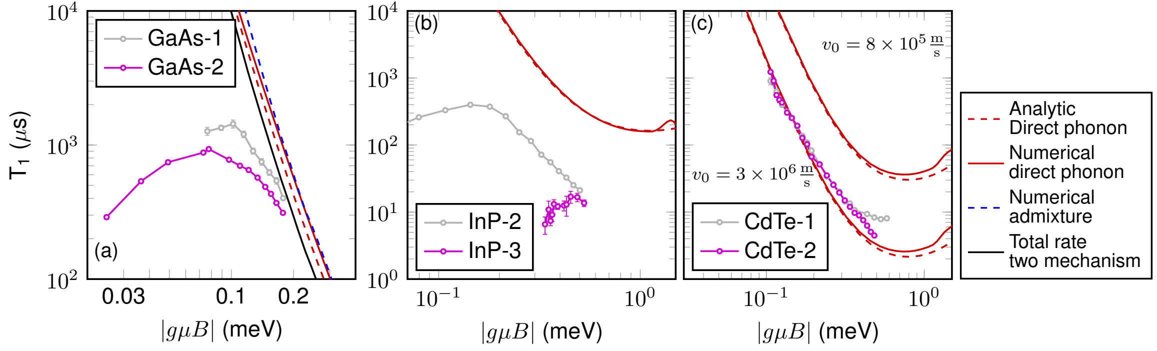

Figure 5.7: Theoretical results for the spin-relaxation time T_1 via the direct spin-phonon mechanism for GaAs (a), InP (b) and CdTe (c). Pink and grey dots show the experimental data. $T = 1.5$ K. The two dashed lines and two solid lines in (c) represent the analytic and numerical calculation results of T_1 using $v_0 = 8 \times 10^5$ m/s (upper curves) and $v_0 = 3 \times 10^6$ m/s (lower curves)

Here $u_{ij} = u_{ji}$ is the deformation tensor, and, as above, $\mathbf{k} = -i\boldsymbol{\nabla} - (e/\hbar)\mathbf{A}$. The coupling constant v_0 has the dimension of velocity. It has been determined by experiment for GaAs and InP but is unknown for CdTe (see Table 5.2). For numerical evaluation for CdTe, we use a spread of values, 8×10^5 m/s $< v_0^{\text{CdTe}} < 3 \times 10^6$ m/s with the lower (upper) bound corresponding to v_0^{GaAs} $\left(v_0^{\text{InSb}}\right)$ [58].

The relaxation rates $\Gamma_{\uparrow\downarrow}$ are calculated using Eq. (5.7) with the first-order matrix element $M_{\uparrow\downarrow} = \langle 1\text{s}, \uparrow | U_{dir} | 1\text{s}, \downarrow \rangle$, as depicted in Fig. 5.5(c). We use an approximate exponential wave function with a characteristic length $l = [(a_B^*)^{-2} + 1/(2l_b^2)]^{-1/2}$ to obtain analytic expressions for $\Gamma_{\uparrow\downarrow}$ and, correspondingly, for the associated longitudinal spin relaxation time $T_{1,dir}$. The choice of the wave function is motivated by the fact that only the 1s orbital state is involved, which is not significantly perturbed at the experimentally accessible magnetic fields. Moreover, the precise symmetry of the wave function for the direct phonon mechanism is not critical. The evaluation of Eq. (5.7) yields (see Appendix D.6):

$$\frac{1}{T_{1,dir}} = \frac{(ev_0 l^2)^2 |g\mu|^5 |B|^7}{560\pi\rho\hbar^6} F_{ph} \left(\frac{1}{s_l^7} \frac{1}{(1+Q_l^2)^6} + \frac{4}{3s_t^7} \frac{1}{(1+Q_t^2)^6} \right), \tag{5.17}$$

where $Q_\alpha = |g\mu B| l / (2\hbar s_\alpha)$. Equation (5.17) demonstrates that the spin-flip time is proportional to B^{-7} at weak magnetic fields. An increase in the field results in a

softening of the B-field dependence due to decrease of the efficiency of the electron-phonon interaction (breakdown of the LWA) described by the factors $(1 + Q_\alpha^2)^{-6}$. In addition to the analytic approximation, we performed the full calculation using the numerically-obtained ground-state donor wave function. The very good agreement between the analytic and numerical calculations, seen in Fig. 5.7, can be attributed to the minor effect of the magnetic field on the ground-orbital-state wave functions at the experimental fields.

A comparison between the theoretical calculations with no fit parameters and the experimental data is also provided in Fig. 5.7. For GaAs, we find that the magnitude of the direct-phonon mechanism is approximately the same as the admixture mechanism. Also included in Fig. 5.7(a) is the sum of these two mechanisms. Accounting for both mechanisms results in a difference between the theory and the data of approximately a factor of 2, which can be easily attributed to the uncertainties in the system parameters in Table 5.2.

For InP and CdTe, the direct spin-phonon mechanism is found to be significantly stronger than the admixture mechanism. For CdTe, the agreement between theory and experiment is extremely good if the direct spin-phonon interaction strength in CdTe is similar to that of InSb. This may be reasonable given the similar valence band spin-orbit splitting in the two materials, 0.8 eV in InSb [37] and 0.9 eV in CdTe [196, 137, 38]. Here, an independent measurement of v_0, like those performed in Ref. [58] for GaAs and InP, or its independent first-principles calculation, is needed to corroborate our result.

There is still a significant discrepancy between theory and experiment for InP, where the experimental spin-relaxation time is 15 to 30 times shorter than the predicted value from the direct spin-phonon coupling. Its origin is not clear and further studies, both experimental and theoretical, are needed to resolve this discrepancy.

5.6 Conclusion

In this work we measure the longitudinal spin relaxation time as a function of magnetic field for electrons bound to donors in three different high-purity direct bandgap semiconductors. We observe for the first time the crossover between low-field spin relaxation resulting from a hyperfine coupling of the electron and lattice nuclear spins and high-field single-phonon-mediated spin relaxation. From a fundamental perspec-

tive, the existence of both regimes is expected. However, the comparison of the data with the developed theory in terms of the magnitude of the relaxation raises new questions. Low field measurements indicate a tens of nanoseconds electron spin correlation time of so far unknown origin. High-field measurements strongly suggest the admixture mechanism is important in GaAs, while the direct spin-phonon interaction is important in both CdTe and GaAs. However for InP, the discrepancy between theory and experiment calls for further investigation.

In the context of possible applications, the high-field $B^{-\nu}$ dependence of T_1, combined with the density and temperature dependent low-field B^2 behavior, has practical implications. If the crossover point can be pushed to lower fields, extremely-long spin-relaxation times may be possible. This could be realized with lower impurity density, lower temperature, larger binding energies, and a nuclear-spin-free matrix. In support of this, we note that no crossover is observed in CdTe even when $k_B T > |g\mu B|$. This may reflect the role of the higher donor binding energy and/or the reduced nuclear-spin environment in CdTe. In this context, isotope purification, which is known to significantly affect spin dephasing, may also significantly increase the maximum achievable T_1 for electrons bound to shallow donors.

Chapter 6

PROGRESS TOWARDS ISOLATING A SINGLE POINT DEFECT

6.1 Introduction

One major roadblock to using donor- or acceptor-bound spins for quantum information is that a single spin has yet to be isolated in a way that both preserves its high homogeneity and allows optical access. Current quantum information processing schemes require error correction, which typically (though not always [30]) need to be performed on isolated qubits. A single deep acceptor can be isolated using scanning tunneling microscopy [211], but this method does not allow optical access. A single donor could possibly be isolated by fabricating structures [49], but proximity to a surface can increase inhomogeneous broadening, and perturb the donor's properties. In general, less-common impurities are easier to isolate optically in bulk materials. Defects composed of two impurities can exist in much lower concentrations, e.g. the NV center in diamond [56] or nitrogen pairs in GaAs [69], can be isolated with far-field microscopy. This chapter focuses on isolating spins bound to shallow donor or acceptors impurities, a promising qubit system.

Common shallow dopants in bulk semiconductor have strong radiative transitions and are highly-homogeneous due to their distance from surfaces. Unfortunately, common shallow dopants also have densities of $\sim 5 \times 10^{13}$ cm^{-3} even in the most pure GaAs samples, making it difficult to isolate one using far-field optical microscopy. Assuming a 6 μm axial resolution, such a sample would have ~90 impurities per diffraction limited spot. A factor of ~10 increase in lateral resolution would be required to isolate a single one, as illustrated in Fig. 6.1.

In this chapter we explore a few possible methods for isolating common shallow donors or acceptors while preserving optical access and maintaining high homogeneity. First, we investigate stimulated emission depletion super-resolution microscopy of A^0X, finding that spin-relaxation processes make this scheme challenging with continuous-wave excitation. Next we briefly explore ground-state-depletion super-

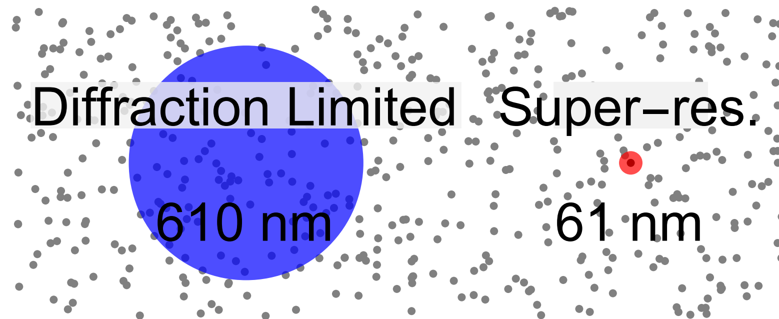

Figure 6.1: Cartoon of impurities (grey dots) and diffraction limited spot size. For an impurity density of $5 \times 10^{13}\,\mathrm{cm}^{-3}$ and a 6 μm axial resolution (or sample thickness) there are $\sim$90 impurities per diffraction limited spot. If the linear resolution can be improved by a factor of 10, there will on average be a single impurity per excitation volume.

resolution microscopy of D^0X, estimating that this could be a promising method to isolate a single donor if the collected signal can be improved with a cycling transition. Lastly, we design a thin semiconductor heterostructure to isolate single impurities, finding promising preliminary results.

6.2 Stimulated emission of acceptor-bound exciton

Solid state qubits are attractive candidates for quantum information processing because they have the potential to scale to large quantum networks. One particular class of solid-state qubits, those with coupled optical transitions, can utilize remote photon interference to generate quantum entanglement networks [36]. Point defect states hold particular promise in these schemes due to their potential for high optical homogeneity. This has ignited significant research activity on nitrogen-vacancy (NV) color centers in diamond, despite the fact that the dominant radiative decay mechanism for NV centers is through the incoherent phonon-assisted radiative recombination, or phonon sideband. In this section we study a scheme that could be used to isolate substitutional impurities in direct band-gap semiconductors. Due to the high defect concentrations even in the purest samples, these impurities cannot be optically isolated using diffraction-limited techniques.

Substitutional acceptors in GaAs combine the strong optical zero-phonon tran-

sitions of quantum dots with the optical homogeneity of NV centers. The acceptor impurity system consists of a neutral acceptor (A^0; impurity and bound hole) and a neutral acceptor bound exciton (A^0X; impurity, bound hole and bound exciton). The optical transitions for A^0X are impressively sharp with little inhomogeneous broadening, ($\lesssim 40$ μeV), and different spin sublevels are well resolved, see Fig. 6.2(a).

However, it is challenging to isolate a single acceptor in a bulk sample. The purest GaAs samples still have a background carbon concentration leading to 90 impurities per diffraction limited spot, see Fig. 6.1. Here, we propose to use stimulated emission depletion microscopy (STED) [91], a super-resolution technique, to isolate a single acceptor. By improving the transverse resolution by a factor of 10, we expect to optically isolate a single acceptor.

While STED resolution enhancements of 28 have been achieved for NV centers, [159], STED of A^0X presents an additional challenge. For NV centers, stimulated emission is performed into phonon sidebands and accordingly one laser can deplete all excited states. Because of the sharp optical transitions for A^0X, a narrow-band depletion laser can only induce stimulated emission for one A^0X sublevel. While stimulated emission of NV centers is an incoherent process due to THz relaxation rates, quantum coherence significantly alters the stimulated emission effect for A^0X. Thus stimulated emission of A^0X contains ingredients of quantum coherence and can act as a probe of A^0X coherence properties.

Here we report the first demonstration of stimulated emission of a substitutional impurity in a semiconductor. A 1.5 μW excitation laser was tuned resonant with the $|A^0, 1s\rangle \rightarrow |A^0X\rangle$ transition a, see Fig. 6.2(a). We then tuned the frequency of a 57 mW stimulated emission laser across the $\left|A^0X\right\rangle \rightarrow \left|A^0, 2s\right\rangle$ transition a' and collected the PL from $\left|A^0X\right\rangle \rightarrow \left|A^0, 1s\right\rangle$ transition b as the STED laser detuning from transition a' is varied. This energy level diagram is depicted in Fig. 6.2(b). In this proof-of-principle experiment, we use two overlapped Gaussian-profile lasers. When the stimulated emission laser is on resonance with the transition, the PL decreases due to the depletion of the excited states, see Fig. 6.2(c). We observed a $(50 \pm 2)\%$ reduction in collected PL when the STED laser is on resonance, a clear demonstration of stimulated emission.

A power dependence of the depletion signal shows that the PL decreases to near-zero at high STED powers, shown in Fig. 6.3. However, a reduction of PL with optical

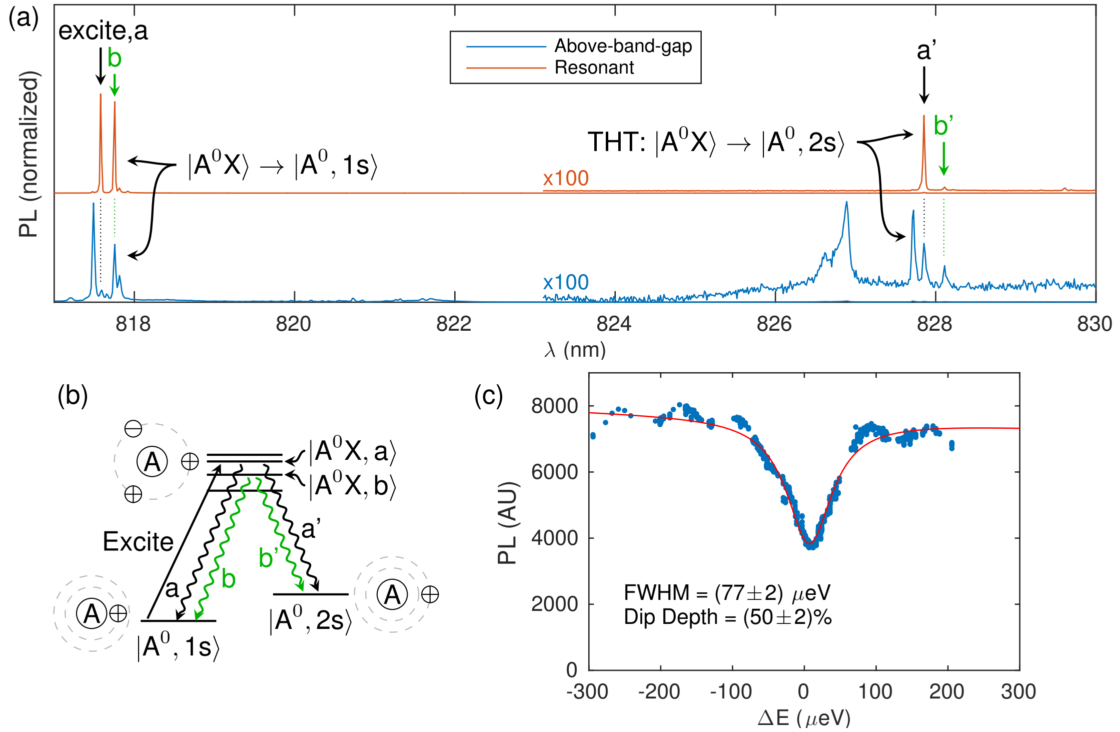

Figure 6.2: (a) Above-band-gap and resonant excitation spectra for A^0X. When exciting transition a, we see strong emission from the related 1s transitions b, and the THT transition a'. Above band-gap spectrum 20 μW, 810 nm, 1.8 K, excite H, collect V. Resonant spectrum 1.9 K. 1.5 μW, excite H, collect V. (b) Energy level diagram for A^0, A^0X system showing stimulated emission transitions. (c) Stimulated emission achieved when depletion laser is resonant with the a' transition. Detuning measured from transition b at 827.9096 nm. 1.5 μW excitation laser, 57 mW STED laser. 7 T. 1.9 K.

power can also be due to other effects, for example sample heating. A careful study is needed to disentangle the magnitude of the depletion effect from other phenomena that lower the PL intensity.

While the A^0X system is extremely homogeneous, it is expected that some inhomogeneous broadening is present. This inhomogeneous broadening can affect the STED efficiency. To measure inhomogeneous broadening, we performed a spectral hole burning experiment: an excitation laser tuned to the center of the inhomogeneous PL line modifies the PLE response. The PLE spectrum contains a narrow dip

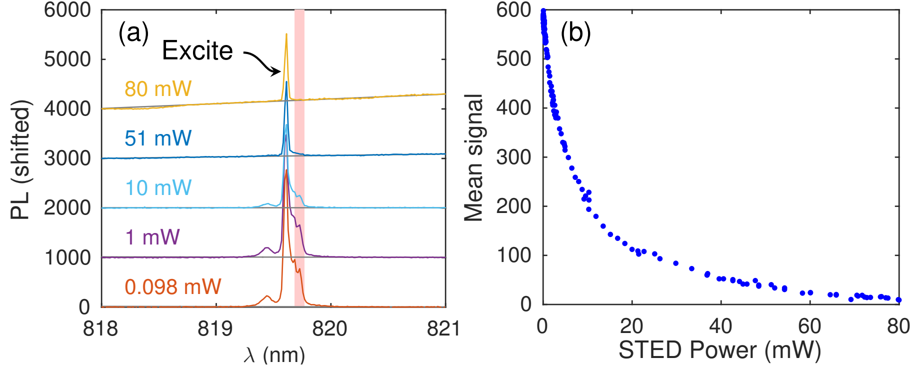

Figure 6.3: Power dependence of stimulated emission depletion effect. (a) Excitation (probe) laser on the main A^0X line labeled "excite" at 819.6089 nm. STED laser resonant with the THT transition at 829.7725 nm. As the power is increased the A^0X signal weakens. The broad slope at higher powers is due to STED laser background. (b) Background-corrected integrated PL from A^0X as a function of STED power. The integration region is specified by the red box in (a), while the laser background is fit to a line (gray) and subtracted. 4.9 K.

with a width related to the homogeneous linewidth due to the nonlinearity of the PL with excitation power. To perform this experiment, we scan a laser over one of the peaks in the $|A^0, 1s\rangle \rightarrow |A^0X\rangle$ multiplet while monitoring the two-hole transition (THT), see Fig. 6.4. A Lorentzian fit of the dip and peak width yields an estimate of the inhomogeneous broadening. The inhomogeneous broadening of A^0X must be less than 40 μeV, the width of the inhomogeneous distribution. The homogeneous linewidth is $\Delta E = \hbar/\tau + 2\hbar\gamma$, where τ is the radiative lifetime, and γ is the dephasing rate. Using a radiative lifetime of 0.61 ns (see Ch. 2), we find that the homogeneous linewidth must be larger than 1 μeV. On the other hand, we observe from the narrow spectral hole a tentative homogeneous linewidth of 5.8 μeV. These linewidths provide bounds on the inhomogeneous broadening of 34−40 μeV.

The interpretation of this dip as a spectral hole burned in an inhomogeneous distribution must be tested further. At higher excitation powers, the narrow dip becomes a narrow peak, possibly indicating the presence of coherent or collective effects.

We modeled the system using a four level density matrix and included population relaxation and decoherence in the dynamics. In the interaction frame, rotating wave

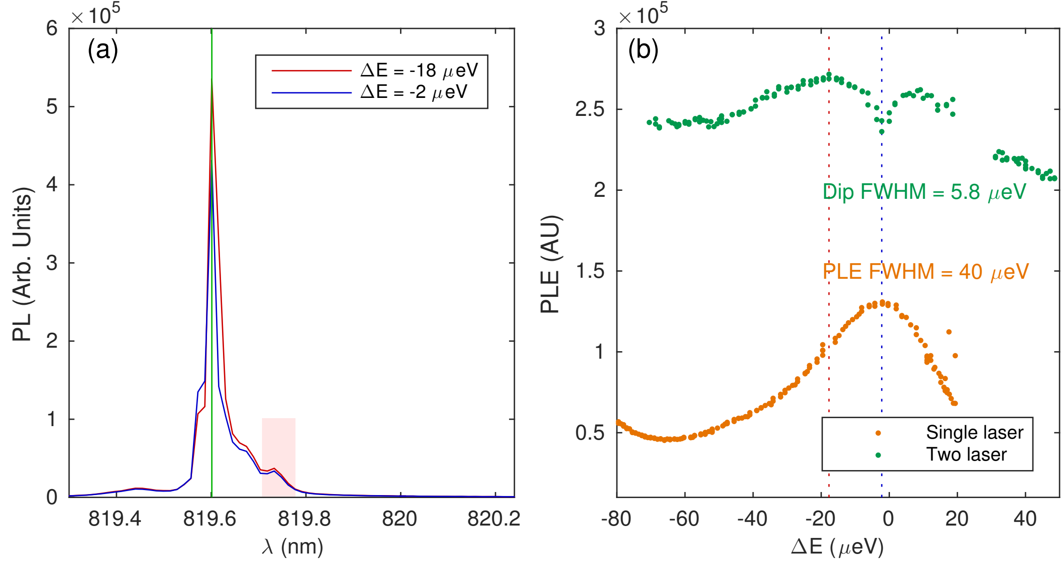

Figure 6.4: Spectral hole burned in inhomogeneous line width of A^0X transition. (a) Spectra for spectral hole burning PLE experiment. Red box shows integration area for PLE, green line shows zero detuning, i.e. $\Delta E = 0$. When the second is on resonance with the transition at $\Delta E = -2\mu$eV, the PLE intensity decreases. (b) For the single laser spectrum, a laser is scanned across one of the A^0X transitions while monitoring the PL intensity in the red box in (a). For the two laser spectrum, a fixed laser is tuned resonant with the transition at $\Delta E = 0$ μeV. A spectral hole is observed when the first laser scans over the transition. Fixed laser power 7.5 μW. Scanning laser power 7.2 μW. 5.1 K.

approximation and constant coefficients picture, the Hamiltonian is

$$H = \begin{pmatrix} \delta_1 & 0 & -\Omega_a/2 & 0 \\ 0 & \delta_2 & -\Omega_b/2 & 0 \\ -\Omega_a/2 & -\Omega_b/2 & 0 & 0 \\ 0 & 0 & 0 & 0 \end{pmatrix}, \quad \begin{array}{l} |1\rangle = |\mathrm{A}^0, 1\rangle \\ |2\rangle = |\mathrm{A}^0, 2\rangle \\ |3\rangle = |\mathrm{A}^0\mathrm{X}, a\rangle \\ |4\rangle = |\mathrm{A}^0\mathrm{X}, b\rangle \end{array} \tag{6.1}$$

and the equation of motion in steady state is

$$0 = \frac{\partial \rho}{\partial t} = \frac{1}{i\hbar}[H, \rho] + L(\rho), \tag{6.2}$$

where $L(\rho)$ is the Limbladian operator describing relaxation and decoherence:

$$L(\rho) = \begin{pmatrix} -\Gamma_{12}\rho_{11} + \Gamma_{21}\rho_{22} + \Gamma_{31}\rho_{33} + \Gamma_{41}\rho_{44} & -\gamma'_{21}\rho_{12} & \cdots \\ -\gamma'_{21}\rho_{21} & \Gamma_{12}\rho_{11} - \Gamma_{21}\rho_{22} + \Gamma_{32}\rho_{33} + \Gamma_{42}\rho_{44} & \\ -\gamma'_{31}\rho_{31} & -\gamma'_{32}\rho_{32} & \\ -\gamma'_{41}\rho_{41} & -\gamma'_{42}\rho_{42} & \end{pmatrix}$$

$$\begin{pmatrix} -\gamma'_{31}\rho_{13} & -\gamma'_{41}\rho_{14} \\ -\gamma'_{32}\rho_{23} & -\gamma'_{42}\rho_{24} \\ -\Gamma_{31}\rho_{33} - \Gamma_{32}\rho_{33} - \Gamma_{34}\rho_{33} + \Gamma_{43}\rho_{44} & -\gamma'_{43}\rho_{34} \\ -\gamma'_{43}\rho_{43} & \Gamma_{34}\rho_{33} - (\Gamma_{41} + \Gamma_{42} + \Gamma_{43})\,\rho_{44} \end{pmatrix} \quad (6.3)$$

where

$$\begin{aligned} \gamma'_{21} &= \gamma_{21} + \tfrac{1}{2}(\Gamma_{12} + \Gamma_{21})\,, \\ \gamma'_{31} &= \gamma_{31} + \tfrac{1}{2}(\Gamma_{12} + \Gamma_{31} + \Gamma_{32} + \Gamma_{34})\,, \\ \gamma'_{32} &= \gamma_{32} + \tfrac{1}{2}(\Gamma_{21} + \Gamma_{31} + \Gamma_{32} + \Gamma_{34})\,, \\ \gamma'_{41} &= \gamma_{41} + \tfrac{1}{2}(\Gamma_{12} + \Gamma_{41} + \Gamma_{42} + \Gamma_{43})\,, \\ \gamma'_{42} &= \gamma_{42} + \tfrac{1}{2}(\Gamma_{21} + \Gamma_{41} + \Gamma_{42} + \Gamma_{43})\,, \\ \gamma'_{43} &= \gamma_{43} + \tfrac{1}{2}(\Gamma_{31} + \Gamma_{32} + \Gamma_{34} + \Gamma_{41} + \Gamma_{42} + \Gamma_{43}). \end{aligned} \quad (6.4)$$

Here Γ_{ij} is the rate of population relaxation from state i to j, and γ_{ij} is the pure dephasing rate between states i and j. The probe and STED laser are described by the detuning δ_1, δ_2 and the Rabi frequencies ω_1, Ω_2 respectively. Inhomogeneous broadening is added by solving the system multiple times for different detunings of the lasers from the excited states and weighting the solutions by a Gaussian.

A useful figure of merit for the stimulated emission dip is the efficiency, the precent reduction in signal due to the application of the stimulated emission laser. In order to isolate a single emitter using STED in a sample with 1×10^{14} cm^{-3} acceptors, the stimulated emission efficiency must approach 99.4% (at 1×10^{13} cm^{-3}, 94% efficiency is needed). There are several ways in which the current efficiency of ~50% might be improved. Fig. 6.5 shows that the STED saturation power, the STED power where 50% efficient depletion occurs, decreases as the spin-relaxation rate decreases. Current experiments are performed at the purple dot in Fig. 6.5(b), with an estimated ps hole spin relaxation time and a ns pure dephasing time [96, 72] We note that hole-spin relaxation times may improve to a ns by splitting the heavy-hole and light-hole states

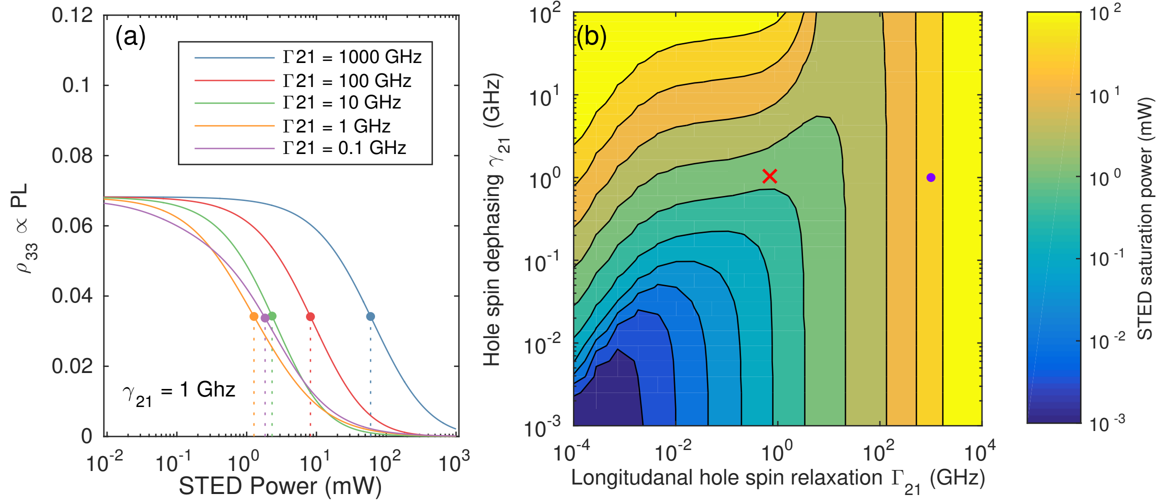

Figure 6.5: (a) Predicted stimulated emission depletion curves. As the ground spin relaxation rate Γ_{21} increases, the STED saturation power (power where signal decreases by 50%). (b) Dependence of the STED saturation power on ground state relaxation Γ_{21} and dephasing γ_{21}. Other model parameters are $\Gamma_{43} = 9$ GHz, branching ratio 1s/2s $f_{\text{branch}} = 142$, $\Gamma_{12} \approx 0$, $\Gamma_{31} = 2.6$ GHz, $\Gamma_{32} = 0.019$ GHz, $\Gamma_{34} = 5.4$ GHz, $\Gamma_{41} = 2.5$ GHz, $\Gamma_{42} = 0.018$ GHz, $\gamma_{31} = \gamma_{32} = 22$ GHz, $\gamma_{41} = \gamma_{42} = \gamma_{43} = 100$ GHz, $\Delta E_{43} = 186$ μeV, $\Delta E_{21} = 19.5$ meV, $\delta_1 = 0$, $\delta_2 = 0$, $\Omega_a = 3000$ GHz$/\sqrt{\text{W}}P_a$, $\Omega_b = 257$ GHz$/\sqrt{\text{W}}P_b$, $P_a = 1$ μW, $T = 4.2$ K, Gaussian-distributed inhomogeneous broadening with standard deviation 12.6 GHz included.

through the application of strain, which would lower the STED saturation power by 1.5 orders of magnitude [red x in Fig. 6.5(b)].

The small inhomogeneous broadening observed for the A^0X system does not significantly affect the STED efficiency. This can be understood by considering the power dependence of the STED dip in Fig. 6.6. Higher STED powers broaden the depletion linewidth, and at high powers acceptors will undergo stimulated emission even at excited state detunings due to inhomogeneous broadening as large as 40 GHz.

Further, in order to achieve higher STED efficiencies, it may be be necessary to move to pulsed stimulated emission schemes. In pulsed-STED, significantly higher power densities can be achieved without heating the sample. In addition, the wider band-width of pulsed lasers can deplete multiple excited levels simultaneously.

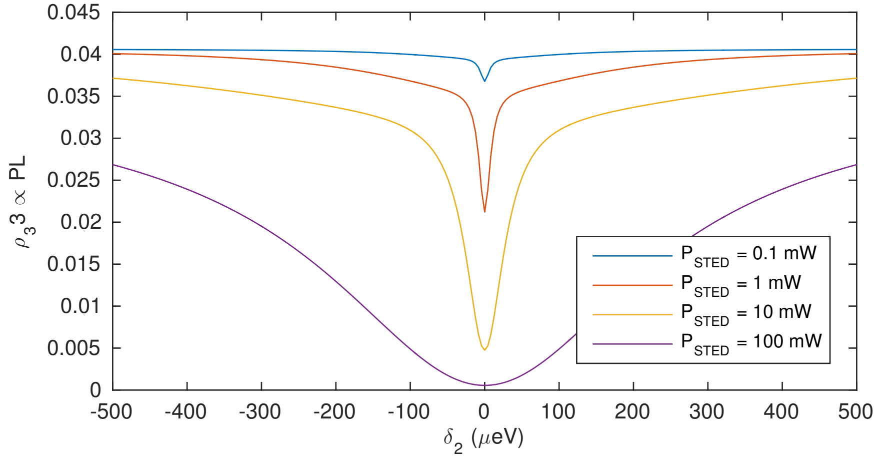

Figure 6.6: The STED dip when the STED laser is scanned across the transition broadens linearly with applied STED power. Due to this power broadening, the small inhomogeneous broadening of A^0X does not significantly affect the STED efficiency at high powers. Model parameters are the same as in Fig. 6.5, except $\gamma_{21} = 1$ GHz, $\Gamma_{21} = 1$ GHz and no inhomogeneous broadening is included.

6.3 Donor isolation with ground state depletion microscopy

Ground state depletion (GSD) microscopy is a relatively new form of super-resolution which may enable optical isolation of a single donor in bulk a bulk semiconductor. The GSD microscopy scheme presented here relies on long spin-relaxation lifetimes, and has the potential to give large super-resolution enhancements with low optical powers.

The GSD microscopy scheme is shown in Fig. 6.7. First, a Gaussian-shaped beam optically pumps all the donors in the spot into the state $|2\rangle$. Next, a beam with a node in the center (doughnut beam) optically pumps electrons in an annulus into the spin state $|1\rangle$. Subsequently, a Gaussian-shaped readout pulse probes the population of the state $|2\rangle$. In this way, the diffraction limit can be surpassed using only far-field optical techniques. This procedure is similar to one performed on nitrogen vacancy centers in diamond [140], albeit with the difference that donors in the annulus are optically pumped into a dark state, in contrast to Ref. [140] where NVs in the annulus are pumped to a bright state. This difference should result in our proposed scheme of GSD microscopy having a much improved signal to noise.

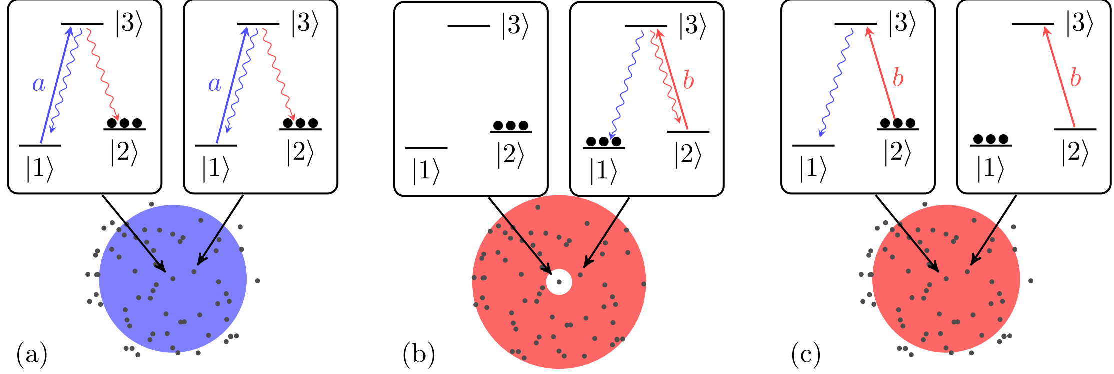

Figure 6.7: Principle of ground state depletion (GSD) microscopy. (a) A Gaussian shaped beam optically pumps the system in to the state $|2\rangle$. (b) A doughnut shaped beam with a node in the center optically pumps donor bound electrons in the annulus back into the state $|1\rangle$. (c) Lastly, a Gaussian shaped readout beam probes the population in $|2\rangle$, yielding luminescence only from the emitter in the center. The ultimate resolution limit is determined by the goodness of the doughnut zero. The first pulse could be an above band scrambling pulse as well.

We performed a proof-of-principle experiment to test whether ground state depletion of D^0 is possible. We overlapped two Gaussian-shaped laser beams, and tuned the energy to the lowest energy D^0–D^0X Λ-system, see Fig. 6.8(a). We compared two pulse sequences, the *pump on* sequence, corresponding to an emitter in the annulus of the doughnut beam and the *pump off* sequence, corresponding to an emitter in the center, see Fig. 6.7(b). We find that the *pump on* sequence is effective at optically pumping the electron spins, leading to an 88% reduced PL intensity upon readout, see Fig. 6.8(c).

We predict that this ground state depletion effect could lead to a factor of 10 improvement in resolution [140]. However, the super-resolution scheme will suffer from a low signal-to-noise ratio. This occurs because optical pumping of electron spins requires a few μs (see, e.g. Fig. D.2). During the readout pulse applied to transition b, and assuming a 1:1 branching ratio from the excited state, the donor will become optically pumped after a few cycles of excitation and radiative decay. This means that each donor only emits a few photons per ~ 10 μs pulse sequence. (We note however that with higher optical powers, the optical pumping time could be

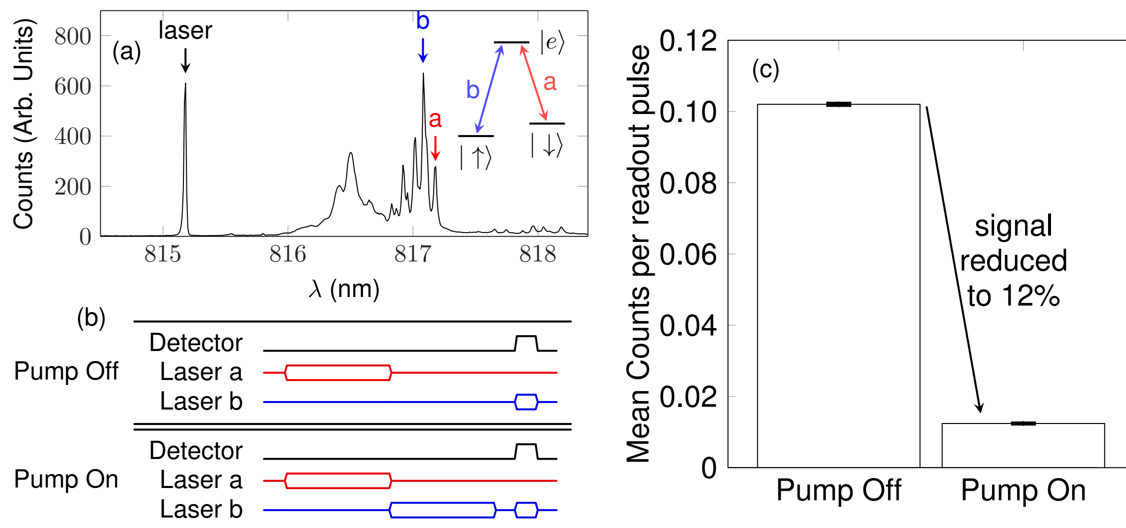

Figure 6.8: Experimental proof of principle of ground state depletion. (a) PL spectrum of n-type GaAs with above-band-gap excitation. The lowest energy D^0–D^0X transitions are labeled a and b. (b-c) Pulse sequence for testing the ground state depletion effect. In the *pump off* sequence, laser a pumps population to $|\uparrow\rangle$, leading to a large amount of PL during the readout pulse using laser b. In the *pump on* pulse sequence, laser b pumps population back to $|\downarrow\rangle$, leading to a much reduced PL signal. 33 μW on transition at 817.18 nm, 22 μW on transition at 817.08 nm. 7 T. 2.3 K. Sample b923.

decreased to $\sim$ 20 ns, a few multiples of the radiative lifetime.) A quick estimation of the collection efficiency using a $\sim$ 10 μs pulse sequence finds that $\sim$ 0.1% of photons emitted will be measured at the photon counter, taking into account the large loss at the GaAs-air interface. Overall, this gives a count rate from a single donor of only 100 counts per second. While these low count rates are not uncommon in rare-earth doped crystals [120], this signal is lower than the dark count rate of many single photon counting modules, and would make microscopy difficult.

There are several possibilities for circumventing this issue. First, a solid immersion lens can increase the collection efficiency by a factor of 10. Also, it is possible that a readout laser applied to a different transition could yield a cycling transition, which would produce many photons per readout pulse. Unfortunately, the general goals of fast optical pumping and a cycling transition are contradictory requirements for an

optical transition. It is possible that a third laser tuned to another transition could create a cycling transition with for efficient readout.

Single donor isolation is an exciting goal and would enable investigations of phenomena that are inaccessible when probing ensembles [69, 119]. For example, single donor imaging may allow observation of quantum tunneling of electron between donors. This could inform modern technologies where defect energy bands are created in highly doped crystals.

6.4 *Isolating a single shallow dopant with a semiconductor heterostructure*

6.4.1 Introduction

Donor-bound electrons are attractive qubits for quantum information processing, however for long-term feasibility, it is necessary to optically address single donors. The diffraction limit of light makes it difficult to isolate a single one with far-field optical microscopy even in very pure samples. In addition, the homogeneity that makes D^0 an attractive qubit also makes it difficult to isolate donors with spectral filtering.

For a typical confocal scan using 820 nm light (the relevant transition energy for D^0-D^0X), the smallest FWHM of a focused beam using our microscope is 550 nm (using a lens with NA = 0.7). In addition, the axial resolution of a confocal microscope is typically $2.5nd$, where n is the index of refraction and d is the lateral resolution. This diffraction limit results in a 2D density that is too high to optically isolate a single donor (Fig. 6.9a). However, if the axial resolution of the microscope is improved with a heterostructure, the number of donors addressed by the laser spot can be reduced to one (Fig. 6.9b).

One possible method to isolate a donor is to create a suitably thin semiconductor crystal where it would be easy to find just one donor in a diffraction limited spot. However, the close presence of a surface would pose a number of serious problems, including high electric fields and Fermi level pinning. In this section, we will explore a semiconductor heterostructure device with a thin active layer of ultra-pure GaAs. The heterostructure stack is designed so that electric fields are minimized in the active layer and to allow optical access to bright, homogeneous, single donors.

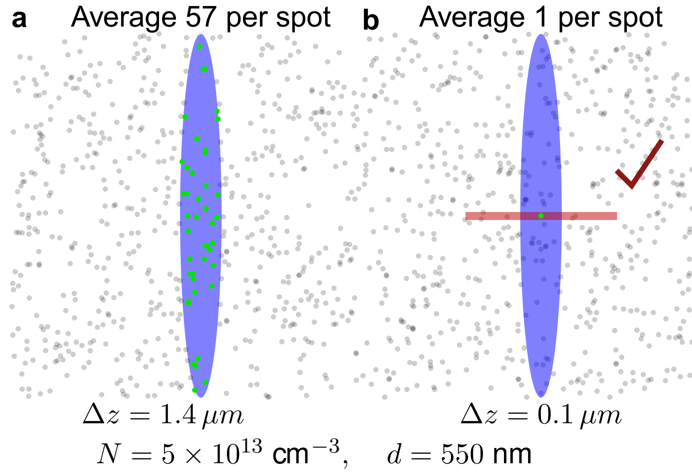

Figure 6.9: **a.** Even in ultra-pure GaAs samples with donor densities of 5×10^{13} cm^{-3}, the poor axial resolution ($2.5nd$, where n is the index of refraction and d the lateral resolution) of the confocal microscope implies that there will be many donors per diffraction limited spot. Experiments on single donors, which have high spectral homogeneity are not possible. **b.** If the axial resolution of the microscope is improved with a semiconductor heterostructure to 100 nm, then there will be an average of one donor per diffraction limited spot, enabling single donor experiments.

6.4.2 Effects of Fermi level pinning

Close proximity of a surface is detrimental to shallow donors and acceptors in several ways. Fermi level pinning can cause near-surface dopants to become ionized in equilibrium by raising the Fermi level above the donor level. Second, the high electric fields near the surface can cause donor/acceptor ionization by a few different mechanisms. Here we estimate the depletion depth and surface fields and discuss three mechanisms for donor ionization.

The band bending near the surface of a GaAs crystal can be estimated using a simple depletion region approximation. In this approximation, we assume that in the bulk all donors are occupied, but close to the surface all donors are ionized because of Fermi level pinning. Fig. 6.10 shows the band bending near the surface in a very pure GaAs crystal. We can estimate the width of the region where all donors are ionized using the same procedure as for a p-n junction except that instead of charge neutrality occurring with free carriers, charge neutrality occurs when electrons bind

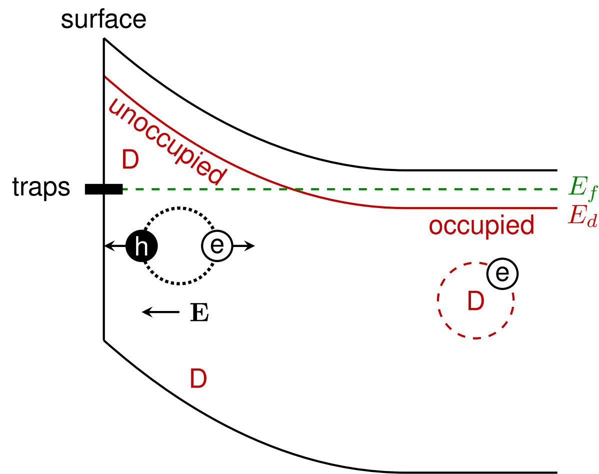

Figure 6.10: Surface Fermi level pinning can deactivate donor bound electrons in multiple ways. The strong electric field near the surface can cause tunneling or impact ionization. In addition, near the surface, the Fermi level falls far below the donor level, leaving the donors ionized in equilibrium.

to donors [9]. Assuming that the Fermi level is pinned at mid gap at the surface, the size of the depletion region is

$$d = \sqrt{\frac{2\epsilon\Delta\phi}{eN_d}}, \tag{6.5}$$

where ϵ is the dielectric constant, e the electron charge, $N_d = 5 \times 10^{13}$ cm^{-3} is the number density of donors, and $\Delta\phi$ is the potential difference between mid-gap and the bulk chemical potential. For low-temperature (2 K or 0.15 meV) GaAs, the bulk chemical potential is close to midway between the donor energy level and the conduction band level (Sec. **??**). Using a donor binding energy of 5.8 meV, in the bulk all donors are occupied and the conduction band is empty. The depletion depth for this system is 4.6 μm, half of our typical 10 μm epilayer sample thickness. The electric field at the surface would be 3300 V/cm, decreasing linearly to zero over the depletion length. Fermi level pinning and the associated electric field can ionize donors by several different mechanisms: equilibrium ionization, tunneling ionization and impact ionization.

Equilibrium Ionization

Fig. 6.10 shows that the Fermi level near the surface rises many k_BT above the donor energy level. Thus in equilibrium donors near the surface will be ionized. In non-equilibrium (e.g. semiconductor exposed to light), carrier generation can create a non-equilibrium population of occupied donors. The time-scale with which the donors re-ionize will depend on the specifics of the experiment. In GaAs, even if donors are unoccupied in equilibrium, experiments on donors can often be performed because light creates a non-equilibrium donor population.

We also note that surface electric fields can disappear under optical excitation due to separation of photo-excited electron hole pairs [52, 216]. Thus in practice, it may be possible to neutralize surface fields by application of above-band-gap light during the measurement.

Tunneling Ionization

Tunneling ionization, also called direct field ionization, occurs when the electric field is strong enough to cause the oppositely charged carriers in a hydrogenic complex to tunnel away from one another [24]. We will first consider the tunneling ionization of an exciton because it has a small binding energy and will thus have the lowest threshold field. Tunneling ionization is discussed for the ground state of hydrogen in Ref. [130]. This derivation uses the WKB approximation to calculate the rate ω that the electron tunnels through the potential barrier to large distances. The result for the tunneling rate in terms of the electric field is

$$\omega = \frac{1}{4}\frac{\omega_a}{E/E_a}\exp\left(-\frac{2}{3}\frac{E_a}{E}\right),$$

with the characteristic rate and field

$$\omega_a = \frac{me^4}{(4\pi\epsilon)^2\hbar^3}, \quad E_a = \frac{m^2e^5}{(4\pi\epsilon)^3\hbar^4},$$

where m is the reduced mass of the hydrogenic problem, ϵ is the dielectric constant and E is the applied electric field. Here the formula from Ref. [130] has been modified for general hydrogenic complexes. This formula is valid in the small tunneling limit, i.e. $|E| << E_a$.

For hydrogen in vacuum, $\omega_a = 4 \times 10^{16}$ s^{-1}, and $E_a = 5 \times 10^9$ V/cm. Thus, quite large fields are required to ionize hydrogen. Excitons on the other hand have a small binding energy and can be ionized at much lower fields. Using the relevant effective masses for electrons and holes in GaAs, the exciton characteristic rate and field are $\omega_a = 1.4 \times 10^{13}$ s^{-1}, and $E_a = 8130$ V/cm. Tunneling ionization is expected to dominate over radiative recombination when the ionization rate surpasses the radiative lifetime, which is on the order of $\sim$1 ns. This occurs at the relatively low field of 390 V/cm, see Fig. 6.11.

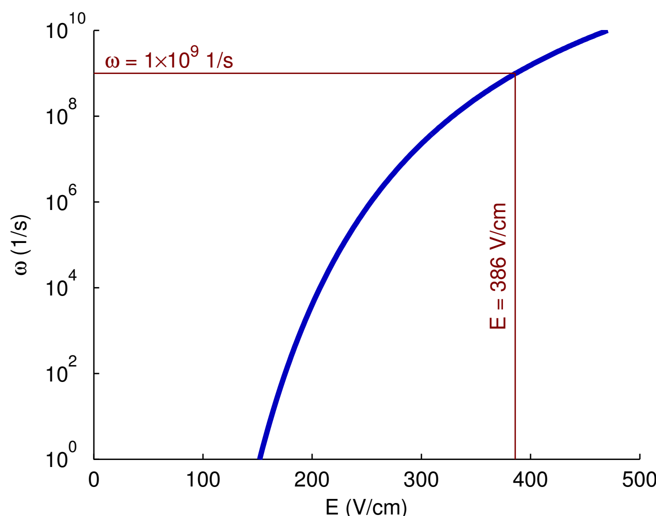

Figure 6.11: Tunneling ionization rate of an exciton in GaAs. Tunneling ionization should prevent radiative recombination when the ionization rate approaches the radiative lifetime of $\sim$1 ns.

The 390 V/cm estimated here is close to the 500 V/cm quoted in Ref. [25]. The estimated tunneling ionization field can be as high as $\sim$3000 V/cm using a rough method [43].

Impact Ionization

A carrier accelerated by an electric field can acquire enough kinetic energy to ionize a donor on impact. The critical field for impact ionization in GaAs can be remarkably low, 1-50 V/cm depending on the experiment [25, 158, 125, 206]. This low threshold

implies that impact ionization may be the dominant ionization mechanism in low-temperature intrinsic GaAs.

The very low impact ionization field is due to the ultra-high mobility of high-purity GaAs, $\sim 10^5$ cm^2/Vs in these experiments [25]. In an electric field of 50 V/cm this mobility leads to an average energy accumulated between scattering events of $\frac{1}{2}m\mu^2E^2 = 3$ meV, sufficient to cause impact ionization of a donor-bound electron. We note the mobilities of the studied sample 14704 of 10^3 cm^2/Vs is somewhat lower than other samples, potentially leading to a higher threshold for impact ionization.

6.4.3 Design principle

In designing the heterostructure, we aim to design a device satisfying the following criteria.

(i) **Thin active layer**. The device should have a thin active layer of intrinsically doped semiconductor. The background concentration of shallow dopants should be low enough to isolate a single donor with far-field optical microscopy. However, the well should not be too thin such that quantum well width fluctuations cause inhomogeneous broadening of the acceptors.

(ii) **Optically accessible**. The GaAs active layer should be accessible to light of energy 1.52 eV and below.

(iii) **Low electric fields**. The electric field in the active layer should be as small as possible, preferably below 1 V/cm.

(iv) **Negligible free carrier concentration**. The active layer should have negligible free carrier concentration so that free carriers do not affect the properties of the shallow dopants.

(v) **Overall device size**. The overall height of the heterostructure should be less than $\sim$10 μm in order for growth by molecular beam epitaxy to be feasible.

The heterostructure design for removing electric fields in the GaAs region is shown in Fig. 6.12. The design principle is to provide isolating layers of semiconductors that protect a thin layer of intrinsic GaAs, the active layer.

The top layer is a highly doped n- or p-type GaAs layer to neutralize the effects of surface Fermi level pinning. The large amount of charge in this layer shields surface

charge in trap states. If the top layer is sufficiently thin, there will be negligible optical absorption and the layer will not block light to or from the active layer. Next, a wide region of intrinsic AlGaAs lowers the magnitude of any electric field that leaks through the highly doped barrier. This is similar to a parallel plate capacitor; for a given charge on the plates, the wider the gap the lower the electric field. The band-gap of AlGaAs is higher than GaAs, allowing optical access to the active layer.

The next layer is the intrinsic GaAs active layer. This layer is grown as pure as possible, but can still be expected to have background doping concentrations of $\sim 5 \times 10^{13}$ cm^{-3}. The next two layers consist of another intrinsic AlGaAs layer and a highly doped layer, providing symmetry with the first two layers. A perfect axial symmetry would ensure that the electric field is zero in the center. Next an AlAs epitaxial lift off (ELO) layer allows the epilayer to be removed by dissolving the AlAs in hydrofluoric acid. Lastly a smoothing superlattice getters impurities during growth and provides a higher quality epitaxial layer.

6.4.4 Simulations

The simulated band structure of the devices is shown in Fig. 6.12. We modeled the heterostructure using a 1D Poisson solver [180, 181, 190, 109]. The surface states were modeled by pinning the Fermi level at the surface of the material to around mid gap (Schottky barrier of 1.01 V). The highly doped layer thickness is 15 nm, which is sufficient to neutralize the surface charge. We modeled two devices – one with n-type blocking layers and another with p-type blocking layers.

We predict this device will succeed in the goals stated above. The Fermi level for these devices is close to the band edges, but this should not be a problem as optical excitation can create a non-equilibrium population of donors bound electrons. The simulations show that despite the strong surface charge, the electric field in the active layer remains small.

6.4.5 Preliminary Experimental Results

The samples 14703 and 14704 (Fig. 6.12) were grown by molecular beam epitaxy by collaborators at Ruhr-Universität Bochum. They include an AlAs layer that can be selectively etched in hydrofluoric acid to lift off the epitaxial layer (ELO). We studied the sample before and after lift off. Before lift off, the device is non-symmetrical, and

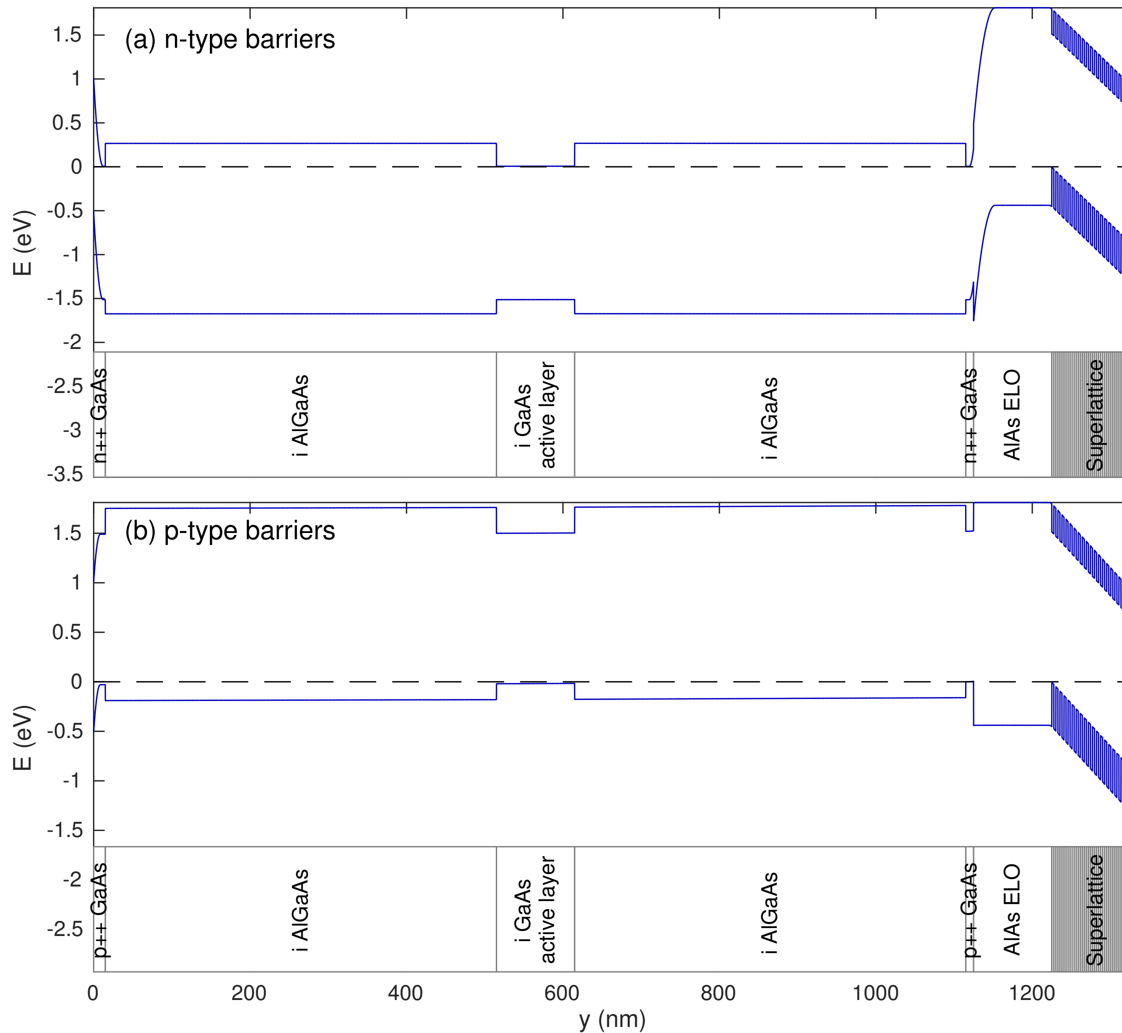

Figure 6.12: (a) Band structure of final heterostructure device for isolating a single impurity using n++ barriers. Sample 14704. The $Al_xGa_{1-x}As$ fraction $x = 0.33$. (b) same as a but with p++ barriers. Sample 14703.

so we may expect large electric fields in the active layer depending on the details of the surface Fermi level pinning and optical excitation conditions. However, it is also possible that the lift-off procedure introduces significant imperfections in the epilayer.

We observe a wide band-edge emission, with a clearly resolved A^0X PL line, see Fig. 6.13(b). The visibility of this line is greatly enhanced when the room lights are on. We attribute this to light above the AlGaAs band gap neutralizing electric fields,

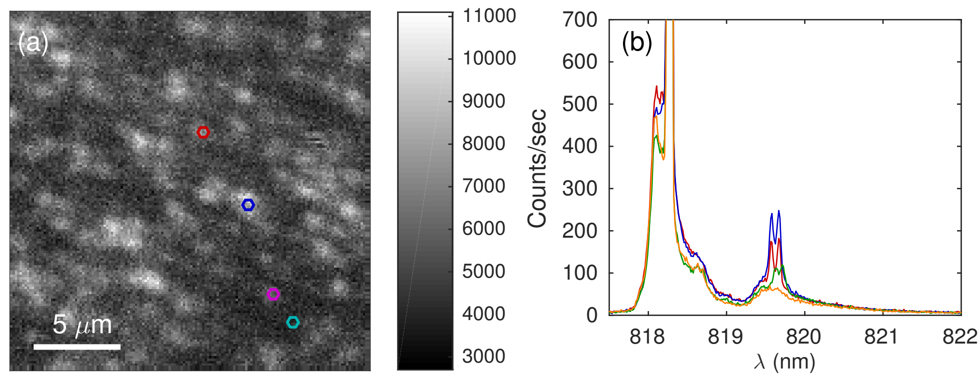

Figure 6.13: (a) Confocal scan of heterostructure on sample 14704. We see localized bright locations of A^0X PL. SPCM collection at 819.76 nm. 7 μW. 1.9 K. excite vertical, collect all. 0 T. Room lights on. (b) Spectra at colored dots in a. The bright locations correspond to higher-intensity acceptor PL. It is unclear whether these dots are due to single or multiple acceptors, or if another physical effect creates a region of bright and occupied acceptors. Same excitation conditions.

resulting in a significant narrowing and blue-shift of the band edge PL.

In a confocal scan of the sample, Fig. 6.13, we observe localized regions with bright A^0X PL. This could either be due to the presence of localized acceptors or the presence of localized regions where acceptors are bright. An autocorrelation measurement could distinguish between these two possibilities.

6.4.6 Conclusion

We have designed a GaAs heterostructure which allows optical isolation of a thin layer of intrinsic GaAs, while keeping electric fields to a minimum. The initial characterization of the heterostructure shows that it may be promising for isolating single acceptors. Future challenges include increasing the collection efficiency in order to perform autocorrelation measurements. The PL intensity detected ($\sim 10,000$ counts per second) is orders of magnitude lower than would be expected based on a few ns lifetime and an overall collection efficiency of 0.1%. This low PL intensity could be due to an ionization process lowering the fraction of time that a given acceptor is occupied.

Chapter 7

OUTLOOK

This work studies the optical and electronic properties of semiconductor defects in direct band-gap semiconductors. In this chapter, we summarize and discuss the main impacts and future directions.

First we develop a convenient formalism for describing the optical properties of multi-carrier excitonic complexes, and apply this theory to the acceptor bound exciton. This work can be applied to a wide variety of complicated defects and can help identify and describe unknown defects in new materials. We use the same formalism to describe the fine structure of the stacking fault exciton.

The large dipole moment and high homogeneity of the stacking fault exciton make it a promising system for observing the complex 2D physics of interacting dipoles. In particular, it may be possible to observe exotic quantum phases, such as exciton superfluids or exciton crystallization in these systems [168, 28, 32]. In order to determine whether these phases are possible, it is necessary to measure the stacking fault exciton lifetime. Long lifetimes are required to achieve high excitonic densities and to allow sufficient thermalization time for condensation into exotic quantum phases [184].

The stacking fault and dislocation studies unambiguously determine the photoluminescence bands for these defects. This information is pertinent for the characterization of GaAs devices where identifying problematic defects is often the first step to improving devices. This work shows that simple PL measurements can be used to identify these common extended defects.

Lastly, we explore several techniques that could enable using common donors and acceptors for quantum information technologies. We perform an in-depth study of donor-bound electron spin relaxation in several materials, a key parameter determining the fundamental limits for the storage-time of quantum information. We find several promising avenues for isolating single dopants using either super-resolution microscopy or a heterostructure device. Given the high homogeneity and strong optical transitions of shallow-dopant bound spins, we hope this work will help determine

the feasibility of using these dopants for next-generation quantum technologies.

Appendix A

DIPOLE OPERATOR FOR BAND-TO-BAND TRANSITIONS

The vector dipole operator $\boldsymbol{\mu} = e\mathbf{r}$ for transitions between the conduction band and the heavy-hole or light-hole band in a zinc-blende direct band gap semiconductor (e.g. GaAs, InP, etc.) can be derived from the electron and hole basis functions. We derive the dipole operator in second quantization, which is convenient for calculating recombination rates for excitons with more than two charge carriers.

The valence band angular momentum states arise from coupling between p-like orbital states and the electron spin $\frac{1}{2}$ [215]. These couple together to form total angular momentum $\frac{3}{2}$ and $\frac{1}{2}$:

$$1 \otimes \frac{1}{2} = \frac{3}{2} \oplus \frac{1}{2}.$$

States $\left|\frac{3}{2}, \pm\frac{3}{2}\right\rangle$ are known as heavy holes, $\left|\frac{3}{2}, \pm\frac{1}{2}\right\rangle$ as light holes and $\left|\frac{1}{2}, \pm\frac{1}{2}\right\rangle$ as split-off holes. Spin-orbit interaction splits the $j = \frac{3}{2}$ from the $j = \frac{1}{2}$ states and typically the $j = \frac{1}{2}$ split-off holes can be ignored in experiments.

Using angular momentum addition rules, the heavy hole and light hole states are

$$\begin{aligned}
\left|\tfrac{3}{2}\right\rangle &= \frac{1}{\sqrt{2}}\left|X - iY, \downarrow\right\rangle \\
\left|\tfrac{1}{2}\right\rangle &= \frac{1}{\sqrt{6}}\left|X - iY, \uparrow\right\rangle + \sqrt{\frac{2}{3}}\left|Z, \downarrow\right\rangle \\
\left|-\tfrac{1}{2}\right\rangle &= -\frac{1}{\sqrt{6}}\left|X + iY, \downarrow\right\rangle + \sqrt{\frac{2}{3}}\left|Z, \uparrow\right\rangle \\
\left|-\tfrac{3}{2}\right\rangle &= -\frac{1}{\sqrt{2}}\left|X + iY, \uparrow\right\rangle
\end{aligned}$$

where X, Y, Z are electron orbital wave functions transforming as x, y, z and $\uparrow, \downarrow$ is the spin of the electron [45]. The hole angular momentum state has the opposite sign of the corresponding electron angular momentum. The conduction band states are $|S, \uparrow\rangle$ and $|S, \downarrow\rangle$ where S denotes a spherically symmetric periodic part of the Bloch

wave function. In spherical symmetry and for a $k = 0$ exciton, the coordinate system can be taken to lie in an arbitrary direction. However for an exciton with non-zero momentum $\mathbf{k}$, the coordinate system must be taken with the z axis in the $\mathbf{k}$ direction, thus somewhat complicating further analysis [45]. In what follows, we will restrict our discussion to $k = 0$ excitations.

These basis functions can be used to calculate matrix elements of the dipole operator $\boldsymbol{\mu}$. As an example, the dipole matrix element for recombination of a spin down electron with a $+\frac{3}{2}$ heavy hole is

$$\begin{aligned}\left\langle \tfrac{3}{2}\right| \boldsymbol{\mu} \left|S,\downarrow\right\rangle &= \frac{e}{\sqrt{2}} \left(\langle X| + i\,\langle Y|\right) \mathbf{r} \,|S\rangle \,\langle \downarrow | \downarrow\rangle \\ &= \frac{e}{\sqrt{2}} \left[\langle X| \,x\, |S\rangle \,\hat{\mathbf{x}} + i\,\langle Y| \,y\, |S\rangle \,\hat{\mathbf{y}}\right].\end{aligned}$$

The ordering of the matrix element $\langle f| \,V\, |i\rangle$ reflects the transition occurring, in this case an electron moving from the conduction band to the valence band. In a bulk cubic crystal, by symmetry the matrix elements

$$\langle X| \,x\, |S\rangle = \langle Y| \,y\, |S\rangle = \langle Z| \,z\, |S\rangle \equiv \frac{1}{e}\mu_o$$

are all identical. Further simplifying, we find this transition results in the production of right handed circularly polarized light:

$$\left\langle \tfrac{3}{2}\right| \boldsymbol{\mu} \left|S,\downarrow\right\rangle = \mu_o \frac{\hat{\mathbf{x}} + i\hat{\mathbf{y}}}{\sqrt{2}}.$$

The same procedure can be used to find the other dipole matrix elements.

We can now introduce creation operators ($e_m^\dagger$) [117, 118] for the creation of an electron in the angular momentum state m and some particular but unspecified spatial state. Because of the anti-symmetrization requirement, the creation and annihilation operators satisfy anti-commutation relations

$$\begin{aligned}\{e_m, e_n^\dagger\} &= \delta_{mn} \\ \{e_m^\dagger, e_n^\dagger\} &= 0 \\ \{e_m, e_n\} &= 0.\end{aligned} \tag{A.1}$$

where the anti-commutator is defined as $\{a, b\} = ab + ba$. We will also introduce cre-

ation operators for holes using $h^{\dagger}_{m,\mathbf{k}} = e_{-m,-\mathbf{k}}$; i.e. the linear and angular momentum of the hole has the opposite sign of the unfilled electron state [117]. Instead of labeling the band index, we restrict hole creation/annihilation operators to act in the valence band and electron operators in the conduction band. For example, an exciton state can be written as

$$|e_{m_1}, h_{m_2}\rangle = e^{\dagger}_{m_1} h^{\dagger}_{m_2} |0\rangle \,.$$

where $|0\rangle$ is the semiconductor vacuum state with a filled valence band and empty conduction band.

The dipole operator can be written in second quantization as

$$\boldsymbol{\mu} = \sum_{mn} \boldsymbol{\mu}_{mn} h_m e_n + \boldsymbol{\mu}^{*}_{mn} e^{\dagger}_n h^{\dagger}_m \tag{A.2}$$

where we have restricted m to be in the valence band and n to be in the conduction band, and $\boldsymbol{\mu}_{mn} = \langle m| e\mathbf{r} |n\rangle$ [117]. The first term corresponds to exciton annihilation and the second to exciton creation. Using the matrix elements calculated above, the dipole operator for a conduction band electron recombining with a heavy-hole or light-hole is

$$\begin{aligned}\boldsymbol{\mu} = \mu_o \Bigg[& \frac{\hat{\mathbf{x}} + i\hat{\mathbf{y}}}{\sqrt{2}} \left(h_{\frac{3}{2}} e_{-\frac{1}{2}} + \frac{1}{\sqrt{3}} h_{\frac{1}{2}} e_{\frac{1}{2}} \right) \\ & - \frac{\hat{\mathbf{x}} - i\hat{\mathbf{y}}}{\sqrt{2}} \left(h_{-\frac{3}{2}} e_{\frac{1}{2}} + \frac{1}{\sqrt{3}} h_{-\frac{1}{2}} e_{-\frac{1}{2}} \right) \\ & + \sqrt{\frac{2}{3}} \hat{\mathbf{z}} \left(h_{-\frac{1}{2}} e_{\frac{1}{2}} + h_{\frac{1}{2}} e_{-\frac{1}{2}} \right) + \text{H.C} \Bigg] \,.\end{aligned} \tag{A.3}$$

Each term in the dipole operator (Eq. A.3) conserves angular momentum; i.e., the total electron and hole spin z projection is transferred to the photon during recombination. The dipole operator is shown schematically in Fig. 2.1.

Appendix B

BASIS STATES AND DIPOLE MATRIX ELEMENTS FOR A^0X

B.1 Basis states for A^0X

The A^0X consists of two holes and one electron. Hole-hole coupling dominates, while the crystal fields split the levels further [139]. From the two holes, there are four possible total spin states: $\frac{3}{2} \otimes \frac{3}{2} = 0 \oplus 1 \oplus 2 \oplus 3$ [165]. The two holes in A^0X lie in a symmetric spatial state. On account of the Pauli principle, the spin state must therefore be antisymmetric with respect to interchange, resulting in only total spin 2 and 0 being allowed.

We will use

$$h^\dagger_{m_1} h^\dagger_{m_2} |0\rangle = \frac{1}{\sqrt{2}} \left(|m_1, m_2\rangle - |m_2, m_1\rangle \right) \tag{B.1}$$

as shorthand for the creation of an antisymmetric state of two holes [117]. Note that the ordering of the creation operators matters, consistent with the commutation relations in Eq. A.1. Using this notation, we can write the total angular momentum states $|j, m\rangle$ for the coupling of the two holes as:

$$\begin{aligned}
|2,2\rangle &= h^\dagger_{\frac{3}{2}} h^\dagger_{\frac{1}{2}} |0\rangle \\
|2,1\rangle &= h^\dagger_{\frac{3}{2}} h^\dagger_{-\frac{1}{2}} |0\rangle \\
|2,0\rangle &= \frac{1}{\sqrt{2}} \left(h^\dagger_{\frac{3}{2}} h^\dagger_{-\frac{3}{2}} + h^\dagger_{\frac{1}{2}} h^\dagger_{-\frac{1}{2}} \right) |0\rangle \\
|2,-1\rangle &= h^\dagger_{\frac{1}{2}} h^\dagger_{-\frac{3}{2}} |0\rangle \\
|2,-2\rangle &= h^\dagger_{-\frac{1}{2}} h^\dagger_{-\frac{3}{2}} |0\rangle \\
|0,0\rangle &= \frac{1}{\sqrt{2}} \left(h^\dagger_{\frac{3}{2}} h^\dagger_{-\frac{3}{2}} - h^\dagger_{\frac{1}{2}} h^\dagger_{-\frac{1}{2}} \right) |0\rangle .
\end{aligned}$$

In zinc-blende semiconductors, hole-hole coupling splits the $j = 2$ and $j = 0$ states (Fig. B.1).

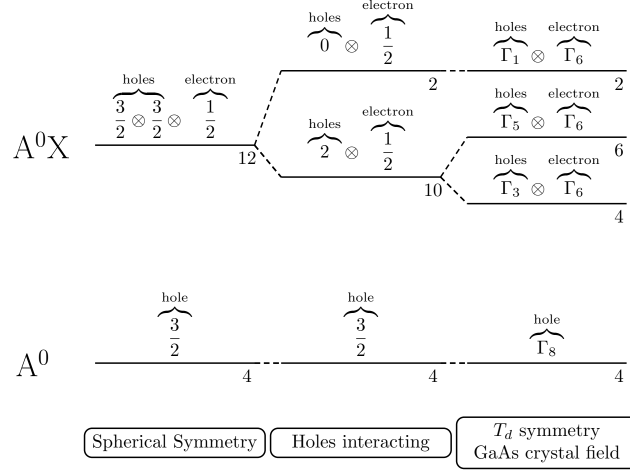

Figure B.1: Hole-hole coupling causes the $j = 2$ states to be split from the $j = 0$ states. Crystal fields breaking spherical symmetry and split Γ_3 and Γ_5. The degeneracy of the level is shown in the bottom right corner.

In the presence of the crystal field with T_d symmetry, the states split into three different irreducible representations [139, 55, 70] (Fig. B.1):

$$
\begin{aligned}
|\Gamma_5^{xy}\rangle &= \frac{1}{\sqrt{2}} \left(|2,2\rangle - |2,-2\rangle \right) \\
|\Gamma_5^{xz}\rangle &= \frac{1}{\sqrt{2}} \left(|2,1\rangle + |2,-1\rangle \right) \\
|\Gamma_5^{yz}\rangle &= \frac{1}{\sqrt{2}} \left(|2,1\rangle - |2,-1\rangle \right) \\
|\Gamma_3^{a}\rangle &= \frac{1}{\sqrt{2}} \left(|2,2\rangle + |2,-2\rangle \right) \\
\left|\Gamma_3^{b}\right\rangle &= |2,0\rangle \\
|\Gamma_1\rangle &= |0,0\rangle \,.
\end{aligned}
$$

In order to derive these basis states, it is necessary to choose a coordinate system in which to write the symmetry operations of the crystal. Since we chose to use axes aligned along [100], [010] and [001], $\hat{\mathbf{x}}$, $\hat{\mathbf{y}}$ and $\hat{\mathbf{z}}$ correspond to the three crystallographic directions.

B.2 Dipole Matrix Elements of $\mathbf{A}^0\mathbf{X}$

We use the dipole operator (2.1) to calculate the dipole matrix element between $\mathrm{A}^0\mathrm{X}$ and A^0. To illustrate the method, we will calculate the matrix element $\left\langle \frac{3}{2} \right| \boldsymbol{\mu} \left| \Gamma_5^{xy} \uparrow \right\rangle$ as an example. First, we expand the matrix element and the dipole operator

$$\begin{aligned}\left\langle \tfrac{3}{2} \right| \boldsymbol{\mu} \left| \Gamma_5^{xy} \uparrow \right\rangle = \mu_o \left\langle 0 \right| h_{\frac{3}{2}} \cdot \\ &\left[\frac{\hat{\mathbf{x}} + i\hat{\mathbf{y}}}{\sqrt{2}} \left(h_{\frac{3}{2}} e_{-\frac{1}{2}} + \frac{1}{\sqrt{3}} h_{\frac{1}{2}} e_{\frac{1}{2}} \right) \right. \\ &- \frac{\hat{\mathbf{x}} - i\hat{\mathbf{y}}}{\sqrt{2}} \left(h_{-\frac{3}{2}} e_{\frac{1}{2}} + \frac{1}{\sqrt{3}} h_{-\frac{1}{2}} e_{-\frac{1}{2}} \right) \\ &\left. + \sqrt{\frac{2}{3}} \hat{\mathbf{z}} \left(h_{-\frac{1}{2}} e_{\frac{1}{2}} + h_{\frac{1}{2}} e_{-\frac{1}{2}} \right) \right] \cdot \\ &\frac{1}{\sqrt{2}} e^\dagger_{\frac{1}{2}} \left(h^\dagger_{\frac{3}{2}} h^\dagger_{\frac{1}{2}} - h^\dagger_{-\frac{1}{2}} h^\dagger_{-\frac{3}{2}} \right) \left| 0 \right\rangle .\end{aligned}$$

All terms with an electron annihilation operator $e_{-\frac{1}{2}}$ go to zero because the electron in $\left| \Gamma_5^{xy} \uparrow \right\rangle$ is spin up. Using the fact that $e_{\frac{1}{2}} e^\dagger_{\frac{1}{2}} \left| 0 \right\rangle = \left| 0 \right\rangle$, the expression becomes

$$\begin{aligned}\left\langle \tfrac{3}{2} \right| \boldsymbol{\mu} \left| \Gamma_5^{xy} \uparrow \right\rangle = &\left\langle 0 \right| h_{\frac{3}{2}} \left[\frac{\hat{\mathbf{x}} + i\hat{\mathbf{y}}}{\sqrt{6}} h_{\frac{1}{2}} - \frac{\hat{\mathbf{x}} - i\hat{\mathbf{y}}}{\sqrt{2}} h_{-\frac{3}{2}} + \right. \\ &\left. \sqrt{\frac{2}{3}} \hat{\mathbf{z}} h_{-\frac{1}{2}} \right] \frac{1}{\sqrt{2}} \left(h^\dagger_{\frac{3}{2}} h^\dagger_{\frac{1}{2}} - h^\dagger_{-\frac{1}{2}} h^\dagger_{-\frac{3}{2}} \right) \left| 0 \right\rangle .\end{aligned} \tag{B.2}$$

Using the fact that $h_m \left| 0 \right\rangle = 0$, and the commutation relations in Eq. A.1, the dipole matrix element is

$$\left\langle \tfrac{3}{2} \right| \boldsymbol{\mu} \left| \Gamma_5^{xy} \uparrow \right\rangle = -\frac{\hat{\mathbf{x}} + i\hat{\mathbf{y}}}{2\sqrt{3}}.$$

Repeating this calculation for each matrix element produces the dipole matrix elements for the $\mathrm{A}^0\mathrm{X}$-A^0 system, given in Table B.1.

Γ_1	$\lvert\Gamma_1\downarrow\rangle$	$\lvert\Gamma_1\uparrow\rangle$
$\langle -\frac{3}{2}\rvert$	$\frac{1}{2}(\hat{\mathbf{x}}+i\hat{\mathbf{y}})$	0
$\langle -\frac{1}{2}\rvert$	$-\frac{1}{\sqrt{3}}\hat{\mathbf{z}}$	$-\frac{1}{2\sqrt{3}}(\hat{\mathbf{x}}+i\hat{\mathbf{y}})$
$\langle \frac{1}{2}\rvert$	$-\frac{1}{2\sqrt{3}}(\hat{\mathbf{x}}-i\hat{\mathbf{y}})$	$\frac{1}{\sqrt{3}}\hat{\mathbf{z}}$
$\langle \frac{3}{2}\rvert$	0	$\frac{1}{2}(\hat{\mathbf{x}}-i\hat{\mathbf{y}})$

Γ_3	$\lvert\Gamma_3^a\downarrow\rangle$	$\lvert\Gamma_3^a\uparrow\rangle$	$\lvert\Gamma_3^b\downarrow\rangle$	$\lvert\Gamma_3^b\uparrow\rangle$
$\langle -\frac{3}{2}\rvert$	$-\frac{1}{2\sqrt{3}}(\hat{\mathbf{x}}-i\hat{\mathbf{y}})$	$\frac{1}{\sqrt{3}}\hat{\mathbf{z}}$	$\frac{1}{2}(\hat{\mathbf{x}}+i\hat{\mathbf{y}})$	0
$\langle -\frac{1}{2}\rvert$	0	$\frac{1}{2}(\hat{\mathbf{x}}-i\hat{\mathbf{y}})$	$\frac{1}{\sqrt{3}}\hat{\mathbf{z}}$	$\frac{1}{2\sqrt{3}}(\hat{\mathbf{x}}+i\hat{\mathbf{y}})$
$\langle \frac{1}{2}\rvert$	$\frac{1}{2}(\hat{\mathbf{x}}+i\hat{\mathbf{y}})$	0	$\frac{1}{2\sqrt{3}}(\hat{\mathbf{x}}-i\hat{\mathbf{y}})$	$-\frac{1}{\sqrt{3}}\hat{\mathbf{z}}$
$\langle \frac{3}{2}\rvert$	$-\frac{1}{\sqrt{3}}\hat{\mathbf{z}}$	$-\frac{1}{2\sqrt{3}}(\hat{\mathbf{x}}+i\hat{\mathbf{y}})$	0	$\frac{1}{2}(\hat{\mathbf{x}}-i\hat{\mathbf{y}})$

Γ_5	$\lvert\Gamma_5^{xy}\downarrow\rangle$	$\lvert\Gamma_5^{xy}\uparrow\rangle$	$\lvert\Gamma_5^{xz}\downarrow\rangle$	$\lvert\Gamma_5^{xz}\uparrow\rangle$	$\lvert\Gamma_5^{yz}\downarrow\rangle$	$\lvert\Gamma_5^{yz}\uparrow\rangle$
$\langle -\frac{3}{2}\rvert$	$\frac{1}{2\sqrt{3}}(\hat{\mathbf{x}}-i\hat{\mathbf{y}})$	$-\frac{1}{\sqrt{3}}\hat{\mathbf{z}}$	$\frac{1}{\sqrt{3}}\hat{\mathbf{z}}$	$\frac{1}{2\sqrt{3}}(\hat{\mathbf{x}}+i\hat{\mathbf{y}})$	$-\frac{1}{\sqrt{3}}\hat{\mathbf{z}}$	$-\frac{1}{2\sqrt{3}}(\hat{\mathbf{x}}+i\hat{\mathbf{y}})$
$\langle -\frac{1}{2}\rvert$	0	$-\frac{1}{2}(\hat{\mathbf{x}}-i\hat{\mathbf{y}})$	$\frac{1}{2}(\hat{\mathbf{x}}+i\hat{\mathbf{y}})$	0	$\frac{1}{2}(\hat{\mathbf{x}}+i\hat{\mathbf{y}})$	0
$\langle \frac{1}{2}\rvert$	$\frac{1}{2}(\hat{\mathbf{x}}+i\hat{\mathbf{y}})$	0	0	$\frac{1}{2}(\hat{\mathbf{x}}-i\hat{\mathbf{y}})$	0	$\frac{1}{2}(-\hat{\mathbf{x}}+i\hat{\mathbf{y}})$
$\langle \frac{3}{2}\rvert$	$-\frac{1}{\sqrt{3}}\hat{\mathbf{z}}$	$-\frac{1}{2\sqrt{3}}(\hat{\mathbf{x}}+i\hat{\mathbf{y}})$	$\frac{1}{2\sqrt{3}}(\hat{\mathbf{x}}-i\hat{\mathbf{y}})$	$-\frac{1}{\sqrt{3}}\hat{\mathbf{z}}$	$\frac{1}{2\sqrt{3}}(\hat{\mathbf{x}}-i\hat{\mathbf{y}})$	$-\frac{1}{\sqrt{3}}\hat{\mathbf{z}}$

Table B.1: Normalized dipole matrix $\mathbf{p}_{ij} = \left\langle \mathrm{A}^0, i \right| \boldsymbol{\mu} \left| \mathrm{A}^0\mathrm{X}, j \right\rangle$ for the $\mathrm{A}^0\mathrm{X}$-A^0 system. $\hat{\mathbf{x}}$, $\hat{\mathbf{y}}$ and $\hat{\mathbf{z}}$ are unit vectors oriented along the crystallographic axes.

Appendix C

GENERALIZED WEISSKOPF-WIGNER THEORY FOR SPONTANEOUS EMISSION FROM MULTIPLE EXCITED LEVELS

The Wiesskopf-Wigner theory of spontaneous emission [170, 18, 97] can be generalized to calculate the spontaneous emission rate from a set of excited states to a set of ground states. The excited and ground states are not necessarily degenerate.

The wavefunction of the system is

$$|\psi(t)\rangle = \sum_i \sum_{\mathbf{k}} c_{i\mathbf{k}}(t) |g, i, \mathbf{k}\rangle + \sum_j b_j(t) |e, j\rangle \tag{C.1}$$

where $|g, i, \mathbf{k}\rangle$ is the state with the atom in ground state i and a photon in mode $\mathbf{k}$, polarization ϵ_σ ($\sigma = 1, 2$), and $|e, j\rangle$ is the j'th excited atomic state and no photon. The sum on $\mathbf{k}$ contains an implicit sum over the two polarizations $\sigma = 1, 2$.

In the interaction picture and rotating wave approximation, the Hamiltonian governing the time evolution of the atom and field is

$$\mathcal{V} = \hbar \sum_{ij} \sum_{\mathbf{k}} \left[g_{\mathbf{k}}^{ij}(\mathbf{r}_o)^* |e, j\rangle \langle g, i| a_{\mathbf{k}} e^{i(\omega_{ij} - \nu_{\mathbf{k}})t} + \text{H.C.} \right] \tag{C.2}$$

where

$$g_{\mathbf{k}}^{ij}(\mathbf{r}_o) = -\frac{\mathbf{p}_{ij} \cdot \hat{\epsilon}}{\hbar} \sqrt{\frac{\hbar \nu_k}{2\epsilon V}},$$

$\mathbf{p}_{ij} = \langle g, i| \boldsymbol{\mu} |e, j\rangle$ are dipole matrix elements, $a_{\mathbf{k}}$ is the annhilation operator for a photon in mode $\mathbf{k}$, $\omega_{ij} = (E_j - E_i)/\hbar$, $\hat{\epsilon}$ is the polarization of the photon, ω is the transition frequency, $\nu_{\mathbf{k}} = c|\mathbf{k}|/n$, ϵ is the material permittivity, n is the material dielectric constant, c is the speed of light, and V is the quantization volume [170].

The time evolution is given by the Schrödinger equation

$$\frac{d}{dt} |\psi(t)\rangle = -\frac{i}{\hbar} \mathcal{V} |\psi(t)\rangle .$$

This yields the coupled differential equations

$$\begin{aligned} \dot{b}_j(t) &= -i \sum_i \sum_{\mathbf{k}} g_{\mathbf{k}}^{ij}(\mathbf{r}_o) c_{i\mathbf{k}}(t) e^{-i(\omega_{ij}-\nu_{\mathbf{k}})t} \\ \dot{c}_{i\mathbf{k}}(t) &= -i \sum_j g_{\mathbf{k}}^{ij}(\mathbf{r}_o)^* b_j(t) e^{i(\omega_{ij}-\nu_{\mathbf{k}})t}. \end{aligned} \tag{C.3}$$

By formally solving the second equation and plugging into the first, the time evolution of the excited state probability amplitude satisfies

$$\begin{aligned} \dot{b}_{j'}(t) = -\sum_{ij} \sum_{\mathbf{k}} g_{\mathbf{k}}^{ij'}(\mathbf{r}_o) g_{\mathbf{k}}^{ij}(\mathbf{r}_o)^* \int_o^t dt' \\ b_j(t') e^{-i(\omega-\nu_{\mathbf{k}})(t-t')+i\Delta_{ij}t'-i\Delta_{ij'}t}, \end{aligned} \tag{C.4}$$

where $\Delta_{ij} = \omega_{ij} - \omega$ and ω is some choice of natural frequency for the system. Assuming the modes are closely spaced in frequency, the sum over $\mathbf{k}$ may be converted to an integral:

$$\sum_{\mathbf{k}} \rightarrow 2\frac{V}{(2\pi)^3} \int d\Omega \int_0^\infty dk\, k^2.$$

By introducing the matrix

$$S_{j'j} = \frac{3}{4\pi} \sum_i \int d\Omega (\mathbf{p}_{ij'} \cdot \hat{\epsilon})^* (\mathbf{p}_{ij} \cdot \hat{\epsilon}) \tag{C.5}$$

and changing variables to integrate on $\nu_{\mathbf{k}} = ck/n$, the equation of motion (Eq. C.4) becomes

$$\begin{aligned} \dot{b}_{j'}(t) = -\frac{1}{6\pi^2} \frac{n^3}{\hbar \epsilon c^3} \cdot \sum_j S_{j'j} \int_o^\infty d\nu_{\mathbf{k}} \nu_{\mathbf{k}}^3 \int_0^t dt' \\ e^{-i(\omega-\nu_{\mathbf{k}})(t-t')} e^{i(\Delta_{ij}t'-\Delta_{ij'}t)} b_j(t'). \end{aligned}$$

Since the integral over t is only appreciable when $\omega \sim \nu_{\mathbf{k}}$, $\nu_{\mathbf{k}}^3$ may be replaced with ω^3 in the integrand and the lower frequency limit may be replaced by $-\infty$ [170, 214]. Using the delta function identity,

$$\int_{-\infty}^\infty d\nu_{\mathbf{k}} e^{-i(\omega-\nu_{\mathbf{k}})(t-t')} = 2\pi\delta(t-t').$$

and

$$\int_0^t dt' \delta(t - t') f(t') = \frac{1}{2} f(t),$$

we arrive at the differential equations in the desired form:

$$\dot{b}_{j'}(t) = -\frac{\alpha}{2} \sum_j S_{j'j} b_j(t) e^{i\Delta_{jj'} t}, \quad \alpha = \frac{1}{4\pi\epsilon} \frac{4\omega^3 n^3}{3\hbar c^3}. \tag{C.6}$$

The matrix $S_{j'j}$ can be computed from $\mathbf{p}_{ij}$ in a simple way. Using the parameterization

$$\hat{\epsilon} = \sin\theta \cos\phi \, \hat{\mathbf{x}} + \sin\theta \sin\phi \, \hat{\mathbf{y}} + \cos\theta \, \hat{\mathbf{z}}.$$

for the polarization, the integrand (C.5) contains a sum of integrals of the form

$$I_{nm} = \int d\Omega (\hat{\mathbf{x}}_{\boldsymbol{n}} \cdot \hat{\epsilon})(\hat{\mathbf{x}}_{\boldsymbol{m}} \cdot \hat{\epsilon})$$

where $\hat{\mathbf{x}}_{\boldsymbol{n}}$ is a unit vector. Performing the angular integrals, this becomes

$$I_{nm} = \frac{4\pi}{3} \delta_{nm}.$$

Thus we arrive at a convenient shorthand for computing $S_{j'j}$ given the dipole matrix:

$$S_{j'j} = \sum_i \mathbf{p}^*_{ij'} \cdot \mathbf{p}_{ij}$$

where the dot product is evaluated using $\hat{\mathbf{x}}_n \cdot \hat{\mathbf{x}}_m = \delta_{nm}$. This shows the angular integral can be replaced with a simple dot product.

In matrix language, the differential equation governing excited state probability amplitudes for degenerate excited states is

$$\frac{d\mathbf{b}}{dt} = -\frac{\alpha}{2} S\mathbf{b}, \quad S = \mathbf{p}^\dagger \cdot \mathbf{p}.$$

By choosing a basis for the excited states in which S is diagonal, the decay of each state is uncoupled from the others. Thus we see that the the eigenstates of αS decay independently at spontaneous emission rates equal to the eigenvalues of αS.

This method can be used to compare spontaneous emission rates between different manifolds of excited states. If the states are split in energy by a large amount

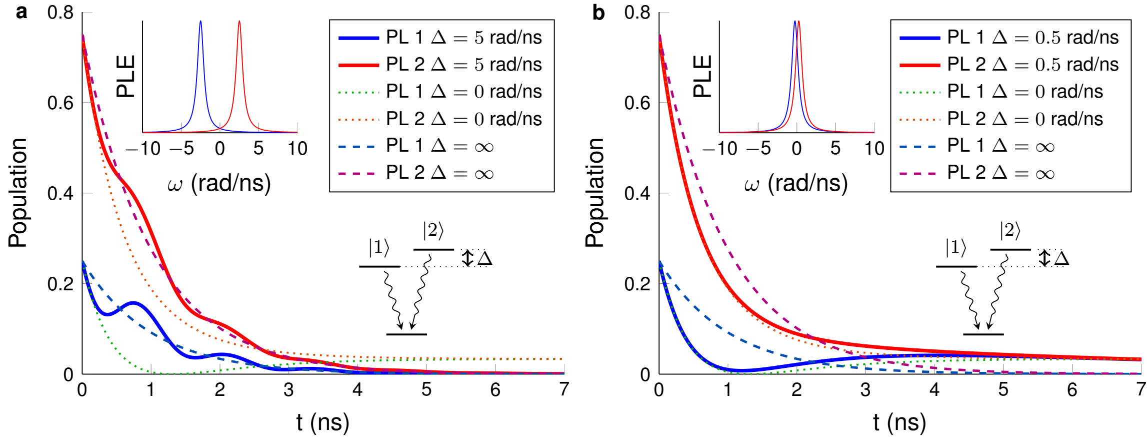

Figure C.1: Time dependence of excited state population depending on detuning between two excited states that can interfere. $\tau = 1$ ns. For a detuning Δ much larger than the spontaneous emission rate $1/\tau$, the population of the two excited states decay independently. When $\Delta = 0$, the lifetimes are modified by interference of the two recombination pathways, and the system progresses towards a dark state. The lifetimes of states in the absence of interference are 1 ns for both transitions. The initial wave function is $|\psi\rangle = \frac{1}{2}|1\rangle + \frac{\sqrt{3}}{2}|2\rangle$. **a.** At intermediate $\Delta = 5$ rad/ns, some interference is seen in the emission, oscillating around the behavior expected for two independent subsystems. **b.** When the transitions are nearly resonant, the emission follows the behavior for degenerate excited states.

compared to the radiative lifetime, the fast oscillating term in Eq. C.6 will result in non-degenerate excited states becoming uncoupled. As an example, we solved Eq. C.6 for two excited states and one ground state, whose lifetimes can be modified if the excited levels are degenerate. The differential equations governing the excited state probability amplitudes are

$$\frac{d}{dt}\begin{pmatrix} b_1 \\ b_2 \end{pmatrix} = -\frac{1}{2\tau}\begin{pmatrix} 1 & e^{i\Delta t} \\ e^{-i\Delta t} & 1 \end{pmatrix}\begin{pmatrix} b_1 \\ b_2 \end{pmatrix}$$

The solution is plotted in Fig. C.1 for $\tau = 1$ ns and various detunings Δ. If the transitions are well resolved, the time dependence of the system follows that of two independent subsystems (Fig. C.1a). On the other hand, if there is significant overlap between the Lorentzian line shapes, interference effects modify the radiative lifetime. In this toy model, near-degeneracy results in the existence of a dark state and long

lived excited state population (Fig. C.1b).

Therefore, to find the spontaneous emission rates for different non-degenerate sets of states, it is only necessary to calculate the eigenvalues of S within each degenerate subspace. When comparing eigenrates between non-degenerate manifolds, the existence of ω^3 in the pre-factor α modifies the lifetimes. For excited state splittings of 10s of GHz (as for A^0X) at optical frequencies, this leads to a correction of a part in 10^4, which can often be neglected.

Appendix D

SUPPLEMENTAL INFORMATION FOR DONOR-BOUND ELECTRON SPIN RELAXATION

D.1 Magneto-photoluminescence spectra for GaAs, InP, and CdTe

Representative magneto-photoluminescence spectra for GaAs-2, InP-2, and CdTe-2 are shown in Fig. D.1. In all three samples we can observe the free exciton (labeled X), donor-bound exciton $D^0X \rightarrow D^0$,1s transition (labeled D^0X), ionized donor-bound exciton transition $D^+X \rightarrow D^+$ (labeled D^+X), and acceptor-bound exciton $A^0X \rightarrow A^0$,1s transition (labeled A^0X). Also observed in GaAs and InP are the D^0X two-electron satellite (TES) transitions which correspond to the $D^0X \rightarrow D^0, nl^m$ transition, where n, l, m specify the quantum numbers of the excited D^0 orbital at $B = 0$. For GaAs and InP, the fine-structure of the D^0X spectra is well resolved due to the hole spin and spin-orbit interaction as well as the nearby D^0X excited orbital states. In the CdTe samples, which are bulk crystals, this structure is unresolved, limiting our ability to optically pump the system to electron Zeeman splittings greater than 0.1 meV.

D.2 GaAs and CdTe T_1 measurements

Representative energy diagrams, spectra, optical pumping traces, and T_1 recovery traces for CdTe and GaAs are shown in Fig. D.2. For GaAs and InP, the lower energy Zeeman pair transition was used for optical pumping. Although this results in a weaker signal due to the lower thermal population in the higher electron spin level, the lower energy transition is clearly resolved from all other D^0X transitions enabling efficient optical pumping. For CdTe, there is significant inhomogeneous optical broadening of the D^0X lines. This can be observed by comparing the non-resonant and resonant excitation spectral linewidths in Fig. D.2(b). Optical pumping visibility is thus significantly smaller in this sample relative to GaAs and InP. Empirically we find the best signal-to-noise is obtained by pumping the high-energy Zeeman pair transition due to the significantly larger thermal population in the lower energy spin

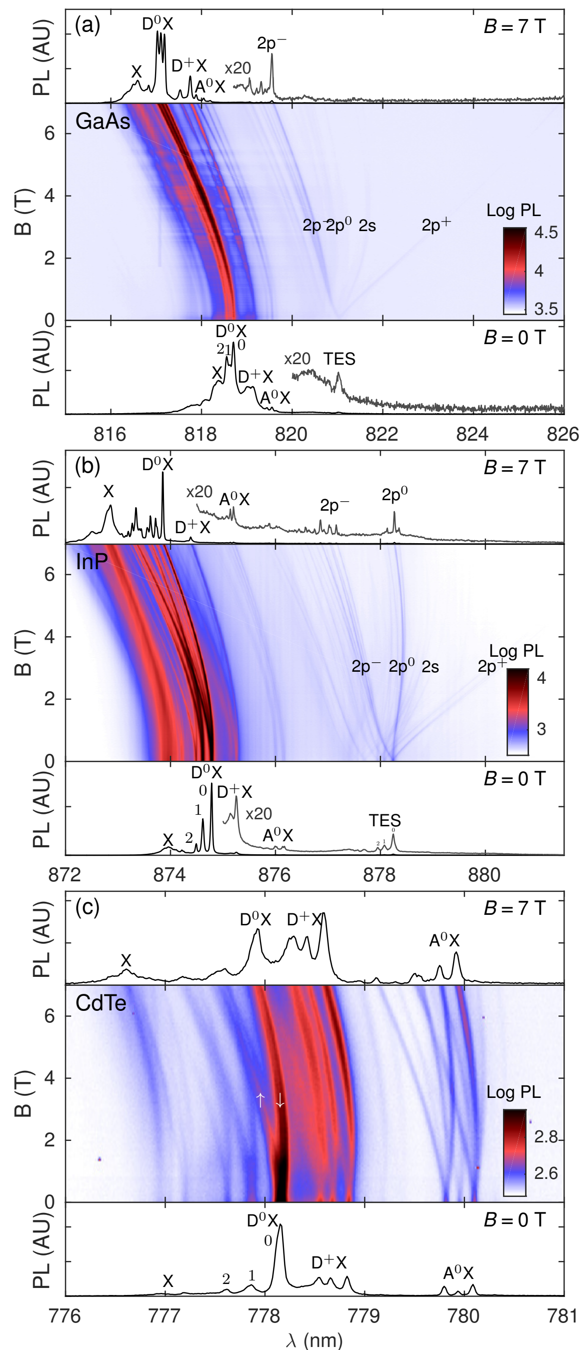

Figure D.1: Magneto-photoluminescence spectra in the Voigt geometry. (a) GaAs-2. The oscillations in photoluminescence intensity with field are attributed to oscillations in magneto-absorption due to the diamagnetic exciton effect [171], $T = 2$ K, excitation and collection are performed in linear polarizations oriented at $\pm 45°$ with respect to the magnetic field direction, 1 mW excitation power at 810 nm. (b) InP-2, $T = 2.3$ K, σ-polarization excitation, all polarizations collected, 40 μW above band-gap excitation power. (c) CdTe-2. $T = 1.6$ K. π-polarization excitation, σ-polarization collection, 20 μW above band-gap excitation power.

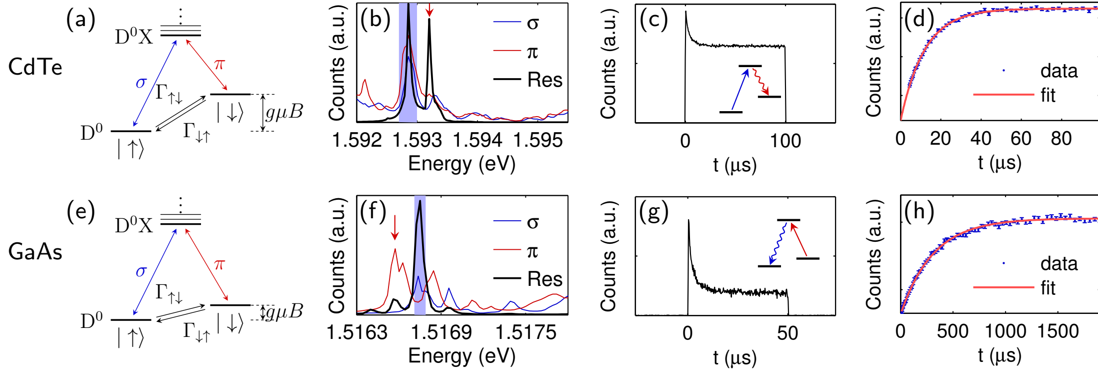

Figure D.2: (a) Energy level diagram for donor system in CdTe. (b) Photoluminescence spectrum of CdTe at $B = 3.5$ T, $T = 1.5$ K. Excitation at 1.653 eV with 50 μW for the two above band spectra (red and blue). Excitation at 1.593 with 50 μW for resonant spectrum (black), as shown by the red arrow. (c) Optical pumping trace for CdTe at 3.5 T, 1.5 K. Power 50 μW. Laser pulse lasts 100 μs. (d) T_1 measurement for CdTe at 3.5 T, 1.5 K. Power 50 μW. $T_1 = (12.0 \pm 0.2)$ μs. (e) Energy level diagram for donor system in GaAs. (f) Photoluminescence spectrum of GaAs at 7 T, 1.5 K. Excitation at 1.530 eV with 18 μW for the two above band spectra (red and blue). Excitation at 1.517 with 10 μW for resonant spectrum (black), as shown by the red arrow. (g) Optical pumping trace for GaAs at 7 T, 1.5 K. Power 10 μW. Laser pulse lasts 50 μs. (d) T_1 measurement for GaAs at 7 T, 1.5 K. Power 10 μW. $T_1 = (313 \pm 5)$ μs. All data are taken with an excitation spot size ~ 30 μm.

state. Due to the large g-factor in CdTe, the thermal population in the high energy state at 7 T and 1.5 K is only 0.6%.

D.3 Surface depletion effects

In the GaAs and InP samples, a μs-scale time-dependent increase in luminescence was observed in all band edge PL after the start of an optical excitation pulse. The magnitude of this effect varied significantly between samples and depended on both the wavelength and intensity of the optical excitation. The effect was greater in InP than in GaAs and was greater in lower doped samples. It did not significantly depend on emission wavelength. Free exciton, D^+X, D^0X, and A^0X transitions all behaved similarly.

Figure D.3a depicts a representative example of this effect in sample InP-2. In

two experiments at 0 T and 1.6 K, the D^0X emission is detected during an excitation pulse. In the first experiment, the sample is excited with a 5 μW excitation pulse resonant with the D^0X transition. During the application of this pulse a small increase in optical emission at the beginning of the pulse can be observed on the microsecond time-scale (blue trace). This effect decreases with increasing field and increases with excitation power intensity. In the second experiment, we use a 5 μW excitation pulse with energy greater than the bandgap. A significant emission increase is observed. Using a pulse sequence similar to the T_1 sequence [Fig. 5.1(e)], we find the sample relaxes to its initial state on the timescale of 50 microseconds. For all T_1 measurements reported in the main manuscript, the resonant excitation power is always kept low enough so that this emission enhancement effect is negligible.

Due to this effect, we are unable to obtain a T_1 measurement for donors in InP-1, the InP sample with the lowest donor concentration. Example optical pumping curves for this sample are shown in Fig. D.3(b) at 4 T and 1.6 K. The blue trace shows data corresponding to the standard optical pumping pulse sequence depicted in Fig. 5.1(c). The visibility is poor and in addition to the small optical pumping feature, we see an increase in the PL intensity after the initial optical pumping phase. For InP-1, this "brightening" effect is observed at all reasonable powers (i.e. powers for which we can obtain enough signal to reliably obtain a T_1 measurement) and the decay of this signal is the dominant contribution in T_1 pulse sequence measurements.

Additionally, we performed a two-pulse experiment where a 50 μs pulse with energy above the bandgap is applied to the sample until 5 μs before the the optical pumping pulse begins. The effect of the pre-pulse is dramatic (Fig. D.3): the larger visibility can be attributed to the pre-pulse depolarizing bound electron spins. However we also note that the intensity in the optically pumped steady-state, near the end of the pulse, is flat and significantly larger in the pre-pulse case. This indicates that in terms of emission intensity, the sample has reached steady-state during the application of the pre-pulse. We attribute the brightening effect to the elimination of near-surface fields in the GaAs and InP samples under optical illumination [210]. There is evidence that very small fields, on the order of V/cm, can substantially quench fluorescence [25]. We do not observe this effect in CdTe, which is a true bulk sample rather than a few-micron-thick film.

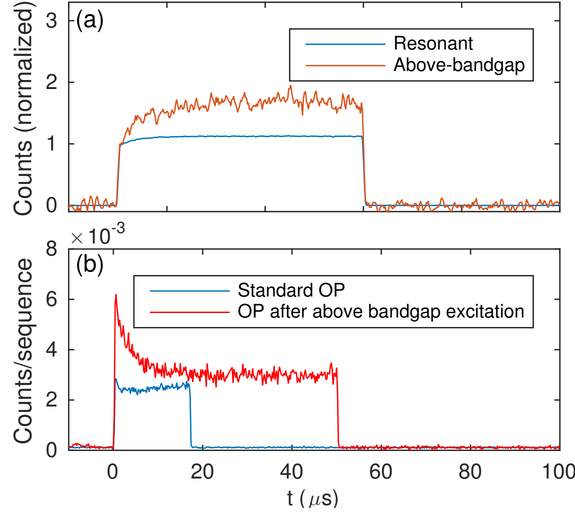

Figure D.3: Time-resolved photoluminescence during optical pulse. (a) Collection of D^0X emission during resonant D^0X excitation (blue curve) and above-bandgap excitation (red curve). A significant increase in emission intensity is observed for above-bandgap excitation. (b) Optical pumping traces for InP-1 at 4 T. Blue curve: Standard optical pumping experiment. Red curve: Prior to the optical pumping pulse, a 50 μs long above-bandgap pre-pulse is applied. The end of the pre-pulse is 5 μs before the start of the optical pumping pulse.

D.4 Numerical solution of donor-bound electron in magnetic field

The numerical solution of the hydrogen atom in a magnetic field is a nontrivial problem [160]. Of particular difficulty is the transition from the low-field to high-field regime, where the solutions cannot be conveniently expanded in hydrogen or Landau orbitals [132]. We have used a readily available finite element solver to find the energies and wave functions of hydrogen in a magnetic field of arbitrary strength [167]. These solutions can be mapped onto the donor-bound electron problem by replacing the electron mass, Bohr radius, g-factor and other parameters by their effective values for the donor-bound electron. The magnetic field is measured by a dimensionless quantity $\beta = B/B_0$, where the reference magnetic field $B_0 = 2\hbar/[|e|(a_B^*)^2]$ is found by considering when the Larmor radius $\sqrt{2\hbar/|eB|}$ is equal to the donor Bohr radius. For GaAs, InP, and CdTe, B_0 is, 13.4 T, 19.3 T and 49.8 T respectively. In our experiment, the maximum applied field is 7 T, implying that the 1s wave function is

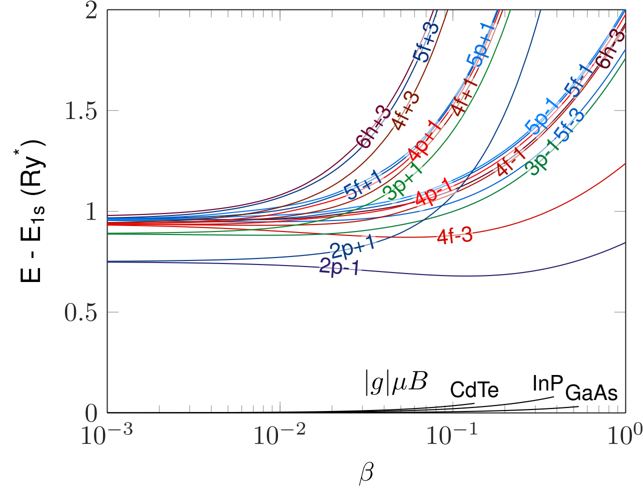

Figure D.4: Energies of excited state orbitals vs. dimensionless magnetic field β from numerical simulation of hydrogen atom in magnetic field. The plot shows the energy difference of 18 excited states from the ground state with the same spin projection. States are labeled by their zero-field quantum numbers. Also plotted is the Zeeman splitting energy $|g|\mu B$ in units of effective Rydberg, the maximum β of the plot being the maximum experimental β obtained for each material. The Zeeman energy can be ignored compared to the orbital energy.

a good approximation for the ground state. However, we note that for higher energy orbitals n, the magnetic field at which magnetic effects begin to dominate Coulomb ones occurs at B_0/n^3 [167]. Thus, higher energy orbitals are significantly perturbed even at small β. The energy difference between the excited states and the ground state are shown in Fig. D.4. The energy is scaled by the effective binding energy $\mathcal{E}^*_{Ry}$, which is 5.8, 7.0 and 13.6 meV for GaAs, InP and CdTe respectively.

D.5 Theory of spin-relaxation via the admixture mechanism

In this appendix, we calculate the spin-relaxation rate due to the admixture mechanism in several different ways. First we provide general simplifications that are common to all calculations. We then evaluate the expression for T_1 numerically at all fields and analytically at low and moderate fields.

D.5.1 General expression for the admixture spin-relaxation rate

It is convenient to represent the spin-relaxation rate, Eq. (5.7), in a simplified form. First, we investigate which excited states may contribute to spin relaxation by symmetry.

The Dresselhaus spin-orbit interaction Hamiltonian (5.12) is cubic in the electron wavevector. It can be conveniently decomposed in the spherical angular harmonics, $Y_l^m(\theta_k, \phi_k)$, where the subscripts $l = 0, 1, 2, \ldots$, $m = -l, -l+1, \ldots, l-1, l$, and θ_k, ϕ_k are the polar and azimuthal angles of the wavevector $\mathbf{k}$ in the spherical coordinate system with z being the polar axis. Corresponding summands in Eq. (5.12) take the form:

$$\frac{k_x(k_y^2 - k_z^2)}{k^3} = \sqrt{\pi}\left(\frac{Y_3^3 - Y_3^{-3}}{\sqrt{35}} + \frac{Y_3^1 - Y_3^{-1}}{\sqrt{21}}\right), \tag{D.1a}$$

$$\frac{k_y(k_z^2 - k_x^2)}{k^3} = \sqrt{\pi}\left(\frac{Y_3^3 + Y_3^{-3}}{i\sqrt{35}} - \frac{Y_3^1 + Y_3^{-1}}{i\sqrt{21}}\right), \tag{D.1b}$$

$$\frac{k_z(k_x^2 - k_y^2)}{k^3} = 2\sqrt{\frac{2\pi}{105}}\left(Y_3^2 + Y_3^{-2}\right). \tag{D.1c}$$

Here the arguments of the spherical harmonics are omitted for brevity. In our frame of axes where $\mathbf{B} \parallel z$, the eigenstates of the donor-bound electron in the magnetic field are characterized by the angular momentum component m onto the z axis. Note that the term $\sigma_z k_z(k_x^2 - k_y^2)$ in Eq. (5.12) does not play a role in the spin flip process. Hence, the intermediate states for the admixture mechanism, in agreement with the first two lines of Eq. (D.1), are those with $m = \pm 1$, $m = \pm 3$. In relatively weak fields where the magnetic field does not perturb the ground and excited stated wave functions, the donor-bound electron has spherical symmetry and Eq. (D.1) imposes a strict selection rule for the excited states: only $l = 3$ (and $m = \pm 1$, $m = \pm 3$) can cause spin-relaxation.

As such, in the sum over excited states in Eq. (5.8), we only need to include $m = \pm 1$ and $m = \pm 3$ states. We also note that due to the azimuthal symmetry,

$$\langle \nu, \pi_z, m | k_x(k_y^2 - k_z^2) | 1\mathrm{s} \rangle = e^{-im\frac{\pi}{2}} \langle \nu, \pi_z, m | k_y(k_x^2 - k_z^2) | 1\mathrm{s} \rangle,$$

it is sufficient to calculate the contribution due to the $\sigma_x k_x(k_y^2 - k_z^2)$ term in the Dresselhaus Hamiltonian. By combining positive and negative m terms and simplifying,

we find

$$|M_{\uparrow\downarrow}|^2 = \frac{2\gamma^2\hbar}{\rho\omega_{\mathbf{q},\alpha}}|eA_{\mathbf{q},\alpha}|^2 \cdot \left|\sum_{\substack{m=1,-3\\ \nu=1,2,\ldots\\ \pi_z=1}}\langle 1\mathrm{s}|e^{i\mathbf{qr}}|\nu,\pi_z,m\rangle\langle\nu,\pi_z,m|k_x(k_y^2-k_z^2)|1\mathrm{s}\rangle G_{\nu;m}\right|^2 \tag{D.2}$$

where

$$G_{\nu;m} = (\Delta E_{\nu,\pi_z,m} - g\mu B)^{-1} - (\Delta E_{\nu,\pi_z,-m} + g\mu B)^{-1},$$

and $\pi_z = 1$ by symmetry. By integrating over phonon modes, we find the general expression

$$\frac{1}{T_1} = F_{ph}\frac{\gamma^2}{2\pi^2\hbar^2\rho}\sum_{\alpha}\sum_{m=1,-3}\frac{|g\mu B|}{s_\alpha^3}\int d\Omega_q|eA_{\mathbf{q},\alpha}|^2\times \\ \left|\sum_{\nu}\left[\langle 1\mathrm{s}|e^{i\mathbf{qr}}|\nu,\pi_z,m\rangle\right]_{q=q_\alpha}\langle\nu,\pi_z,m|k_x(k_y^2-k_z^2)|1\mathrm{s}\rangle G_{\nu;m}\right|^2, \tag{D.3}$$

where the phonon matrix element is evaluated at a wavevector q magnitude corresponding to the Zeeman energy $q = q_\alpha \equiv |g\mu B|/\hbar s_\alpha$. In the following sections, we will evaluate Eq. (D.3) using numerically calculated functions and an analytic approximation for the hydrogenic wavefunctions in a magnetic field.

D.5.2 Numerical calculation of admixture spin-relaxation rate

For the two matrix elements in Eq. (D.3), the integrals over the azimuthal angle of the position vector $\mathbf{r}$ can be performed analytically. This greatly speeds the evaluation time and improves the accuracy of the numerical calculation. The wave functions are written in cylindrical coordinates as $\langle\mathbf{r}|\nu,\pi_z,m\rangle = \Phi_{\nu,\pi_z,m}(\rho,z)e^{im\phi}$, where ρ is the radial coordinate, z the axial coordinate and ϕ the azimuthal angle. By transforming

the differential operators into cylindrical coordinates and integrating over ϕ, we find

$$\begin{aligned}
&\langle \nu, \pi_z, \pm 1 |\, k_x (k_y^2 - k_z^2)\, | 1\mathrm{s} \rangle = \\
&-\frac{\pi}{4} \int \rho\, d\rho\, dz\, \Phi_{\nu,\pi_z,\pm 1} \left[\frac{1}{\rho^2} \partial_\rho - \frac{1}{\rho} \partial_\rho^2 - \partial_\rho^3 + 4 \partial_\rho \partial_z^2 \right] \Phi_{1\mathrm{s}}, \\
&\langle \nu, \pi_z, \pm 3 |\, k_x (k_y^2 - k_z^2)\, | 1\mathrm{s} \rangle = \\
&-\frac{\pi}{4} \int \rho\, d\rho\, dz\, \Phi_{\nu,\pi_z,\pm 3} \left[\frac{3}{\rho^2} \partial_\rho - \frac{3}{\rho} \partial_\rho^2 + \partial_\rho^3 \right] \Phi_{1\mathrm{s}},
\end{aligned} \tag{D.4}$$

and that the matrix element is zero for any other excited state magnetic quantum number, as it must be by symmetry.

Similarly, for the matrix element $\langle \nu, \pi_z, m | e^{i\mathbf{qr}} | 1\mathrm{s} \rangle$, we note that aligning the $\phi = 0$ plane along $\mathbf{q}$ results in multiplying the integrand by a phase $\exp(-im\phi_q)$, where ϕ_q is the azimuthal angle of the phonon wavevector $\mathbf{q}$. The ϕ integral can then be performed analytically with the help of a Bessel function identity. Using a few additional simplifications involving the z-parity of the wave functions, the matrix element becomes

$$\begin{aligned}
\langle \nu, \pi_z, m | e^{i\mathbf{qr}} | 1\mathrm{s} \rangle = \; & 4\pi\, e^{-im\phi_q} \int_0^\infty \rho\, d\rho \int_0^\infty dz \cdot \\
& \Phi_{\nu,\pi_z,m} \Phi_{1\mathrm{s}} \cos(z\, q \cos\theta_q) J_m(\rho\, q \sin\theta_q),
\end{aligned} \tag{D.5}$$

where θ_q is the polar angle of the wavevector $\mathbf{q}$, and J_m is the mth Bessel function of the first kind.

Lastly, we evaluate the integral over the phonon azimuthal angle ϕ_q in Eq. (D.3). We additionally note that $m = \pm 1$ states cannot interfere with $m = \pm 3$ states due to the $e^{-im\phi_q}$ factor in Eq. (D.5). We thus arrive at the expression for T_1 via the admixture mechanism,

$$\begin{aligned}
\frac{1}{T_1} = F_{ph} \frac{\gamma^2 |g\mu B|}{2\pi\hbar^2\rho} \int \sin\theta_q d\theta_q \sum_\alpha \sum_{m=1,-3} \times \\
\left| \sum_{\nu=1}^{\infty} \left[\langle 1\mathrm{s} | e^{i\mathbf{qr}} | \nu, \pi_z, m \rangle \right]_{\phi_q=0}^{q=q_\alpha} \langle \nu, \pi_z, m |\, k_x (k_y^2 - k_z^2)\, | 1\mathrm{s} \rangle \right|^2 P_\alpha(\theta_q)\,,
\end{aligned} \tag{D.6}$$

where the phonon matrix element is evaluated at the wavevector corresponding to

the Zeeman energy and at $\phi_q = 0$. (Since ϕ_q just adds a phase, the expression is valid for any choice of ϕ_q.) The functions $P_\alpha(\theta_q)$ describe the contributions of different phonon modes and different electron-phonon interaction mechanisms. We take into account both the piezoelectric interaction with longitudinal and transverse modes, Eq. (5.10), as well as the deformation potential interaction. The latter is described by the Hamiltonian [76, 173]

$$U_{ph}^{(dp)}(\mathbf{r}) = \sqrt{\frac{\hbar}{2\rho\omega_{\mathbf{q}\alpha}}} e^{i\mathbf{qr}} q(\xi_i \hat{e}_i) D b^{\dagger}_{\mathbf{q}\alpha} + \text{c.c.}, \tag{D.7}$$

where D is the deformation potential constant and involves longitudinal phonons only. As a result, disregarding the interference of piezo and deformation potential interactions, we have

$$\begin{aligned} P_1(\theta_q) &= \frac{9e^2 h_{14}^2}{s_l^3} \cos^2\theta_q \sin^4\theta_q \,, \\ P_2(\theta_q) &= \frac{e^2 h_{14}^2}{8 s_t^3} (27 + 28\cos 2\theta_q + 9\cos 4\theta_q) \,, \\ P_3(\theta_q) &= \frac{2(g\mu B)^2 D^2}{\hbar^2 s_l^5}. \end{aligned} \tag{D.8}$$

The simplified matrix elements Eq. (D.4), (D.5) are calculated numerically using standard procedures. The scripts have been made readily available [110].

D.5.3 Admixture mechanism in moderate magnetic fields

In the regime of moderate fields, when $l_b \sim a_B^*$, we take into account the modification of the excited state wavefunctions by the magnetic field. In this regime, admixture with the lowest energy excited states (p-shell states) is allowed and we will further take into account only these two states assuming a Gaussian form of the wavefunctions:

$$\begin{aligned} \psi_{1\text{s}} &= \frac{1}{\pi^{3/4} l_\rho \sqrt{l_z}} \exp\left(-\frac{x^2+y^2}{2(l_{\rho,1\text{s}})^2} - \frac{z^2}{2(l_{z,1\text{s}})^2} \right), \\ \psi_{2\text{p}_\pm} &= \frac{(x \pm iy)}{\pi^{3/4} \chi^{5/2} l_\rho^2 \sqrt{l_z}} \exp\left(-\frac{x^2+y^2}{2(l_{\rho,2\text{p}})^2} - \frac{z^2}{2(l_{z,2\text{p}})^2} \right). \end{aligned} \tag{D.9}$$

Further, for simplicity, we will assume a proportionality $l_{\rho,2\mathrm{p}} = \chi l_{\rho,1\mathrm{s}}$ and $l_{z,2\mathrm{p}} = \chi l_{z,1\mathrm{s}}$ for the analytic wavefunctions. Here $l_{\rho,1\mathrm{s}} = [1/(a_B^*)^2 + 1/(2l_b^2)]^{-1/2}$ and $l_{z,1\mathrm{s}} = a_B^*$ are the wave function effective sizes in the (xy)-plane and the z-direction, respectively. At zero field, $l_{\rho,1\mathrm{s}}$ is just the Bohr radius and both lengths coincide. A non-zero magnetic field shrinks the wave function in the (xy)-plane leading to anisotropy of the 1s-state with $l_{\rho,1\mathrm{s}} < l_{z,1\mathrm{s}}$. In the limit of very strong fields $l_{\rho,1\mathrm{s}} = \sqrt{2}l_b$, in agreement with the free-electron wave function in a magnetic field in the symmetric gauge. The exact numerical wavefunctions (Appendix D.4) are used to determine the value of χ for the analytic wavefunctions, Eq. (D.9). To determine the best value of χ, we numerically optimized the overlap integral between the analytic wavefunctions, Eq. (D.9), and the numerical ones. The ratio of the wavefunction size for the $2\mathrm{p}_{-1}$ and 1s states are shown in Fig. D.5. In the figure we have also shown the limiting values of β for which the experimental high-field dependence is observed. By averaging over the ratio of lengths for ρ and z directions, we obtain a best-choice χ of 1.5, 1.7 and 2.2 for GaAs, InP, and CdTe respectively.

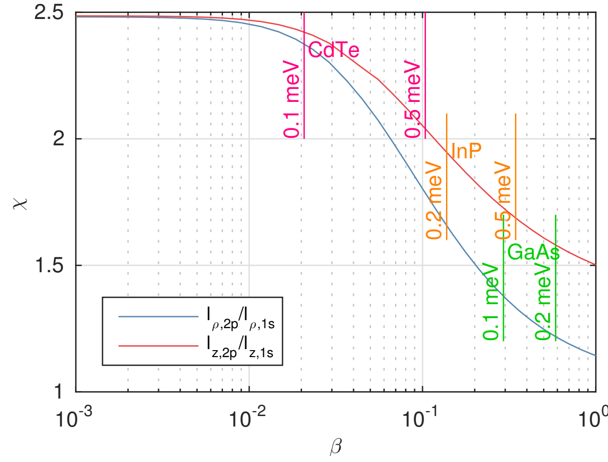

Figure D.5: The overlap integral between the Gaussian approximation for the wavefunction, Eq. (D.9), and the numerical solution was maximized as a function of β. The ratio of the radial and axial Gaussian sizes is plotted as a function of B. Also shown are the experimental limits of the "high-field" regime where T_1 goes as $B^{-\nu}$ for the three different materials. Using these limits, reasonable choices of χ are 1.5, 1.7 and 2.2 for GaAs, InP, and CdTe respectively.

To obtain the matrix element $M_{\downarrow\uparrow}$ given by Eq. (5.8), we need to calculate

$\langle 2p_\pm|\partial_x(\partial_y^2-\partial_z^2)|1s\rangle$ and $\langle 1s|e^{i\mathbf{qr}}|2p_\pm\rangle$. Utilizing the Gaussian wave functions we assumed, Eq. (D.9), the results for the integrals are

$$\begin{aligned}\langle 2\mathrm{p}_\pm|\partial_x(\partial_y^2-\partial_z^2)|1\mathrm{s}\rangle &= \frac{\sqrt{2}\chi^{5/2}}{(1+\chi^2)^{7/2}l_b^2 l_\rho}\,, &\text{(D.10a)}\\ \langle 2\mathrm{p}_\pm|\partial_y(\partial_z^2-\partial_x^2)|1\mathrm{s}\rangle &= \pm\frac{i\sqrt{2}\chi^{5/2}}{(1+\chi^2)^{7/2}l_b^2 l_\rho}\,. &\text{(D.10b)}\end{aligned}$$

and

$$\langle 1\mathrm{s}|e^{i\mathbf{qr}}|2p_\pm\rangle = i2\sqrt{2}\left(\frac{\chi}{1+\chi^2}\right)^{5/2}(q_x\pm iq_y)l_\rho\times \\ \times\exp\left(-\frac{\chi^2}{2(1+\chi^2)}[(q_x^2+q_y^2)l_\rho^2+q_z^2l_z^2]\right)\,. \quad \text{(D.11)}$$

Note that nonzero matrix elements in Eq. (D.10) are proportional to B, so that they vanish in the limit of low fields (this regime is considered below in Appendix D.5.4). As the magnetic fields in our experiments are not very strong, the change of the characteristic length is small and we can neglect the difference between l_ρ and l_z in the exponential part of Eq. (D.11) by setting $l_{z,1\mathrm{s}}=l_{\rho,1\mathrm{s}}=l$. In fact, the wavefunction size l is important only when the long-wavelength approximation for the electron-acoustic phonon interaction fails, in which case the result may be quite sensitive to the overall shape of the wave function, and, additionally, the deformation-potential interaction may be important.

Substituting these into Eqs. (5.7),(5.8), the relaxation rate is

$$\frac{1}{T_1}=\frac{32}{\pi\hbar\rho}\frac{\chi^{10}}{(1+\chi^2)^{12}}\frac{\gamma^2(eh_{14})^2}{l_b^4}\left(\frac{1}{\Delta E_R}-\frac{1}{\Delta E_R+\hbar\omega_c}\right)^2 \\ \times F_{ph}\sum_\alpha\frac{q_\alpha^3}{s_\alpha^2}\exp\left(-\frac{\chi^2}{1+\chi^2}q_\alpha^2l^2\right)\left\langle\sin^2\theta_q a_{\mathbf{q},\alpha}^2\right\rangle_\Omega\,. \quad \text{(D.12)}$$

The quantity $\Delta E=E_{2\mathrm{p}_-}-E_{1\mathrm{s}}$. Numerically we find that $\Delta E=3/4\mathcal{E}_{Ry}^*$ is a good approximation across the entire experimental range of fields (see Fig. D.4).

For longitudinal phonons we have

$$\left\langle\sin^2\theta_q a_{q,l}^2\right\rangle_\Omega=\frac{8}{35}\,, \quad \text{(D.13)}$$

while for transverse modes

$$\langle \sin^2 \theta_q a_{q,t}^2 \rangle_\Omega = \frac{32}{105} \,. \tag{D.14}$$

Substituting these integrals into the Eq. (D.12), the final result for the spin relaxation rate is

$$\frac{1}{T_1} = \frac{256\chi^{10}}{35(1+\chi^2)^{12}} \frac{\gamma^2 e^4 h_{14}^2 (g\mu)^3 B^5}{\pi \rho \hbar^6} \left(\frac{1}{\Delta E_R} - \frac{1}{\Delta E_R + \hbar\omega_c} \right)^2 F_{ph} \times \\ \times \left[\frac{1}{s_l^5} \exp\left(-\frac{\chi^2 q_l^2 l^2}{1+\chi^2} \right) + \frac{4}{3s_t^5} \exp\left(-\frac{\chi^2 q_t^2 l^2}{1+\chi^2} \right) \right] \,, \tag{D.15}$$

in agreement with Eq. (5.15) of the main text.

We note that in the limit of very strong magnetic fields where $l_b \ll a_B^*$ and $\hbar\omega_c \gg \Delta E_R$ one has to take into account the modification of the separation between the ground and the excited states by the magnetic field. As a rough estimate one may replace ΔE_R in Eq. (D.15) by $\hbar\omega_c$, in which case, within the LWA, one has $T_1 \propto B^3$. Our estimates show that this limit is not fulfilled in any sample for the magnetic fields under study.

Finally, we briefly analyze the deformation potential interaction in which case instead of Eq. (5.10) one has Eq. (D.7). It follows from Eq. (D.7) that transition can be assisted by the logitudinal acoustic phonons only. Making use of the analytical form of the wavefunctions, Eq. (D.9), and the matrix elements of the Dresselhaus spin-orbit interaction, Eq. (D.10), as well as Eq. (D.11) we obtain

$$\frac{1}{T_1} = \frac{64\chi^{10}}{3\pi\hbar\rho(1+\chi^2)^{12}} \left(\frac{g\mu B}{\hbar s_l} \right)^5 \frac{\gamma^2 D^2}{s_l^2 l_b^4} F_{ph} \left(\frac{1}{\Delta E_R} - \frac{1}{\Delta E_R + \hbar\omega_c} \right)^2 \exp\left(-\frac{\chi^2 q_l^2 l^2}{1+\chi^2} \right). \tag{D.16}$$

The angular integrations over the phonon wavevectors has been carried out, as before, neglecting the difference between $l_{\rho,1\mathrm{s}}$ and $l_{z,1\mathrm{s}}$ in the exponent and using the expression $\langle (\xi_i \hat{e}_i)^2 (\xi_x^2 + \xi_y^2) \rangle_\Omega = 2/3$. The analysis shows that the deformation potential contribution is much smaller than the piezo-interaction, Eq. (D.15) for the relevant magnetic fields. The contribution from the deformation potential interaction is more important than the piezo-interaction at high fields due to its stronger B-field dependence. The crossover field for GaAs is about 40 T, which is much larger than the magnetic fields in this study. The crossover fields for InP and CdTe are 9.1 T and 3.9 T. Although deformation potential interaction for these two materials is com-

parable to the piezo-interaction at the fields achievable in our experiment, it is still much weaker than the direct spin-phonon interaction.

D.5.4 Admixture mechanism in low magnetic fields

In the low-field limit we take the wave functions of the ground 1s and excited ($|e\rangle = |n\mathrm{f}, m\rangle$, where f denotes f-orbitals) states in a hydrogen-like form:

$$\begin{aligned} \psi_{1\mathrm{s}} &= \frac{1}{\sqrt{\pi a^3}} e^{-r/a} \,, \\ \psi_{n\mathrm{f},m} &= R_{n3}(r) Y_3^m(\theta,\phi) \,. \end{aligned} \tag{D.17}$$

Here and R_{n3} are the radial functions of the f-orbitals ($l = 3$).

To calculate the spin-flip rate we use the matrix element $M_{\downarrow\uparrow}$ given by Eq. (5.8). We note that in the absence of a magnetic field the following relation for the matrix elements of H_{so} holds

$$\langle 1\mathrm{s} \uparrow | H_{so} | \, n\mathrm{f}, m \downarrow \rangle = - \, \langle n\mathrm{f}, -m \uparrow | H_{so} | \, 1\mathrm{s} \downarrow \rangle \ . \tag{D.18}$$

Using this relation and keeping in mind that the energies of m and $-m$ states are the same at zero magnetic field the second order matrix element, Eq. (5.8), vanishes as $B \to 0$ [116]. At nonzero magnetic field $M_{\downarrow\uparrow}$ becomes nonzero due to (i) Zeeman splitting of spin sublevels and (ii) orbital splitting of $m = \pm 3$ and $m = \pm 1$ states. Taking into account only the Zeeman splitting we obtain the following expression for the matrix element $M_{\downarrow\uparrow}$ in the low-field limit (the effect of the field-induced orbital splitting is briefly addressed in the end of this subsection)

$$M_{\downarrow\uparrow} = 2g\mu B \sum_{n,m} \frac{\langle 1\mathrm{s}, \downarrow | U_{ph} | n\mathrm{f}, m, \downarrow \rangle \langle n\mathrm{f}, m, \downarrow | H_{so} | 1\mathrm{s}, \uparrow \rangle}{(E_{n\mathrm{f},m} - E_{1\mathrm{s}})^2} \,. \tag{D.19}$$

Here the wavefunctions and energies are taken at $B = 0$. The sum over m in Eq. (D.19) can be evaluated using the fact that at $B = 0$ the energy spectrum is degenerate with

respect to m and the following formula:

$$\sum_m \langle 1\mathrm{s}, \downarrow | e^{i\mathbf{qr}} | n\mathrm{f}, m, \downarrow \rangle \langle n\mathrm{f}, m, \downarrow | H_{so} | 1\mathrm{s}, \uparrow \rangle = \\ -4\pi \frac{\gamma}{a^3} \langle R_{n3}(r)\Phi(r)\rangle_r \langle \psi_{1\mathrm{s}}(r) R_{n3}(r) j_3(qr)\rangle_r F(\boldsymbol{\xi}) \,. \quad \text{(D.20)}$$

Here $\Phi = (1 + 3a/r + 3a^2/r^2)\psi_{1\mathrm{s}}$, j_3 is the spherical Bessel function of the third order, $F(\boldsymbol{\xi}) = \xi_x(\xi_y^2 - \xi_z^2) + i\xi_y(\xi_z^2 - \xi_x^2)$, and $\boldsymbol{\xi} = \mathbf{q}/q$. Angular brackets with the subscript r denote integration over r, i.e. $\langle f_1(r) f_2(r)\rangle_r = \int r^2 f_1 f_2 dr$. Equation (D.20) is obtained using the decomposition of $e^{i\mathbf{qr}}$ over the spherical harmonics, Eqs. (D.1) and orthogonality of Y_l^m with respect to m.

The spin-flip rate calculated according to Eqs. (5.7) and (D.19) has a form:

$$\frac{1}{T_1} = \frac{32\pi}{105^2} \frac{(\gamma e h_{14})^2}{\rho \hbar^8 (\mathcal{E}_{Ry}^*)^4} S^2 (g\mu B)^9 \sum_\alpha \frac{1}{s_\alpha^9} \left\langle |F(\boldsymbol{\xi})|^2 a_{\mathbf{q},\alpha}^2 \right\rangle_\Omega \,, \quad \text{(D.21)}$$

where $a_{\mathbf{q},\alpha} = A_{\mathbf{q},\alpha}/h_{14}$, $\langle \ldots \rangle_\Omega$ denotes an average over the angles θ_q and ϕ_q of $\mathbf{q}$, and

$$S = \sum_{n \geq 4} \frac{1}{\left(1 - E_{n\mathrm{f}}/\mathcal{E}_{Ry}^*\right)^2} \left\langle R_{n3}\Phi \right\rangle_r \left\langle \psi_{1\mathrm{s}} \bar{r}^3 R_{n3} \right\rangle_r \quad \text{(D.22)}$$

is the dimensionless sum over all excited states with different n (including the states of the continuous spectrum) and $\bar{r} = r/a_B^*$. In the evaluation of Eq. (D.21) we used the long wavelength approximation for phonons by using the asymptotic $j_3(qr) \approx (qr)^3/105$ at $qr \ll 1$.

For longitudinal acoustic phonons, $\hat{\mathbf{e}}^{(\mathbf{q},l)} = \boldsymbol{\xi}$, and hence

$$\left\langle |F(\boldsymbol{\xi})|^2 a_{\mathbf{q},\alpha}^2 \right\rangle_\Omega = \frac{96}{5005} \,. \quad \text{(D.23)}$$

For transverse acoustic modes, the polarization vectors satisfy $\langle \hat{e}_i^{(\mathbf{q},t)} \hat{e}_j^{(\mathbf{q},t)} \rangle = (\delta_{ij} - \xi_i \xi_j)/2$. Considering that there are two transverse modes, we obtain

$$\left(\sum_{i,j,k} \beta_{ijk} \xi_i \xi_j \hat{e}_k^{(\mathbf{q},t)} \right)^2 = 4(\xi_x^2 \xi_y^2 + \xi_x^2 \xi_z^2 + \xi_y^2 \xi_z^2 - 9\xi_x^2 \xi_y^2 \xi_z^2) \,,$$

and

$$\left\langle |F(\boldsymbol{\xi})|^2 a^2_{\mathbf{q},\alpha} \right\rangle_\Omega = \frac{2048}{45045} \,. \tag{D.24}$$

Using these averages one finally obtains for the spin relaxation rate

$$\frac{1}{T_1} = \zeta \frac{(\gamma e h_{14})^2}{\rho \hbar^8 (\mathcal{E}^*_{Ry})^4} S^2 (g\mu B)^9 \left[\frac{1}{s_l^9} + \left(\frac{4}{3}\right)^3 \frac{1}{s_t^9} \right] , \tag{D.25}$$

with $\zeta = 1024\pi/(1287 \times 35^3) \approx 0.000175$.

Let us now turn to the evaluation of the S parameter. It comprises the sum over the discrete spectrum (index n) and the integral over the continuum spectrum (index η):

$$S = \sum_{n=4}^{+\infty} \frac{1}{(1-1/n^2)^2} \left\langle R_{n3}\Phi \right\rangle_r \left\langle \psi_{1s} \bar{r}^3 R_{n3} \right\rangle_r + \int_0^{+\infty} \frac{\left\langle R_{\eta 3}\Phi \right\rangle_r \left\langle \psi_{1s} \bar{r}^3 R_{\eta 3} \right\rangle_r}{(1+\eta^2)^2} d\eta \,. \tag{D.26}$$

Matrix elements entering Eq. (D.26) are calculated analytically using formulas (f,1) and (f,2) of Ref. [129]:

$$\begin{aligned} \left\langle \psi_{1s} \bar{r}^3 R_{n3} \right\rangle_r &= \frac{96}{\sqrt{\pi} n^5} \sqrt{\frac{(n+3)!}{(n-4)!}} \frac{(1-1/n)^{n-5}}{(1+1/n)^{n+5}} , \\ \left\langle \psi_{1s} \bar{r}^3 R_{\eta 3} \right\rangle_r &= \frac{96}{\sqrt{\pi}} \left(\frac{\eta}{1-e^{-2\pi/\eta}} \right)^{1/2} \sqrt{\prod_{s=1}^{3} (s^2\eta^2+1)} \frac{(1-i\eta)^{-i/\eta-5}}{(1+i\eta)^{-i/\eta+5}} , \end{aligned} \tag{D.27}$$

and

$$\begin{aligned} \left\langle R_{n3}\Phi \right\rangle_r &= \frac{16}{7!\sqrt{\pi} n^5} \sqrt{\frac{(n+3)!}{(n-4)!}} \sum_{\nu=4,5,6} c_\nu \frac{(\nu-1)!}{(1+1/n)^\nu} {}_2F_1 \left(4-n, \nu, 8, \frac{2}{n+1} \right) , \\ \left\langle R_{\eta 3}\Phi \right\rangle_r &= \frac{16}{7!\sqrt{\pi}} \left(\frac{\eta}{1-e^{-2\pi/\eta}} \right)^{1/2} \sqrt{\prod_{s=1}^{3} (s^2\eta^2+1)} \\ &\quad \cdot \sum_{\nu=4,5,6} c_\nu \frac{(\nu-1)!}{(1+i\eta)^\nu} {}_2F_1 \left(\frac{i}{\eta}+4, \nu, 8, \frac{2i\eta}{1+i\eta} \right) . \end{aligned} \tag{D.28}$$

Here $c_4 = 3$, $c_5 = 3$, $c_6 = 1$, and ${}_2F_1$ is the ordinary hypergeometric function. Using

these matrix elements, a numerical summation in Eq. (D.26) is performed yielding $S \approx 0.487$. To analyze the contribution of the excited states we provide two estimates for S: $S_{\rm low} < S < S_{\rm up}$. Here the lower limit ($S_{\rm low}$) is the first term in the sum with $n = 4$, and the upper limit ($S_{\rm up}$) is the sum over a complete set of functions $\{R_{n3}, R_{\eta 3}\}$ with a fixed denominator equal to an energy distance between the 4f and 1s state:

$$S_{\rm low} = \frac{256}{225} \left\langle {\rm R}_{43}\Phi \right\rangle_r \left\langle \psi_{1{\rm s}}\bar{r}^3{\rm R}_{43} \right\rangle_r \approx 0.006 \, , \tag{D.29}$$

$$S_{\rm up} = \frac{256 \left\langle \Phi\bar{r}^3\psi_{1{\rm s}} \right\rangle_r}{225} \approx 1.9 \, . \tag{D.30}$$

Noteworthy, S exceeds $S_{\rm low}$ by more than two orders of magnitude, demonstrating the importance of accounting for all excited states of the spectrum. However, for highly excited states the LWA breaks down which somehow reduces the estimate of S. Moreover, for the experimental donor densities the overlap of states with large $n \gtrsim 5$ belonging to different donors is not negligible. The account for such an overalap is beyond the scope of the present paper.

Equation (D.25) was derived assuming that the Zeeman splitting dominates the orbital B-linear splitting of the excited states with opposite values of m. Such an approximation works well in quantum dot systems where the dot anisotropy lifts the degeneracy in m. For the donor-bound electron this is not the case, since the problem (at $B = 0$) has a spherical symmetry. In this situation, the splitting of the nf states with m and $-m$ is $|m|\hbar\omega_c \gg g\mu B$. To estimate T_1 in this case one should replace $(g\mu B)^9$ in Eq. (D.25) by $(g\mu B)^7(\hbar\omega_c)^2$ in agreement with Eq. (5.13) in the main text.

D.6 Spin relaxation via the direct spin-phonon mechanism

D.6.1 General expression for the direct spin-phonon spin-relaxation rate

The direct spin-phonon interaction Hamiltonian [58, 151, 71] is

$$U_{dir} = \frac{\hbar v_0}{2}[\sigma_x(u_{xy}k_y - u_{xz}k_z) + \sigma_y(u_{yz}k_z - u_{xy}k_x)], \tag{D.31}$$

where we ignore the σ_z term because it does not contribute to spin relaxation, $\mathbf{k} = -i\boldsymbol{\nabla} - (e/\hbar)\mathbf{A}$, and we use the symmetric gauge $\mathbf{A} = (-By/2, Bx/2, 0)$. The

deformation tensor u_{ij} due to phonon $\mathbf{q}, \alpha$ is

$$u_{ij}^{\mathbf{q},\alpha} = \sqrt{\frac{\hbar}{2\rho\omega_{\mathbf{q},\alpha}}} e^{i(\mathbf{qr}-\omega_{\mathbf{q},\alpha}t)} \frac{i(\hat{e}_i^{(\mathbf{q},\alpha)} q_j + \hat{e}_j^{(\mathbf{q},\alpha)} q_i)}{2} b_{\mathbf{q},\alpha}^{\dagger} + \text{c.c.} \tag{D.32}$$

where $\boldsymbol{e}_\alpha$ is the polarization of phonon mode α:

$$\begin{aligned} \mathbf{e}_l &= q^{-1}[q_x, q_y, q_z], \\ \mathbf{e}_{t_1} &= (q_x^2 + q_y^2)^{-1/2}[q_y, -q_x, 0], \\ \mathbf{e}_{t_2} &= q^{-1}(q_x^2 + q_y^2)^{-1/2}[q_x q_z, q_y q_z, -(q_x^2 + q_y^2)]. \end{aligned} \tag{D.33}$$

Subscripts t_1 and t_2 denote two degenerate transverse modes. The relaxation rate $\Gamma_{\downarrow\uparrow}$ is found from Eq. (5.8) using

$$M_{\downarrow\uparrow} = \langle 1\text{s}, \downarrow | U_{dir} | \, 1\text{s}, \uparrow \rangle \ . \tag{D.34}$$

According to the general principles of quantum mechanics, the momentum operator and deformation tensor in Eq. (D.31) must be symmetrized, i.e. $u_{ij} k_l \to \{u_{ij}, k_l\}$, where $\{a, b\} = (ab + ba)/2$ [116, 207, 101]. Due to this symmetrization and the fact that the ground state is a localized state, all terms with k_z integrate to zero. Further simplifications yield

$$\begin{aligned} \langle 1\text{s}, \downarrow | U_{dir} | 1\text{s}, \uparrow \rangle = i \frac{\hbar v_0}{4} \sqrt{\frac{\hbar}{2\rho\omega_{\mathbf{q},\alpha}}} \left(\hat{e}_x^{(\mathbf{q},\alpha)} q_y + \hat{e}_y^{(\mathbf{q},\alpha)} q_x \right) \times \\ \left[\langle 1\text{s} | \{ \exp(i\mathbf{qr}), k_y \} | 1\text{s} \rangle - i \langle 1\text{s} | \{ \exp(i\mathbf{qr}), k_x \} | 1\text{s} \rangle \right], \end{aligned}$$

$$\begin{aligned} \langle 1\text{s} | \{ \exp(i\mathbf{qr}), k_x \} | 1\text{s} \rangle &= \frac{eB}{2\hbar} \langle 1\text{s} | \exp(i\mathbf{qr}) y | 1\text{s} \rangle \ , \\ \langle 1\text{s} | \{ \exp(i\mathbf{qr}), k_y \} | 1\text{s} \rangle &= -\frac{eB}{2\hbar} \langle 1\text{s} | \exp(i\mathbf{qr}) x | 1\text{s} \rangle \ . \end{aligned} \tag{D.35}$$

Substituting Eq. (D.34) into Eq. (5.7) and taking the phonon factor F_{ph} into consideration, we obtain the general expression for the spin-relaxation rate

$$\frac{1}{T_1} = F_{ph} \frac{v_0^2 e^2 B^2}{2^9 \pi^2 \hbar \rho} \sum_\alpha \frac{q_\alpha^3}{s_\alpha^2} \int d\Omega_q \left| \left(\hat{e}_x^{\mathbf{q},\alpha} \xi_y + \hat{e}_y^{\mathbf{q},\alpha} \xi_x \langle \, 1\text{s} | \exp(i\mathbf{q}_\alpha \mathbf{r})(x - iy) | 1\text{s} \rangle \right|^2 , \tag{D.36}$$

which can be evaluated either numerically or using an analytic approximation.

D.6.2 Numerical calculation of direct spin-phonon spin-relaxation rate

Similar to Appendix D.5.2, the azimuthal part of the integral $\langle 1\mathrm{s}|\exp(i\mathbf{q}_\alpha\mathbf{r})(x-iy)|1\mathrm{s}\rangle$ can be calculated analytically to simplify the numerical calculation. We introduce the notation for this matrix element:

$$\kappa_\alpha(\theta_q) = e^{i\phi_q}\langle 1\mathrm{s}|e^{i\mathbf{q}_\alpha\mathbf{r}}(x-iy)|1\mathrm{s}\rangle,$$

and obtain

$$\kappa_\alpha(\theta_q) = 4\pi\int_0^\infty \rho^2\,d\rho\int_0^\infty dz\,\Phi_{1\mathrm{s}}^2(\rho,z)\cos(z\,q_\alpha\cos\theta_q)J_1(\rho\,q_\alpha\sin\theta_q)\,. \tag{D.37}$$

The simplified expression for the spin-relaxation rate is

$$\frac{1}{T_1} = F_{ph}\frac{\nu_0^2 e^2 B^2}{2^9\pi\hbar\rho}\int_0^\pi d\theta_q\,\sin^3\theta_q\left[\sin^2\theta_q\frac{q_l^3}{s_l^2}|\kappa_l|^2 + (1+\cos^2\theta_q)\frac{q_t^3}{s_t^2}|\kappa_t|^2\right]\,, \tag{D.38}$$

which can be calculated numerically using standard procedures.

D.6.3 Analytic calculation of direct spin-phonon spin-relaxation rate

To derive an analytical result we use trial wavefunctions of a Gaussian or exponential form. First, we approximate the ground state wave function by a Gaussian

$$\psi_{1\mathrm{s}} = \frac{1}{(\sqrt{\pi}l)^{3/2}}e^{-r^2/(2l^2)}, \tag{D.39}$$

with $l = [1/(a_B^*)^2 + 1/(2l_b^2)]^{-1/2}$. The matrix element can be found analytically,

$$\langle 1\mathrm{s}|\exp(i\mathbf{q}\mathbf{r})r_j|1\mathrm{s}\rangle = \frac{1}{2}iq_j l^2 e^{-q^2l^2/4}\,, \tag{D.40}$$

where $j = x, y$.

Using Eqs. (5.7), (D.34) we obtain the relaxation rate assuming that the spin-up

state has a higher energy as compared with the spin-down one

$$\Gamma_{\downarrow\uparrow} = \frac{(N_{ph}+1)v_0^2}{256\pi\rho\hbar}(eBl^2)^2\sum_\alpha \frac{(g\mu B)^5}{\hbar^5 s_\alpha^7} I_\alpha e^{-q_\alpha^2 l^2/2}, \tag{D.41}$$

$$I_\alpha = \left\langle \left(\hat{e}_x^{\mathbf{q},\alpha}\xi_y + \hat{e}_y^{\mathbf{q},\alpha}\xi_x\right)^2 \xi_x^2 \right\rangle_\Omega . \tag{D.42}$$

The integrals over phonon angle for the longitudinal and both transverse modes are $I_l = 4/35$ and $I_t = 16/105$. Taking into account the phonon factor F_{ph}, the final result for the relaxation rate by the direct spin-phonon process is

$$\frac{1}{T_1} = \frac{1}{2240\pi}\frac{(ev_0 l^2)^2(g\mu)^5 B^7}{\rho\hbar^6}\left(\frac{e^{-q_l^2 l^2/2}}{s_l^7} + \frac{4e^{-q_t^2 l^2/2}}{3s_t^7}\right) F_{ph} . \tag{D.43}$$

Another possible choice of wave function for the donor-bound electron is an exponential

$$\psi_{1\mathrm{s}} = \frac{1}{\sqrt{\pi l^3}} e^{-r/l}. \tag{D.44}$$

For this wave function,

$$\langle 1\mathrm{s}|\exp(i\mathbf{qr}) r_j|1\mathrm{s}\rangle = \frac{i\, l^2 q_j}{(1+q^2l^2/4)^3} . \tag{D.45}$$

The relaxation rate using an exponential wave function is the same as Eq. (D.43) with $\exp(-q_\alpha^2 l^2/2)$ replaced by $4/(1+q_\alpha^2 l^2/4)^6$, in agreement with Eq. (5.17) of the main text.

We note that in the presence of a magnetic field the form of the donor-bound electron functions depends on the gauge, which calls for special care in evaluating the matrix elements in Eq. (D.35). Particularly, Eqs. (D.39) and (D.44) are valid in the symmetric gauge. For instance, in the Landau gauge, where $\mathbf{A} = (0, Bx, 0)$, Eqs. (D.39) and (D.44) acquire extra phase factors $\exp[ieBxy/(2\hbar)]$. Taking these phase factors into account one can readily check that Eqs. (D.35) and, correspondingly, Eqs. (D.41), (D.43) and (5.17) are gauge invariant.

Appendix E

NUMERICAL MODELING OF TIME AND POLARIZATION-RESOLVED A^0X PHOTOLUMINESCENCE

E.1 Density matrix model for time-resolved photoluminescence

The time evolution of the excited state density matrix ρ is described by

$$\frac{d\rho}{dt} = \frac{1}{i\hbar}[H_o, \rho] - \frac{1}{2}\left\{\rho, \alpha \mathbf{p}^{\dagger} \cdot \mathbf{p}\right\} + L(\rho) \tag{E.1}$$

where H_o is a diagonal matrix of the energies of the excited state energies, $\mathbf{p}$ is the dipole matrix with elements $\mathbf{p}_{ij} = \langle g, i| \boldsymbol{\mu} |e, j\rangle$ and $L(\rho)$ is the Linbladian operator. The first term describes unitary evolution, the second term spontaneous emission and the third excited state relaxation and decoherence. In this section, we describe the construction of this model.

A population transfer out of the system is mathematically identical to the spontaneous emission process in the excited state subspace. Population reduction can be accomplished mathematically using an anti-commutator $\{A, B\} = AB + BA$ [170]. The spontaneous emission process is characterized by the decay of diagonal density matrix terms in the basis of the spontaneous emission eigenstates:

$$\left(\frac{d\rho}{dt}\right)_{\text{radiative}} = -\frac{1}{2}\sum_{j} \left\{\rho, \gamma_j \left|\phi_j\right\rangle \left\langle\phi_j\right|\right\}, \tag{E.2}$$

where γ_j and $|\phi_j\rangle$ are the spontaneous emission eigenvalues and eigenstates of αS. Using the fact that any operator is diagonal in the basis of it's eigenvectors, this becomes

$$\left(\frac{d\rho}{dt}\right)_{\text{radiative}} = -\frac{\alpha}{2}\left\{\rho, S\right\},$$

Numerically, it is an advantage to include spontaneous emission in this way as the ground states do not need to be included in the density matrix. For A^0X, the excited

state density matrix has 56 differential equations (ignoring off diagonal terms between non-degenerate excited states), whereas a treatment using the full density matrix including ground states would have 120.

Phenomenological relaxation between the excited states is included as a population transfer and decoherence. The excited state relaxation rate R_{ij} from state i to j arises from coupling between the spins and their environment. This model includes an intralevel relaxation rate between states in a degenerate manifold, and an interlevel rate between different manifolds. For i and j in different manifolds, the rates are modulated by the energy difference between the initial and final states,

$$R_{ij} \propto R_o e^{-\frac{(E_i - E_j)}{2k_B T}},$$

where R_o is the interlevel relaxation rate. This correctly reproduces the fact that in equilibrium the ratio of populations in different states is given by a Boltzmann factor. Many of the rates R_{ij} from states in the same irreducible representation Γ_n can be shown to be the same by symmetry. For the purposes of this model, we assumed that all states within a given irreducible representation Γ_n have the same phenomenological relaxation rate.

Phenomenological relaxation affects both the on- and off-diagonal elements of the density matrix. The total rate of population leaving (L_i) or entering (E_i) state i is

$$L_i = \rho_{ii} \sum_j R_{ij}, \quad E_i = \sum_j \rho_{jj} R_{ji}.$$

This population relaxation also causes a decay of the off-diagonal terms in the density matrix. This can be accomplished with the anti-commutator:

$$L(\rho) = -\frac{1}{2} \sum_j (L_i \delta_{ij} \rho_{jk} + \rho_{ij} L_j \delta_{jk}) + E_i \delta_{ik} \tag{E.3}$$

where the second term enforces conservation of excited state population.

E.2 Fit of time resolved data to model

We numerically integrated the equation of motion Eq. E.1 to find the excited state density matrix as a function of time $\rho(t)$. In the case that Γ_n is excited with polar-

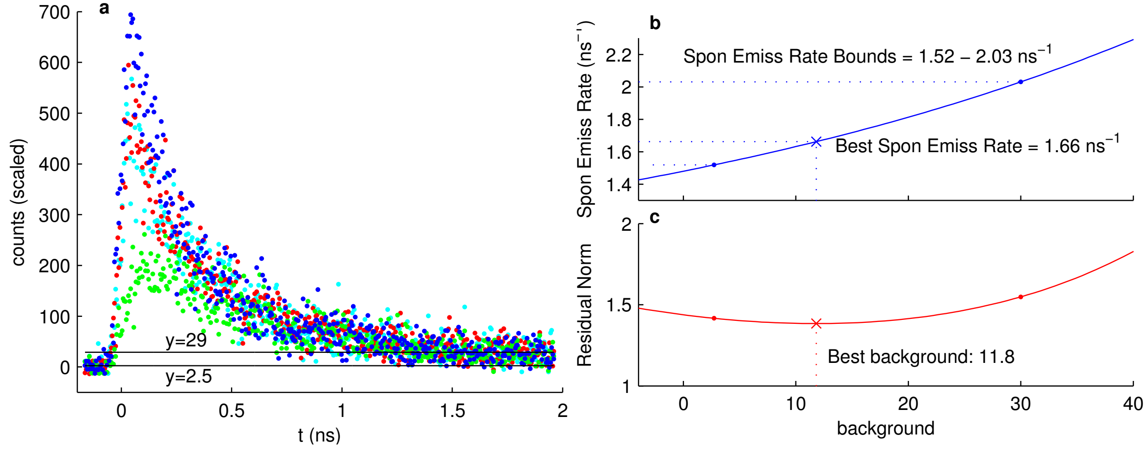

Figure E.1: **a.** Raw data before binning used for time-resolved experiment. Before the pulse arrives, the mean background level is 2.5 ± 0.6 counts. At the end of the trace at 2 ns, the mean level is 29 ± 6, which is somewhat higher than the theory would predict. **b-c.** Best fit spontaneous emission rate as a function of background level in the model. The best fit background value lies in between the limits chosen by inspection in a. These limits are used to find the uncertainty in the spontaneous emission rate due to the background level.

ization $\hat{\epsilon}_{\mathrm{i}}$, the initial density matrix in the Γ_n subspace is

$$\rho_e^{(\Gamma_n)}(t=0) = M_{\epsilon_{\mathrm{i}}}^{(\Gamma_n)\dagger} M_{\epsilon_{\mathrm{i}}}^{(\Gamma_n)}, \tag{E.4}$$

where $M_{\epsilon_{\mathrm{i}}}^{(\Gamma_n)} = \mathbf{p}^{(\Gamma_n)} \cdot \hat{\epsilon}_{\mathrm{i}}$ and all other terms of the density matrix are zero. From the solution of the density matrix as a function of time $\rho_e(t)$, the PL emitted from Γ_n at polarization $\hat{\epsilon}_{\mathrm{f}}$ as a function of time is

$$\mathrm{PL}^{(\Gamma_n)}(t) = \mathrm{tr}\left(M_{\epsilon_{\mathrm{f}}}^{(\Gamma_n)} \rho_e^{(\Gamma_n)}(t) M_{n\epsilon_{\mathrm{f}}}^{(\Gamma_n)\dagger}\right). \tag{E.5}$$

These PL curves predict the time dependence of A^0X emission under different excitation conditions.

The model was fit to the data using a weighted least-squares residual due to the Poisson distributed nature of photon counting data [195]. Temperature was included as a fit parameter because in individual fits with $T = 1.9$ K, the best fit $\Gamma_3 \rightarrow \Gamma_5$ relaxation rate depended on the excitation state. This implies that the effective exci-

ton temperature was higher than 1.9 K, consistent with experiments on free excitons in GaAs where the effective temperature of free excitons was found to be somewhat higher than that of the bath [163].

We tested modifying the relaxation rate matrix R_{ij} so that electron spin flips can occur. In this case, the model also fits the data with different rates of interstate relaxation: interlevel relaxation (0.45 ns^{-1}), intralevel Γ_3 relaxation (1.2 ns^{-1}) and intralevel Γ_5 relaxation (0.71 ns^{-1}). Because we obtain good fits with either electron spin flips allowed or disallowed, the experiment is not sensitive to the rate of electron spin flips. However, the best fit spontaneous emission rate constant was the same 1.48 ns^{-1} regardless of whether electron spin flips are allowed.

In order to estimate the uncertainty in the the measured spontaneous emission rate, we characterized the uncertainty due to random Poisson noise in the measurement data as well as systematic error due to the uncertainty in model parameters (e.g. pulse arrival time, background level). The largest uncertainty in measured spontaneous emission rate arises from the uncertainty of background level (Tab. E.1). The raw data shown in Fig. E.1 shows that there is a long lived emission above the background. This long lived emission may indicate some long lived state, e.g. exciton hopping into a metastable state and subsequent slow repopulation. Due to the uncertainty of the true background value, the A^0X best fit parameters acquire some uncertainty. Choosing a higher background level results in a faster best fit spontaneous emission rate, as the effective curvature of the decay becomes greater (Fig. E.1). We take the confidence interval of the background level to be 0 to 30, this produces an uncertainty in spontaneous emission rate of ± 0.26 ns^{-1} (Fig. E.1). Another way to estimate this uncertainty would be to incorporate a metastable excitonic level in the model. Because this introduces the danger of overfitting the model with too many adjustable parameters, we used the background level as a proxy for the uncertainty introduced by possible metastable states.

Next, we investigated whether changing the maximum number of data points collected (1-2 ns) modified the best fit spontaneous emission rate. In fitting the data, there is a somewhat arbitrary choice of when additional data points at longer times no longer improve the fit. Within reasonable choices of the data time cut-off of 1-2 ns, we found that the best fit spontaneous emission rate changed from 1.36 to 1.66 ns^{-1}. This level of uncertainty is lower than that present from the unknown background

Table E.1: Summary of uncertainties in measurement of the spontaneous emission rate.

Effect	Uncert. (±) in Spon. Emission
Background Level	0.26 ns^{-1}
Data Cut Off	0.15 ns^{-1}
Poisson Noise	0.0082 ns^{-1}
5% Laser Power Fluctuations	0.0047 ns^{-1}

level.

Next, we used a Monte Carlo simulation to determine the uncertainty in spontaneous emission due to Poisson noise. The raw data was used as the mean for new Poisson-distributed datasets. The model was fit to the new random datasets using the same weighted least-squares algorithm. The standard deviation of the resultant spontaneous emission rates is 0.0082 ns^{-1}.

Monte Carlo simulations were also employed to calculate the uncertainty due to laser power fluctuations between experimental runs. The photon counting data was modulated by random 5% power fluctuations and passed through the least squares algorithm. We found the standard deviation of best fit spontaneous emission rates to be 0.0047 ns^{-1} due to power fluctuations of the laser. These simulations demonstrate that the measurement is robust against Poisson noise and laser power fluctuations.

In summary, we have found that the spontaneous emission rate for A^{0}X lies within the range 1.36 to 2.03 ns^{-1}. This corresponds to a lifetime constant in the range of 0.49 to 0.74 ns.

E.3 Polarization of PL to determine dominant coupling in A^{0}X

While the splitting of the A^{0}X states into three sets of states is now understood, it was at one point a subject of debate. Two theories, the $j-j$ coupling scheme (JJCS) and the crystal-field scheme (CFS) can be used to explain some of the optical properties of A^{0}X [108, 139]. In both schemes, hole-hole coupling first rearranges the two $j=\frac{3}{2}$ hole states into $j=0$ and $j=2$ manifolds. In the JJCS, electron-hole coupling further splits the A^{0}X states, resulting in $j=\frac{1}{2}$ (arising from $j=0$) and $\frac{3}{2}$, $\frac{5}{2}$ (from $j=2$). On the other hand in the CFS, GaAs crystal fields split the A^{0}X states into Γ_1 ($j=0$) and Γ_3, Γ_5 ($j=2$).

$\frac{1}{2}$	$\vert\frac{1}{2},-\frac{1}{2}\rangle$	$\vert\frac{1}{2},\frac{1}{2}\rangle$
$\langle -\frac{3}{2}\vert$	$\frac{1}{2}(\hat{\mathbf{x}}+i\hat{\mathbf{y}})$	0
$\langle -\frac{1}{2}\vert$	$-\frac{1}{2\sqrt{3}}\hat{\mathbf{z}}$	$-\frac{1}{4\sqrt{3}}(\hat{\mathbf{x}}+i\hat{\mathbf{y}})$
$\langle \frac{1}{2}\vert$	$-\frac{1}{4\sqrt{3}}(\hat{\mathbf{x}}-i\hat{\mathbf{y}})$	$\frac{1}{2\sqrt{3}}\hat{\mathbf{z}}$
$\langle \frac{3}{2}\vert$	0	$\frac{1}{2}(\hat{\mathbf{x}}-i\hat{\mathbf{y}})$

$\frac{3}{2}$	$\vert\frac{3}{2},-\frac{3}{2}\rangle$	$\vert\frac{3}{2},-\frac{1}{2}\rangle$	$\vert\frac{3}{2},\frac{1}{2}\rangle$	$\vert\frac{3}{2},\frac{3}{2}\rangle$
$\langle -\frac{3}{2}\vert$	$-\sqrt{\frac{2}{15}}\hat{\mathbf{z}}$	$-\frac{1}{2\sqrt{10}}(\hat{\mathbf{x}}+i\hat{\mathbf{y}})$	0	0
$\langle -\frac{1}{2}\vert$	$-\sqrt{\frac{2}{5}}(\hat{\mathbf{x}}-i\hat{\mathbf{y}})$	$\sqrt{\frac{2}{15}}\hat{\mathbf{z}}$	$\sqrt{\frac{2}{15}}(\hat{\mathbf{x}}+i\hat{\mathbf{y}})$	0
$\langle \frac{1}{2}\vert$	0	$-\sqrt{\frac{2}{15}}(\hat{\mathbf{x}}-i\hat{\mathbf{y}})$	$\sqrt{\frac{2}{15}}\hat{\mathbf{z}}$	$\sqrt{\frac{2}{5}}(\hat{\mathbf{x}}+i\hat{\mathbf{y}})$
$\langle \frac{3}{2}\vert$	0	0	$\frac{1}{2\sqrt{10}}(\hat{\mathbf{x}}-i\hat{\mathbf{y}})$	$-\sqrt{\frac{2}{15}}\hat{\mathbf{z}}$

$\frac{5}{2}$	$\vert\frac{5}{2},-\frac{5}{2}\rangle$	$\vert\frac{5}{2},-\frac{3}{2}\rangle$	$\vert\frac{5}{2},-\frac{1}{2}\rangle$	$\vert\frac{5}{2},\frac{1}{2}\rangle$	$\vert\frac{5}{2},\frac{3}{2}\rangle$	$\vert\frac{5}{2},\frac{5}{2}\rangle$
$\langle -\frac{3}{2}\vert$	$-\frac{1}{\sqrt{6}}(\hat{\mathbf{x}}-i\hat{\mathbf{y}})$	$\sqrt{\frac{6}{5}}\hat{\mathbf{z}}$	0	0	0	0
$\langle -\frac{1}{2}\vert$	0	$\frac{1}{\sqrt{10}}(\hat{\mathbf{x}}-i\hat{\mathbf{y}})$	$\sqrt{\frac{2}{15}}\hat{\mathbf{z}}$	$\sqrt{\frac{2}{15}}(\hat{\mathbf{x}}+i\hat{\mathbf{y}})$	0	0
$\langle \frac{1}{2}\vert$	0	0	$-\sqrt{\frac{2}{15}}(\hat{\mathbf{x}}-i\hat{\mathbf{y}})$	$\sqrt{\frac{2}{15}}\hat{\mathbf{z}}$	$\frac{1}{\sqrt{10}}(\hat{\mathbf{x}}+i\hat{\mathbf{y}})$	0
$\langle \frac{3}{2}\vert$	0	0	0	0	$-\sqrt{\frac{6}{5}}\hat{\mathbf{z}}$	$-\frac{1}{\sqrt{6}}(\hat{\mathbf{x}}+i\hat{\mathbf{y}})$

Table E.2: Normalized dipole matrix $(\mathbf{p}_{ij})^{\text{JJCS}} = \left\langle \text{A}^0, i\right| \boldsymbol{\mu} \left|\text{A}^0\text{X}, j\right\rangle$ for the A^0X-A^0 system in the (incorrect) JJCS. $\hat{\mathbf{x}}$, $\hat{\mathbf{y}}$ and $\hat{\mathbf{z}}$ are unit vectors oriented along the crystallographic axes.

In previous studies, the stress dependence of $\text{A}^0\text{X} \rightarrow \text{A}^0$ emission was used to determine that only the CFS adequately describes the A^0X [108, 139]. Low temperature stress dependencies are challenging experiments, requiring the use of special equipment. In this section, we demonstrate that simple polarization measurements can also distinguish between the JJCS and CFS.

In order to predict the polarization dependence of A^0X in the JJCS, we first calculate the dipole matrix elements using the JJCS basis states by the procedure in Sec. B.2. The dipole matrix elements are given in Tab. E.2.

We will now calculate the polarization dependence of the PL intensity in the case of no excited state relaxation for Γ_3 (CFS). When A^0X absorbs a photon resonant with the Γ_3 transition, the excited state density matrix is proportional to

$$\rho_e^{(\Gamma_3)} = M_{\epsilon_{\text{i}}}^{(\Gamma_3)\dagger} \rho_0 M_{\epsilon_{\text{i}}}^{(\Gamma_3)}, \tag{E.6}$$

where $\rho_0 = \frac{1}{4}I$ is the ground state density matrix before excitation and $M_{\Gamma_3,\epsilon_{\text{i}}} = \mathbf{p}_{(\Gamma_n)} \cdot \hat{\epsilon}_i$ are the dipole matrix elements given in Tab. B.1 evaluated with the polarization $\epsilon_i = \cos\phi_{\text{i}}\hat{\mathbf{x}} + \sin\phi_{\text{i}}\hat{\mathbf{y}}$ in the $x - y$ plane. After absorption, the part of the excited

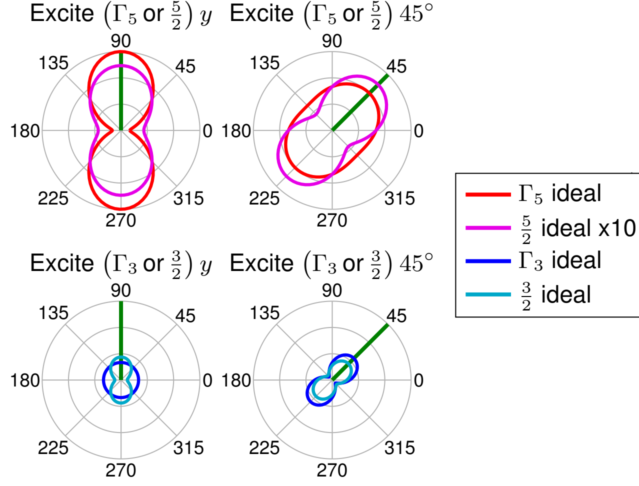

Figure E.2: Comparison of polarization dependence of photoluminescence for the JJCS and CFS. Qualitatively different behavior is observed when exciting $\Gamma_3\, y$ or $\frac{3}{2}\, y$. This difference can be used to determine the validity of the CFS for describing A^0X.

state density matrix corresponding to Γ_3 is

$$\rho_e^{(\Gamma_3)} = \begin{pmatrix} \frac{1}{12} & 0 & -\frac{i\sin(2\phi_\mathrm{i})}{8\sqrt{3}} & 0 \\ 0 & \frac{1}{12} & 0 & -\frac{i\sin(2\phi_\mathrm{i})}{8\sqrt{3}} \\ \frac{i\sin(2\phi_\mathrm{i})}{8\sqrt{3}} & 0 & \frac{1}{12} & 0 \\ 0 & -\frac{i\sin(2\phi_\mathrm{i})}{8\sqrt{3}} & 0 & \frac{1}{12} \end{pmatrix}$$

with all other excited state density matrix elements equal to zero. (Here we are working in the crystal field scheme basis.) To find the amount of PL emitted with linear polarization $\epsilon_\mathrm{f} = \cos\phi_\mathrm{f}\hat{\mathbf{x}} + \sin\phi_\mathrm{f}\hat{\mathbf{y}}$, we evaluate

$$\mathrm{PL}^{(\Gamma_3)} = \mathrm{tr}\left(M_{\epsilon_\mathrm{f}}^{(\Gamma_3)}\,\rho_e\,M_{\epsilon_\mathrm{f}}^{(\Gamma_3)\dagger}\right).$$

Simplifying, and repeating this procedure for Γ_1 and Γ_5, the angular dependence of

polarization in the case of no excited relaxation is

$$\begin{aligned}
\mathrm{PL}^{(\Gamma_5)} &= \frac{I_o}{18}[5 + 4\cos(2\phi_\mathrm{i})\cos(2\phi_\mathrm{f}) + \sin(2\phi_\mathrm{i})\sin(2\phi_\mathrm{f})] \\
\mathrm{PL}^{(\Gamma_3)} &= \frac{I_o}{36}[4 + 3\sin(2\phi_\mathrm{i})\sin(2\phi_\mathrm{f})] \\
\mathrm{PL}^{(\Gamma_1)} &= \frac{I_o}{18}.
\end{aligned}$$

On the other hand, if the JJCS dipole operator (Tab. E.2) is used, the PL from the three manifolds is

$$\begin{aligned}
\mathrm{PL}^{(5/2)} &= I_o\left[\frac{1}{36} + \frac{1}{75}\cos(2\phi_\mathrm{f} - 2\phi_\mathrm{i})\right] \\
\mathrm{PL}^{(3/2)} &= I_o\left[\frac{533}{5760} + \frac{4}{75}\cos(2\phi_\mathrm{f} - 2\phi_\mathrm{i})\right] \\
\mathrm{PL}^{(1/2)} &= I_o\frac{169}{4608}.
\end{aligned}$$

The two coupling schemes show qualitatively different angular polarization dependences, shown in Fig. E.2. By comparing with the experimental data shown in Fig. 2.4(a) in the main text, we conclude that only the CFS adequately describes the angular dependence of A^0X photoemission.

E.4 Photoluminescence Excitation Spectroscopy of A^0X

The A^0X system is a remarkably homogeneous excitonic system. To investigate the inhomogeneous broadening of the A^0X system, we perform photoluminescence excitation (PLE) spectroscopy on a p-type GaAs sample mounted in a cold-finger cryostat at 4.2 K. The method of mounting the sample introduced some strain into the sample, which splits the heavy hole (HH) and light hole (LH) states. A narrow band (<10 neV) continuous-wave laser is scanned over the A^0-1s to A^0X transition while monitoring PL from A^0X to A^0-2s (Fig. E.3).

We fit the PLE lines to a sum of five Voigt functions, the convolution of a Lorentzian and a Gaussian. The Lorentzian width is due to homogeneous effects while the Gaussian width arises from inhomogeneous broadening. In the fit, the inhomogeneous broadening is the same for all peaks. The best fit Lorentzian full width at half maximum are $(39 \pm 2)\,\mu$eV for Γ_3-HH, $(43 \pm 2)\,\mu$eV for Γ_3-LH, $(29 \pm 2)\,\mu$eV

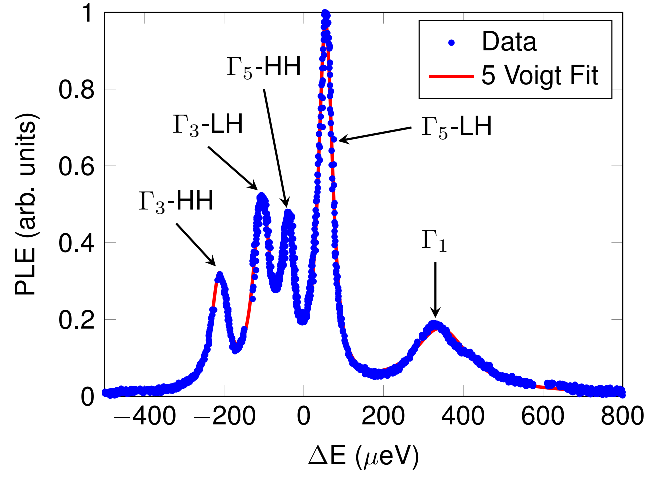

Figure E.3: Photoluminescence excitation spectroscopy of A^0X. The method of mounting the sample introduces strain, which splits the heavy-hole and light-hole ground states. A linear offset due to donor acceptor pair emission was subtracted for clarity. The curve was fit to a sum of five Voigt functions.

for Γ_5-HH, $(33 \pm 1)\,\mu$eV for Γ_5-LH and $(170 \pm 7)\,\mu$eV for Γ_1. The inhomogeneous broadening full width at half maximum was $(19 \pm 1)\,\mu$eV. Thus we find that A^0X is a remarkably homogeneous excitonic system.

Appendix F

DETAILS OF STACKING FAULT EXPERIMENTS AND THEORY

F.1 Stacking Fault formation

Stacking fault (SF) structures can grow from the substrate-epilayer interface during epitaxial growth [106, 41]. In the present work, SFs form in a 10 μm GaAs layer grown by molecular beam epitaxy with room temperature electron density $n \sim 1.9 \times 10^{14}$ cm^{-3} and mobility ~ 7400 cm^2/Vs. The entire structure consists of the 10 μm GaAs layer on 100 nm AlAs on a 5 nm/5 nm AlAs/GaAs (10$\times$) superlattice grown directly on a semi-insulating (100) GaAs vertical gradient freeze substrate (Wafer Technology Ltd), started with AlAs. The sample was grown at a pyrometer temperature of 600°C with the relatively low As_4 beam equivalent pressure of 8×10^{-6} Torr, measured by a flux tube. The growth rate was 0.7 ML/s for the GaAs and 0.35 ML/s for the AlAs. Oxide removal before growth was performed at 620°C under As flux. This growth procedure resulted in oval defects in the sample surface, a feature commonly associated with stacking faults [114, 106, 85, 41]. We observe two types of stacking fault defects, a SF pyramid and a SF pair defect, shown in Fig. F.1. The size of the pyramid structure (14.1 μm top edge in Fig. 3.1a) is consistent with stacking faults that nucleate near the substrate-epilayer interface and grow along $\{111\}$ planes through the 10 μm thick epilayer.

F.2 Stacking fault photoluminescence linewidth

Figure F.2 shows a high resolution PL spectrum of the SF. In order to extract the true PL linewidth, we need to take into account the spectral resolution of our setup. The spectrometer instrument resolution is found by taking a spectrograph of a narrow band Ti:Sapphire laser and fitting to a Voigt function, see Fig. F.3(a). We find that neither a Gaussian nor a Lorentzian accurately describe the spectral point spread function, so we use a Voigt fit. For spectral lines that are nearly as narrow as the

spectrometer FWHM (full width at half maximum), the measured FWHM will be wider than the true FWHM. Figure F.3(b) shows the FWHM of a line obtained by the convolution of a Lorentzian or Gaussian spectral lineshape with the spectrometer response function. For example, a measured linewidth of 94 μeV corresponds to a true linewidth of 72 or 82 μeV, depending on whether the true lineshape is assumed to be Lorentzian or Gaussian. Hence, to evaluate the intrinsic linewidth of the SF emission we fit the spectrum in Fig. F.2 with a weighted Lorentzian and use the deconvolution procedure [Fig. F.3(b)] to obtain an intrinsic PL linewidth of only (77 ± 19) μeV. Here, the uncertainty combines the original fit uncertainty and the uncertainty of the deconvolution procedure.

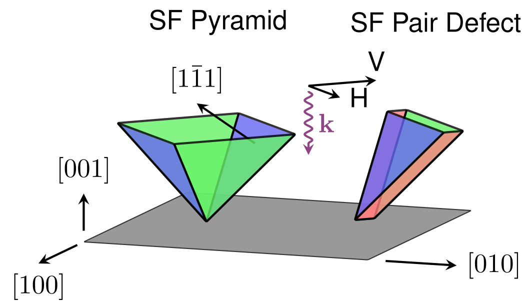

Figure F.1: Diagram showing the types of defects visible in the sample. The SF pyramid consists of four stacking faults arranged in a pyramid shape. The SF pair defect is a set of two SFs with a small ∼nm separation.

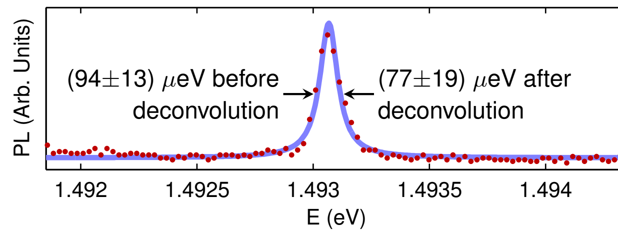

Figure F.2: High resolution PL spectrum of *up* SF. The FWHM of the line is (77 ± 19) μeV from a weighted Lorentzian fit, taking into account the instrument resolution. Before deconvolution the FWHM is (94 ± 13) μeV. Excitation at 1.65 eV, 1.44 K, 1.4 nW.

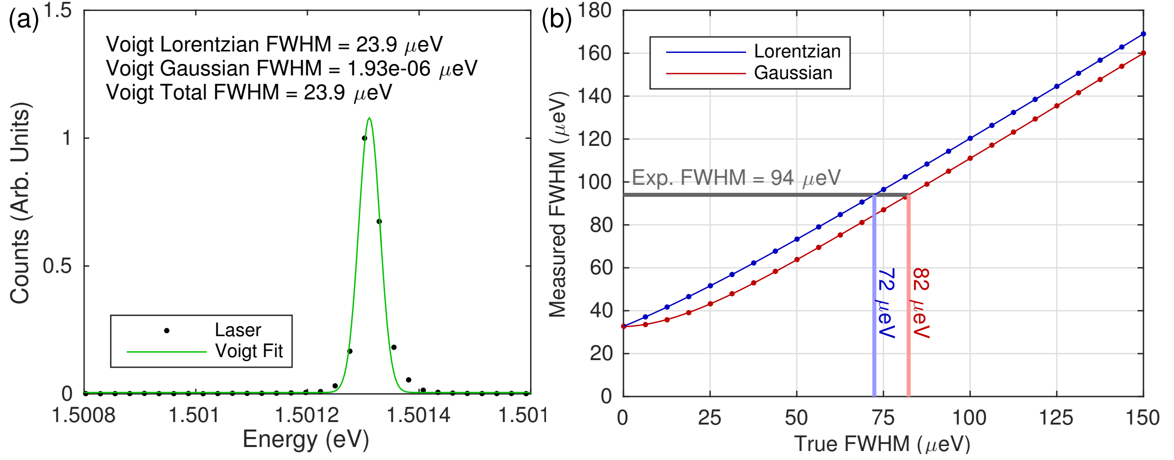

Figure F.3: (a) Spectrum of the narrow band Ti:Sapphire laser used to determine the spectrometer instrument resolution. The best fit is a Voigt function with a 32.7 μeV FWHM. The Voigt lineshape is the convolution of a Lorentzian and a Gaussian with best fit widths provided as an inset in the figure. (b) Convolution of the spectrometer instrument response in a with a Lorentzian or Gaussian lineshape. By interpolating backwards, the deconvoluted FWHM of a spectral line can be found.

F.3 Homogeneity of PL from the SF pyramid structure

Both the pyramid and pair defect (also called a trapezoid) show bright photoluminescence (PL) 20-30 meV below the GaAs band gap. We took PL spectra on 5 different pyramid structures and 28 different trapezoid structures (Fig. F.4). The PL linewidths of most trapezoid SF excitons are significantly larger than the linewidths of the pyramid SF excitons. In addition, the excitons from different trapezoid structures have different energy, while the excitons from different pyramid structure have almost identical energies. This high homogeneity between different pyramid structures is explained if the 4 SF planes in the pyramid are only single intrinsic or extrinsic SF planes.

In general, we observe PL from the trapezoid structure to be lower in energy compared to the pyramid structure (Fig. F.4a-b). This could be explained by a stronger binding energy of the excitons to the two SFs in the trapezoid structure compared to the one SF in the pyramid structure.

The emission lines for the 5 pyramid structures occur in two narrow bands at

(1495.92 ± 0.061) meV and (1492.82 ± 0.053) meV, where the emission energy is obtained using a Lorentzian fit and the uncertainty is the standard deviation over 5 different pyramid structures.

The observation of two distinct exciton energies over the 5 different pyramid structures is consistent with assigning the four SFs in a pyramid structure to intrinsic-extrinsic-intrinsic-extrinsic (i-e-i-e). Four of the pyramids observed have higher energy PL on the right and left SFs, while one pyramid has higher energy PL on the up and down SFs (Fig. F.4b and Fig. F.5). This demonstrates that the emission energy is not tied to the crystal axis. In addition, edge emission (colored red) is only observed on one of the five pyramid structures studied. For example, Fig. F.5 shows a confocal scan of a pyramid without edge emission.

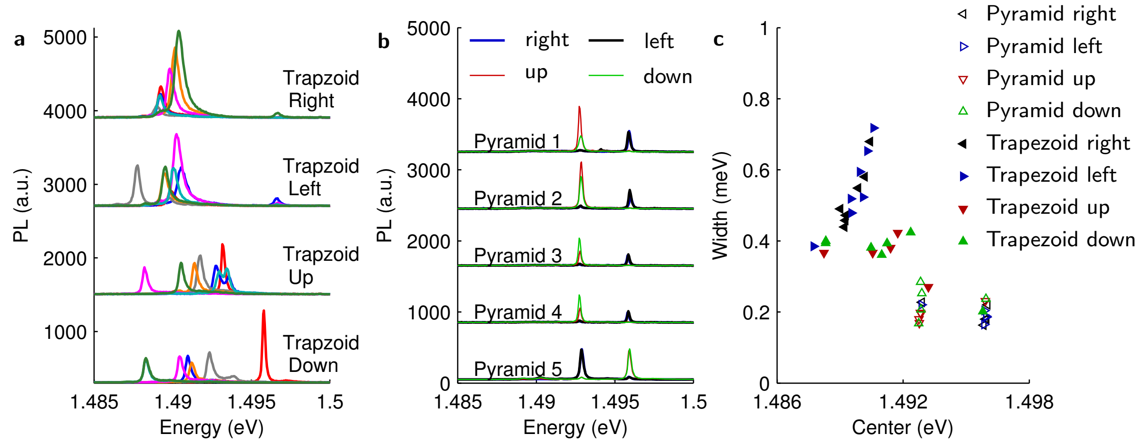

Figure F.4: **a**. Spectra for different SF trapezoid structures. Seven spectra were taken on each orientation of the trapezoid structure (right, left, up and down), shown in different colors. Excitation power 2 μW. Excitation energy 1.53 eV. 2 K. **b**. Spectra for 5 different pyramid structures, where the red (green) thin line represents the up (down) triangles, and the blue (black) thick line represents the right (left) triangles. **c**. Wavelength and FWHM of different SF structures obtained from a Lorentzian fit. As these spectra are taken on a lower resolution spectrometer grating, the FWHM here is larger than the result shown in Fig. F.12. The mean emission energy for the two types of SFs in the pyramid are (1.49283 ± 0.00006) eV and (1.49592 ± 0.00005)eV.

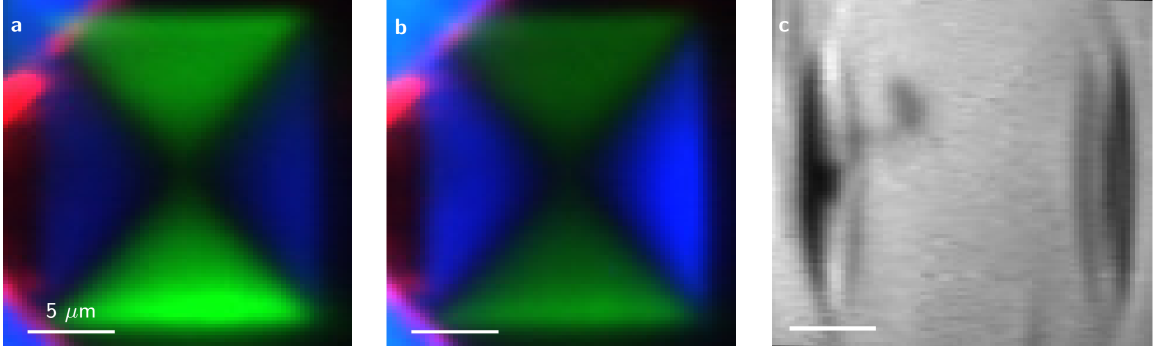

Figure F.5: Confocal scan of the pyramid structure with high-energy PL on the right and left SFs and low energy PL on the up and down SFs. The image is made by coloring emission bands red, blue or green in the same way as Fig. 3.1. Excitation energy 1.53 eV. Power 4.2 uW. 6.2 K. **a**. Exciting and collecting with horizontal polarization. **b**. Exciting and collecting at vertical polarization. **c**. Laser reflection image.

F.4 Temperature and power dependence

The temperature dependence of the SF PL linewidth for the pyramid structure is nearly linear, with a minimum linewidth of (220 ± 20) μeV at the excitation power of 40 μW, Fig. F.6(a). The linear dependence of linewidth with temperature is indicative of broadening by acoustic phonons [81] and implies that the low temperature linewidth is due to static inhomogeneities or lifetime broadening.

Potentials due to crystal phase changes (e.g. stacking faults, polytypism) in nanowires are often considered as a quantum well with type II band alignment (one carrier is attracted to the 2D potential while the other is repelled) [102, 47, 157]. In analogy with the quantum wire work, we would consider the SF as a monolayer of wurtzite in between zinc-blende, and thus expect the SF to bind heavy-hole excitons because the valence band maximum is heavy-hole in wurtzite GaAs [178]. Heavy-hole excitons are also observed in polytype quantum disks embedded in GaAs nanowires [103]. In type II band alignment, the PL center energy is predicted to blue shift with increasing excitation power [102]. Blue shifts of 30 meV are observed in GaN nanowires when the power is varied over two orders of magnitude [102]. In

contrast, in our sample the SF PL center shifts by less than 0.1 meV when the excitation power changes by two orders of magnitude (Fig. F.12c). Thus the question of whether only one carrier or both carriers are attracted to the stacking fault remains unresolved.

The smallest linewidth at zero applied field is observed at the lowest excitation power and temperature (Fig. F.2 and F.6). A Lorentzian fit of the measured spectrum gives a FWHM of (94 ± 13) μeV. After deconvolution with the spectrometer response function (Sec. F.2), the stacking fault linewidth becomes (77 ± 19) μeV.

F.5 Magneto-Stark Hamiltonian

Microscopically, the magneto-Stark effect can be derived from the Hamiltonian for an electron and hole in a magnetic field $\boldsymbol{B} = B_y\hat{\mathbf{y}}$:

$$H = \frac{\hbar^2}{2m_e}\left(\mathbf{k}_e + \frac{e}{\hbar c}\mathbf{A}\right)^2 + \frac{\hbar^2}{2m_h}\left(\mathbf{k}_h - \frac{e}{\hbar c}\mathbf{A}\right)^2, \tag{F.1}$$

where $\mathbf{k}_e$ ($\mathbf{k}_h$) is the wavevector of the electron (hole), m_e (m_h) is the effective mass of the electron (hole) and the vector potential is $\mathbf{A} = B_y z\,\hat{\mathbf{x}}$. The Coulomb interaction between the electron and the hole as well as the SF potential are omitted in Eq. (F.1) for brevity. We use the standard definition of center of mass (COM) and relative coordinates

$$\begin{aligned} \mathbf{k}_e &= \frac{m_e}{M}\mathbf{K} + \mathbf{k} \\ \mathbf{k}_h &= \frac{m_h}{M}\mathbf{K} - \mathbf{k} \end{aligned} \tag{F.2}$$

where $M = m_e + m_h$. With these substitutions, Eq. F.1 becomes

$$\begin{aligned} H = {} & \overbrace{\frac{\hbar^2 K^2}{2M}}^{\text{COM Kinetic}} + \overbrace{\frac{\hbar^2 k^2}{2\mu}}^{\text{Rel. Kinetic}} \overbrace{-\frac{e\hbar}{Mc}(z_h - z_e)K_x B_y}^{\text{COM Magneto-Stark}} \\ & + \overbrace{\frac{e\hbar}{c}\left(\frac{z_h}{m_h} + \frac{z_e}{m_e}\right)k_x B_y}^{\text{Orb. Zeeman}} + \overbrace{\frac{e^2 B_y^2}{2c^2}\left(\frac{z_e^2}{m_e} + \frac{z_h^2}{m_h}\right)}^{\text{Diamagnetic}} \end{aligned} \tag{F.3}$$

where $\mu = (m_e^{-1} + m_h^{-1})^{-1}$ [118]. The first term is the COM kinetic energy of the exciton. The second term is the kinetic energy associated with the electron-hole

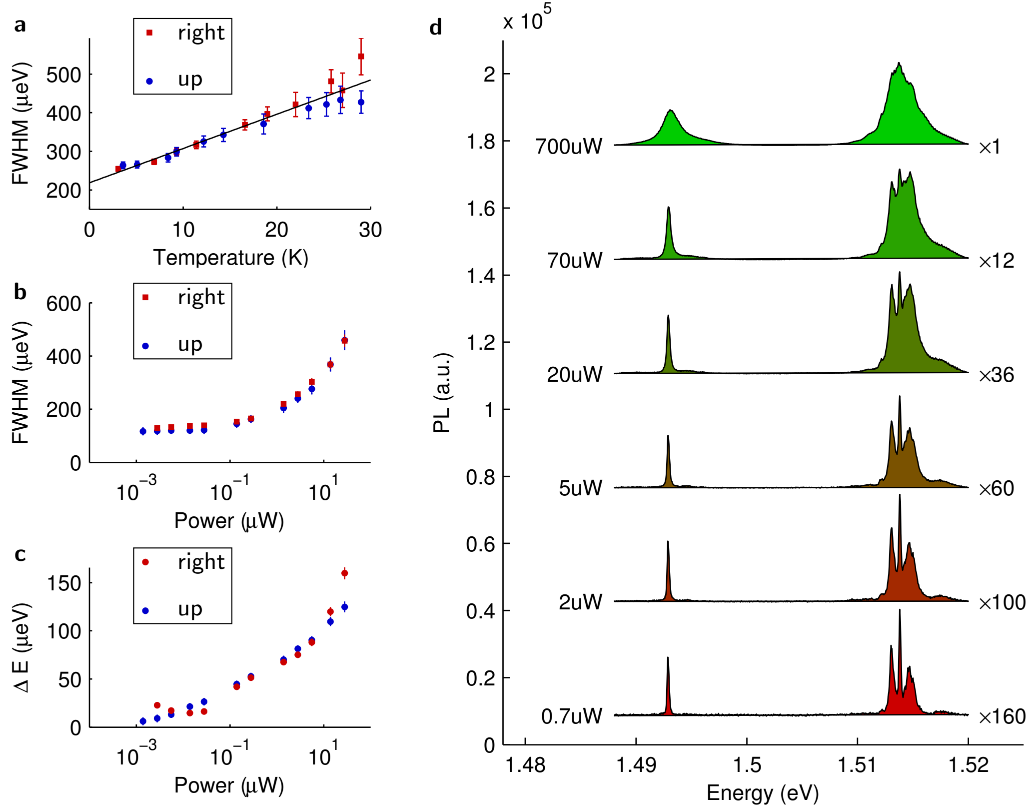

Figure F.6: Temperature and power dependence of the SF PL line at zero applied field. **a**. Temperature dependence of the linewidth found by a Lorentzian fit for the right and up SF of the pyramid structure. The black line is a fit to FWHM $= a + bT$. The fit result is $b = (9 \pm 1)$ μeV/K and $a = (220 \pm 20)$ μeV. 4 μW. **b**. Power dependence of the linewidth for the up and right SF. The narrowest linewidth is 136 ± 9 μeV. 1.7 K. **c**. Power dependence of the SF PL line center $\Delta E = E - E_0$ for the right and up triangle, where E is the energy of the SF emission and E_0 is an offset (1496.14 meV for right SF and 1493.06 meV for up SF). 1.7 K. **d**. Typical spectra at different power for the up SF . The PL around 1.513 eV arises from the GaAs bulk, dominated by the free exciton, donor bound exciton, and ionized donor bound exciton. 1.7 K.

relative motion. The third term describes the magneto-Stark effect for the exciton COM motion. The fourth term describes the orbital Zeeman effect [118]. The fifth term is the harmonic potential created by the magnetic field which produces the diamagnetic shift and would produce Landau quantization for higher magnetic fields.

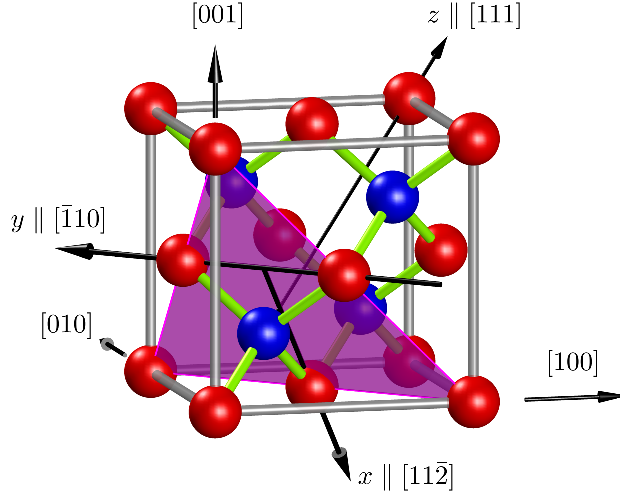

Figure F.7: GaAs crystalline lattice. Stacking fault plane is a (111) plane, shown as a triangle. The mirror reflection plane for a SF sends $y \to -y$. Note that $x \to -x$ is not a mirror reflection plane.

The COM magneto-Stark term is the same as Eq. (3.3) in the main text, derived from relativistic arguments.

F.6 Heavy hole – light hole splitting

The possible carrier spin states entering into the SF exciton can be predicted on general symmetry considerations. Due to spin orbit coupling, the valence band in bulk GaAs splits into the heavy-hole/light-hole ($j = \frac{3}{2}$) bands and split-off ($j = \frac{1}{2}$) band. At the Γ point, the heavy-hole (HH) and light-hole (LH) bands are degenerate and transform according to the four-dimensional Γ_8 irreducible spinor representation of the T_d point symmetry group [21], see Refs. [122, 123, 55] for notations.

A SF oriented in one of the $\{111\}$ planes possesses the lower C_{3v} point symmetry, as illustrated in Fig. F.7. The C_{3v} symmetry group contains six symmetry operations: E (identity), C_3 (rotation by $2\pi/3$ about $\hat{\mathbf{z}}$), C_3^{-1} (rotation by $-2\pi/3$ about $\hat{\mathbf{z}}$), σ_v (reflection $y \to -y$), σ_v' ($\sigma_v' = \sigma_v C_3^{-1}$), and σ_v'' ($\sigma_v'' = \sigma_v C_3$). These operations are depicted in Fig. F.8. We note that the SF symmetry group is different from the C_{6v} symmetry of wurtzite [22].

When a SF is introduced into a zinc-blende crystal, the degeneracy of the valence

and conduction band edges could be lifted. The compatibility analysis shows that the conduction band edge transforms according to the two-dimensional irreducible representation Γ_4 of the C_{3v} point group, i.e. the conduction band does not split. On the other hand, the degeneracy of the valence band is lifted: the Γ_8 irreducible representation of T_d decomposes into $\Gamma_4 \oplus \Gamma_5 \oplus \Gamma_6$ of C_{3v}. The two degenerate states Γ_4 transform as the spinors $|3/2, 1/2\rangle, |3/2, -1/2\rangle$ (or $|1/2, 1/2\rangle, |1/2, -1/2\rangle$), where $|j, m_j\rangle$ signifies the basic function for angular momentum j and angular momentum z-component j_m. The Γ_5 and Γ_6 hole states transform as linear combinations the spinors $|3/2, 3/2\rangle$ and $|3/2, -3/2\rangle$, see Table I. At $\boldsymbol{B} = 0$ and $\boldsymbol{K} = 0$, the two states Γ_5 and Γ_6 are guaranteed to be degenerate by time reversal symmetry [54, 92, 63]. It follows that the levels of excitons bound to a SF are split into sublevels of symmetry $\Gamma_4^c \times \Gamma_4^v$ and $\Gamma_4^c \times (\Gamma_5^v \oplus \Gamma_6^v)$ where the superscripts c, v refer to the conduction and valence bands. For convenience, the former and latter excitonic states are called the light- and heavy-hole excitons, or the LH and HH excitons, irrespective of the relation between the exciton binding energy and the splitting Δ_{HL} between the HH and LH sublevels.

The experimental data imply that the in-plane hole g-factor in the ground exciton state is negligible. This is exactly true for the HH exciton $\Gamma_4^c \times (\Gamma_5^v \oplus \Gamma_6^v)$ at zero magnetic field B_y and zero wavevector $\boldsymbol{K}_\parallel$. This implies that the splitting Δ_{HL} is high enough to prevent the mixing between the LH and HH sublevels induced by the finite value of K_x realized in the experiment and by the applied magnetic field, $|B| \leq 7$ T.

In order to confirm that the SF splits HH and LH states, we we can estimate whether the HH-LH splitting is much greater than interactions which mix HH and LH. The magnetic-field-induced HH-LH mixing can be estimated by using the hole Zeeman Hamiltonian

$$\mathcal{H}_\mathrm{Z} = -2\mu_B \varkappa (\boldsymbol{J} \cdot \boldsymbol{B}), \tag{F.4}$$

where μ_B is the Bohr magneton, $\varkappa$ is the magnetic Luttinger parameter on the order of unity, $\boldsymbol{J} = (J_x, J_y, J_z)$ are the matrices of the angular momentum 3/2 operator, and we neglect a weak cubic anisotropy [166]. According to Eq. (F.4), the magnitude of the Zeeman HH-LH coupling matrix element at the maximum field of 7 T is < 1 meV. As for the HH-LH mixing caused by the nonzero value of K_x, we note that the maximum exciton wavevector measured in our system is 5 $\mu\mathrm{m}^{-1}$. In this case the terms of the

Luttinger-Kohn Hamiltonian that couple the HH and LH excitons have magnitudes less than 2 μeV [21]. Thus, we conclude that no significant mixing occurs if the splitting Δ_{HL} is greater than a few meV. The lack of significant HH-LH mixing in our experiments is in agreement with the HH-LH splitting of 16 meV estimated for interface excitons in polytypic zinc-blende/wurtzite GaAs nanowires [186].

In order to determine the dipole moment of the SF exciton using Eq. 3.5, it is necessary to estimate the in-plane exciton effective mass, the sum of the electron and hole in-plane effective masses. While the electron mass is isotropic in GaAs, the effective in-plane hole mass depends on the detailed nature of the stacking fault potential. We note here that HH-LH mixing can affect the in-plane HH effective mass [101]. Using second-order perturbation theory, we obtain:

$$\frac{m_o}{m_{hh,||}} = \gamma_1 + \gamma_3 + (4\gamma_2^2 + 2\gamma_3^2)\frac{\hbar^2}{m_o}\sum_n \frac{|\langle LH, n|\,\hat{k}_z\,|HH\rangle|^2}{E_{HH} - E_{LH,n}}, \tag{F.5}$$

where the summation goes over all the light-hole states n (both bound and continuum), $|HH\rangle$ denotes the ground subband HH envelope function along the z axis and $|LH, n\rangle$ denote the LH envelopes and $\hat{k}_z = -\partial/\partial z$ and $\gamma_1, \gamma_2, \gamma_3$ are the Luttinger parameters [21]. The sum in Eq. F.5 is sensitive to the details of the HH and LH envelope functions as well as to the energy positions of the size-quantized levels [101, 100].

The estimate of the exciton dipole moment involves the exciton's effective mass, $M = m_h^* + m_e^*$, see Eq. (3.5), where m_h^* and m_e^* are the in-plane effective masses of the hole and electron. The electron effective mass is isotropic and therefore its in-plane value is $m_e^* = 0.067\, m_o$. Due to the anisotropy of the hole effective mass and the unknown extent of HH-LH coupling, determining the correct value of m_h^* requires a complex calculation, which we do not perform here. However, we can estimate the HH effective mass using some simple arguments. If HH-LH coupling is neglected, the in-plane heavy hole mass is that of a heavy-hole in the (111) plane, $m_h^* = 0.10\, m_o$ [100]. Another estimate of the in-plane heavy hole mass can be made from the spatially averaged heavy-hole mass of $0.45\, m_e$. We will use the lower value to estimate the dipole moment, and the higher value to estimate the error in our measurement of the dipole moment. This conservative procedure yields the minimum possible value of the dipole moment.

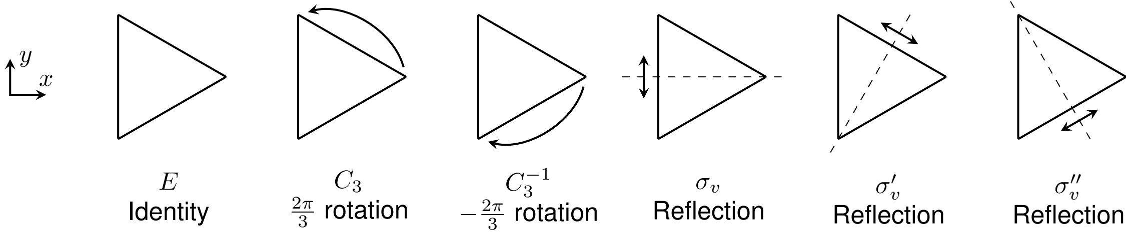

Figure F.8: Symmetry operations of C_{3v}, the point group for a (111) SF in GaAs.

F.7 Hamiltonian by symmetry

The form of the Hamiltonian describing the SF-bound exciton state can be derived based on the symmetry of the SF system. Specifically, we would like to find terms of the Hamiltonian that are odd with magnetic field and can thus explain the magnetic non-reciprocity data.

It is first necessary to find how the symmetry operations affect a vector, such as a position vector $\boldsymbol{r} = (x, y, z)$, and a pseudo-vector, such as magnetic field $\boldsymbol{B} = (B_x, B_y, B_z)$. In free space, $\boldsymbol{r}$ and $\boldsymbol{B}$ transform according to the D_1^- and D_1^+ irreducible representations, where $\pm$ denotes parity with respect to space inversion. Making use of the compatibility tables for C_{3v} point symmetry, one can readily check that $D_1^- = \Gamma_1 \oplus \Gamma_3$, while $D_1^+ = \Gamma_2 \oplus \Gamma_3$. Taking into account that under rotations the components of polar and axial vectors transform identically and making use of Fig. F.8 we find that z and B_z transform according to the irreducible representations Γ_1 and Γ_2, respectively, while the pairs (x, y) and $(-B_y, B_x)$ form equivalent bases of the two-dimensional Γ_3 irreducible representation of C_{3v}, see Table G.2.

To apply the method of invariants, we need to establish transformation rules for the basic 2×2 matrices acting in the spin subspaces of electrons and heavy-holes. We introduce basic electron matrices I^e (the 2×2 unit matrix) and $\boldsymbol{\sigma}^e = (\sigma_x^e, \sigma_y^e, \sigma_z^e)$ (Pauli matrices) acting in the basis of $|s = \pm 1/2\rangle$ electron spinors. The decomposition $\Gamma_4 \otimes \Gamma_4^* = \Gamma_1 + \Gamma_2 + \Gamma_3$ indicates the ways in which the basic electron spin matrices transform. By calculating the effect of the C_{3v} symmetry operators on the matrices, one finds that I^e is invariant, σ_z^e transforms according to Γ_2 and (σ_x^e, σ_y^e) form a basis of the two-dimensional irreducible representation Γ_3 with σ_x^e and σ_y^e transforming equivalently to B_x and B_y respectively (Tab. G.2). The basic matrices for the light-

hole doublet transform in exactly the same way.

By contrast, the heavy-hole spin doublet transforms according to the reducible representation $\Gamma_5 \oplus \Gamma_6$. The direct product

$$(\Gamma_5 \oplus \Gamma_6) \otimes (\Gamma_5 \oplus \Gamma_6)^* = 2\Gamma_1 \oplus 2\Gamma_2. \tag{F.6}$$

indicates that among the four basic matrices, I^{hh}, $\boldsymbol{\sigma}^{hh} = (\sigma_x^{hh}, \sigma_y^{hh}, \sigma_z^{hh})$ acting in the space $|\pm 3/2\rangle$, two are invariant and two transform as B_z [166]. Taking into account that at the mirror reflection $\sigma_v||(\bar{1}10)$ the matrix σ_y^{hh} does not change sign, we find that I^{hh} and σ_y^{hh} transform according to Γ_1 (note that σ_y^{hh} changes its sign under time reversal whereas I^{hh} does not), while σ_z^{hh}, σ_x^{hh} transform according to Γ_2, see Tab. G.2 and Ref. [166].

Using the transformation properties of the relevant basis functions (Tab. G.2), we can build the effective Hamiltonian. Any valid term of the Hamiltonian must transform as the identity representation Γ_1 and be even under time reversal. In order to know which combinations of basis functions transform as Γ_1, we use the product rules for irreducible representations. From this information, we can build the linear in $\boldsymbol{B}$ Hamiltonian. For the electron, this analysis produces the result that the in-plane and out-of-plane g-factors are potentially different:

$$H_{\mathrm{Z,e}} = \frac{1}{2} g_{zz}^e \mu_B B_z \sigma_z^e + \frac{1}{2} g_{||}^e \mu_B (B_x \sigma_x^e + B_y \sigma_y^e) \tag{F.7}$$

For the heavy holes, the Hamiltonian takes the form [166]:

$$H_{\mathrm{Z},hh} = \frac{1}{2} \mu_B B_z \left(g_{zz}^{hh} \sigma_z^{hh} + g_{zx}^{hh} \sigma_x^{hh} \right). \tag{F.8}$$

Eqquation F.8 implies that the heavy hole has a zero in-plane g-factor, and that an out-of-plane component B_z creates a tilted effective field with a spin precession vector lying in the xz plane. We note that the atomic-scale symmetry of the SF makes the two in-plane directions x and y inequivalent.

The magneto-Stark Hamiltonian can be derived by symmetry using a similar procedure. The combination of the two Γ_3 irreducible representations (K_x, K_y) and

$(-B_y, B_x)$ contains an invariant representation, leading to the Hamiltonian

$$H_{\text{magneto-Stark}} = \beta'(K_x B_y - K_y B_x)$$

Furthermore, the Hamiltonian describing the diamagnetic shift is derived from the invariants B_z^2 and $B_x^2 + B_y^2$, namely,

$$H_{\text{dia}} = \beta_1 B_z^2 + \beta_2(B_x^2 + B_y^2).$$

For Eq. (3.1) of the main text, we take into account only an in-plane field effect and set $\beta_2 \equiv \beta$.

We note for completeness that, besides B-linear, B-quadratic and KB-terms, the effective Hamiltonian also includes K linear terms, $\sigma_x^e K_y - \sigma_y^e K_x$, which arise from spin-orbit coupling. Our estimates show that these terms are not significant for the relevant wavevectors and do not lead to the non-reciprocal emission spectra to first-order in B.

F.8 Supplemental Angle Resolved Data

For the angle resolved experiment that tests the magneto-Stark effect, PL spectra were acquired on multiple different SF pyramids positioned at various angles. The spectra of the *up* and *down* SF at ±6.5 T are shown in Fig. F.9. We note that the PL spectra show a strong and a weak doublet. The origin of the weak doublet is unknown, but we tentatively attribute it to scatter of PL from other exciton populations.

We note that there are two types of SF pyramids: one where the *left/right* SFs show higher energy PL than the *up/down* SFs (type a), and a second type where the emission energies are swapped (type b). For example, using this naming scheme the SF pyramid shown in Fig. 3.1(d) is of type a. Here, the *left/right* directions refer to the direction of the majority of the intrinsic/extrinsic pair defects, visible as single triangles in Fig. 3.1(a). We also define a *standard* and *rotated* orientation of the bulk crystal depending on whether the sample is mounted as it is in Fig. 3.1(a) (standard) or rotated by 90° about [001] (rotated).

The PL emission energy as a function of magnetic field for the 6 SFs is shown in Fig. F.10. These plots show that d_{he}, i.e., the electron-hole separation, changes sign for different SF pyramids. The sign of the splitting $\Delta E_{up/down}$ reflects the direction

of the exciton dipole moment along the SF normal. From Fig. F.10, we find that the atomic structure of the SF pyramid has a reflection symmetry in the {110} set of planes, i.e. where the *up* and *down* SFs are interchanged.

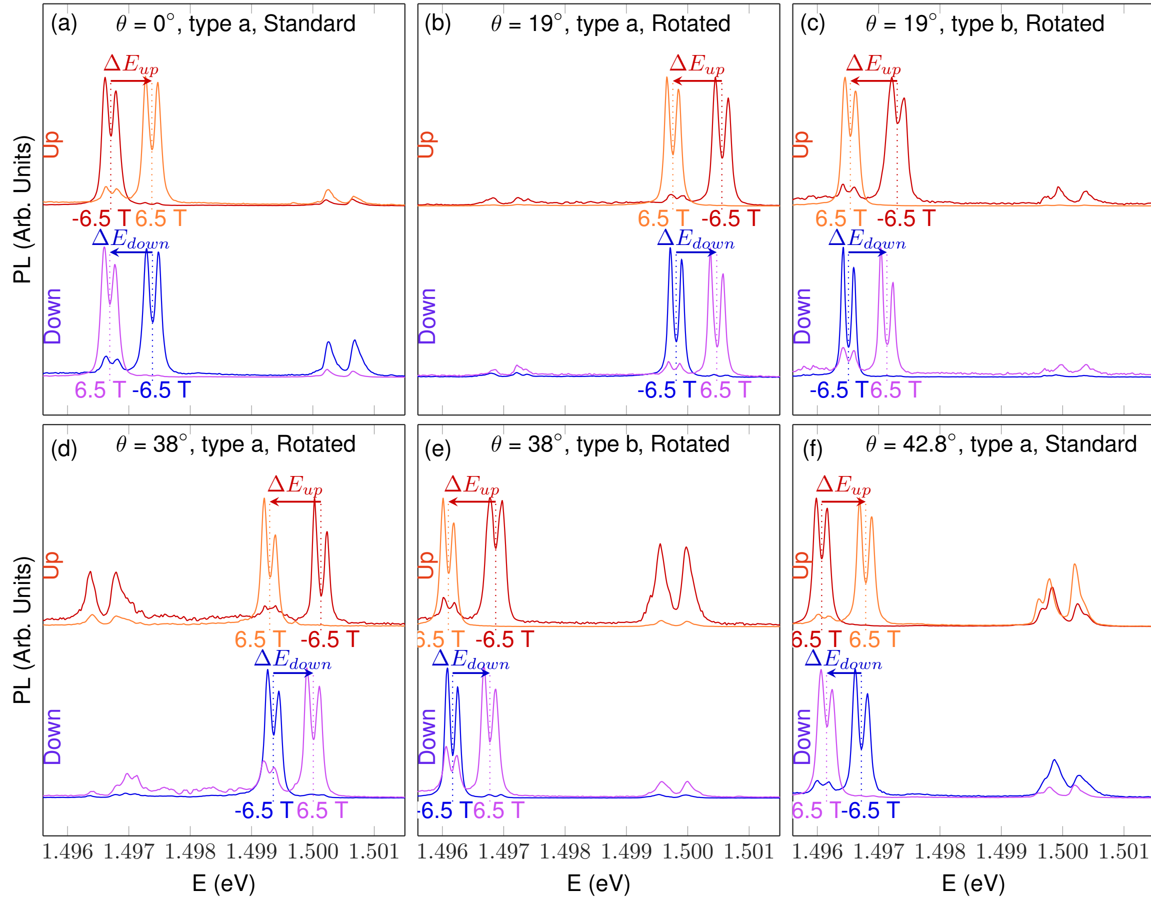

Figure F.9: Spectra at -6.5 T and 6.5 T for the up and down SF for six different SF pyramid defects. The difference between ΔE_{up} and ΔE_{down} is visible when $\theta \neq 0$. 1 μW, 1.5 K, excite at 1.65 eV, excite and collect H polarization.

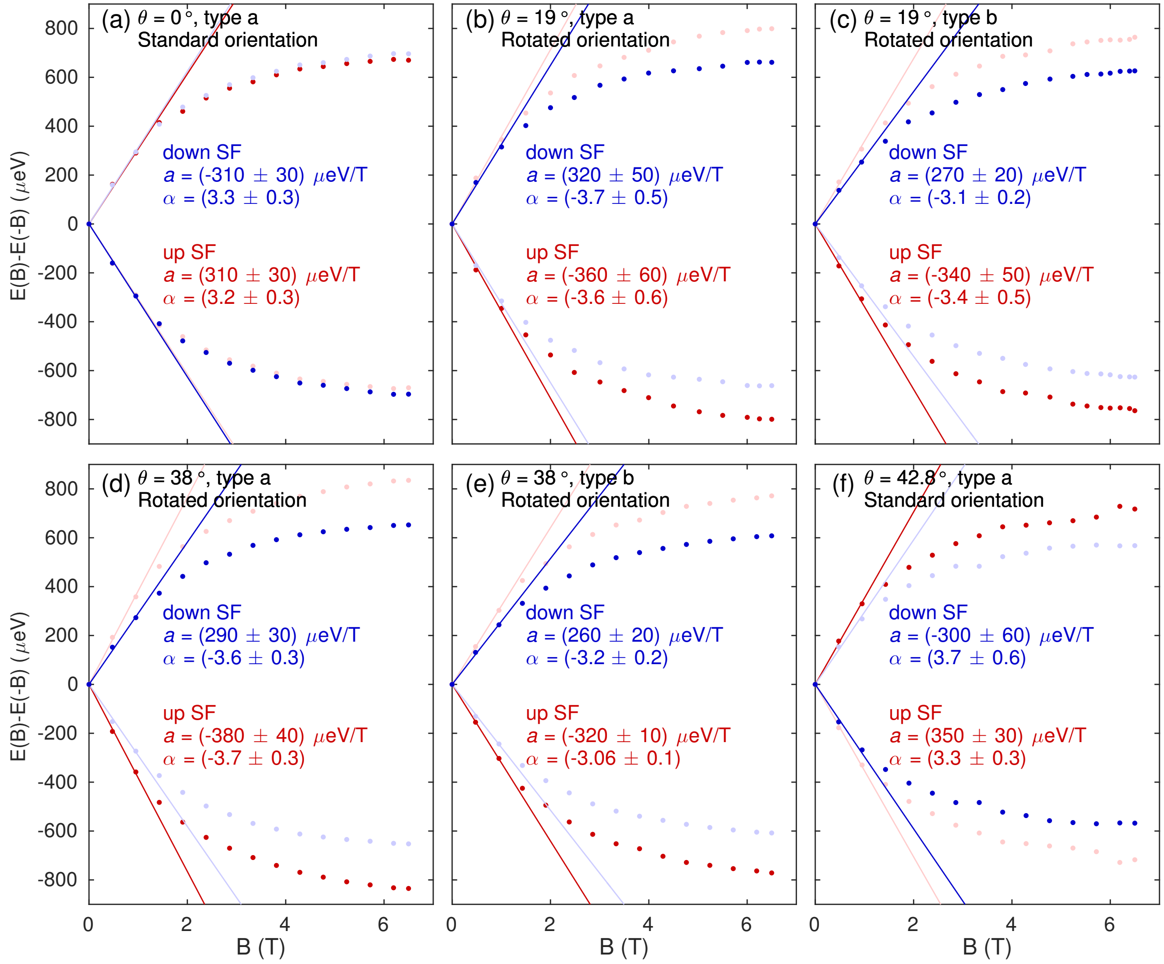

Figure F.10: The energy of the strong two peaks position in Fig. F.9 is averaged to make $E(B)$. Here we plot the difference between the peak position at positive and negative B. The slope at $B = 0$ is extracted with a linear fit ($\Delta E = aB_y$) to the first three data points. The different panels show the experimental result at a variety of angles. The light colored curves are the negative of the dark colored curves, useful for comparing the absolute value of ΔE. The mean value of the dimensionless dipole moment in Eq. (F.9) and (F.10) is $\alpha = 3.2 \pm 0.2$.

F.9 Quantitative interpretation of Angle Resolved Data

Combining Eq. (3.2) and (3.3) of the main text and averaging over two spin states of the exciton's electron, the observed magneto-Stark shift is

$$\begin{aligned} E_{up} &= +\alpha\mu_B B_y \sin(\theta_{SF} + \theta'), \\ E_{down} &= -\alpha\mu_B B_y \sin(\theta_{SF} - \theta'), \end{aligned} \tag{F.9}$$

where the light emission angles are related by Snell's law: $n \sin\theta' = \sin\theta$, $\theta_{SF} = \cos^{-1}\left(1/\sqrt{3}\right) = 54.7°$ is the angle the SF normal makes with the [001] axis and $\mu_B = e\hbar/2m_e c$ is the Bohr magneton (CGS units). Here α is a dimensionless measure of the dipole moment:

$$\alpha = -\frac{en\hbar\omega}{Mc^2\mu_B} d_{he} = \frac{-1}{3.2}\frac{d_{he}}{\mathrm{nm}}, \tag{F.10}$$

where $d_{he} = \langle z_h - z_e \rangle$ is the hole-electron separation in the exciton, z_h and z_e are the hole and electron coordinates and $\langle \ldots \rangle$ denotes the quantum mechanical average (note CGS units). The numerical value uses the estimated in-plane exciton mass described in Appendix F.6. The quantity $\Delta E_{up/down}(B) = E_{up/down}(B) - E_{up/down}(-B)$ is the odd part of $E_{up/down}$ doubled, which is insensitive to overall offsets and the diamagnetic shift. When $\theta = \theta' = 0$, PL from the *up* and *down* SFs arises from excitons with the same absolute value of momentum and hence ΔE_{up} and ΔE_{down} have the same magnitude [Fig. 3.3(d)]. When the angle is increased, ΔE_{up} and ΔE_{down} have different magnitudes [Fig. 3.3(e)].

In the linear in B_y regime, the magnetic field is not expected to significantly perturb the exciton dipole moment, and so to first order ΔE should be proportional to B_y. Experimentally, we find the energy shift is linear with B_y for $B_y < 1$ T, and we extract the proportionality constant using a fit to $\Delta E = aB_y$. The estimate of the dimensionless dipole moment α depends somewhat on the fitting method used to find the slope ΔE vs. B_y at $B_y = 0$ from the experimental data. Using different methods, we obtain values of α ranging from 3.2 to 4.3, and we conservatively use the lowest value of $\alpha = 3.2 \pm 0.3$ to estimate the exciton dipole moment. Given the uncertainty in the measurement of α and the estimation of the in-plane exciton effective mass (Sec. F.6), the best guess for the dipole moment is 10 nm, with the true

value estimated to fall between 9 and 30 nm.

We note that the combination

$$r(\theta) = \frac{|\Delta E_{up}| - |\Delta E_{down}|}{\frac{1}{2}\big(|\Delta E_{up}| + |\Delta E_{down}|\big)} \tag{F.11}$$

depends only on given geometry and the index of refraction (to first order in B), and is independent of the exciton dipole moment. Using Eq. F.9 and expanding about small θ, we can produce a small-θ approximation for $r(\theta)$,

$$r(\theta) \approx \frac{2\cot\theta_{SF}}{n}\theta \tag{F.12}$$

correct to within 10% for angles up to 45° and $n = 3.5$. We obtain good agreement between $r(\theta)$ calculated experimentally from the $B = 0$ slope of ΔE with Eq. F.11. (Fig. 3.3h). We emphasize that this model agrees with the data without any fit parameters.

F.10 Spectrally resolved confocal imaging of stacking fault structures

The confocal scan of the stacking fault structures presented in Fig. 3.1a is processed with different spectral integration regions in Fig. 4.1. We make note of several features of stacking faults which can be seen from the spectrally resolved confocal images.

1. **Edge photoluminescence.** PL from the edges of SFs (Fig. 4.1a) shows a broad-band emission around 1.47 eV. At high power, the emission lines broaden into a single $\sim 5-15$ meV wide peak (Fig. 4.1b), whereas at low power, numerous sharp localized peaks are observed (Fig. 3.1f). We tentatively attribute this to a transition from 1D excitons at high power, to 0D defect bound excitons at low power. The edge PL center energy varies between defects, with emission from the SF pyramid structure showing higher energy emission than that from the SF pair structures. We also note that other stacking fault pyramids do not show this edge luminescence (Appendix F.5).

2. **2D stacking fault.** Figures 4.1c-d show that the stacking fault pair structures (visible as single triangles) have an emission energy that varies over ∼10 meV.

In addition, the highest energy SF related PL is observed on the pyramid defect at 1.4969 eV.

3. **Edge emission depending on SF orientation.** Fig. 4.1c shows some pair defects oriented in the up or down direction, but these stacking faults curiously have no edge PL visible in Fig. 4.1a.

4. **Band edge emission.** The presence of a SF does not strongly affect the band-edge PL (Fig. 4.1e-f). Only at the intersections of SFs with the sample surface does the band-edge PL decrease due to either quenching or scattering (Fig. 4.1e). We also observe circular spots at which emission is significantly quenched (e.g. light blue spectrum). These defects are not correlated with the stacking faults.

5. **Oval defects.** A laser reflection image (Fig. 4.1g-h) reveals oval defects which occur at the intersection of the right/left stacking faults with the sample surface [106]. The circularly shaped quenching defects, observed in Fig. 4.1e, are not observed in this surface-sensitive image. SEM images of the sample further revealing the surface topology are presented in Appendix F.18.

The PL emission energy is remarkably homogeneous over a single SF (Fig. F.11). The PL emission line center has a standard deviation of only $\sim 20 - 50$ μeV in the center region of the SF.

F.11 Temperature and power dependence

The temperature dependence of the SF PL linewidth for the pyramid structure is nearly linear, with a minimum linewidth of (220 ± 20) μeV at the excitation power of 40 μW (Fig. F.12a). The linear dependence of linewidth with temperature is possibly indicative of broadening by acoustic phonons [81] and implies that the low temperature linewidth is due to static inhomogeneities or lifetime broadening.

Potentials due to crystal phase changes (e.g. stacking faults, polytypism) in nanowires are often considered as a quantum well with type II band alignment (one carrier is attracted to the 2D potential while the other is repelled) [102, 47, 157]. In analogy with the quantum wire work, we would consider the SF as a monolayer

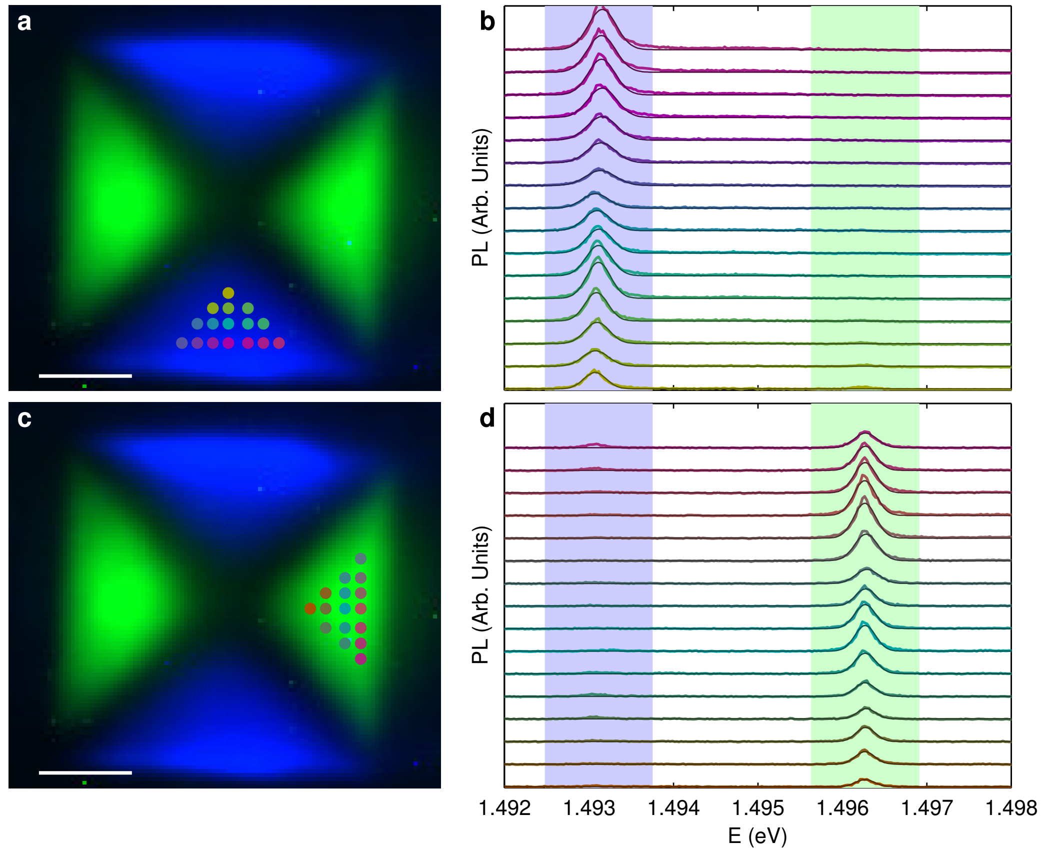

Figure F.11: Homogeneity of SF emission line center over a single SF. **a**. Confocal scan of a stacking fault pyramid, with sixteen points of interest marked. The emission bands are shown as colored rectangles in b. **b**. Spectra at colored dots in a. From a Gaussian fit, the mean emission energy for these 16 spectra is 1.49312 eV with a standard deviation of 20 μeV. The mean uncertainty in the fit center is 11 μeV. **c-d**. Same as a-b, but with spectra taken from right SF. Mean emission energy for these 16 spectra is 1.49627 eV with a standard deviation of 50 μeV. The mean uncertainty in the fit center is 11 μeV. Scale bar 5 μm. 4.9 K. Excite 45°, collect all polarizations. 10 μW. Excitation energy 1.53 eV.

of wurtzite in between zinc-blende, and thus expect the SF to bind heavy-hole excitons because the valence band maximum is heavy-hole in wurtzite GaAs [178]. Heavy-hole excitons are also observed in polytype quantum disks embedded in GaAs nanowires [103]. In type II band alignment, the PL center energy is predicted to blue shift with increasing excitation power [102]. Blue shifts of 30 meV are observed

in GaN nanowires when the power is varied over two orders of magnitude [102]. In contrast, in our sample the SF PL center shifts by less than 0.1 meV when the excitation power changes by two orders of magnitude (Fig. F.12c). Thus the question of whether only one carrier or both carriers are attracted to the stacking fault remains unresolved.

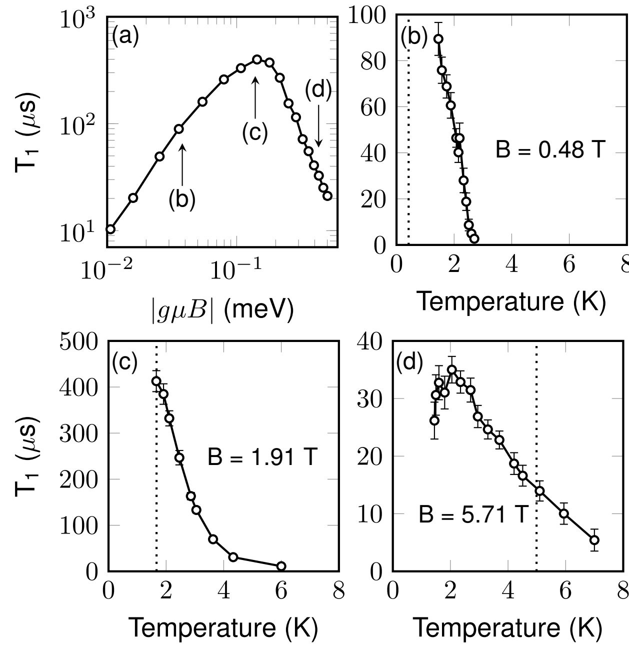

Figure F.12: Temperature and power dependence of the SF PL line at zero applied field. **a**. Temperature dependence of the linewidth found by a Lorentzian fit for the right and up SF of the pyramid structure. The black line is a fit to FWHM $= a + bT$. The fit result is $b = (9 \pm 1)$ μeV/K and $a = (220 \pm 20)$ μeV. 4 μW. **b**. Power dependence of the linewidth for the up and right SF. The narrowest linewidth is 136 ± 9 μeV. 1.7 K. **c**. Power dependence of the SF PL line center $\Delta E = E - E_0$ for the right and up triangle, where E is the energy of the SF emission and E_0 is an offset (1496.14 meV for right SF and 1493.06 meV for up SF). 1.7 K. **d**. Typical spectra at different power for the up SF . The PL around 1.513 eV arises from the GaAs bulk, dominated by the free exciton, donor bound exciton, and ionized donor bound exciton. 1.7 K.

F.12 Polarization dependence of Stacking Fault PL

Here we derive the polarization dependence of stacking fault exciton photoluminescence when exciting above band. In this model, we assume electron-hole pairs are created, quickly bind together to form excitons and then experience spin relaxation and dephasing due to interaction with the environment. After a time t, excitons bind to the SF and recombine. We additionally rely on the following assumptions:

1. The dipole matrix elements for above band excitation are well approximated by their values at the Γ point.

2. All hole spin transitions occur with the same rate. For example, the rate of relaxation $|3/2\rangle \rightarrow |1/2\rangle$ is the same as $|3/2\rangle \rightarrow |-1/2\rangle$.

3. Each carrier interacts independently with the environment.

4. Relaxation and dephasing happens for the same amount of time for each carrier.

The amount of electron and hole spin relaxation expected during the radiative lifetime of the carriers varies over a wide range. Typical hole spin relaxation rates in the bulk are fast (110 fs),[96], but can increase to 1 ns in quantum wells [162]. Similarly, the radiative lifetime of excitons ranges from $\sim$ 100 ps in a quantum well [200] to a few ns in bulk GaAs [156]. For the stacking fault exciton, the total amount of spin relaxation is the product of the spin relaxation rate and the radiative lifetime. Since it is unknown the fraction of time the above-band photo-excited carriers spend in the bulk vs on the stacking fault, the amount of spin relaxation is an unknown quantity that could vary over several orders of magnitude.

We emphasize that the assignment of the stacking fault exciton as heavy-hole or light-hole can be done qualitatively using the following argument. The dipole moment for heavy-hole excitons is left and right circularly polarized when viewed along the stacking fault axis [111]. When viewed from above (along [001]), this results in the largest PL response when exciting and collecting $\theta = 0$ (x direction in Fig. F.13). In comparison, the light hole has a dipole projection along [111], and therefore gives the strongest emission when exciting and collecting along $\theta = \pi/2$. Experimentally, we observe the larges PL response when exciting and collecting $\theta = 0$, confirming

that the excitons are composed of an electron and a heavy-hole. In the following we give a quantitative density matrix model that yields an analytic expression for the polarization dependence.

F.12.1 Coordinate transformation

Incident above band light creates free electron-hole pairs according to the optical selection rules for bulk GaAs. If the excitation light has an energy near the band edge, the dipole matrix elements can be approximated by those at the Γ point. For convenience, we align the quantization axis of the free exciton along the [111] direction in order to easily transfer the density matrix into the stacking fault basis. (In bulk GaAs, the coordinate system may be aligned along any axis desired.) The unprimed lab coordinate system is related to the primed SF coordinate system via the transformation

$$\begin{cases} x' = x \\ y' = y\cos\xi + z\sin\xi \\ z' = -y\sin\xi + z\cos\xi \end{cases} \tag{F.13}$$

where $\xi = \cos^{-1}(1/\sqrt{3})$ is the angle the stacking fault normal makes with the [001] axis. The coordinate systems are shown schematically in Fig. F.13.

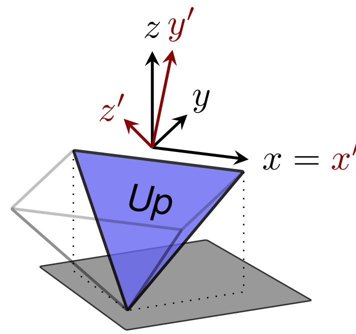

Figure F.13: Coordinate system for the derivation of the stacking fault polarization dependence showing unprimed lab coordinates and primed SF coordinates.

F.12.2 Laser excitation of free exciton

Light emission and absorption occurs via a dipole transition. The arbitrary polarization dependencies can be calculated according to the method outlined in Ref. [111]. We write the dipole matrix elements for the free exciton with the basis $\left\{\left|\frac{1}{2},\frac{3}{2}\right\rangle,\left|\frac{1}{2},\frac{1}{2}\right\rangle,\left|\frac{1}{2},-\frac{1}{2}\right\rangle,\left|\frac{1}{2},-\frac{3}{2}\right\rangle,\left|-\frac{1}{2},\frac{3}{2}\right\rangle,\left|-\frac{1}{2},\frac{1}{2}\right\rangle,\left|-\frac{1}{2},-\frac{1}{2}\right\rangle,\left|-\frac{1}{2},-\frac{3}{2}\right\rangle\right\}$ where the electron state is written first and the hole state second.

The excited state density matrix ρ_o is equal to $M^\dagger_{\epsilon_i} M_{\epsilon_i}$, where $M_{\epsilon_i} = \mathbf{p}\cdot\hat{\epsilon}_i$ is the coordinate referenced dipole matrix elements, $\hat{\epsilon}_i$ is the incident polarization and $\mathbf{p}$ are the dipole matrix elements. The dipole matrix elements $\mathbf{p} = \langle 0|\,\boldsymbol{\mu}\,|e_i h_j\rangle$, corresponding to recombination of an electron-hole pair into the semiconductor vacuum state. The dipole matrix elements are found by inspection of Eq. 2.1:

$\mathbf{p}$	$\left\|\frac{1}{2},\frac{3}{2}\right\rangle$	$\left\|\frac{1}{2},\frac{1}{2}\right\rangle$	$\left\|\frac{1}{2},-\frac{1}{2}\right\rangle$	$\left\|\frac{1}{2},-\frac{3}{2}\right\rangle$	$\left\|-\frac{1}{2},\frac{3}{2}\right\rangle$	$\left\|-\frac{1}{2},\frac{1}{2}\right\rangle$	$\left\|-\frac{1}{2},-\frac{1}{2}\right\rangle$	$\left\|-\frac{1}{2},-\frac{3}{2}\right\rangle$
$\langle 0\|$	0	$\frac{1}{\sqrt{6}}(\hat{\mathbf{x}}+i\hat{\mathbf{y}})$	$\sqrt{\frac{2}{3}}\hat{\mathbf{z}}$	$\frac{1}{\sqrt{2}}(\hat{\mathbf{x}}-i\hat{\mathbf{y}})$	$\frac{1}{\sqrt{2}}(\hat{\mathbf{x}}+i\hat{\mathbf{y}})$	$\sqrt{\frac{2}{3}}\hat{\mathbf{z}}$	$\frac{1}{\sqrt{6}}(\hat{\mathbf{x}}-i\hat{\mathbf{y}})$	0

Using the incident polarization vector in the lab coordinate system of $\hat{\epsilon}_i = x_i\hat{\mathbf{x}} + y_i\hat{\mathbf{y}} + z_i\hat{\mathbf{z}}$, the coordinate referenced dipole matrix elements M_{ϵ_i} are found by writing $\mathbf{p}$ with $(\hat{\mathbf{x}},\hat{\mathbf{y}},\hat{\mathbf{z}}) \to (\hat{\mathbf{x}}',\hat{\mathbf{y}}',\hat{\mathbf{z}}')$ and then using Eq. F.13 to transform the unit vectors to the lab frame:

$$M_{\epsilon_i} = \frac{1}{\sqrt{6}}\begin{pmatrix} 0 & x_i + \frac{i}{\sqrt{3}}y_i & -\sqrt{\frac{8}{3}}y_i & \sqrt{3}x_i - iy_i & \sqrt{3}x_i + iy_i & -\sqrt{\frac{8}{3}}y_i & x_i - \frac{i}{\sqrt{3}}y_i & 0 \end{pmatrix}, \tag{F.14}$$

where $z_i = 0$ for light incident along [001]. This procedure chooses the spin quantization axis to lie in the primed stacking fault coordinate system, but keeps the polarization of light in the lab coordinate system.

The excited density matrix is

$$\rho_o = M^\dagger_{\epsilon_i} M_{\epsilon_i} \tag{F.15}$$

before any relaxation or dephasing and in the limit of low excited-state population. The polarization projections x_i and y_i can be complex numbers, e.g. for circularly polarized light.

F.12.3 Spin relaxation and dephasing

The initial excited density matrix evolves in time due to spin relaxation and dephasing processes. We use a rate Γ_h to describe hole spin flips and the associated dephasing process. To apply hole spin flips, we create 16 Lindblad operators, corresponding to the 16 channels of hole spin flips. Each of the 16 Lindblad operator is constructed using

$$L_j = D\rho D^\dagger - \frac{1}{2}D^\dagger D\rho - \frac{1}{2}\rho D^\dagger D \tag{F.16}$$

where $D_{nm} = \Gamma\delta_{ni}\delta_{mf}$ is the j'th relaxation channel from state i to state f at rate Γ. For example, hole spin flips from state 2 to state 1 is accomplished with

$$L^{\text{hole}}_{2\to 1} = \Gamma_h \begin{pmatrix} \rho_{22} & -\frac{1}{2}\rho_{12} & 0 & 0 & 0 & 0 & 0 & 0 \\ -\frac{1}{2}\rho_{21} & -\rho_{22} & -\frac{1}{2}\rho_{23} & -\frac{1}{2}\rho_{24} & -\frac{1}{2}\rho_{25} & -\frac{1}{2}\rho_{26} & -\frac{1}{2}\rho_{27} & -\frac{1}{2}\rho_{28} \\ 0 & -\frac{1}{2}\rho_{32} & 0 & 0 & 0 & 0 & 0 & 0 \\ 0 & -\frac{1}{2}\rho_{42} & 0 & 0 & 0 & 0 & 0 & 0 \\ 0 & -\frac{1}{2}\rho_{52} & 0 & 0 & 0 & 0 & 0 & 0 \\ 0 & -\frac{1}{2}\rho_{62} & 0 & 0 & 0 & 0 & 0 & 0 \\ 0 & -\frac{1}{2}\rho_{72} & 0 & 0 & 0 & 0 & 0 & 0 \\ 0 & -\frac{1}{2}\rho_{82} & 0 & 0 & 0 & 0 & 0 & 0 \end{pmatrix}.$$

The total Lindblad operator describing hole spin flips $L_1 = \sum_j L_j$ is the addition of each decay channel:

$$L_h = \Gamma_h \begin{pmatrix} -3\rho_{11}+\rho_{22}+\rho_{33}+\rho_{44} & -3\rho_{12} & -3\rho_{13} & -3\rho_{14} \\ -3\rho_{21} & \rho_{11}-3\rho_{22}+\rho_{33}+\rho_{44} & -3\rho_{23} & -3\rho_{24} \\ -3\rho_{31} & -3\rho_{32} & \rho_{11}+\rho_{22}-3\rho_{33}+\rho_{44} & -3\rho_{34} \\ -3\rho_{41} & -3\rho_{42} & -3\rho_{43} & \rho_{11}+\rho_{22}+\rho_{33}-3\rho_{44} \\ -3\rho_{51} & -3\rho_{52} & -3\rho_{53} & -3\rho_{54} \\ -3\rho_{61} & -3\rho_{62} & -3\rho_{63} & -3\rho_{64} \\ -3\rho_{71} & -3\rho_{72} & -3\rho_{73} & -3\rho_{74} \\ -3\rho_{81} & -3\rho_{82} & -3\rho_{83} & -3\rho_{84} \end{pmatrix.$$
$$\begin{matrix} -3\rho_{15} & -3\rho_{16} & -3\rho_{17} & -3\rho_{18} \\ -3\rho_{25} & -3\rho_{26} & -3\rho_{27} & -3\rho_{28} \\ -3\rho_{35} & -3\rho_{36} & -3\rho_{37} & -3\rho_{38} \\ -3\rho_{45} & -3\rho_{46} & -3\rho_{47} & -3\rho_{48} \\ -3\rho_{55}+\rho_{66}+\rho_{77}+\rho_{88} & -3\rho_{56} & -3\rho_{57} & -3\rho_{58} \\ -3\rho_{65} & \rho_{55}-3\rho_{66}+\rho_{77}+\rho_{88} & -3\rho_{67} & -3\rho_{68} \\ -3\rho_{75} & -3\rho_{76} & \rho_{55}+\rho_{66}-3\rho_{77}+\rho_{88} & -3\rho_{78} \\ -3\rho_{85} & -3\rho_{86} & -3\rho_{87} & \rho_{55}+\rho_{66}+\rho_{77}-3\rho_{88} \end{matrix}\Bigg).$$

Here we have made the assumption that all hole spin flips occur with the same rate. For example, a flip with $\Delta m_h = \pm 1$ flip has the same rate as one with $\Delta m_h = \pm 2$. An analogous expression can be created for electron spin flips:

$$L_e = \Gamma_e \begin{pmatrix} -\rho_{11}+\rho_{55} & -\rho_{12} & -\rho_{13} & -\rho_{14} & -\rho_{15} & -\rho_{16} & -\rho_{17} & -\rho_{18} \\ -\rho_{21} & -\rho_{22}+\rho_{66} & -\rho_{23} & -\rho_{24} & -\rho_{25} & -\rho_{26} & -\rho_{27} & -\rho_{28} \\ -\rho_{31} & -\rho_{32} & -\rho_{33}+\rho_{77} & -\rho_{34} & -\rho_{35} & -\rho_{36} & -\rho_{37} & -\rho_{38} \\ -\rho_{41} & -\rho_{42} & -\rho_{43} & -\rho_{44}+\rho_{88} & -\rho_{45} & -\rho_{46} & -\rho_{47} & -\rho_{48} \\ -\rho_{51} & -\rho_{52} & -\rho_{53} & -\rho_{54} & -\rho_{55}+\rho_{11} & -\rho_{56} & -\rho_{57} & -\rho_{58} \\ -\rho_{61} & -\rho_{62} & -\rho_{63} & -\rho_{64} & -\rho_{65} & -\rho_{66}+\rho_{22} & -\rho_{67} & -\rho_{68} \\ -\rho_{71} & -\rho_{72} & -\rho_{73} & -\rho_{74} & -\rho_{75} & -\rho_{76} & -\rho_{77}+\rho_{33} & -\rho_{78} \\ -\rho_{81} & -\rho_{82} & -\rho_{83} & -\rho_{84} & -\rho_{85} & -\rho_{86} & -\rho_{87} & -\rho_{88}+\rho_{55} \end{pmatrix}$$

Dephasing processes do not cause population relaxation, but cause a loss of phase coherence between different states. We assume that each carrier interacts independently

with the environment [40]. For electron dephasing, the Lindblad operator is

$$L_{\text{e,deph}} = -\gamma_e \sum_{e_1 \neq e_2} \sum_{h_1 = h_2} |e_1 h_1\rangle \langle e_2 h_2| = -\gamma_e \begin{pmatrix} 0 & 0 & 0 & 0 & \rho_{15} & 0 & 0 & 0 \\ 0 & 0 & 0 & 0 & 0 & \rho_{26} & 0 & 0 \\ 0 & 0 & 0 & 0 & 0 & 0 & \rho_{37} & 0 \\ 0 & 0 & 0 & 0 & 0 & 0 & 0 & \rho_{48} \\ \rho_{51} & 0 & 0 & 0 & 0 & 0 & 0 & 0 \\ 0 & \rho_{62} & 0 & 0 & 0 & 0 & 0 & 0 \\ 0 & 0 & \rho_{73} & 0 & 0 & 0 & 0 & 0 \\ 0 & 0 & 0 & \rho_{84} & 0 & 0 & 0 & 0 \end{pmatrix}.$$

For hole dephasing, the Lindblad operator is

$$L_{\text{h,deph}} = -\gamma_h \sum_{e_1 = e_2} \sum_{h_1 \neq h_2} |e_1 h_1\rangle \langle e_2 h_2| = -\gamma_h \begin{pmatrix} 0 & \rho_{12} & \rho_{13} & \rho_{14} & 0 & 0 & 0 & 0 \\ \rho_{21} & 0 & \rho_{23} & \rho_{24} & 0 & 0 & 0 & 0 \\ \rho_{31} & \rho_{32} & 0 & \rho_{34} & 0 & 0 & 0 & 0 \\ \rho_{41} & \rho_{42} & \rho_{43} & 0 & 0 & 0 & 0 & 0 \\ 0 & 0 & 0 & 0 & 0 & \rho_{56} & \rho_{57} & \rho_{58} \\ 0 & 0 & 0 & 0 & \rho_{65} & 0 & \rho_{67} & \rho_{68} \\ 0 & 0 & 0 & 0 & \rho_{75} & \rho_{76} & 0 & \rho_{78} \\ 0 & 0 & 0 & 0 & \rho_{85} & \rho_{86} & \rho_{87} & 0 \end{pmatrix}.$$

The total Lindblad operator is the sum of all the relaxation and dephasing channels $L = L_h + L_e + L_{\text{h,deph}} + L_{\text{e,deph}}$.

F.12.4 Time evolution of density matrix

The excited state density matrix in Eq. F.15 evolves according to

$$\frac{d\rho}{dt} = L(\rho).$$

The density matrix at a later time t is found by ordering the (8x8) density matrix into a 1x64 list and rewriting the Lindbladian as a 64x64 matrix in the same order. The time dependence of the density matrix is then found my matrix exponentiation

$$\rho_{\text{flat}}(t) = \exp(L_{\text{flat}} t)\rho_{\text{flat}}(0),$$

which can be performed analytically. Rewriting $\rho_{\text{flat}}(t)$ as an 8x8 matrix yields $\rho(t)$.

The parameter t quantifies the amount of relaxation and decoherence that occurs before binding of the exciton to the SF. In this model, no relaxation or decoherence occurs between exciton binding to the SF and recombination.

F.12.5 Binding of exciton to stacking fault

There are two possibilities for the spin spates entering into the stacking fault exciton: either light hole or heavy hole (Sec. F.6). We model exciton binding to the SF by removing certain elements of the density matrix. If only heavy-hole spin states are retained (i.e. set all LH density matrix elements to zero), we are left with $\rho_{\text{hh}}(t)$.

$$\rho_{\text{hh}}(t) = \sum_{e_1,e_2} \sum_{h_1=\pm\frac{3}{2}} \sum_{h_2=\pm\frac{3}{2}} |e_1 h_1\rangle \langle e_1 h_1| \, \rho(t) \, |e_2 h_2\rangle \langle e_2 h_2|$$

In a matrix language this is

$$\rho_{\text{hh}}(t) = K_{\text{hh}} \, \rho(t) \, K_{\text{hh}}^{\dagger}, \quad K_{\text{hh}} = \begin{pmatrix} \begin{matrix} 1 & 0 & 0 & 0 \\ 0 & 0 & 0 & 1 \end{matrix} & 0 \\ 0 & \begin{matrix} 1 & 0 & 0 & 0 \\ 0 & 0 & 0 & 1 \end{matrix} \end{pmatrix}.$$

Similarly, retaining only the light-hole density matrix elements creates $\rho_{\text{lh}}(t)$:

$$\rho_{\text{hh}}(t) = \sum_{e_1,e_2} \sum_{h_1=\pm\frac{3}{2}} \sum_{h_2=\pm\frac{3}{2}} |e_1 h_1\rangle \langle e_1 h_1| \, \rho(t) \, |e_2 h_2\rangle \langle e_2 h_2|$$

In a matrix language this is

$$\rho_{\text{lh}}(t) = K_{\text{lh}} \, \rho(t) \, K_{\text{lh}}^{\dagger}, \quad K_{\text{lh}} = \begin{pmatrix} \begin{matrix} 0 & 1 & 0 & 0 \\ 0 & 0 & 1 & 0 \end{matrix} & 0 \\ 0 & \begin{matrix} 0 & 1 & 0 & 0 \\ 0 & 0 & 1 & 0 \end{matrix} \end{pmatrix}.$$

F.12.6 PL Emission polarization dependence

The PL emission with polarization ϵ_{f} is proportional to $\mathrm{tr}(M_{\epsilon_f}\rho_e M_{\epsilon_f}^\dagger)$ where $\epsilon_f = (x_f, y_f, z_f)$ is the collected polarization. The referenced dipole matrix elements M_{ϵ_f} are the same as M_{ϵ_i} (Eq. F.14) with $i \to f$. We use linearly polarized light for excitation ($\epsilon_i = (\cos\theta_i, \sin\theta_i, 0)$) and collection ($\epsilon_f = (\cos\theta_f, \sin\theta_f, 0)$), which greatly simplifies the polarization dependence of the PL.

Including all relaxation and dephasing processes discussed above, the polarization dependence of PL from heavy-hole excitons is

$$\begin{aligned}\mathrm{PL_{hh}} = \frac{I_o}{72}\Big[&8 + 4\cos 2\theta_f \\ &+ 4\beta_h^3\left[\beta_e + 2\beta_e^2\beta_h\right] \\ &+ 4\beta_h^3\left[2\beta_e + \beta_h + \beta_e^2\beta_h\right]\cos 2\theta_i \\ &+ 4\beta_h^3\left[2\beta_e + \beta_e^2\beta_h\right]\cos 2\theta_f \\ &+ \beta_h^3\left[14\beta_e + \beta_h + \beta_e^2\beta_h\right]\cos(2\theta_f - 2\theta_i) \\ &+ \beta_h^3\left[2\beta_e + \beta_h + \beta_e^2\beta_h\right]\cos(2\theta_f + 2\theta_i)\Big].\end{aligned} \tag{F.17}$$

where $\beta_h = e^{-\Gamma_h t}$ and $\beta_e = e^{-\Gamma_e t}$. We note that the heavy-hole PL does not depend on electron or hole spin dephasing. This arises from the dark-exciton states $\left|\frac{1}{2}, \frac{3}{2}\right\rangle$ and $\left|-\frac{1}{2}, -\frac{3}{2}\right\rangle$. Because dipole transitions are forbidden to dark exciton states, the initial density matrix (Eq. F.15) has zero dark exciton population, and therefore off-diagonal terms of ρ_o corresonding to dark excitons must also be zero, i.e. $0 = \left\langle\frac{1}{2}, \frac{3}{2}\right|\rho_o\left|m_e, m_h\right\rangle = \left\langle-\frac{1}{2}, -\frac{3}{2}\right|\rho_o\left|m_e, m_h\right\rangle$ for all m_e and m_h. Therefore, electron and hole dephasing has no effect on the heavy hole density matrix because the initial density matrix has no off-diagonal terms between heavy-hole states, and because neither electron or hole dephasing alone can cause dephasing of $\left|\frac{1}{2}, \frac{3}{2}\right\rangle$ with respect to $\left|-\frac{1}{2}, -\frac{3}{2}\right\rangle$.

For light holes, the polarization dependence is

$$\begin{aligned}\mathrm{PL_{lh}} = \frac{I_o}{648}\Big[&72 - 36\cos 2\theta_f \\ &+ 4\beta_h^3\left[(17+4\alpha_e+4\alpha_h)\beta_e + 2\beta_e^2\beta_h\right] \\ &- 4\beta_h^3\left[2(7+2\alpha_e+2\alpha_h)\beta_e + 9\beta_h + 5\beta_e^2\beta_h\right]\cos 2\theta_i \\ &- 4\beta_h^3\left[2(7+2\alpha_e+2\alpha_h)\beta_e + 5\beta_e^2\beta_h\right]\cos 2\theta_f \\ &+ \beta_h^3\left[2(23+16\alpha_e+16\alpha_h)\beta_e + 9\beta_h + 25\beta_e^2\beta_h\right]\cos(2\theta_f - 2\theta_i) \\ &+ \beta_h^3\left[2(17-8\alpha_e-8\alpha_h)\beta_e + 9\beta_h + 25\beta_e^2\beta_h\right]\cos(2\theta_f + 2\theta_i)\Big]\end{aligned} \tag{F.18}$$

where $\alpha_h = e^{-\gamma_h t}$ and $\alpha_e = e^{-\Gamma_e t}$. Here, dephasing rates affect the polarization dependence.

In fitting Eq. F.18 and Eq. F.17 with the observed polarization dependence in Fig. F.14, we found that the best fit occurs with the heavy-hole exciton theory with no electron spin flips ($\beta_e = 1$). For no electron spin flips, the arbitrary polarization dependence for hh excitons takes a remarkably simple form:

$$\begin{aligned}\mathrm{PL_{hh}} = \frac{I_o}{36}\Big[&4 + 2\cos 2\theta_f + \beta_h^3\Big[2\,(1+2\beta_h) + 4\,(1+\beta_h)\cos 2\theta_i + 2\,(2+\beta_h)\cos 2\theta_f \\ &+ (7+\beta_h)\cos(2\theta_f - 2\theta_i) + (1+\beta_h)\cos(2\theta_f + 2\theta_i)\Big]\Big].\end{aligned} \tag{F.19}$$

The analogous polarization dependence for light holes with $\beta_e = \alpha_e = \alpha_h = 1$ is

$$\begin{aligned}\mathrm{PL_{lh}} = \frac{I_o}{324}\Big[&36 - 18\cos 2\theta_f + \beta_h^3\Big[2\,(25+2\beta_h) - 2\,(22+14\beta_h)\cos 2\theta_i \\ &- 2\,(22+5\beta_h)\cos 2\theta_f + (55+17\beta_h)\cos(2\theta_f - 2\theta_i) + (1+17\beta_h)\cos(2\theta_f + 2\theta_i)\Big]\end{aligned} \tag{F.20}$$

Eq. F.19 and F.20 are plotted in Fig. F.14(b)-(c) with $\Gamma_h t = 0.57$. The stacking fault studied experimentally in the paper [the left-most triangle in Fig. 3.1(d)] has a coordinate system rotated by 90 degrees compared to the up-most triangle (Fig. F.13) whose polarization dependence is derived here. Therefore, for clarity we have aligned the coordinate systems so that $\theta = 0$ corresponds to exciting along the long edge of the SF when viewed from above.

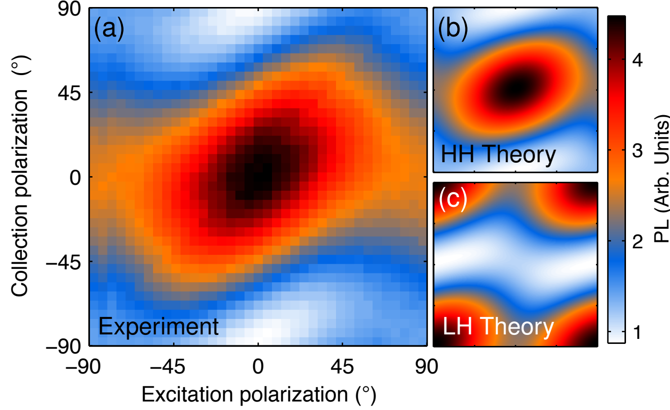

Figure F.14: **a.** Experimental polarization dependence of PL emitted from left SF in Fig. 3.1d ($\theta = 0$ corresponds to vertical.). Excitation laser above band-gap at 1.53 eV. 1.8 K, 40 μW, pinhole in. **b.** Fit of polarization dependence to theory of HH described in Supplemental Sec. F.12. Fit parameters are $\Gamma_h t = (0.572 \pm 0.009)$, $\Gamma_e t = 0$ (fixed at bound), norm $= (13\,400 \pm 200)$, bg $= (600 \pm 20)$, $\Delta\theta_{\text{in}} = (-0.3 \pm 0.5)°$, $\Delta\theta_{\text{out}} = (-2.7 \pm 0.3)°$. The polarization dependence of the up SF also confirms the heavy-hole nature of the SF exciton (Supplementary Sec. F.13). **c.** Plot of LH theory for same parameters as b.

F.13 Experimental polarization dependence

In the main text, we provide the polarization dependence for the left SF in the pyramid structure (Fig. 3.1d). Figure F.15 shows the polarization dependence for the up SF. The polarization dependencies both follow what is expected for heavy-hole excitons (Fig. F.14). The $\theta = 0$ angle for the up SF in Fig. F.15 lies in the horizontal direction (Fig. 3.1), compared with the vertical direction for the left SF in Fig. F.14.

The collection optics introduce a small imperfection in the polarization dependence. Because the collection beam path is taken from the reflected side of a beam splitter placed at 45° (Fig. F.16), the polarization analysis is somewhat non-ideal. The beam splitter used (Thorlabs BST11) has a 40% difference in reflected power for S and P polarizations, and introduces an unknown phase between S and P. It should be emphasized that this issue does not affect the collection of pure S or P light, and hence the main conclusion of the polarization dependence, that the SF exciton is a heavy-hole exciton, is not compromised.

F.14 Methods

F.15 Photoluminescence spectroscopy system

The sample is excited with a continuous wave Sirah Matisse Ti:Sapphire laser. The laser is focused to a spot size of $\sim$1 μm on the sample using an aspheric lens (numerical aperture 0.77) mounted inside a liquid helium immersion cryostat (Janis), see Fig. F.16a. Coarse positioning of the sample was performed with slip-stick positioners (Attocube). For confocal scanning, spatial selectivity is achieved with a pinhole in the intermediate image plane and a scanning mirror to raster the excitation and collection spot over the sample. The photoluminescence (PL) is imaged on a spectrometer (Andor).

The excitation polarization is adjusted using polarizer P_1 (Newport 10GT04) followed by a half-waveplate HWP_1. We chose the lenses f_1, f_2 and the distances d_1, d_2 so that the excitation beam fills the aperture of the final aspheric lens (Edmund Optics 83-674, f = 3.1, NA = 0.77) and is stationary on the aspheric lens as the scanning mirror changes angle. The lenses f_1 and f_2 are spaced by a distance $f_1 + f_2$

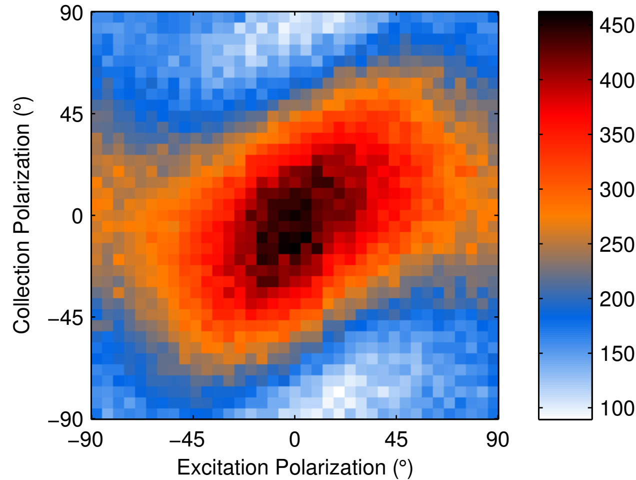

Figure F.15: Polarization dependence of stacking fault emission from the uppermost SF in Fig. 3.1(d). The polarization dependence follows the heavy-hole theory, similar to the left SF shown in Fig. F.14(a). Here $\theta = 0$ is aligned in the horizontal direction. Excitation energy 1.53 eV. 1.73 K. 15 μW.

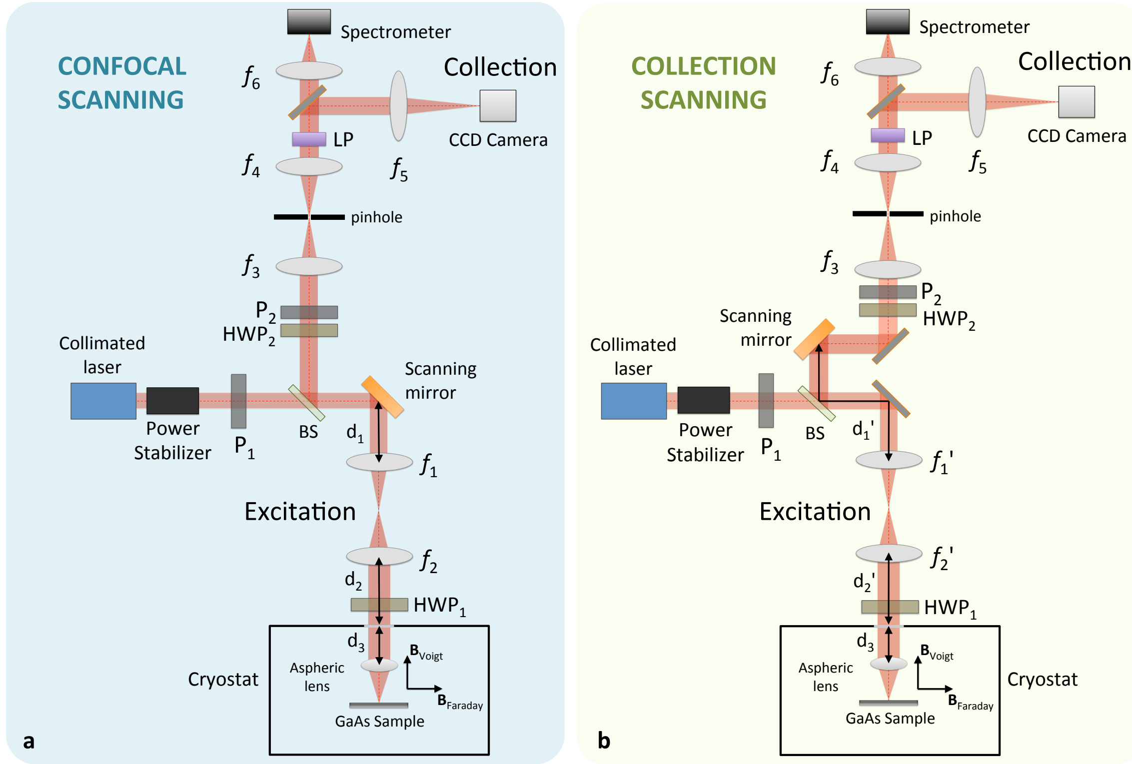

Figure F.16: **a.** Schematic of the scanning confocal microscopy system. A galvanometer mirror scans the focused excitation laser spot across the sample. PL is detected by a spectrometer or a CCD camera. **b.** Schematic of the collection scanning microscopy system. The collection scanning system is similar to the confocal scanning system except that the scanning mirror is moved to the collection path, keeping the excitation beam stationary on the sample while the collection point scans over the sample.

so that the beam stays collimated. The excitation path of the microscope is modeled using ray transfer matrices for free space and thin lenses. For the position of the laser on the final lens to be independent of the scanning mirror angle, we require

$$f_1 - \frac{(d_2 + d_3)f_1}{f_2} + f_2 - \frac{d_1 f_2}{f_1} = 0. \tag{F.21}$$

Using Eq. F.21 and enforcing constraints on the parameters based on the physical size limitations of the system and the cryostat, we chose $f_1 = 30$ mm, $f_2 = 100$ mm, $d_1 = 55$ mm, $d_2 \sim 80$ mm and $d_3 \sim 145$ mm.

The GaAs sample and final aspheric lens are mounted inside of a liquid-He immersion cryostat (Janis Model 7THL-SOM2-11), with focus and positioning controlled by piezo positioners (Attocube ANC300, ANPX51). The scattered laser and photoluminescence from the sample is collected by the aspheric lens inside the cryostat, and sent down the collection path with a 70/30 beam splitter (Thorlabs BST11) oriented to maximize collection efficiency. The collected polarization is set by rotating half-waveplate HWP_2 before linear polarizer P_2 (Newport 10GT04). The collection beam is spatially filtered through a 100 μm pinhole with two lenses (f_3 and f_4, Thorlabs AC254-100-B). For photoluminescence imaging, the collected PL is spectrally analyzed using a spectrometer (Andor Technology SR-750-01). Excitation light can optionally be filtered out using a long-pass filter (Semrock FF01-83012-25), useful for observing the stacking fault edge emission. By inserting a mirror, the excitation laser or PL can be viewed in a CCD camera (Celestron Skyris CCD) for focusing and sample positioning.

In order to investigate exciton transport properties, the excitation scanning confocal microscopy system is modified so the excitation beam remains stationary on the sample while the collection point scans over the sample (Fig. F.16b). The scanning mirror (Mad City Labs Nano-MTA2X) is placed in the collection path of the confocal microscopy system. Due to a smaller scanning angle of the piezo scanning mirror compared with the galvo scanning mirror, the lenses f_1, f_2, d_1 and d_2 ($f_1' = 100$ mm, $f_2' = 150$ mm, $d_1' \sim 160$ mm, $d_2' \sim 80$ mm) were modified to increase field of view while still satisfying Eq. F.21.

The confocal scans are calibrated by imaging a resolution test target (Thorlabs 1951 USAF Resolution Test Target R1DS1P). This scaling is found to agree very well with the expected geometrical size of the triangular features of the stacking faults observed in PL. The known length of the stacking fault structures is then used to calibrate the spatial scale of the images for collection-only scans.

The diffraction limited optical resolution of the imaging system can be estimated using the Abbe diffraction limit $d = \frac{\lambda}{2NA}$, where λ is the excitation wavelength, NA the numerical aperture of the final aspheric lens, and d the minimum resolvable feature size [87]. The theoretical minimum spot size FWHM is less than 384 nm ($0.75\lambda/2$NA, using an excitation wavelength of 810 nm and NA= 0.77) [169]. By taking confocal scans of point emitters (quantum dots), we measured a system resolution of FWHM $\sim$

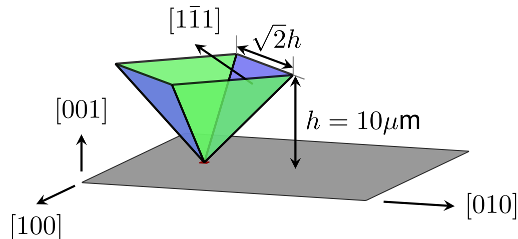

Figure F.17: Simple stacking fault geometry implies that the observed long edge length of the photoluminescence (PL) isosceles triangles should be 14.14 μ m, in good agreement with the observed PL length of approximately 14.1 μm. The stacking faults are equilateral triangles.

600 nm.

F.16 2D Exciton Transport

We performed photoluminescence excitation (PLE) spectroscopy of the 2D stacking fault emission line by exciting the up stacking fault at 1.4929 eV and collecting the right stacking fault at 1.4961 eV (Fig. F.18). In this experiment, 2D excitons are created in the up SF and travel through the 1D edge into the neighboring right SF. The observed luminescence occurs 3.2 meV above the excitation energy, which is much larger than the thermal energy ($k_B T = 0.16$ meV). The tunneling of the SF exciton to higher energy could be explained by exciton-exciton interactions.

To further confirm that transport is due to the 2D SF exciton and not to diffusion of bulk carriers, we set the laser resonant with the higher energy SF exciton, and collected at the low energy SF exciton energy. PL is observed at the right and left SF when the laser spot is spatially located on the up SF (Fig. F.19a) and not when the laser is focused outside of the pyramid (Fig. F.19b). This confirms that the excitation of 2D excitons in the left and right SF is due to transport from the up SF, and not due to a bulk diffusion process.

The same phenomenon is observed when the collection energy is changed to the broad band edge emission (Fig. F.19d-f). The 1D edge emission is only observed when the excitation laser is spatially located at the up SF and not when it is spatially located outside the pyramid structure.

Fig. F.20a-c shows the raw data used for Fig. 3.5a. In the laser reflection image (Fig. F.20a), a large amount of laser scatter is observed. The PL image (Fig. F.20b) shows some luminescence from the SF on top of emission from donor-acceptor pairs (DAP), an avenue of radiative recombination in bulk GaAs. Fig. 3.5a is made by a linear interpolation of the DAP emission on the higher and lower energy sides of the SF line. The line is then used as a background to skim off the SF PL.

Fig. F.20d shows the raw data used for Fig. 3.5c. In this scan, the DAP emission at each spatial point is fit to an exponential, and the interpolated data is used as a background to find the edge emission. Fig. F.20d shows the emission in the edge collection region without any subtraction. When the laser excites outside of the SF pyramid structure, no edge PL is observed (Fig. F.20e). This confirms that the excitation of edge PL occurs through the 2D SF exciton rather than through a bulk process.

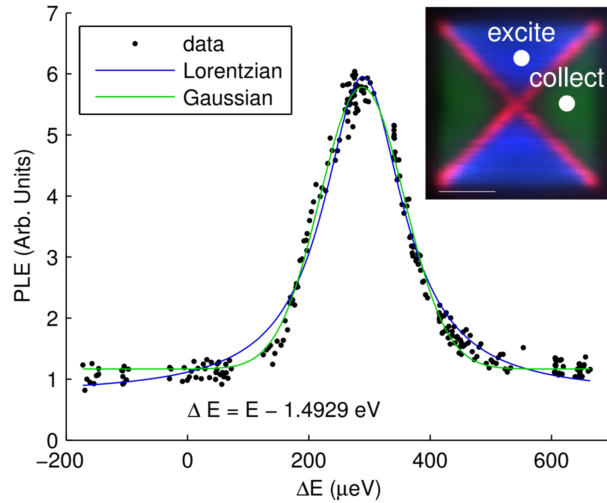

Figure F.18: PLE spectroscopy exciting on the up SF exciton at 1.4929 eV and collection of right SF at 1.4961 eV. The PLE line follows a Gaussian and not a Lorentzian. The FWHM of the Gaussian line is (164 ± 3) μeV. T = 1.82 K, 19.3 μW. Excitation and collection are cross polarized. Inset shows Fig. 3.1c from the main text with the excitation and collection spots marked. Scale bar 5 μm.

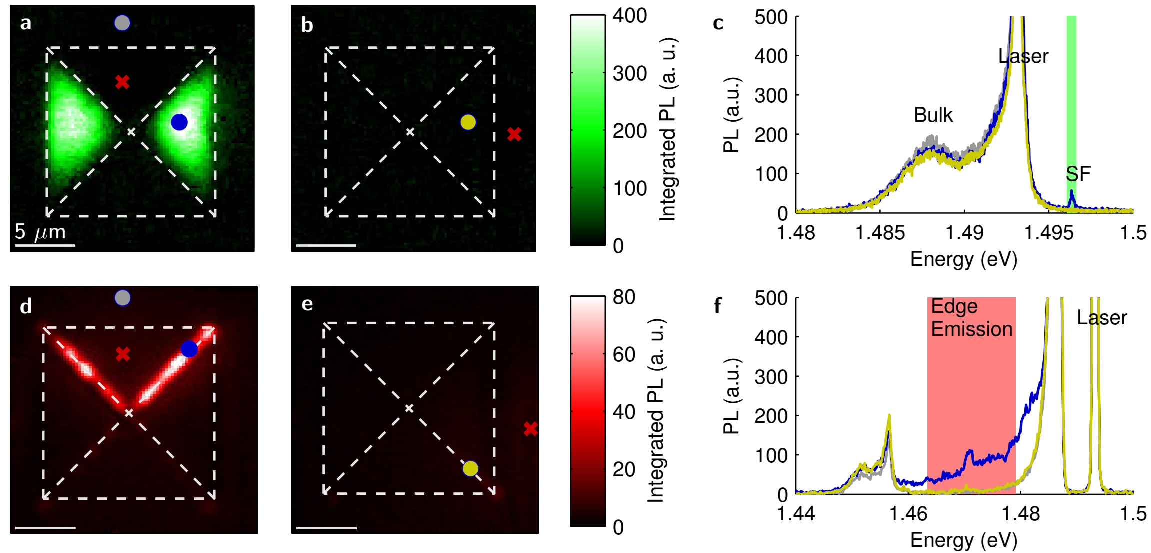

Figure F.19: **a-b**. Collection confocal scan with laser focused on up SF or outside the pyramid (red cross denotes position of laser). The excitation energy is resonant with the low energy (up) SF at 1.493 eV with excitation power 20 μW. **c**. Spectra at locations specified by colored dots in a and b. The green rectangle shows the collected energy range for the images in a and b. **d-e** Same as a-b, but collecting the 1D emission (red rectangle in f) with excitation power 400 μW. **f**. Spectra at locations specified by colored dots in d and e. The abrupt drop of the PL intensity above 1.492 eV is due to an 831 nm long pass filter. The red bar shows the collected energy range for d and e.

F.17 Stacking Fault Generation

The MBE growth was performed with the relatively low As beam equivalent pressure of 8×10^{-6} torr at a pyrometer reading of 600° C. Against our general practice, the growth was not started with a non-intentionally doped GaAs-seed-layer, but right with the 5 nm AlAs part of the first period of the 10× 5 nm/5 nm AlAs/GaAs short-period superlattice. The superlattice was then covered by 100 nm AlAs, all not intentionally doped. The top 10 μm GaAs-layer was grown with a low n-type doping of the Si-cell, operated at the unusually low temperature of 770° C. We speculate that the MBE-growth start with the 5 nm AlAs layer, together with the low As-pressure,

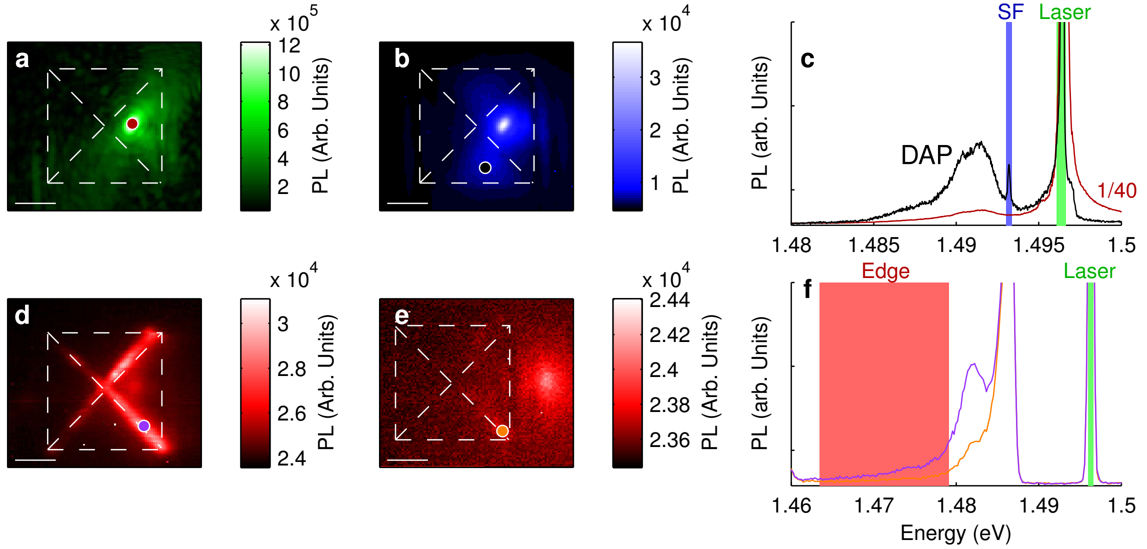

Figure F.20: Resonant excitation of stacking fault exciton and observation of transport without background subtraction. **a.** Laser spatially fixed on right SF at 1.496 eV and collecting laser scatter. Integration band is the green rectangle in c. **b.** Same scan as a, but collecting PL at 1.493 eV. The laser tail and donor-acceptor pair emission are visible as broad backgrounds. Same data as in Fig. 3.5a, except processed without subtraction. **c.** Spectra at colored dots in a and b. 'Laser' and 'SF' shaded ranges indicate the integration bands plotted in a and b respectively. DAP emission is visible. **d.** Laser excites right SF, and PL is collected from the 1D SF edges. Same data as Fig. 3.5c, except processed without subtraction of DAP line. **e.** Same as d except laser focused off the SF pyramid. Luminescence from the 1D edges no longer observed. **f.** Spectra at locations specified by colored dots in d and f. Luminescence collected from the 1D stacking fault edge is drastically reduced when exciting outside the SF pyramid compared with exciting the right SF. a-c used 20 μW at 5.8 K. d-f used 400 μW at 6.0 K.

initiated the generation of the observed stacking faults in the sample.

F.18 SEM of surface

The stacking fault defect sample is a 10 μm GaAs epitaxial layer grown on a (001) oriented GaAs substrate. In this sample, we observe two different stacking fault (SF) structures, an inverted pyramid structure and a trapezoid sturcture (also called a pair defect) consisting of two parallel SFs, as illustrated in Fig. F.21a. Due to the

geometry of the structures (Fig. F.17), the intersection of the SF with the epilayer surface is a 14.14 μm long feature (Fig. F.17).

Figure F.21b shows a scanning electron micrograph (SEM) of the sample surface. When a pair-defect is oriented in the left or right direction, the intersection with the substrate surface is an oval defect [106]. On the other hand, when a pair defect is oriented in the up or down direction, no oval defect is observed at the surface. The majority of the pair-defects are oriented in the left-right direction, which can be seen both in the SEM (Fig. F.21) and the optical confocal scan (Fig. 4.1). The pyramid structure contains four different {111} SF planes, and has four different line surface defects as shown in Fig. F.21(c).

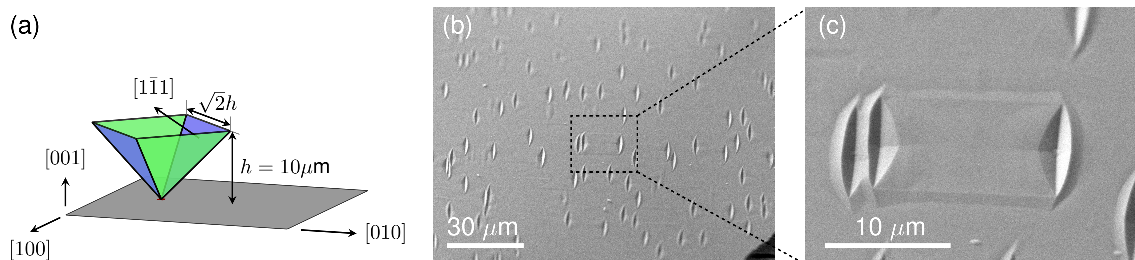

Figure F.21: (a) Geometry of the pyramid structure (left). The angle between the stacking fault plane and the substrate is $\tan^{-1}(\sqrt{2})$. Due to this geometry, the 10 μm thick epitaxial layer results in a 14.14 μm line defect on the surface. (b) SEM of the sample surface. The sample is tilted at around 60° in the up down direction, making the pyramid defect (outlined) look wider than tall. (c) Detail on the pyramid structure.

Appendix G

SELECTED CHARACTER TABLES

Table G.1: Character table for double group T_d [55]. B_x, B_y, B_z correspond to the three cartesian components of an integer angular momentum. T_d is the symmetry group of a zinc-blende crystal

T_d	E	$\overline{E}$	$8C_3$	$8\overline{C}_3$	$3C_2$ $3\overline{C}_2$	$6S_4$	$6\overline{S}_4$	$6\sigma_d$ $6\overline{\sigma}_d$	Bases
Γ_1	1	1	1	1	1	1	1	1	xyz
Γ_2	1	1	1	1	1	-1	-1	-1	$B_xB_yB_z$
Γ_3	2	2	-1	-1	2	0	0	0	$(2z^2-x^2-y^2), \sqrt{3}(x^2-y^2)$
Γ_4	3	3	0	0	-1	1	1	-1	B_x, B_y, B_z
Γ_5	3	3	0	0	-1	-1	-1	1	x, y, z
Γ_6	2	-2	1	-1	0	$\sqrt{2}$	$-\sqrt{2}$	0	$\lvert\frac{1}{2},\frac{1}{2}\rangle, \lvert\frac{1}{2},-\frac{1}{2}\rangle$
Γ_7	2	-2	1	-1	0	$-\sqrt{2}$	$\sqrt{2}$	0	$\Gamma_6 \otimes \Gamma_2$
Γ_8	4	-4	-1	1	0	0	0	0	$\lvert\frac{3}{2},\frac{3}{2}\rangle, \lvert\frac{3}{2},\frac{1}{2}, \lvert\frac{3}{2},-\frac{1}{2}, \lvert\frac{3}{2},-\frac{3}{2}\rangle$

Table G.2: Character table for the double group of C_{3v}. Double group characters given in Ref. [31].

C_{3v}	E	$\overline{E}$	C_3 $\overline{C}_3^2$	C_3^2 $\overline{C}_3$	$3\sigma_v$	$3\overline{\sigma}_v$	Basis Functions
Γ_1	1	1	1	1	1	1	Scalar; z; x^2+y^2; $B_x^2+B_y^2$; $B_y^3-3B_yB_x^2$; I; σ_y^{hh}
Γ_2	1	1	1	1	-1	-1	B_z; $B_x^3-3B_xB_y^2$; σ_z^e; σ_x^{hh}; σ_z^{hh}; σ_z^{lh}
Γ_3	2	2	-1	-1	0	0	(K_x, K_y); $(-B_y, B_x)$; $(-\sigma_y^e, \sigma_x^e)$; $(-\sigma_y^{lh}, \sigma_x^{lh})$; $(B_y^2-B_x^2, 2B_xB_y)$
Γ_4	2	-2	1	-1	0	0	$\left\lvert\frac{1}{2},-\frac{1}{2}\right\rangle, \left\lvert\frac{1}{2},\frac{1}{2}\right\rangle$
Γ_5	1	-1	-1	1	i	$-i$	$\frac{1}{\sqrt{2}}\left(\left\lvert\frac{3}{2},-\frac{3}{2}\right\rangle + i\left\lvert\frac{3}{2},\frac{3}{2}\right\rangle\right)$
Γ_6	1	-1	-1	1	$-i$	i	$\frac{1}{\sqrt{2}}\left(\left\lvert\frac{3}{2},-\frac{3}{2}\right\rangle - i\left\lvert\frac{3}{2},\frac{3}{2}\right\rangle\right)$

Table G.3: Character table for double group O_h [55]. Double group characters given in Ref. [122]. We use the Koster notation. The superscript on the specification of the irreducible representation specifies the parity under spatial inversion. Basis functions for Γ_3^+ are $x^2 - y^2, 2z^2 - x^2 - y^2$. Basis functions for Γ_5^- are $z(x^2-y^2), x(y^2-z^2), y(z^2-x^2)$.

O_h	E	$\overline{E}$	$8C_3$	$8\overline{C}_3$	$3C_2$ $3\overline{C}_2$	$6C_4$	$6\overline{C}_4$	$6C_2'$ $6\overline{C}_2'$	I	$\overline{I}$	$8S_6$	$8\overline{S}_6$	$3\sigma_h$ $3\overline{\sigma}_h$	$6S_4$	$6\overline{S}_4$	$6\sigma_d$ $6\overline{\sigma}_d$	Basis fn's
Γ_1^+	1	1	1	1	1	1	1	1	1	1	1	1	1	1	1	1	scalar
Γ_2^+	1	1	1	1	1	-1	-1	-1	1	1	1	1	1	-1	-1	-1	$B_xB_yB_z$
Γ_3^+	2	2	-1	-1	2	0	0	0	2	2	-1	-1	2	0	0	0	$x^2 - y^2...$
Γ_4^+	3	3	0	0	-1	1	1	-1	3	3	0	0	-1	1	1	-1	B_x, B_y, B_z
Γ_5^+	3	3	0	0	-1	-1	-1	1	3	3	0	0	-1	-1	-1	1	$\Gamma_4^+ \otimes \Gamma_2^+$
Γ_1^-	1	1	1	1	1	1	1	1	-1	-1	-1	-1	-1	-1	-1	-1	
Γ_2^-	1	1	1	1	1	-1	-1	-1	-1	-1	-1	-1	-1	1	1	1	xyz
Γ_3^-	2	2	-1	-1	2	0	0	0	-2	-2	1	1	-2	0	0	0	
Γ_4^-	3	3	0	0	-1	1	1	-1	-3	-3	0	0	1	-1	-1	1	x, y, z
Γ_5^-	3	3	0	0	-1	-1	-1	1	-3	-3	0	0	1	1	1	-1	$\Gamma_4^- \otimes \Gamma_2^+$
Γ_6^+	2	-2	1	-1	0	$\sqrt{2}$	$-\sqrt{2}$	0	2	-2	1	-1	0	$\sqrt{2}$	$-\sqrt{2}$	0	$j = 1/2$
Γ_7^+	2	-2	1	-1	0	$-\sqrt{2}$	$\sqrt{2}$	0	2	-2	1	-1	0	$-\sqrt{2}$	$\sqrt{2}$	0	$\Gamma_6^+ \otimes \Gamma_2^+$
Γ_8^+	4	-4	-1	1	0	0	0	0	4	-4	-1	1	0	0	0	0	$j = 3/2$
Γ_6^-	2	-2	1	-1	0	$\sqrt{2}$	$-\sqrt{2}$	0	-2	2	-1	1	0	$-\sqrt{2}$	$\sqrt{2}$	0	$\Gamma_6^+ \otimes \Gamma_1^-$
Γ_7^-	2	-2	1	-1	0	$-\sqrt{2}$	$\sqrt{2}$	0	-2	2	-1	1	0	$\sqrt{2}$	$-\sqrt{2}$	0	$\Gamma_7^+ \otimes \Gamma_1^-$
Γ_8^-	4	-4	-1	1	0	0	0	0	-4	4	1	-1	0	0	0	0	$\Gamma_8^+ \otimes \Gamma_1^-$

BIBLIOGRAPHY

[1] http://www.ioffe.ru/SVA/NSM/Semicond/, 2016. Accessed: 2016-05-16.

[2] Best research-cell efficiencies, January 2016. National Renewable Energy Laboratory, Golden, CO.

[3] E. Abrahams. Donor electron spin relaxation in silicon. *Phys. Rev.*, 107:491–496, July 1957.

[4] M. S. Abrahams and C. J. Buiocchi. Twins and stacking faults in vapor grown GaAs. *Journal of Physics and Chemistry of Solids*, 28(6):927–930, June 1967.

[5] N. Akopian, G. Patriarche, L. Liu, J. C. Harmand, and V. Zwiller. Crystal phase quantum dots. *Nano Lett.*, 10(4):1198–1201, April 2010.

[6] R. E. Algra, M. A. Verheijen, M. T. Borgstrom, L. F. Feiner, G. Immink, W. J. P. van Enckevort, E. Vlieg, and E. P. A. M. Bakkers. Twinning superlattices in indium phosphide nanowires. *Nature*, 456(7220):369–372, November 2008.

[7] S. Amasha, K. MacLean, I. P. Radu, D. M. Zumbühl, M. A. Kastner, M. P. Hanson, and A. C. Gossard. Electrical control of spin relaxation in a quantum dot. *Phys. Rev. Lett.*, 100:046803, Jan 2008.

[8] A. Amo, T. C. H. Liew, C. Adrados, R. Houdre, E. Giacobino, A. V. Kavokin, and A. Bramati. Exciton-polariton spin switches. *Nature Photonics*, 4(6):361–366, April 2010.

[9] N. W. Ashcroft and N. D. Mermin. *Solid State Physics*. Cengage Learning, 1 edition, January 1976.

[10] A. Aspuru-Guzik, A. D. Dutoi, P. J. Love, and M. Head-Gordon. Simulated quantum computation of molecular energies. *Science*, 309(5741):1704–1707, September 2005.

[11] S. Assali, I. Zardo, S. Plissard, D. Kriegner, M. A. Verheijen, G. Bauer, A. Meijerink, A. Belabbes, F. Bechstedt, J. E. M. Haverkort, and E. P. A. M. Bakkers.

Direct band gap wurtzite gallium phosphide nanowires. *Nano Lett.*, 13(4):1559–1563, April 2013.

[12] J. E. Ayers. *Heteroepitaxy of semiconductors: theory, growth, and characterization*. CRC Press, 1 edition, January 2007.

[13] G. Balasubramanian, P. Neumann, D. Twitchen, M. Markham, R. Kolesov, N. Mizuochi, J. Isoya, J. Achard, J. Beck, J. Tissler, V. Jacques, P. R. Hemmer, F. Jelezko, and J. Wrachtrup. Ultralong spin coherence time in isotopically engineered diamond. *Nat. Mater.*, 8:383–387, 2009.

[14] R. Balili, B. Nelsen, D. W. Snoke, L. Pfeiffer, and K. West. Role of the stress trap in the polariton quasiequilibrium condensation in GaAs microcavities. *Phys. Rev. B*, 79:075319, February 2009.

[15] S. D. Barrett and P. Kok. Efficient high-fidelity quantum computation using matter qubits and linear optics. *Phys. Rev. A*, 71, 2005.

[16] A. Belabbes, C. Panse, J. Furthmüller, and F. Bechstedt. Electronic bands of III-V semiconductor polytypes and their alignment. *Phys. Rev. B*, 86:075208, 2012.

[17] G. Benenti, G. Casati, and G. Strini. *Principles of quantum computation and information - vol.1: basic concepts*. World Scientific Pub Co Inc, October 2004.

[18] P. R. Berman and V. S. Malinovsky. *Principles of laser spectroscopy and quantum optics*. Princeton University Press, Princeton, New Jersey, December 2011.

[19] H. Bernien, B. Hensen, W. Pfaff, G. Koolstra, M. S. Blok, L. Robledo, T. H. Taminiau, M. Markham, D. J. Twitchen, L. Childress, and R. Hanson. Heralded entanglement between solid-state qubits separated by three metres. *Nature*, 497(7447):86–90, May 2013.

[20] F. Berski, J. Hübner, M. Oestreich, A. Ludwig, A. D. Wieck, and M. Glazov. Interplay of electron and nuclear spin noise in n-type GaAs. *Phys. Rev. Lett.*, 115:176601, October 2015.

[21] G. L. Bir and G. E. Pikus. *Symmetry and strain-induced effects in semiconductors*. Halsted Press, New York, 1974.

[22] J. L. Birman. Some selection rules for band-band transitions in wurtzite structure. *Phys. Rev.*, 114:1490–1492, 1959.

[23] R. Blatt and C. F. Roos. Quantum simulations with trapped ions. *Nature Physics*, 8(4):277–284, April 2012.

[24] D. F. Blossey. Wannier exciton in an alectric field. I. optical absorption by bound and continuum states. *Phys. Rev. B*, 2:3976–3990, November 1970.

[25] W. Bludau and E. Wagner. Impact ionization of excitons in GaAs. *Phys. Rev. B*, 13:5410–5414, June 1976.

[26] E. Hal Bogardus and H. Barry Bebb. Bound-Exciton, Free-Exciton, Band-Acceptor, Donor-Acceptor, and Auger Recombination in GaAs. *Physical Review*, 176(3):993–1002, December 1968.

[27] K. Böhm and B. Fischer. Photoluminescence at dislocations in GaAs and InP. *Journal of Applied Physics*, 50(8):5453–5460, August 1979.

[28] J. Böning, A. Filinov, and M. Bonitz. Crystallization of an exciton superfluid. *Phys. Rev. B*, 84:075130, Aug 2011.

[29] K. Bothe, R. Sinton, and J. Schmidt. Fundamental boron-oxygen-related carrier lifetime limit in mono- and multicrystalline silicon. *Prog. Photovolt: Res. Appl.*, 13(4):287–296, June 2005.

[30] E. Brion, L. H. Pedersen, M. Saffman, and K. Mølmer. Error correction in ensemble registers for quantum repeaters and quantum computers. *Phys. Rev. Lett.*, 100:110506, Mar 2008.

[31] G. Burns. *Introduction to group theory with applications: materials science and technology.* Academic Press, London, January 1977.

[32] L. V. Butov. Condensation and pattern formation in cold exciton gases in coupled quantum wells. *Journal of Physics: Condensed Matter*, 16(50):R1577–R1613, December 2004.

[33] L. V. Butov, A. C. Gossard, and D. S. Chemla. Macroscopically ordered state in an exciton system. *Nature*, 418(6899):751–754, August 2002.

[34] L. V. Butov, C. W. Lai, A. L. Ivanov, A. C. Gossard, and D. S. Chemla. Towards Bose–Einstein condensation of excitons in potential traps. *Nature*, 417:47, 2002.

[35] L. V. Butov, A. Zrenner, G. Abstreiter, G. Böhm, and G. Weimann. Condensation of indirect excitons in coupled AlAs/GaAs quantum wells. *Phys. Rev. Lett.*, 73:304–307, Jul 1994.

[36] C. Cabrillo, J. Cirac, P. García-Fernández, and P. Zoller. Creation of entangled states of distant atoms by interference. *Physical Review A*, 59(2):1025–1033, February 1999.

[37] M. Cardona, N. E. Christensen, and G. Fasol. Relativistic band structure and spin-orbit splitting of zinc-blende-type semiconductors. *Phys. Rev. B*, 38:1806–1827, July 1988.

[38] M. Cardona, K. L. Shaklee, and F. H. Pollak. Electroreflectance at a semiconductor-electrolyte interface. *Phys. Rev.*, 154:696–720, February 1967.

[39] P. Caroff, J. Bolinsson, and J. Johansson. Crystal phases in III–V nanowires: from random toward engineered polytypism. *IEEE Journal of Selected Topics in Quantum Electronics*, 17(4):829–846, July 2011.

[40] A. R. R. Carvalho, F. Mintert, and A. Buchleitner. Decoherence and multipartite entanglement. *Phys. Rev. Lett.*, 93:230501, 2004.

[41] Y. G. Chai, Y-c, and T. Hierl. Elimination of “pair” defects from GaAs layers grown by molecular beam epitaxy. *Applied Physics Letters*, 47(12):1327–1329, December 1985.

[42] E. A. Chekhovich, A. B. Krysa, M. S. Skolnick, and A. I. Tartakovskii. Direct measurement of the hole-nuclear spin interaction in single InP/GaInP quantum dots using photoluminescence spectroscopy. *Phys. Rev. Lett.*, 106(2):027402, January 2011.

[43] A. E. Cherednichenko and V. A. Kiselev. Surface aspects of excitons in semiconductors. *Progress in Surface Science*, 36(3):179–287, January 1991.

[44] L. Childress, J. M. Taylor, A. S. Sorensen, and M. D. Lukin. Fault-Tolerant Quantum Repeaters with Minimal Physical Resources and Implementations Based on Single-Photon Emitters. *Phys. Rev. A*, 72:52330, 2005.

[45] S. L. Chuang. *Physics of Photonic Devices (Wiley Series in Pure and Applied Optics)*. John Wiley & Sons, Inc., Hoboken, New Jersey, 2 edition, January 2009.

[46] A. Colli, E. Pelucchi, and A. Franciosi. Controlling the native stacking fault density in II-VI/III-V heterostructures. *Applied Physics Letters*, 83(1):81–83, July 2003.

[47] P. Corfdir, C. Hauswald, J. K. Zettler, T. Flissikowski, J. Lähnemann, S. Fernández-Garrido, L. Geelhaar, H. T. Grahn, and O. Brandt. Stacking faults as quantum wells in nanowires: Density of states, oscillator strength, and radiative efficiency. *Physical Review B*, 90(19), November 2014.

[48] P. Corfdir and P. Lefebvre. Importance of excitonic effects and the question of internal electric fields in stacking faults and crystal phase quantum discs: The model-case of GaN. *Journal of Applied Physics*, 112(5):053512, September 2012.

[49] K. De Greve, S. M. Clark, D. Sleiter, K. Sanaka, T. D. Ladd, M. Panfilova, A. Pawlis, K. Lischka, and Y. Yamamoto. Photon antibunching and magnetospectroscopy of a single fluorine donor in ZnSe. *Applied Physics Letters*, 97(24):241913, 2010.

[50] C. de Mello Donegá, M. Bode, and A. Meijerink. Size- and temperature-dependence of exciton lifetimes in CdSe quantum dots. *Phys. Rev. B*, 74:085320, August 2006.

[51] C. R. Dean, L. Wang, P. Maher, C. Forsythe, F. Ghahari, Y. Gao, J. Katoch, M. Ishigami, P. Moon, M. Koshino, T. Taniguchi, K. Watanabe, K. L. Shepard, J. Hone, and P. Kim. Hofstadter's butterfly and the fractal quantum Hall effect in moiré superlattices. *Nature*, 497(7451):598–602, May 2013.

[52] T. Dekorsy, T. Pfeifer, W. Kütt, and H. Kurz. Subpicosecond carrier transport in GaAs surface-space-charge fields. *Phys. Rev. B*, 47:3842–3849, Feb 1993.

[53] M. H. Devoret and R. J. Schoelkopf. Superconducting Circuits for Quantum Information: An Outlook. *Science*, 339(6124):1169–1174, March 2013.

[54] G. Dresselhaus. Spin-orbit coupling effects in zinc blende structures. *Phys. Rev.*, 100:580–586, 1955.

[55] M. S. Dresselhaus, G. Dresselhaus, and A. Jorio. *Group Theory: Application to the Physics of Condensed Matter*. Springer, Berlin, Germany, 2008 edition, January 2008.

[56] M. V. Gurudev Dutt, L. Childress, L. Jiang, E. Togan, J. Maze, F. Jelezko, A. S. Zibrov, P. R. Hemmer, and M. D. Lukin. Quantum register based on individual electronic and nuclear spin qubits in diamond. *Science*, 316(5829):1312–1316, 2007.

[57] M. I. Dyakonov. *Spin physics in semiconductors*. Springer-Verlag, Berlin, Heidelberg, 2008.

[58] M. I. D'yakonov, V. A. Marushchak, V. I. Perel', and A. N. Titkov. The effect of strain on the spin relaxation of conduction electrons in III-V semiconductors. *Zh. Eksp. Teor. Fiz.*, 90:655–1123, 1986.

[59] M. I. Dyakonov and V. I. Perel'. Optical orientation in a system of electrons and lattice nuclei in semiconductors. Theory. *JETP*, 38:177, January 1974.

[60] M. I. Dyakonov and V. I. Perel. *Optical orientation*, chapter 2, pages 15–30. North-Holland, 1984.

[61] R. I. Dzhioev, K. V. Kavokin, V. L. Korenev, M. V. Lazarev, Ya, M. N. Stepanova, B. P. Zakharchenya, D. Gammon, and D. S. Katzer. Low-temperature spin relaxation in n-type GaAs. *Physical Review B*, 66:245204, December 2002.

[62] A. Efros, M. Rosen, M. Kuno, M. Nirmal, D. J. Norris, and M. Bawendi. Band-edge exciton in quantum dots of semiconductors with a degenerate valence band: Dark and bright exciton states. *Phys. Rev. B*, 54:4843–4856, August 1996.

[63] R. J. Elliott. Spin-orbit coupling in band theory–character tables for some "double" space groups. *Phys. Rev.*, 96:280–287, 1954.

[64] J. M. Elzerman, R. Hanson, L. H. Willems van Beveren, B. Witkamp, L. M. K. Vandersypen, and L. P. Kouwenhoven. Single-shot read-out of an individual electron spin in a quantum dot. *Nature*, 430(6998):431–435, 2004.

[65] P. R. Emtage. Binding of electrons, holes, and excitons to dislocations in insulators. *Phys. Rev.*, 163:865–872, 1967.

[66] R. H. Finch, H. J. Queisser, G. Thomas, and J. Washburn. Structure and Origin of Stacking Faults in Epitaxial Silicon. *Journal of Applied Physics*, 34(2):406–415, February 1963.

[67] E. Finkman, M. D. Sturge, and R. Bhat. Oscillator strength, lifetime and degeneracy of resonantly excited bound excitons in GaAs. *Journal of Luminescence*, 35(4):235–238, July 1986.

[68] M. M. Fogler, L. V. Butov, and K. S. Novoselov. High-temperature superfluidity with indirect excitons in van der Waals heterostructures. *Nature Communications*, 5, July 2014.

[69] S. Francoeur, J. F. Klem, and A. Mascarenhas. Optical spectroscopy of single impurity centers in semiconductors. *Phys. Rev. Lett.*, 93:067403, Aug 2004.

[70] S. Francoeur and S. Marcet. Effects of symmetry-breaking perturbations on excitonic states bound to systems of reduced symmetry. *Journal of Applied Physics*, 108(4), 2010.

[71] D. M. Frenkel. Spin relaxation in GaAs-$Al_xGa_{1-x}As$ heterostructures in high magnetic fields. *Phys. Rev. B*, 43:14228–14231, 1991.

[72] K.-M. C. Fu. *Optical Manipulation of Electron Spins Bound to Neutral Donors in GaAs*. PhD thesis, Stanford University, June 2007.

[73] K.-M. C. Fu, C. Santori, C. Stanley, M. C. Holland, and Y. Yamamoto. Coherent population trapping of electron spins in a high-purity n-type GaAs semiconductor. *Phys. Rev. Lett.*, 95:187405, October 2005.

[74] K.-M. C. Fu, W. Yeo, S. Clark, C. Santori, C. Stanley, M. C. Holland, and Y. Yamamoto. Millisecond spin-flip times of donor-bound electrons in GaAs. *Physical Review B*, 74:121304, September 2006.

[75] K. K. Fung, N. Wang, and I. K. Sou. Direct observation of stacking fault tetrahedra in ZnSe/GaAs(001) pseudomorphic epilayers by weak beam dark-field transmission electron microscopy. *Appl. Phys. Lett.*, 71(9):1225–1227, September 1997.

[76] V. F. Gantmakher and Y. B. Levinson. *Carrier scattering in metals and semiconductors*. North-Holl., 1987.

[77] A. Gavini and M. Cardona. Modulated piezoreflectance in semiconductors. *Phys. Rev. B*, 1:672–682, 1970.

[78] J. F. Geisz, J. M. Olson, M. J. Romero, C. S. Jiang, and A. G. Norman. Lattice-mismatched GaAsP Solar Cells Grown on Silicon by OMVPE. In *Conference Record of the 2006 IEEE 4th World Conference on Photovoltaic Energy Conversion*, volume 1, pages 772–775. IEEE, May 2006.

[79] M. M. Glazov. Spin noise of localized electrons: Interplay of hopping and hyperfine interaction. *Phys. Rev. B*, 91:195301, May 2015.

[80] A. V. Gorbunov and V. B. Timofeev. Large-scale coherence of the bose condensate of spatially indirect excitons. *JETP Letters*, 84(6):329, 2006.

[81] A. M. Graham, P. Corfdir, M. Heiss, S. Conesa-Boj, E. Uccelli, Fontcuberta, and R. T. Phillips. Exciton localization mechanisms in wurtzite/zinc-blende GaAs nanowires. *Phys. Rev. B*, 87:125304, March 2013.

[82] E. F. Gross, B. P. Zakharchenya, and O. V. Konstantinov. Effect of magnetic field inversion in spectra of exciton absorption in CdSe crystal. *Sov. Phys. Solid State*, 3:221, 1961.

[83] M. Gueron. Density of the Conduction Electrons at the Nuclei in Indium Antimonide. *Phys. Rev.*, 135:A200–A205, July 1964.

[84] S. Guha, J. M. DePuydt, M. A. Haase, J. Qiu, and H. Cheng. Degradation of II-VI based blue-green light emitters. *Applied Physics Letters*, 63(23):3107–3109, December 1993.

[85] J. E. M. Haverkort, M. P. Schuwer, M. R. Leys, and J. H. Wolter. Spatial variations of photoluminescence line broadening around oval defects in GaAs/AlGaAs multiple quantum wells. *Semiconductor Science and Technology*, 7(1A), 1992.

[86] J. R. Haynes. Experimental Proof of the Existence of a New Electronic Complex in Silicon. *Phys. Rev. Lett.*, 4:361–363, April 1960.

[87] E. Hecht. *Optics (4th Edition)*. Addison-Wesley, 4 edition, August 2001.

[88] W. Heinke and H. J. Queisser. Photoluminescence at dislocations in GaAs. *Phys. Rev. Lett.*, 33:1082–1084, 1974.

[89] D. Heiss, M. Kroutvar, J. J. Finley, and G. Abstreiter. Progress towards single spin optoelectronics using quantum dot nanostructures. *Solid State Communications*, 135(9–10):591–601, 2005. Fundamental Optical and Quantum Effects in Condensed Matter.

[90] M. Heiss, S. Conesa-Boj, J. Ren, H. H. Tseng, A. Gali, A. Rudolph, E. Uccelli, F. Peiró, J. R. Morante, D. Schuh, E. Reiger, E. Kaxiras, J. Arbiol, and Fontcuberta. Direct correlation of crystal structure and optical properties in wurtzite/zinc-blende GaAs nanowire heterostructures. *Phys. Rev. B*, 83:045303, 2011.

[91] S. W. Hell and J. Wichmann. Breaking the diffraction resolution limit by stimulated emission: stimulated-emission-depletion fluorescence microscopy. *Optics Letters*, 19(11):780–782, June 1994.

[92] C. Herring. Effect of time-reversal symmetry on energy bands of crystals. *Phys. Rev.*, 52:361–365, 1937.

[93] A. A. High, A. T. Hammack, J. R. Leonard, Sen Yang, L. V. Butov, T. Ostatnický, M. Vladimirova, A. V. Kavokin, T. C. H. Liew, K. L. Campman, and A. C. Gossard. Spin currents in a coherent exciton gas. *Physical Review Letters*, 110(24), June 2013.

[94] A. A. High, J. R. Leonard, A. T. Hammack, M. M. Fogler, L. V. Butov, A. V. Kavokin, K. L. Campman, and A. C. Gossard. Spontaneous coherence in a cold exciton gas. *Nature*, 483(7391):584–588, 2012.

[95] A. A. High, A. K. Thomas, G. Grosso, M. Remeika, A. T. Hammack, A. D. Meyertholen, M. M. Fogler, L. V. Butov, M. Hanson, and A. C. Gossard. Trapping indirect excitons in a GaAs quantum-well structure with a diamond-shaped electrostatic trap. *Phys. Rev. Lett.*, 103:087403, 2009.

[96] D. J. Hilton and C. L. Tang. Optical orientation and femtosecond relaxation of spin-polarized holes in GaAs. *Phys. Rev. Lett.*, 89:146601, September 2002.

[97] W. R. Hindmarsh. *Atomic Spectra (Commonwealth Library)*. Pergamon Press, Oxford, England, 0 edition, August 1967.

[98] Y. H. Huo, B. J. Witek, S. Kumar, J. R. Cardenas, J. X. Zhang, N. Akopian, R. Singh, E. Zallo, R. Grifone, D. Kriegner, R. Trotta, F. Ding, J. Stangl, V. Zwiller, G. Bester, A. Rastelli, and O. G. Schmidt. A light-hole exciton in a quantum dot. *Nat Phys*, 10(1):46–51, January 2014.

[99] C. J. Hwang. Lifetimes of Free and Bound Excitons in High-Purity GaAs. *Phys. Rev. B*, 8:646–652, July 1973.

[100] Z. Ikonic, V. Milanovic, and D. Tjapkin. Valence subband structure of [100]-, [110]-, and [111]-grown GaAs-(Al,Ga)As quantum wells and the accuracy of the axial approximation. *Physical Review B*, 46(7):4285–4288, August 1992.

[101] E. L. Ivchenko and G. E. Pikus. *Superlattices and other heterostructures: symmetry and optical phenomena*. Springer, 1997.

[102] G. Jacopin, L. Rigutti, L. Largeau, F. Fortuna, F. Furtmayr, F. H. Julien, M. Eickhoff, and M. Tchernycheva. Optical properties of wurtzite/zinc-blende heterostructures in GaN nanowires. *Journal of Applied Physics*, 110(6):064313, September 2011.

[103] U. Jahn, J. Lähnemann, C. Pfüller, O. Brandt, S. Breuer, B. Jenichen, M. Ramsteiner, L. Geelhaar, and H. Riechert. Luminescence of GaAs nanowires consisting of wurtzite and zinc-blende segments. *Physical Review B*, 85(4), January 2012.

[104] J. M. Jancu, R. Scholz, de Andrada, and G. C. La Rocca. Atomistic spin-orbit coupling and k·p parameters in III-V semiconductors. *Phys. Rev. B*, 72:193201, 2005.

[105] A. Jarmola, V. M. Acosta, K. Jensen, S. Chemerisov, and D. Budker. Temperature- and Magnetic-Field-Dependent Longitudinal Spin Relaxation in Nitrogen-Vacancy Ensembles in Diamond. *Phys. Rev. Lett.*, 108:197601, May 2012.

[106] H. Kakibayashi, F. Nagata, Y. Katayama, and Y. Shiraki. Structure analysis of oval defect on molecular beam epitaxial GaAs layer by cross-sectional transmission electron microscopy observation. *Japanese Journal of Applied Physics*, 23:L846–L848, November 1984.

[107] E. Kammann, T. C. H. Liew, H. Ohadi, P. Cilibrizzi, P. Tsotsis, Z. Hatzopoulos, P. G. Savvidis, A. V. Kavokin, and P. G. Lagoudakis. Nonlinear optical spin Hall effect and long-range spin transport in polariton lasers. *Phys. Rev. Lett.*, 109:036404, 2012.

[108] V. A. Karasyuk, M. L. W. Thewalt, and A. J. SpringThorpe. Strain Effects on Bound Exciton Luminescence in Epitaxial GaAs Studied Using a Wafer Bending Technique. *phys. stat. sol. (b)*, 210(2):353–359, 1998.

[109] T. Karin. onedp: Matlab interface for Gregory Snider's 1D Poisson solver. . *Mathworks Central File Exchange*, File ID: #54505, December 2015.

[110] T. Karin. h2dblab - Energies, wavefunctions and matrix elements for hydrogen atom in magnetic field. *Mathworks Central File Exchange*, File ID: #56792, April 2016.

[111] T. Karin, R. J. Barbour, C. Santori, Y. Yamamoto, Y. Hirayama, and K.-M. C. Fu. Radiative properties of multicarrier bound excitons in GaAs. *Phys. Rev. B*, 91:165204, April 2015.

[112] T. Karin, X. Linpeng, M. V. Durnev, R. Barbour, M. M. Glazov, E. Y. Sherman, S. Watkins, S. Seto, and K.-M. C. Fu. Longitudinal spin-relaxation of donor-bound electrons in direct bandgap semiconductors, May 2016.

[113] Todd Karin, Xiayu Linpeng, M. M. Glazov, M. V. Durnev, E. L. Ivchenko, Sarah Harvey, Ashish K. Rai, Arne Ludwig, Andreas D. Wieck, and Kai-Mei C. Fu. Giant permanent dipole moment of two-dimensional excitons bound to a single stacking fault. *Phys. Rev. B*, 94:041201, Jul 2016.

[114] J. Kasai and M. Kawata. Microphotoluminescence of oval defects in a GaAs layer grown by molecular beam epitaxy. *Applied Physics Letters*, 73(14):2012–2014, October 1998.

[115] K. V. Kavokin. Spin relaxation of localized electrons in n-type semiconductors. *Semicond. Sci. Technol.*, 23(11):114009, November 2008.

[116] A. V. Khaetskii and Y. V. Nazarov. Spin-flip transitions between Zeeman sublevels in semiconductor quantum dots. *Phys. Rev. B*, 64:125316, 2001.

[117] M. Kira and S. W. Koch. *Semiconductor quantum optics*. Cambridge University Press, Cambridge, England, 1 edition, April 2012.

[118] R. S. Knox. *Theory of excitons - supplement 5 solid state physics*. Academic Press, New York, New York, December 1963.

[119] P. M. Koenraad and M. E. Flatte. Single dopants in semiconductors. *Nat Mater*, 10(2):91–100, February 2011.

[120] R. Kolesov, K. Xia, R. Reuter, R. Stöhr, A. Zappe, J. Meijer, P. R. Hemmer, and J. Wrachtrup. Optical detection of a single rare-earth ion in a crystal. *Nature Communications*, 3:1029, August 2012.

[121] T. Komatsu. Optical properties of excitons confined two-dimensionally in a stacking fault plane in BiI3. *Journal of Luminescence*, 40-41:495–496, February 1988.

[122] G. F. Koster. *Space Groups and Their Representations*. Academic Press, January 1957.

[123] G. F. Koster, J. O. Dimmock, and R. G. Wheeler. *Properties of the thirty-two point groups*. M.I.T. Press, 1963.

[124] M. Kroutvar, Y. Ducommun, D. Heiss, M. Bichler, D. Schuh, G. Abstreiter, and J. J. Finley. Optically programmable electron spin memory using semiconductor quantum dots. *Nature*, 432(7013):81–84, November 2004.

[125] J. Kundrotas. Impact ionization coefficient of excitons in n-GaAs. *Semiconductor Science and Technology*, 14(5):461, May 1999.

[126] T. D. Ladd, F. Jelezko, R. Laflamme, Y. Nakamura, C. Monroe, and J. L. O'Brien. Quantum computers. *Nature*, 464(7285):45–53, March 2010.

[127] J. Lähnemann, O. Brandt, U. Jahn, C. Pfüller, C. Roder, P. Dogan, F. Grosse, A. Belabbes, F. Bechstedt, A. Trampert, and L. Geelhaar. Direct experimental determination of the spontaneous polarization of GaN. *Phys. Rev. B*, 86:081302, 2012.

[128] J. Lähnemann, U. Jahn, O. Brandt, T. Flissikowski, P. Dogan, and H. T. Grahn. Luminescence associated with stacking faults in GaN. *Journal of Physics D: Applied Physics*, 47(42):423001, October 2014.

[129] L. D. Landau and E. M. Lifshitz. *Quantum mechanics: Non-relativistic theory (vol. 3)*. Butterworth-Heinemann, Oxford, 1977.

[130] L. D. Landau and L. M. Lifshitz. *Quantum Mechanics, Third Edition: Non-Relativistic Theory (Volume 3)*. Butterworth-Heinemann, 3 edition, January 1981.

[131] S. D. Lester, F. A. Ponce, M. G. Craford, and D. A. Steigerwald. High dislocation densities in high efficiency GaN-based light-emitting diodes. *Applied Physics Letters*, 66(10):1249–1251, March 1995.

[132] Z. Li-Bo and D. Meng-Li. High Accuracy Calculation for Excited-State Energies of H Atoms in a Magnetic Field. *Communications in Theoretical Physics*, 52(2):339, 2009.

[133] C.-Y. Lu, Y. Zhao, A. N. Vamivakas, C. Matthiesen, S. Fält, A. Badolato, and M. Atatüre. Direct measurement of spin dynamics in InAs/GaAs quantum dots using time-resolved resonance fluorescence. *Phys. Rev. B*, 81:035332, Jan 2010.

[134] J. M. Luttinger. Quantum Theory of Cyclotron Resonance in Semiconductors: General Theory. *Physical Review Online Archive (Prola)*, 102(4):1030–1041, May 1956.

[135] O. Madelung. *Semiconductors: Data handbook*. Springer, 3rd edition, January 2004.

[136] O. Madelung, U. Rössler, and M. Schulz, editors. *II-VI and I-VII Compounds; Semimagnetic Compounds*. Landolt-Börnstein - Group III Condensed Matter, Volume 41B. Springer-Verlag, 1999.

[137] D. T. F. Marple and H. Ehrenreich. Dielectric constant behavior near band edges in CdTe and Ge. *Phys. Rev. Lett.*, 8:87–89, February 1962.

[138] F. Marquardt and V. A. Abalmassov. Spin relaxation in a quantum dot due to Nyquist noise. *Phys. Rev. B*, 71:165325, April 2005.

[139] H. Mathieu, J. Camassel, and F. Ben Chekroun. Stress effects on excitons bound to neutral acceptors in InP. *Physical Review B*, 29:3438–3448, March 1984.

[140] P. C. Maurer, J. R. Maze, P. L. Stanwix, L. Jiang, A. V. Gorshkov, A. A. Zibrov, B. Harke, J. S. Hodges, A. S. Zibrov, A. Yacoby, D. Twitchen, S. W. Hell, R. L. Walsworth, and M. D. Lukin. Far-field optical imaging and manipulation of individual spins with nanoscale resolution. *Nat Phys*, 6(11):912–918, November 2010.

[141] F. Meier and B. Zakharchenya. *Optical orientation*. North Holland, November 1984.

[142] I. A. Merkulov, A. L. Efros, and M. Rosen. Electron spin relaxation by nuclei in semiconductor quantum dots. *Phys. Rev. B*, 65:205309, April 2002.

[143] C. Monroe and J. Kim. Scaling the Ion Trap Quantum Processor. *Science*, 339(6124):1164–1169, March 2013.

[144] V. Naumann, D. Lausch, A. Hähnel, J. Bauer, O. Breitenstein, A. Graff, M. Werner, S. Swatek, S. Großer, J. Bagdahn, and C. Hagendorf. Explanation of potential-induced degradation of the shunting type by Na decoration of stacking faults in Si solar cells. *Solar Energy Materials and Solar Cells*, 120:383–389, January 2014.

[145] B. Nelsen, R. Balili, D. W. Snoke, L. Pfeiffer, and K. West. Lasing and polariton condensation: Two distinct transitions in GaAs microcavities with stress traps. *Journal of Applied Physics*, 105(12):122414, June 2009.

[146] H. S. Nguyen, D. Vishnevsky, C. Sturm, D. Tanese, D. Solnyshkov, E. Galopin, A. Lemaître, I. Sagnes, A. Amo, G. Malpuech, and J. Bloch. Realization of a double-barrier resonant tunneling diode for cavity polaritons. *Phys. Rev. Lett.*, 110:236601, 2013.

[147] J. L. O'Brien, A. Furusawa, and J. Vuckovic. Photonic quantum technologies. *Nature Photonics*, 3(12):687–695, December 2009.

[148] B. Pal, K. Goto, M. Ikezawa, Y. Masumoto, P. Mohan, J. Motohisa, and T. Fukui. Type-II behavior in wurtzite InP/InAs/InP core-multishell nanowires. *Applied Physics Letters*, 93(7):073105, August 2008.

[149] P. M. Petroff, R. A. Logan, and A. Savage. Nonradiative recombination at dislocations in III–V compound semiconductors. *Journal of Microscopy*, 118(3):255–261, March 1980.

[150] M. D. Petrovićfi and N. Vukmirović. Spin relaxation in CdTe quantum dots with a single Mn atom. *Phys. Rev. B*, 85:195311, May 2012.

[151] G. E. Pikus, V. A. Maruschak, and A. N. Titkov. Spin splitting of energy bands and spin relaxation of carriers in cubic III-V crystals. *Sov. Phys. Semicond.*, 22:115, 1988.

[152] D. Pines, J. Bardeen, and C. P. Slichter. Nuclear polarization and impurity-state spin relaxation processes in silicon. *Phys. Rev.*, 106:489–498, May 1957.

[153] E. Poem, Y. Kodriano, C. Tradonsky, N. H. Lindner, B. D. Gerardot, P. M. Petroff, and D. Gershoni. Accessing the dark exciton with light. *Nature Physics*, 6(12):993–997, November 2010.

[154] S. V. Poltavtsev, Yu Efimov, Yu Dolgikh, S. A. Eliseev, V. V. Petrov, and V. V. Ovsyankin. Extremely low inhomogeneous broadening of exciton lines in shallow (In,Ga)As/GaAs quantum wells. *Solid State Communications*, 199:47–51, December 2014.

[155] N. Proukakis. *Quantum gases: finite temperature and non-equilibrium dynamics (cold atoms).* Imperial College Press, 1 edition, February 2013.

[156] G. W. p't Hooft, W. A. J. A. van der Poel, L. W. Molenkamp, and C. T. Foxon. Giant oscillator strength of free excitons in GaAs. *Phys. Rev. B*, 35:8281–8284, May 1987.

[157] Y. T. Rebane, Y. G. Shreter, and M. Albrecht. Stacking faults as quantum wells for excitons in wurtzite GaN. *Phys. Stat. Sol. (a)*, 164(1):141–144, November 1997.

[158] R. A. Reynolds. Impact ionization breakdown of n-type epitaxial GaAs at liquid helium temperatures. *Solid-State Electronics*, 11(4):385–390, April 1968.

[159] E. Rittweger, D. Wildanger, and S. W. Hell. Far-field fluorescence nanoscopy of diamond color centers by ground state depletion. *EPL (Europhysics Letters)*, page 14001, April 2009.

[160] W. Rosner, G. Wunner, H. Herold, and H. Ruder. Hydrogen atoms in arbitrary magnetic fields. I. Energy levels and wavefunctions. *Journal of Physics B: Atomic and Molecular Physics*, 17(1):29, 1984.

[161] K. Rottner, R. Helbig, and G. Müller. Piezoelectric constant of InP. *Appl. Phys. Lett.*, 62(4):352–353, January 1993.

[162] P. Roussignol, P. Rolland, R. Ferreira, C. Delalande, G. Bastard, A. Vinattieri, J. Martinez-Pastor, L. Carraresi, M. Colocci, J. F. Palmier, and B. Etienne. Hole polarization and slow hole-spin relaxation in an textitn-doped quantum-well structure. *Phys. Rev. B*, 46:7292–7295, September 1992.

[163] W. Rühle and W. Klingenstein. Excitons bound to neutral donors in InP. *Phys. Rev. B*, 18:7011–7021, December 1978.

[164] Kamyar Saeedi, Stephanie Simmons, Jeff Z. Salvail, Phillip Dluhy, Helge Riemann, Nikolai V. Abrosimov, Peter Becker, Hans-Joachim Pohl, John J. L. Morton, and Mike L. W. Thewalt. Room-Temperature Quantum Bit Storage Exceeding 39 Minutes Using Ionized Donors in Silicon-28. *Science*, 342(6160):830–833, November 2013.

[165] J. J. Sakurai and Jim J. Napolitano. *Modern Quantum Mechanics (2nd Edition)*. Addison-Wesley, San Francisco, California, 2 edition, July 2010.

[166] G. Sallen, B. Urbaszek, M. M. Glazov, E. L. Ivchenko, T. Kuroda, T. Mano, S. Kunz, M. Abbarchi, K. Sakoda, D. Lagarde, A. Balocchi, X. Marie, and T. Amand. Dark-bright mixing of interband transitions in symmetric semiconductor quantum dots. *Phys. Rev. Lett.*, 107:166604, 2011.

[167] C. Schimeczek and G. Wunner. Accurate 2d finite element calculations for hydrogen in magnetic fields of arbitrary strength. *Computer Physics Communications*, 185(2):614–621, February 2014.

[168] J. Schleede, A. Filinov, M. Bonitz, and H. Fehske. Phase diagram of bilayer electron-hole plasmas. *Contrib. Plasma Phys.*, 52(10):819–826, November 2012.

[169] M. Schrader, S. W. Hell, and H. T. M. van der Voort. Potential of confocal microscopes to resolve in the 50-100 nm range. *Applied Physics Letters*, 69(24):3644–3646, December 1996.

[170] M. O. Scully and M. S. Zubairy. *Quantum optics*. Cambridge University Press, Cambridge, England, 1 edition, September 1997.

[171] R. P. Seisyan. Diamagnetic excitons and exciton magnetopolaritons in semiconductors. *Semicond. Sci. Technol.*, 27(5):053001, 2012.

[172] S. Seto, A. Tanaka, Y. Masa, S. Dairaku, and M. Kawashima. Annealing behavior of bound exciton lines in high quality CdTe. *Appl. Phys. Lett.*, 53(16):1524–1526, 1988.

[173] Sherman and D. J. Lockwood. Spin relaxation in quantum dots with random spin-orbit coupling. *Phys. Rev. B*, 72:125340, September 2005.

[174] J. Y. Shi, L. P. Yu, Y. Z. Wang, G. Y. Zhang, and H. Zhang. Influence of different types of threading dislocations on the carrier mobility and photoluminescence in epitaxial GaN. *Applied Physics Letters*, 80(13):2293–2295, April 2002.

[175] Y. Shilo, K. Cohen, B. Laikhtman, K. West, L. Pfeiffer, and R. Rapaport. Particle correlations and evidence for dark state condensation in a cold dipolar exciton fluid. *Nat Commun*, 4, 2013.

[176] B. I. Shklovskii and A. L. Efros. *Electronic Properties of Doped Semiconductors*. Springer Series in Solid-State Sciences. Springer-Verlag Berlin Heidelberg, 1984.

[177] A. V. Shumilin and V. V. Kabanov. Kinetic equations for hopping transport and spin relaxation in a random magnetic field. *Phys. Rev. B*, 92:014206, July 2015.

[178] G. Signorello, E. Lörtscher, P. A. Khomyakov, S. Karg, D. L. Dheeraj, B. Gotsmann, H. Weman, and H. Riel. Inducing a direct-to-pseudodirect bandgap transition in wurtzite GaAs nanowires with uniaxial stress. *Nature Communications*, 5, April 2014.

[179] C. Simon, M. Afzelius, J. Appel, A. Boyer de la Giroday, J. S. Dewhurst, N. Gisin, Y. C. Hu, F. Jelezko, S. Kröll, H. J. Müller, J. Nunn, S. E. Polzik, G. J. Rarity, H. De Riedmatten, W. Rosenfeld, J. A. Shields, N. Sköld, M. R. Stevenson, R. Thew, A. I. Walmsley, C. M. Weber, H. Weinfurter, J. Wrachtrup, and J. R. Young. Quantum memories. *Eur. Phys. J. D*, 58(1 %@ 1434-6079):1–22, 2010.

[180] G. Snider. 1d poisson. `http://www3.nd.edu/~gsnider/`. Accessed: 2016-06-26.

[181] G. L. Snider, I.-H. Tan, and E. L. Hu. Electron states in mesa-etched one-dimensional quantum well wires. *Journal of Applied Physics*, 68(6):2849–2853, September 1990.

[182] D. Snoke, S. Denev, Y. Liu, L. Pfeiffer, and K. West. Long-range transport in excitonic dark states in coupled quantum wells. *Nature*, 418(6899):754–757, 2002.

[183] D. W. Snoke. Coherence and optical emission from bilayer exciton condensates. *Advances in Condensed Matter Physics*, 2011:1–7, 2011.

[184] David W. Snoke. Dipole excitons in coupled quantum wells: toward an equilibrium exciton condensate, August 2012.

[185] D. Spirkoska, J. Arbiol, A. Gustafsson, S. Conesa-Boj, F. Glas, I. Zardo, M. Heigoldt, M. H. Gass, A. L. Bleloch, S. Estrade, M. Kaniber, J. Rossler, F. Peiro, J. R. Morante, G. Abstreiter, L. Samuelson, and Fontcuberta. Structural and optical properties of high quality zinc-blende/wurtzite GaAs nanowire heterostructures. *Phys. Rev. B*, 80:245325, December 2009.

[186] D. Spirkoska, A. L. Efros, W. R. L. Lambrecht, T. Cheiwchanchamnangij, A. F. Morral, and G. Abstreiter. Valence band structure of polytypic zinc-blende/wurtzite GaAs nanowires probed by polarization-dependent photoluminescence. *Phys. Rev. B*, 85:045309, 2012.

[187] C. R. Stanley, M. C. Holland, A. H. Kean, M. B. Stanaway, R. T. Grimes, and J. M. Chamberlain. Electrical characterization of molecular beam epitaxial gaas with peak electron mobilities up to $\simeq 4 \times 10^5 \mathrm{cm}^2\mathrm{V}^{-1}\mathrm{s}^{-1}$. *Applied Physics Letters*, 58(5):478–480, February 1991.

[188] M. Steger, K. Saeedi, M. L. W. Thewalt, J. J. L. Morton, H. Riemann, N. V. Abrosimov, P. Becker, and H. J. Pohl. Quantum information torage

for over 180 s Using Donor Spins in a ^{28}Si "Semiconductor Vacuum". *Science*, 336(6086):1280–1283, June 2012.

[189] M. Syperek, D. R. Yakovlev, I. A. Yugova, J. Misiewicz, I. V. Sedova, S. V. Sorokin, A. A. Toropov, S. V. Ivanov, and M. Bayer. Long-lived electron spin coherence in CdSe/Zn(S,Se) self-assembled quantum dots. *Phys. Rev. B*, 84:085304, August 2011.

[190] I.-H. Tan, G. L. Snider, L. D. Chang, and E. L. Hu. A self-consistent solution of Schrödinger-Poisson equations using a nonuniform mesh. *Journal of Applied Physics*, 68(8):4071–4076, October 1990.

[191] C. Testelin, F. Bernardot, B. Eble, and M. Chamarro. Hole–spin dephasing time associated with hyperfine interaction in quantum dots. *Phys. Rev. B*, 79(19):195440, May 2009.

[192] D. G. Thomas and J. J. Hopfield. A magneto-Stark effect and exciton motion in CdS. *Phys. Rev.*, 124:657–665, 1961.

[193] T. N. D. Tibbits, P. Beutel, M. Grave, C. Karcher, E. Oliva, G. Siefer, A. Wekkeli, M. Schachtner, F. Dimroth, A. W. Bett, R. Krause, M. Piccin, N. Blanc, M. Muñoz Rico, C. Arena, E. Guiot, C. Charles-Alfred, C. Drazek, F. Janin, L. Farrugia, B. Hoarau, J. Wasselin, A. Tauzin, T. Signamarcheix, T. Hannappel, K. Schwarzburg, and A. Dobrich. New efficiency frontiers with wafer-bonded multi-junction solar cells. 29th European PV Solar Energy Conference and Exhibition, September 2014.

[194] J. Tribollet. Theory of the electron and nuclear spin coherence times of shallow donor spin qubits in isotopically and chemically purified zinc oxide. *Eur. Phys. J. B*, 72(4):531–540, 2009.

[195] D. A. Turton, G. D. Reid, and G. S. Beddard. Accurate analysis of fluorescence decays from single molecules in photon counting experiments. *Anal. Chem.*, 75(16):4182–4187, June 2003.

[196] A. Twardowski, E. Pokita, and J. A. Gaj. Valence band spin-orbit splitting in CdTe and $Cd_{1-x}Mn_xTe$ and giant Zeeman effect in the Γ_7 band of $Cd_{1-x}Mn_xTe$. *Solid State Commun.*, 36(11):927–930, 1980.

[197] A. M. Tyryshkin, J. J. L. Morton, S. C. Benjamin, A. Ardavan, G. A. D. Briggs, J. W. Ager, and S. A. Lyon. Coherence of spin qubits in silicon. *Journal of Physics: Condensed Matter*, 18(21), 2006.

[198] A. M. Tyryshkin, S. Tojo, J. J. L. Morton, H. Riemann, N. V. Abrosimov, P. Becker, H. J. Pohl, T. Schenkel, M. L. W. Thewalt, K. M. Itoh, and S. A. Lyon. Electron spin coherence exceeding seconds in high-purity silicon. *Nat. Mater.*, 11(2):143–147, 2012.

[199] N. Vainorius, S. Lehmann, D. Jacobsson, L. Samuelson, K. A. Dick, and M. E. Pistol. Confinement in thickness-controlled GaAs polytype nanodots. *Nano Lett.*, 15(4):2652–2656, April 2015.

[200] A. Vinattieri, Jagdeep Shah, T. C. Damen, D. S. Kim, L. N. Pfeiffer, M. Z. Maialle, and L. J. Sham. Exciton dynamics in GaAs quantum wells under resonant excitation. *Phys. Rev. B*, 50:10868–10879, October 1994.

[201] N. Wang, K. K. Fung, and I. K. Sou. Direct observation of stacking fault nucleation in the early stage of ZnSe/GaAs pseudomorphic epitaxial layer growth. *Applied Physics Letters*, 77(18):2846–2848, October 2000.

[202] N. Wang, I. K. Sou, and K. K. Fung. Transmission electron microscopy study of stacking faults and the associated partial dislocations in pseudomorphic epilayers of ZnSe/GaAs(001). *Journal of Applied Physics*, 80(9):5506–5508, November 1996.

[203] N. Wang, I. K. Sou, and K. K. Fung. Transmission electron microscopy study of stacking-fault trapezoids and stacking-fault tubes in ZnSe/GaAs(001) pseudomorphic epitaxial layers. *Philosophical Magazine Letters*, 76(3):153–158, September 1997.

[204] R. J. Warburton, C. Schulhauser, D. Haft, C. Schäflein, K. Karrai, J. M. Garcia, W. Schoenfeld, and P. M. Petroff. Giant permanent dipole moments of excitons in semiconductor nanostructures. *Phys. Rev. B*, 65:113303, February 2002.

[205] C. Weisbuch and Borge Vinter. *Quantum semiconductor structures: fundamentals and applications*. Academic Press, 1991.

[206] H. Weman, G. M. Treacy, H. P. Hjalmarson, K. K. Law, J. L. Merz, and A. C. Gossard. Impact ionization of excitons and donors in $\mathrm{Al}_x\mathrm{Ga}1 - x\mathrm{As}/(n$-type GaAs):Si quantum wells. *Phys. Rev. B*, 45:6263–6266, 1992.

[207] R. Winkler. *Spin–orbit coupling effects in two-dimensional electron and hole systems*. Springer, 2003.

[208] L. M. Woods, T. L. Reinecke, and Y. Lyanda-Geller. Spin relaxation in quantum dots. *Phys. Rev. B*, 66(16):161318, October 2002.

[209] H.-R. Xia, C.-Y. Ye, and S.-Y. Zhu. Experimental observation of spontaneous emission cancellation. *Phys. Rev. Lett.*, 77:1032–1034, August 1996.

[210] E. Yablonovitch, B. J. Skromme, R. Bhat, J. P. Harbison, and T. J. Gmitter. Band bending, Fermi level pinning, and surface fixed charge on chemically prepared surfaces. *Appl. Phys. Lett.*, 54(6):555–557, 1989.

[211] A. M. Yakunin, A. Yu. Silov, P. M. Koenraad, J. H. Wolter, W. Van Roy, J. De Boeck, J.-M. Tang, and M. E. Flatté. Spatial structure of an individual Mn acceptor in GaAs. *Phys. Rev. Lett.*, 92:216806, May 2004.

[212] M. Yamaguchi, A. Yamamoto, and Y. Itoh. Effect of dislocations on the efficiency of thin-film GaAs solar cells on Si substrates. *Journal of Applied Physics*, 59(5):1751–1753, March 1986.

[213] Y. Yamamoto. Present Status and Future Prospects of Quantum Information Processing: With Special Focus on Optically Controlled Semiconductor Spins and Single-Photon Technologies. *Japanese Journal of Applied Physics*, 50(10):100001, October 2011.

[214] Y. Yamamoto and A. Imamoglu. *Mesoscopic quantum optics*. Wiley-Interscience, New York, New York, 1 edition, October 1999.

[215] P. Y. Yu and M. Cardona. *Fundamentals of semiconductors: physics and materials properties*. Springer, London, England, 2010.

[216] X. Zhou, T. Y. Hsiang, and R. J. D. Miller. Monte Carlo study of photogenerated carrier transport in GaAs surface space-charge fields. *Journal of Applied Physics*, 66(7):3066–3073, October 1989.

[217] S. Y. Zhu and M. O. Scully. Spectral line elimination and spontaneous emission cancellation via quantum interference. *Physical Review Letters*, 76:388–391, January 1996.